University of Southampton

Faculty of Engineering and Physical Sciences
Tony Davies High Voltage Laboratory
Electrical and Power Engineering Group
Advanced Photonic Sensing

Partial Discharge Detection Using Distributed Acoustic Sensing

Author:
Laurie Kirkcaldy
laurie.kirkcaldy@soton.ac.uk

Supervisor:
Prof. Paul Lewin
pll@ecs.soton.ac.uk
2nd Supervisor:
Dr. James Pilgrim
jp2@ecs.soton.ac.uk

Thesis submitted in partial fulfilment for the degree of Doctor of Philosophy

19th October 2022

A catalogue copy is available from the University of Southampton Library Service, an electronic catalogue copy is available from ePrints Soton.

ORCID: 0000-0003-1726-7951
Cite as: L. J. Kirkcaldy, *Partial Discharge Detection Using Distributed Acoustic Sensing*, PhD Thesis, University of Southampton (2022)

Typeset using LaTeX 2_ε

Abstract

University of Southampton
Faculty of Engineering and Physical Sciences
Tony Davies High Voltage Laboratory
Electrical and Power Engineering Group
Advanced Photonic Sensing

Partial Discharge Detection Using Distributed Acoustic Sensing

Laurie Kirkcaldy

The performance and reliability of high voltage systems are critical for power generation and distribution, allowing power to continue flowing for everyday life. Partial discharge is both a cause and important indicator of damage developing within electrical insulation. By monitoring partial discharge activity during an electrical asset's lifetime, an assessment of the insulation condition can be made and used to inform decisions about repairs or replacement. Most existing methods for partial discharge detection are only able to cover either a single device or short distance, requiring many discrete sensors for total coverage. Distributed acoustic sensing is already used widely in other commercial areas for geophysics and seismic data acquisition. However, it has been dismissed for detection of partial discharge due to low sample rates in comparison to the frequency of acoustic emissions from partial discharges. This thesis demonstrates through aliasing mechanisms, that detection of these high-frequency acoustic emissions can be downsampled and identified.

This thesis reports report fibre-optic based distributed acoustic sensing for detection and measurement of partial discharge providing a continuous detection region of 5 km with inherent positional information within 1.25 m. The acoustic-strain interaction on the fibre optic, including the surrounding acoustic environment, is modelled demonstrating significant ringing due to reverberations of the initial impulse, as well as demonstrating an important aliasing method permitting the detection of much higher frequency signals than the original sampling rate. Laboratory partial discharge sources of both void and treeing varieties were manufactured and used to demonstrate this detection experimentally, covering a range of partial discharge sizes and sensor placements.

This work also includes development of an alternative synchronisation method to allow for detailed sample-for-sample comparisons between different electrical, acoustic and distributed acoustic sensing measurements; each with different data types and sample rates.

Contents

List of Figures

List of Abbreviations

φ-OTDR Phase optical time domain reflectometry

AE acoustic emissions

APC Angled physical contact

AS Anti-stokes

COTDR Coherent optical time domain reflectometry

DAS Distributed acoustic sensing

DFT Discrete Fourier transform

DGA Dissolved gas analysis

DTS Distributed temperature sensing

FBE Frequency band energy

FBG Fibre Bragg grating

FDM Frequency division multiplexing

FFT Fast Fourier transform

FUT Fibre under test

HFCT High frequency current transformer

HV High voltage

OFDR Optical frequency domain reflectometry

OTDR Optical time domain reflectometry

PD Partial discharge

PM Polarization maintaining

POTDR Polarisation optical time domain reflectometry

PRPD phase resolved partial discharge

PSA Pulse sequence analysis

PZT Piezo-electric transducer

RFCT Radio frequency current transformer

S Stokes

SM Single-mode

SNR Signal to noise ratio

UHF Ultra-high frequency

XLPE Cross-linked polyethylene

Nomenclature

ϵ	Permittivity, $\mathrm{F\,m^{-1}}$
λ	Wavelength, nm
ν	Poisson's Ratio
ρ	Density, $\mathrm{kg\,m^{-3}}$
ρ	Optical phase, rad
σ	Stress, $\mathrm{N\,m^{-1}}$
ε	Strain
ξ	Fibre length temporary change due to stress, Pa
B	Bulk Modulus, Pa
D	Electric Flux Density, $\mathrm{C\,m^{-2}}$
E_{ext}	Extinction field, $\mathrm{V\,m^{-1}}$
E_{inc}	Inception field, $\mathrm{V\,m^{-1}}$
E_{i}	Electric field within an insulator, $\mathrm{V\,m^{-1}}$
E_{v}	Electric field within a void, $\mathrm{V\,m^{-1}}$
I	Intensity
l	Length, m
L_{G}	Gauge length, m
P	Gas pressure, Pa
p	Relative gas pressure, Pa
P_0	Steady state pressure, Pa
p_{ab}	Photo-elastic constant in the direction a>b
P_{w}	Wave pressure, Pa

Q	Charge, C
T	Temperature, K
u	Velocity, $\mathrm{m\,s^{-1}}$
V	Voltage / Potential Difference, V
w	Sensing window period, s
Y	Modulus of elasticity, Pa
Z	Impedance, Acoustic
$И$	Iterator operator

Declaration of Authorship

I, Laurie Kirkcaldy, declare that this thesis (Partial Discharge Detection Using Distributed Acoustic Sensing) and the work presented in it are my own and has been generated by me as the result of my own original research. I confirm that:

1. This work was done wholly or mainly while in candidature for a research degree at this University;
2. Where any part of this thesis has previously been submitted for a degree or any other qualification at this University or any other institution, this has been clearly stated;
3. Where I have consulted the published work of others, this is always clearly attributed;
4. Where I have quoted from the work of others, the source is always given. With the exception of such quotations, this thesis is entirely my own work;
5. I have acknowledged all main sources of help;
6. Where the thesis is based on work done by myself jointly with others, I have made clear exactly what was done by others and what I have contributed myself;
7. Parts of this work have been published in the works listed.

Signed: *Date:*

19th October 2022

Publications and Conferences

1. L. J. Kirkcaldy, J. Pilgrim, R. Rogers, G. Lees, "Distributed Acoustic Sensing of Partial Discharge: Initial Findings", *Jicable'19*, F2-11 (2019) - Best **Poster** and **Paper**

2. L. J. Kirkcaldy, P. Lewin, G. Lees, R. Rogers, "Partial Discharge Detection Using Distributed Acoustic Sensing at the Oil-Pressboard Interface", *IEEE Sensors Applications Symposium* (2021) - **Paper** and **Talk**

3. L. J. Kirkcaldy, P. Lewin, G. Lees, R. Rogers, "Time Synchronised Distributed Acoustic Sensing of Partial Discharge", *IEEE Transactions on Dielectrics and Electrical Insulation* - **Paper**

Acknowledgements

Firstly, I would like to thank my original primary supervisor Dr. James Pilgrim for his supervision and original inspiration to study at Southampton and stay on as a PhD student. I would also like to thank Prof. Paul Lewin for his extensive experience and detailed ideas.

I gratefully acknowledge Advanced Photonic Sensing (APSensing) for both sponsoring this PhD as well as providing support and the hardware necessary for all the DAS & DTS experiments. Optics11 also generously provided an OptimAE system free-of-charge for experimental results of their acoustic sensors with different partial discharge sources. This alone allowed for a much more cohesive story through this thesis from PD to acoustic to DAS.

I am thankful for the many open-source software packages used within this research from the data processing to the generation of this very report. To mention a few specifically: *J.D. Hunter* for providing the Python library MatPlotLib, used for a majority of the graphing and data visualisation; Python the programming language itself, and Emmanuel Bossy for development of SimSonic a software suite for simulation of ultrasound propagation in an actually useable and intuitive software package. I should acknowledge the support of my house mates, Olly, Rex, and Josh, all of whom are, or were students at the university, for the discussions and advice on both technical and administerial matters throughout the last 4 years, especially in the gap between transferring supervisors. I especially recognise and appreciate my parents who have supported me staying as a student for another 4 years on top of my undergraduate degree, maintaining a lack of a "proper" job for so long.

Finally, but by no means least, thanks also to the amazing laboratory and the technicians at the Tony Davies high voltage laboratory at Southampton, specifically, Alan Welford, Ian Virtanen, and Charlie Reed for their continued support and help throughout the entire project.

Chapter 1

Introduction

Damage to high voltage equipment such as transformers and cables can cause large power outages and reduction in power transfer ability [1]. Despite being built to withstand harsh conditions and continuous operation, at least one fault is likely to occur during the lifetime of the equipment [2, 3]. The repairs to these problems can cost a large amount of money and down-time. Due to the nature of high voltage breakdowns, the cause of a fault may not be obvious: the breakdown or damage usually occurs within the insulation, hidden from view, extending the time to repair [1]. Prevention is often better than a cure. Many methods exist to identify and analyse pre-breakdown phenomena, looking for various tell-tale signs of this damage occurring. Electrical methods of examining voltage and current waveforms are the most ubiquitous [4–6], and can be applied on-line (with operating voltage still present) [7, 8]; although connections to equipment may have to be undertaken off-line. Other methods include searching for RF emissions [9, 10], thermal analysis [11, 12] as well as acoustical methods [13]. These are typically more used to pinpointing locations, or on specific/problematic High voltage (HV) equipment rather than cables and other distributed elements.

Most, if not all of these methods, are looking for phenomena caused by Partial discharge (PD). Partial discharge is a key indicator of damage alongside causing damage by its very nature, and is one of the most consistent and widely accepted precursors to problematic issues within HV systems [14–18]. Partial discharges are, by definition, a type of discharge in which a localised breakdown occurs, but does not fully bridge two conductors [19]. The breakdown occurs due to the electric field exceeding the dielectric strength of the insulating medium [20]. The processes behind PD are “inherently complex stochastic processes that exhibit significant statistical variability" [21]; resulting in a range of amplitude, shapes and time of occurrence. The term PD covers a relatively wide range of phenomena: from discharges within gaps in solid insulation to corona discharge in air or other gases. Each localised breakdown event emits energy in a variety of forms: heat, electromagnetic waves, and acoustic [19]. All of these phenomena have matching detection methods applied with respective advantages and disadvantages; for example, detecting visible light from a PD is not much use within a cable.

Distributed acoustic sensing (DAS) uses optical methods within a conventional glass fibre optic; not to directly pick up emitted light from a PD event, but instead measures strain, and therefore, can measure acoustic emissions [22]. As the sensing element itself is a glass fibre, this allows for the sensing element to pass through hostile environments without worry of compromising insulation or degradation of the sensing elements over time. As DAS is not only a singular measurement, but a distributed array of measurements over a notable distance, only one system is required to measure thousands, if not tens of thousands of separate points. This allows for a single fibre optic cable to be passed around the entire perimeter and volume of multiple devices or cables and provide location-aware information. DAS as a distributed sensing technique has already been deployed in a wide range of industries [23] from earthquake detection systems [24] to oil and gas pipeline monitoring [25]. Each looking for tell-tale acoustic signatures along their lengths. Distributed fibre sensing has not yet been tested for detection of partial discharge or related HV phenomena. Given its tremendous detection ranges, and location abilities, it could be an excellent addition to partial discharge detection and analysis tools.

This work provides experimental results and analysis of a DAS system for the purpose of detecting and measuring PD. Only relying on standard DAS techniques, the acoustic emissions (AE) from a PD cannot normally be seen due to the large mismatch between the high frequency AE, and the relatively lower frequency sample rate of DAS systems. Instead, specific methods are developed such as a type of undersampling: a special effect of aliasing, and the parallel methods for displaying and understanding the resultant data. Through the use of modelling based on fundamental DAS and acoustic concepts, it was found and then matched by experiment that AE from PDs can be detected under certain circumstances. Novel synchronisation methods are utilised, allowing for comparison between different measurement techniques, data types and sample rates by many orders of magnitude. As is demonstrated in this Thesis, DAS is suitable for PD detection, and could be a significant aid in long-distance detection of PD on cables, or better and quicker localisation of faults within equipment.

Below details a brief description of the following chapters in this thesis:

- Chapter 2 describes the different types of PD, their formation and evolution, and why they are such a big issue in HV components. Current detection methods are compared and contrasted in addition to discussing the types of AE typically seen for each type of discharge.

- Chapter 3 covers the fundamental principles of acoustic waves, how they interact at boundaries and the difference of waves in fluids like air and solid materials. The light scattering processes fundamental to DAS are explored, and finally how all these are combined into a distributed sensing system, its uses and limitations.

- Chapter 4 introduces novel ways of using a DAS system by changing the processing of the raw samples extracted from the measuring system in the DAS device in order to allow for undersampling. This is modelled using a variety of tools to emulate a full DAS sampling system from source acoustic emission to data-on-screen. An experiment of using DAS to look

at breakdown events is used as a proof of concept to determine if DAS is at all capable of detecting discharges, and whether this begins to match expectations from modelling. This section also explains the undersampling process key to detecting PD with DAS.

- Chapter 5 describes the experimental methods and results of using a sensing DAS fibre embedded in various partial discharge void test-cells, as well as comparing those results with a conventional capacitive coupling measurement in addition to high-sample rate, discrete, acoustic sensors.

- Chapter 6 repeats experiments with the same measurement and synchronisation techniques as Chapter 5, but with a needle-plane source across an oil-impregnated pressboard to initiate treeing discharge rather than void. Comparison of different fibre positioning is also performed using the distributed elements of the DAS system in addition to synchronising the DAS results with the line-voltage allowing for phase resolved partial discharge analysis.

- Chapter 7 concludes the results and findings of this Thesis, discusses applications well suited to the DAS method of PD detection and details the recommendations of further work of this research.

Chapter 2

Partial Discharge and its Detection

Partial discharge, as implied by its name, is a process of electrical breakdown where the discharge partially bridges insulating material between conductors [21]. The size of the discharge varies on many factors including applied voltage, size and shape of surrounding materials [21, 26], and any damage or lingering effects from previous events [27]. But the discharge is typically very small compared to the available power travelling through the neighbouring conductors. The location of initial discharges is often accompanied by a change in insulation medium with a lower dielectric constant than that of the insulation, such as an air void leading to an increased localised electric field [28]. This uneven distribution then produces, during a discharge event, displacement of charge as the insulating properties of the local area breaks down [29]. Due to these building discharges, the existence of large PD can be serious as the progression can lead to a complete failure of the entire insulation system.

From all these different parameters and environments there are several defined types that the partial discharges can be categorised into. This Chapter defines the different types, their properties, how they form and what this means for detection. Furthermore, the different existing detection methods are described along with their advantages and disadvantages towards certain PD types.

PD only occurs in gases: the presence of PD within liquids has been confirmed to show that the liquid is transformed to a vapour phase before PD occurs [30]. This is due to an avalanche process that can only occur within a gas with free molecules at the electric field strengths at which PDs, would occur. Solid insulation materials if completely homogeneous, would only experience a total breakdown, not PD [30]; therefore, when PD is experienced within a solid, it is because there is some sort of gap or void containing a gas. PDs in these gas pockets are, by definition, self-quenching arcs and other continuous-style discharges such as arcs are excluded from the PD bracket. The discharges are self-quenching either because the accumulated charge dissipates during the discharge, or that the field strength is not large enough to support continued

growth.

2.1 PD Initiation

The process during a PD event is as follows: if the electric field is sufficiently high, free electrons can accelerate towards a positively charged region (such as the positive conductor) at a sufficient speed that colliding with gas molecules ionises them, thereby releasing more free electrons. These new electrons also begin to accelerate and can go on to cause more liberation of electrons through ionisation. This cascading avalanche is known as a Townsend avalanche, pictured in Figure 2.1, resulting in a migration of charge and a discharge occurring. For this to occur, an electron must be provided with enough acceleration to ionise a molecule before actually colliding with said molecule on average; this acceleration occurs due to the electric field E. Therefore, there is a threshold value for the electric field at which point the acceleration is high enough. This is known as the inception point of partial discharge at which point and above the electric field, caused by the applied voltage in the local area, is great enough to cause avalanches [31].

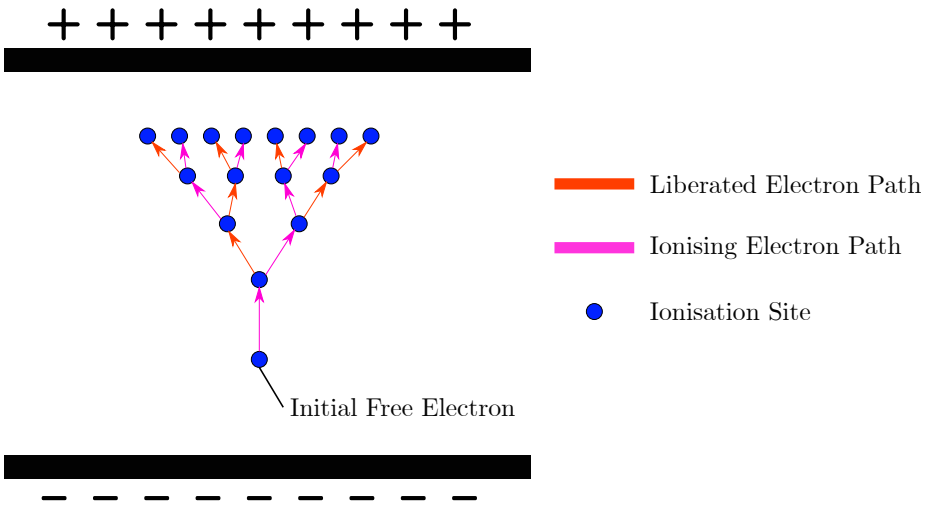

Figure 2.1: Diagram of Townsend avalanche. An initial free electron collides with other molecules, ionising them and liberating more electrons that then go on to cause more collisions.

These movements of charges are also known as streamers where the ionised molecules form briefly conductive channels in a void or cavity [32]. As the streamer is conductive, the built-up electric field begins to decrease as current flows. After a short duration, typically under 100 ns [33], the field across the localised area in the gas reduces enough, to below what is known as the extinction field E_{ext} [34], that the streamer channel collapses and the discharge stops.

Consider a void within otherwise homogeneous insulation material. The

electric field within the insulation E_i and within the void E_v are given as:

$$E_{\mathrm{i}} = \frac{D}{\epsilon_{\mathrm{i}}} \tag{2.1}$$

$$E_{\mathrm{v}} = \frac{D}{\epsilon_{\mathrm{v}}} \tag{2.2}$$

where D is the electric flux density between the conductors at a distance R with a charge Q defined as $D = \frac{Q}{4\pi R^2}$. ϵ_i and ϵ_v are the absolute permittivity of the insulating and void material respectively. As D is directly proportional to the applied voltage, as this is increased, the electric field will be greater in the cavity due to the lower permittivity of the gas in the cavity: $\epsilon_{\mathrm{i}} > \epsilon_{\mathrm{v}} \rightarrow E_{\mathrm{i}} > E_{\mathrm{v}}$.

A widely used inception value at which the electric field is high enough to initiate an avalanche for an air filled void of some kind, E_{inc}, can be found in Equation 2.3 [33, 35]. $(E/P)_{\mathrm{cr}}$ =25.2 $\mathrm{V\,Pa^{-1}\,m^{-1}}$ is the critical constant of proportionality required to sustain the discharge between the electric field E and the gas pressure P, l is the length of the void in the discharge direction, and B is a characteristic of the ionization processes in air taken as 8.6 $\mathrm{m^{-1/2}\,Pa^{-1/2}}$ [36].

$$E_{\mathrm{inc}} = \left(\frac{E}{P}\right)_{\mathrm{cr}} P\left(1 + \frac{B}{\sqrt{Pl}}\right) \tag{2.3}$$

Trapped charges from previous partial discharges can aid or work against new avalanche breakdowns occurring by modifying the resultant electric field [37]. The magnitude of the resultant electric field after a discharge depends on both the applied electric field from HV conductors, and also any remaining charges from previous partial discharge events either through embedding of charges in insulating surfaces, or persisting ionised molecules. This avalanche process as already mentioned, requires an initial free electron to begin this process [38]. This could come from a wide number of sources including field-emitted electrons from surfaces, field induced ionisation of surrounding molecules or even external ionisation sources such as x-rays or cosmic rays. Emission from surfaces is usually quite rare as the materials surrounding a PD site tend to be insulators, and specifically designed not to have free electrons: as to give the insulative properties. This could occur, however, where a sharp point from a conductor points into an area of insulation or gap.

For measurement purposes, in order to find any possible voids, external ionisation sources of high energy X-rays have been used [39] to “force" voids into an increased PD pulse repetition rate. Otherwise, it is likely that small voids do not encounter any free electrons over a long period (minutes) during the test, and would therefore be missed by testing [40]. Additionally, with external initiation such as this, inception voltage is reduced as the source electron can already have a high velocity and not require as much acceleration during the avalanche process. Under natural processes, a combination of these initiation sources occur at differing rates, but is usually dominated by local over-voltage conditions [35].

The size of PDs are defined by the charge dissipated during the discharge event; typically given in pico-Coulombs. However, the absolute charge trans-

ferred at the PD site is not able to be measured and therefore only apparent charge can be observed at the point of measurement. This apparent charge is assumed to be equal to the charge dissipation at the PD site, but attenuation where the measurement point is further away can introduce errors. For measurements in the experimental sections of this Thesis, the distance from PD site to measurement is under 2 m and therefore this error is negligible. The words small, medium, and large are often loosely cited to when referring to sizes of discharges and can produce confusion when engaging in conversation. To clarify this, within this thesis, small discharges will refer to discharges of <20 pC, medium discharges refer to the range 20 pC to 200 pC, and anything over 200 pC can be considered large.

Partial discharge can appear to be stochastic in nature over time due to its probabilistic processes leading to build-up and inception influenced by a great number of different factors [21,38]. Therefore, statistical analysis of partial discharge becomes much more prevalent in describing features when comparing different detection methods rather than the fundamental relationships behind each detected discharge. For most purposes, up to 4 qualities are wanted: the amplitude or size of the electrical discharge, the number of that kind of discharge, its phase relationship to the voltage and possibly its frequency spectra whether in electrical or acoustic domains. From these, much research has been achieved in quantifying the relationships between these and the physical mechanisms of the unseen discharge within a high voltage system [7, 41–50] and are used regularly to compare different detection systems. These methods will be explored in detail in the sections following.

2.2 PD Types

Despite PDs only occurring within gases, depending on the location and surrounding materials the PD can occur in different forms producing their own characteristic traits and damage to insulation. These forms include void, treeing, floating, surface, and corona. Most PD in practice consists of void or treeing discharge within high voltage equipment internally [51–54], and of course corona discharge in air-insulated exposed equipment like overhead lines [37].

2.2.1 Void

Void discharge often occurs in solid insulation, as the name implies, within a gap in the otherwise homogeneous material, shown in Figure 2.2. Insulation in which void discharge can occur that do not have any sort of self-healing properties, such as Cross-linked polyethylene (XLPE), can easily become permanently damaged [55]. Cavities or voids could be from the manufacturing process: although this is unlikely as almost all cables or equipment containing these solid dielectrics are tested for PD before entering service. More often than not, these cavities are caused by repeated heat or physical stress on the insulation mediums, or formed during the installation process [56]. Repeating bending or expansion and contraction due to temperatures generated by the flowing current or surrounding conditions are sufficient under certain circumstances to rip

small voids or form cracks in the insulation. Therefore, the voids often appear near the highest regions of these thermal or mechanical stresses, next to the conductors. Figure 2.2 shows a cross-sectional view of example locations of voids in a medium. These newly-formed void filled with some sort of gas, air or otherwise, undergoes the previously mentioned electron avalanche process triggered by the increased electric field resulting in a discharge in the confined area, that can damage or even vaporize surrounding insulating material. As the permittivity of the gas is less than the surrounding insulation, the electric field is higher in the cavity [26]. This, combined with the lower dielectric strength of the gas means that PD can occur. Typically, voids in the real-world will not manifest as perfect spheroids, but rather a thin, ripped section of insulation or similar non-uniform geometry.

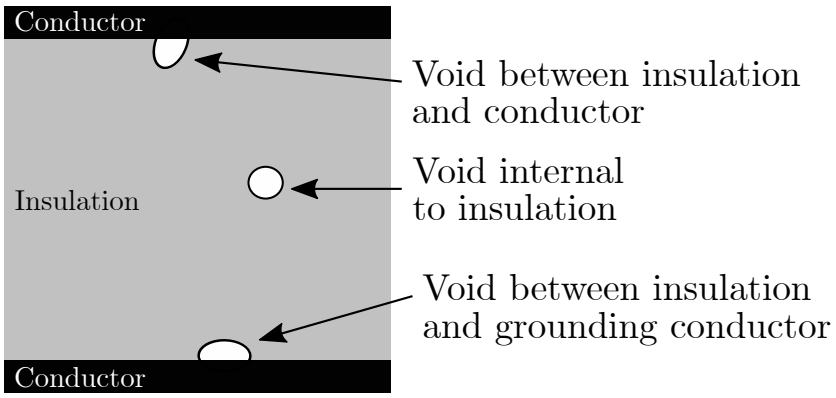

Figure 2.2: Cross-sectional illustration of voids in an insulation medium, showing the different places it can occur.

These cavities existing with an increased electric field applied across them are not however the only requisite for PD to occur because an avalanche needs an initiating electron. As the void is surrounded by intact insulation, there can be a significant time-lag for a discharge-initiating electron to appear to start the discharge process [39]. Conventional testing often uses a higher-than-operating voltage in order to attempt to force these cavities into discharge [57]. Once discharge has been initiated, free electrons will stay in the void for a period of time due to ionisation products from the PD. This means, successive discharges are likely once the inception has occurred, even to below the initial inception voltage.

Electrons and ionisation products can also embed into the surrounding insulation forming space charge in the surrounding material. This, depending on the amplitude and number of discharges, can accumulate enough charge to increase rates of discharge, but also prevent further discharge until the remaining space charge has dissipated enough. That is, if the electric field resulting from remaining space charge when summated with the applied electric field does not exceed the required field to accelerate electrons to cause ionisation events, the Townsend avalanche process will not occur.

2.2.2 Treeing

Treeing discharge is usually initiated from other kinds of discharge where the previous repeated PD has caused damage to the insulation [58]. Repeated discharge in the same area exposing the insulation to extreme heat can cause carbonisation to occur in materials with hydrocarbon chains or similar chemical breakdown processes, so that the area becomes partially conductive. A conductive pathway allows the electric field stress to migrate along to the tip of the channel resulting in a more concentrated field and therefore the growth of the channel [59]. These pathways often spread out in a fractal-like pattern towards an electrode of opposite polarity [60]. After these conductive paths have expanded, eventually, the remaining electric field across the insulation will exceed its dielectric strength and cause a full breakdown and arcing usually resulting in total failure.

As the tree starts growing, the PD amplitude increases and the resultant discharges change characteristics where discharges raise rapidly in amplitude towards the peak voltage points [59]. Once the tracks have extended their lengths, the amplitude drops as the length of the track acts as a potential divider. Additional current flow through the earlier parts of the tree adds to damage, forming a thicker trunk; thereby decreasing resistance and increasing later discharges.

Discharges that occur at the tips of the trees, where the trunk of the tree from previous discharges is conductive, typically produce very small discharges of 30 pC or less [61]. Any branches that are not fully conductive can produce large discharges as current flows along the conductive patches towards the end. This duality of this discharge produces measurements that switch from regions of very little in amplitude, to brief sections of much more intense discharge.

2.2.3 Floating

Floating plane discharge occurs where a conductive surface or object is in the presence of a high electric field and due to surrounding insulating mediums such as oil, cannot charge at the same rate of the applied AC voltage [43]. This results in an increasing electric field between a charged electrode and the object which can exceed the dielectric strength of the insulation, resulting in small breakdowns to the object. The capacitance of such conductive objects can be quite high, creating a wide range of discharge amplitudes from 10 pC to thousands of picocoloumbs that can interfere with other PD measurements [13, 37, 40]. A typical example of this floating plane discharge would be a grounding wire attached to a post under oil, where due to lack of proper termination, a small film of oil insulates the post to the wire resulting in floating plane discharge.

2.2.4 Surface

Surface discharge occurs when the electric field across the surface of an insulation medium exceeds its breakdown strength. From a negatively charged electrode, a greater number of discharges can be expected as the electron avalanche process has more electrons readily available from the electrode [38]. This

effect in addition to the electric fields not being symmetrical on each half-cycle also causes a bias in terms of discharge towards the negative half-cycle.

The discharges occur as charge is accumulated on the insulator surface, this, as in void discharge, influences the build-up and development of future discharges [32] allowing arcs to spread further than a simple electrode gap in air. These discharges are typically large, above 200 pC from experimental results and can easily mask other smaller discharge types that could be happening at the same time.

2.2.5 Corona

Corona is a type of PD where an electron avalanche discharge occurs in free air (or any gas) from one conductor, usually to a grounded surface such as the base of an insulator. Molecules in the gas are ionised from the bombardment of electrons flowing in the avalanche process. The presence of certain gases, such as electro-negative oxygen impedes this process by affecting the electric field distribution once ionised [37]. Again, on negative electrodes, more electrons are readily available producing a heavy bias towards the negative half-cycle. As the surrounding gas is presumed to be a relatively large volume, any space charges generated by a discharge through ionization, are likely to be rapidly swept away from the PD area before the next discharge [62]. This restricts the build-up and continuous discharge that can occur, given a certain applied voltage. Nonetheless, these charges are an important mechanism for developing a continuous pulsed discharge by the rapid accumulation of space charge through overlapping avalanches.

Corona often manifests as small streamers originating from a conductor with both audible and optical indicators mostly in the UV regime, but also extending into visible blue/violet [63][1].

2.3 Existing Detection and Analysis Methods

As these discharges damage the insulation systems over time, detecting PD is important throughout a piece of equipment's lifetime [4]. Beginning at its construction for checking for imperfections, all the way to using PD metrics as a remaining lifetime indicator. As such, a huge amount of research has been done into various detection techniques from classical electrical techniques like the coupling capacitor [42, 64], to novel analysis with neural networks [65].

Many measurement methods are coupled with the accepted standard approach to analysis of the phase resolved partial discharge (PRPD) method. PRPD plots consist of placing scatter points for each discharge on a graph with the x-axis referring to the phase angle of the applied voltage at the time of discharge, against the y-axis of measurement amplitude. Additional false axes are applied through use of colour to show the density of points indicating biases towards certain areas of the graph. This allows for visual representation of complex patterns of PD that can be interpreted to show the classification and number of discharges, along with a multitude of additional parameters.

[1] The blue-UV spectra is specifically due to the presence of nitrogen in air. Other gases experiencing corona would emit their respective emission spectra.

An example of this analysis tool is shown in Figure 2.3, taken from a later experiment of an air void under oil. From this image, and additional statistics pane shown on the right-hand side of the figure, not only can basic details be read such as the applied voltage of 17.78 kV, the minimum threshold of 10 pC, or a peak PD event of 575 pC; but from the shapes shown on the graph multiple types of PD can be distinguished. The intensity of PDs refers the number of repeated events at the same apparent charge and phase, building in colour scale from blue to red. Highlighted pairs of regions A,B & C are indicative of separate voids in their early stages of strong discharge for A&B due to the symmetric, so-called "rabbit ears" [66] where the pattern follows the rising slope of the voltage waveform, and a different stage of progression for C. The patterns highlighted in pair of regions labelled D could be examples of PD at a triple junction interface: where the metal electrode of one conductor and the insulation surrounding the void do not come into perfect contact, allowing for the insulating oil to form the third junction. This region due to the mismatch of permittivities between the fluids and solids form a local enhancement of the electric field, allowing for small discharges to appear [67,68]. Other information that is important to note appears in the extra “Statistics” tab, such as the number of PDs per second (shown as n) and the power dissipation of the partial discharges.

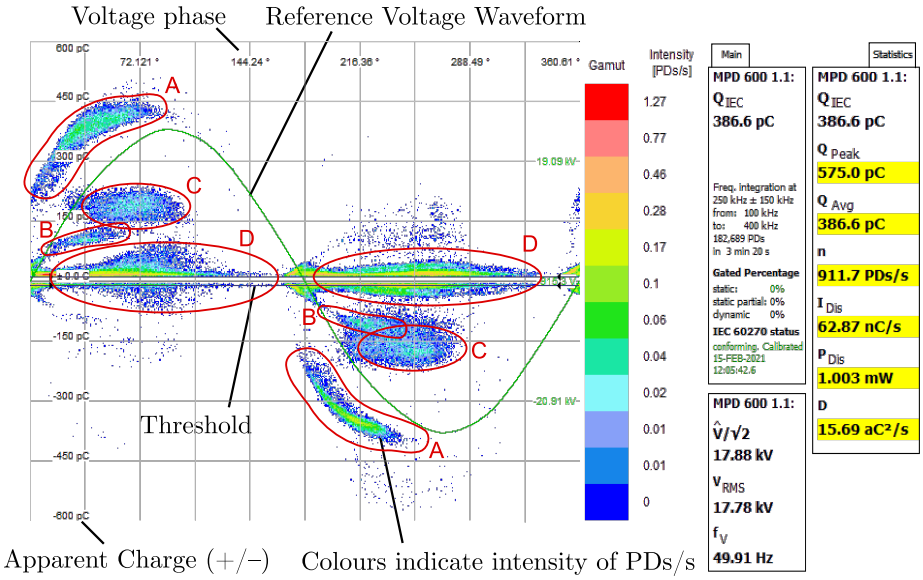

Figure 2.3: An example PRPD graph from the Omicron MPD system showing the various available measurements as well as annotations A-D highlighting different discharge sources. The two panes on the right show the extra main and statistics menu that are available from the software package.

Another analysis method is Pulse sequence analysis (PSA). PSA considers the correlations between consecutive discharges, rather than relying solely upon phase-angle of the applied voltage to distinguish different PD events [69]. This allows for PSA to better interpret the underlying physical phenomena as space

charge from previous PD events remains and influences the inception conditions of following pulses. PSA plots tend to look at the voltage change, corresponding to the local electric field change at the discharge site, of an event on one axis versus the voltage change of the previous event on the other. This gives rise to distinct groupings of voltage differences, especially when coupling the individual events together with lines following the sequence order of the pulses. By dividing the change in voltage by the difference in time between the pulses, this resulting plot can emphasize events that occur close together and are more likely to have influenced each other [70].

The following separate approaches used to detect PD can all be used to facilitate the discussed methods of analysis.

2.3.1 Coupling Capacitor

Localised AC PD detection is often performed using a coupling capacitor [5, 29, 71] to sense the small voltage transients caused by PDs. Through calibration against a known PD source or charge injector, the magnitude of detected PD can be determined as the electrical current impulses passing from the coupling capacitor to the discharge site as demonstrated by the equivalent circuit in Figure 2.4, are proportional to the PD amplitude. However, as the current impulse passes through the connecting cables and insulation, all of these items have impedance and will affect the signal. Therefore, what the coupling capacitor measures is only an "apparent" charge and not the true size of the original event. For most tests carried out in a laboratory setting, as distances between the coupling capacitor and device under test are short, this effect can be neglected. But as a PD source moves further away from the coupling capacitor, the impedance of the cable or connected device will begin to attenuate the high frequency content due to the combined inductance and capacitance of the cable itself. As such, for long export cables where lengths can exceed many kilometres the distance is significant and severely attenuates signals producing events with much lower apparent charges than absolute charge at the event site.

As the sensing requires detecting very small signals (nano-coulombs or less), these methods can be sensitive to external noise in the same frequency; therefore detection filtering often employs band pass filters centred on areas of typical peak PD amplitude [72]. From the time that the event is sensed compared against the applied voltage waveform, the PD can be plotted against phase. This is usually used to indicate the type of PD that is occurring as well as providing information on the stage of degradation [35, 55].

This method can be applied online: however, for systems of extra high voltage, the use of a coupling capacitor is not practical and other methods must be used.

2.3.2 HFCT

High frequency current transformers (HFCTs) (also known as Radio frequency current transformers (RFCTs)) are used to detect discharge currents flowing, usually, within the grounding conductor [8]. HFCTs have frequency ranges of 2.5 kHz to Ultra-high frequency (UHF) regions of 3 GHz. As the currents that are being detected from small discharges are minute, some amplification

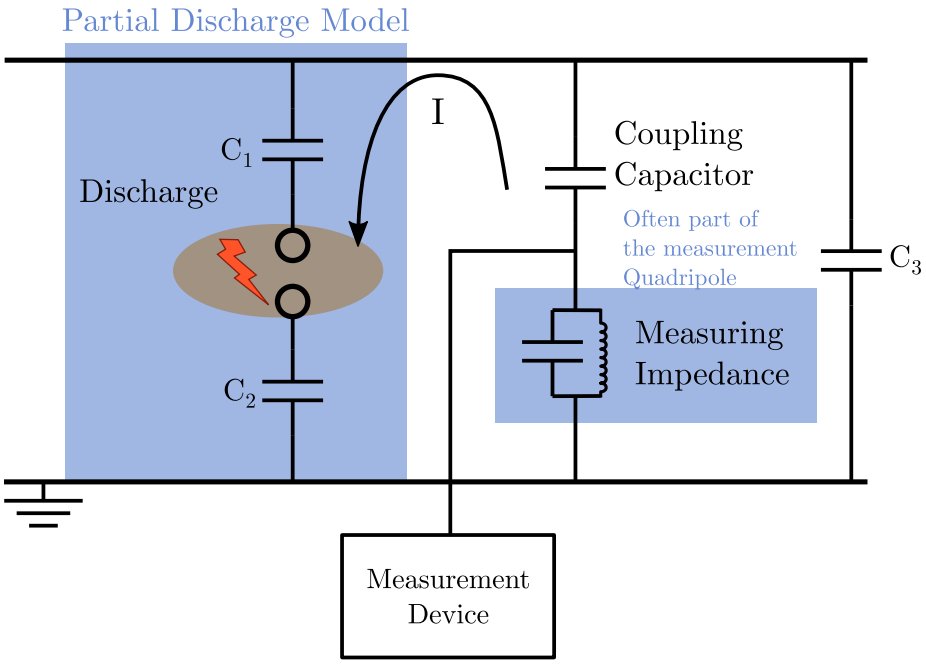

Figure 2.4: Equivalent schematic of a coupling capacitor and capacitor-modelled partial discharge. C_1 and C_2, the dielectric above and below the discharge site, could be combined to simply for calculations. C_3 represents the capacitance of everything outside the circuit (cables etc).

is necessary, although this introduces noise. Through Fast Fourier transform (FFT) filtering or other de-noising methods such as wavelets, the Signal to noise ratio (SNR) can be again improved. As HFCTs work at high frequencies, typically the higher frequency used, assuming that the wanted discharges emit emissions in this range, the lower the noise floor. This is an advantage compared to other methods that are stuck at lower frequencies, around which sources of noise such as corona or interference from radio transmissions are more prevalent. However, as HFCTs encompass such a large range, it is extremely hard to accurately calibrate them, such as would be done with a coupling capacitor. This is because, unlike coupling capacitors, HFCTs have a much wider bandwidth and measurement of a calibration pulse such as specified in IEC60502 would measure differently on different bandwidth transformers from different manufacturers making it harder to infer the PD amplitude for a given pulse from the CT.

HFCT detection can be used anywhere the current pulse from a PD event travels such as the grounding conductor. This method can be less intrusive to install in comparison to coupling capacitors and the like, as the high voltage conductor does not need to be interfered with. Because of this, HFCTs are easy to retrofit to existing installations or HV equipment only requiring somewhere where a current carrying conductor is accessible.

2.3.3 Acoustic

Detection can also be done acoustically from measuring the AE of a PD. When a discharge occurs, the released heat can evaporate, causing expansion or contraction, or even vaporisation of the adjacent material, producing an acoustic wave. The intensity of the emitted energy is proportional to the energy released in the discharge [48]. From this relationship, the charge transfer from the PD event can be inferred as the energy released is proportional to the charge[2]. The cavity in which the partial discharge occurs is significant: the physical size and shape of the cavity will have an influence on the spectra of the AE from the discharge. Without delving too far into acoustic theory at this point, there will be resonance peaks in the frequency spectra emitted corresponding to standing waves that can fit within the void or similar source of the discharge[3]. The spectrum may then also be modified by attenuation within the insulation of the cable, specifically in the higher frequencies. These emissions are usually captured by HF piezo-transducers or other types of microphones and location is only seen in transformers using time of flight between multiple sensors.

From the spectra that can be obtained from acoustic sensors, it is possible given enough measurement bandwidth, to classify the observed discharge into the different PD types. [45, 50, 73] show that with a high bandwidth of 400 kHz, it is possible to characterize AE into different shaped cavity/void discharges and treeing. *Boczar et al.* [74] also demonstrates that the supply voltage at which the PD occurs, does not influence the frequency or time waveforms of the AE; therefore, this classification method can be applied across any voltage.

Phase correlation to the applied voltage waveform must be achieved through additional synchronisation mechanisms as the voltage waveform will not be present in AE. With phase correlation information, the results can be analysed such as with the PRPD mechanism. This synchronisation may be time-delayed compared to an electrical measurement due to the fact the acoustic wave must propagate through the surrounding medium to the sensing element; therefore, possibly introducing a phase delay in a PRPD plot. As will be mentioned later, distortion from various sources such as reflections may also reduce the correlation of the time-of-arrival and the underlying discharge phase relation [48].

As acoustic sensors require close proximity to the source discharges and online electrical equipment, sensors utilising electrical detection heads, such as piezoelectric, can experience distortion from the electric field emission from a PD. This means that it can be hard to distinguish using these acoustic sensors the difference between the true acoustical measurement, and electrical interference inducing voltage and currents in the measurement à la a coupling capacitor.

2.3.4 UHF

During a partial discharge, as charge is transferred, there will be an amount of electromagnetic radiation emitted. This radiation transmits outwards through the surrounding mediums. As the time duration of these discharges is short,

[2] Often simply calculated like the energy stored in a capacitor: $\frac{QV}{2}$ or $\frac{Q^2}{2C}$

[3] The series on PD by *L.E. Lundgaard* [47] goes into the specifics of why different types of discharge produce such differing frequency emissions. More acoustics detail will also be given in Section 3.1

the frequency spectrum has more energy at higher frequencies, up into the UHF (3 MHz-3 GHz) range. Metal enclosures, like those of a transformer tank wall, will reflect and stop the UHF, meaning measurement must be done either inside, or through the use of EM-transparent windows.

UHF measurements are typically low-noise as any noise sources can be filtered out due to being types of known radio-signals. However, as the electromagnetic wave spreads out in all directions, its energy falls of at a relationship of the distance squared. This results in receivers requiring to be physically close to the possible sources of PD measurement and means they cannot be used at long distances; like on a cable. Due to some receiver's pick-up patterns, the antennas used can present high immunity to noisy environments due to the high directivity [8]; but this can also be a hindrance: as the detection is directional, PD events could be missed from the positioning of a sensor, or blocked by the construction of the equipment under review.

2.3.5 Chemical

Chemical analysis can only be done on fluid-based insulation such as oil or SF_6 as it is looking for the presence of, or lack of, particular tell-tale chemicals produced during discharge. Therefore, whilst there are many innovative sensing solutions based on this, it cannot be applied to one of the main focuses of this research: cables. The chemical process uses Dissolved gas analysis (DGA) for oil, looking for products that may arise from decomposition of the oil under discharge [75]. As this requires chemical indicators it cannot easily be applied as a continuous monitoring solution. Trace gases can also be analysed for in gas insulated substations.

2.4 Conclusion

This chapter has summarised the various methods of PD and their underlying processes such as initiation requirements and progression. For PD to occur there must be a sufficient applied field, largely due to concentration effects at sharp peaks or other material joint properties. Many of these discharge types will be studied using an assortment of these measurement methods in the later chapters. Specifically, void and treeing discharge are the most studied as they have the largest impacts in HV equipment. Additionally, the detection methods using a coupling capacitor and acoustic sensors will be used for comparison against the primary focus of trialling DAS as a measurement system. DAS allows for a continuous detection range far beyond classical methods whilst also allowing for direct localisation of events and remaining immune to electrical and magnetic interference. The analysis method of PRPD will be used for measurements to allow for comparisons between different systems, alongside time-domain plots. Alternative analysis methods are not suitable due to the DAS measurement methods not detecting every pulse in sequence. For PD initiated in a laboratory, the source is typically designed to constantly be in a state where the electric field is higher than the inception field allowing for constant, continuous discharge. However, when trying to detect PD on real-world equipment, this is not necessarily the case and PD may be a lot more

difficult to locate due to the sporadic nature of events.

Chapter 3

Distributed Acoustic Sensing

Fibre based sensors provide numerous advantages over other acoustic-based sensors such as their lightweight continuous construction, as well as being inherently immune to electrical and magnetic interference. Distributed fibre sensing solutions such as Distributed acoustic sensing (DAS) extend these advantages and provide measurement of physical parameters in spatially resolved, distributed manner negating the need for an array of discrete sensors. These distributed techniques have been deployed in a wide range of industries [23] but have yet to be adopted as a high voltage monitoring technique.

Specifically, DAS provides strain sensing using a fibre by measuring backscatter from a laser pulse travelling within the fibre. Through time-of-flight measurement of these interrogation pulses, positioning is extracted for each sensing location [22]. These sensing locations, or channels, are separated by a distance known as spatial resolution, continuously distributed down the fibre length. As the channels can be concurrently interrogated multiple times a second, acoustic signals consisting of multiple frequencies impacting the fibre and causing minute strain changes can be recreated. The maximum lengths at which DAS can operate up to are extremely long - hundreds of kilometres [76] - with a sensing unit only required at one end of the fibre. However, the trade-off is the frequency at which the fibre can be interrogated. Therefore, sampling frequency is reduced at long measurement distances [77].

As DAS is measuring acoustic waves, it is important to look at the underlying acoustic theory and processes in order to understand how a sound wave can interact with a fibre optic to eventually cause a measurable output. The subject area of acoustics is wildly vast and deserves much more discussion that can be contained here. However, the following sections will give an overview of the specific processes and effects involved in the interactions of acoustic emission of partial discharge, and capturing that information with various sensors like DAS.

3.1 Acoustic Concepts

3.1.1 The Acoustic Wave Equation

Wave propagation at its simplest can be thought as how a ripple moves out across a surface of a pond. The elasticity of the water surface, from an impulse such as a stone being dropped, will generate a set of decreasing in amplitude ripples that emanate out in all directions at a speed defined by the physical properties of the water and surrounding environment.

The acoustic wave equation is a well-known descriptor of these waves and how they travel [78]. The equation describes how the acoustic pressure and particle velocity change as a function of time and position. From deriving this, and the solution thereof, a good understanding can be grasped of how these waves cause changes that can be detected by various acoustic means; as well as additional affects such as resonances.

The following section will discuss relevant acoustic equations describing how acoustic waves from, for example, an acoustic emission of partial discharge, can interact with solids causing measurable strain changes, as well as the processes standing and reflected waves.

To derive the wave equation, Figure 3.1 shows the description of a small cube of fluid δx by δy by δz in dimensions. A absolute pressure, P, along the x axis acts on the starting face, with the opposite pressure plus a small change, δp on the opposite side.

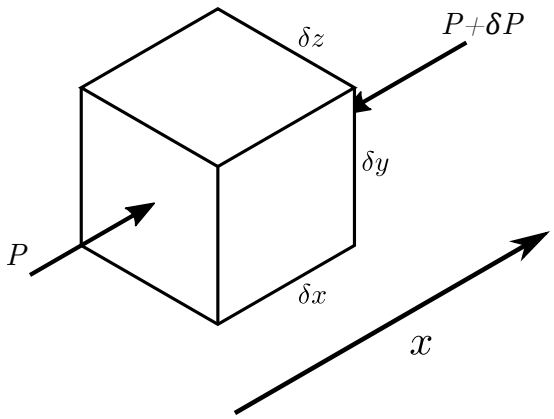

Figure 3.1: Diagram of a cube of sides δx, δy, δz with pressure P and $P + \delta P$ acting on the cube in the x direction.

By only considering a 1-axis change along the x axis and knowing that the pressure is a function of both time and distance, The change in pressure δP is:

$$\delta P = P(x + \delta x, t) - P(x, t) \tag{3.1}$$

It follows that this δP for the limit as δx tends to 0, can be written P with respect to x given a constant time.

$$= \left.\frac{\partial P}{\partial x}\right|_t \delta x \tag{3.2}$$

From Newton's second law, substitute in the mass, the density ρ multiplied by the volume, and the acceleration will be the rate of the change in velocity $\frac{\partial u}{\partial t}$, where u is displacement, given a constant position.

$$\begin{aligned} F_x &= ma_x \\ F_x &= \rho\delta x\delta y\delta z \cdot \left.\frac{\partial u}{\partial t}\right|_x \end{aligned} \tag{3.3}$$

Then, given the force on the surface of the cuboid will be given by the pressure multiplied by the area[1]:

$$\begin{aligned} -\frac{\partial P}{\partial x}\delta x\delta y\delta z &= \rho\delta x\delta y\delta z \cdot \frac{\partial u}{\partial t} \\ \frac{\partial P}{\partial x} &= -\rho\frac{\partial u}{\partial t} \end{aligned} \tag{3.4}$$

Taking the Ideal gas law ($PV = nRT$, n: amount of gas in moles, R: the ideal gas constant, T: absolute temperature of the gas) under adiabatic (without transferring heat or mass out of the system) conditions, the pressure will be linearly proportional to the density: $P \propto \rho$. The pressure can therefore be written as a Taylor expansion as a function of *density*.

$$P(\rho) = P(\rho_o) + \frac{\partial P}{\partial \rho}(\rho - \rho_o) + \frac{\partial^2 P}{\partial \rho^2}(\rho - \rho_o)^2 + ... \tag{3.5}$$

By linearising the P and ρ terms into their respective normal, P_0, and difference (due to the wave pressure), P_w, terms ($P = P_0 + P_w$ and $\rho = \rho_o + \rho_w$) as well as assuming that $p_w \ll p_0$ and $\rho_w \ll \rho_o$ so that terms in the Taylor expansion can be simplified by neglecting terms above the 1st derivative, it can be found that the two terms remaining in the expansion line up with the normal and difference pressures thereby finding P_w:

$$P(\rho) = P(\rho_0) + \frac{\partial P}{\partial \rho}(\rho - \rho_0) \tag{3.6}$$

[1]This force term is negative as a force would be positive for increasing in the positive x direction: here, the force is in the opposite direction

Hence:

$$P_0 = P(\rho_0) \tag{3.7}$$

$$P_{\mathrm{w}} = \frac{\partial P}{\partial \rho}(\rho - \rho_0) \tag{3.8}$$

The bulk modulus, B, of a material ties the pressure and density together as it describes how pressure influences the density of a given substance. Different materials that an acoustic wave travels through will have different properties for how the density changes with a given pressure. By substituting Equation 3.7, the following is obtained:

$$\begin{aligned} B &= \rho_0 \left(\frac{\partial P}{\partial \rho} \right)_{\text{adiabatic}} \\ P_{\mathrm{w}} &= \frac{\rho_w - \rho_0}{\rho_0} B \\ &= Bs \end{aligned} \tag{3.9}$$

Where s is the "Condensation" defined as the change in density for a given ambient fluid density. Differentiating with respect to time to link it to Equation 3.4.

$$\begin{aligned} \frac{\partial P_{\mathrm{w}}}{\partial t} &= \frac{\partial}{\partial t}(Bs) \\ \frac{\partial s}{\partial t} &= \frac{1}{\rho_0} \frac{\partial \rho_{\mathrm{w}}}{\partial t} \\ \frac{\partial P_{\mathrm{w}}}{\partial t} &= B \left(\frac{1}{\rho_0} \frac{\partial \rho_{\mathrm{w}}}{\partial t} \right) \end{aligned} \tag{3.10}$$

Equation 3.10 is still in terms of pressure and density, to combine all of them into terms of pressure consider the fluid continuity equation (based upon the conservation of mass) where the first term is change in mass, and the second the flow in or out of a volume:

$$\frac{\partial \rho}{\partial t} + \nabla \cdot (\rho u) = 0 \tag{3.11}$$

Hence for a one-dimensional system:

$$\frac{\partial \rho}{\partial t} = -\rho_0 \frac{\partial u}{\partial x} \tag{3.12}$$

Combining Equation 3.9 and Equation 3.12:

$$\frac{\partial P_{\mathrm{w}}}{\partial t} = -B \frac{\partial u}{\partial x} \tag{3.13}$$

Now, in the final steps differentiating Equation 3.4 (from Newton's second Law - NII) and Equation 3.13 (from Ideal gas law - IGL) with respect to time, it can be found that both have a similar partial derivative. Equation 3.13 can be converted to absolute pressure P, rather than the pressure deviation by assuming that average or standard pressure, P_0, is a constant during this wave process, and by differentiating with respect to x, the constant pressure term is dropped after the first derivative.

$$\begin{aligned} \text{NII:} \quad & \frac{\partial^2 P}{\partial x^2} = -\rho \frac{\partial^2 u}{\partial x \partial t} \\ \text{IGL:} \quad & \frac{\partial^2 P}{\partial t^2} = -B \frac{\partial^2 u}{\partial t \partial x} \end{aligned} \tag{3.14}$$

As the order of partial derivatives ($\frac{\partial^2 u}{\partial x \partial t} = \frac{\partial^2 u}{\partial t \partial x}$) does not matter, it is possible to combine these two results:

$$\begin{aligned} \frac{\partial^2 P}{\partial x^2} &= -\rho \left(-\frac{1}{B} \frac{\partial^2 P}{\partial t^2} \right) \\ &= \frac{\rho}{B} \frac{\partial^2 P}{\partial t^2} \end{aligned} \tag{3.15}$$

Therefore, Equation 3.15 can be written in terms of the pressure deviation p (and c the wave speed).

$$\frac{\partial^2 p}{\partial x^2} = \frac{\rho}{B} \frac{\partial^2 p}{\partial t^2} \tag{3.16}$$

$$\text{Or more commonly:} \quad \frac{\partial^2 p}{\partial x^2} = \frac{1}{c^2} \frac{\partial^2 p}{\partial t^2} \tag{3.17}$$

$$\text{Where } c = \sqrt{\frac{B}{\rho}}$$

Of course, waves in solid mediums are more complex than in fluids as the resulting wave from a displacement can propagate in more ways: longitudinal (P-waves) and shear / transverse (S-waves). [79]. However, for the special case of waves that only vibrate in the direction of propagation, the descriptive equations for these sets of movements reduce to the familiar wave equation [80]. For example, a stress pulse within a bar results in pressure being replaced by displacement, or strain, and the bulk modulus instead using the Young's modulus of the material.

Solution

A common solution derived by d'Alembert [81] is 2 waves propagating through a medium described by a forward-travelling function F and one in reverse, G. c is speed at which these waves move.

$$u(x,t) = F(x - ct) + G(x + ct) \tag{3.18}$$

This equation can describe not only a singular wave, or even impulse, moving from left to right or right to left, but also standing waves [82]. This is where waves reflect off boundary conditions at a periodic spacing that corresponds with the wavelength of the wave frequency, and can be described by the two functions having the same periodic function causing interference producing the in and out of phase peaks typically seen with a standing wave.

These equations and solutions other than describing certain phenomena, are heavily used within many acoustic modelling tools including those used in the following sections. However, with all modelling systems, they are a simplification ignoring losses such as attenuation, and must be expanded to work in more than one dimension.

3.1.2 Transmission, Attenuation, Absorption

At any interface between two or more differing materials, an acoustic wave will experience reflections. Reflections off of the boundary can create reverberations where a signal repeatedly reflects off these internal interfaces, extending the resultant acoustic wave. To quantify these interactions, an acoustic impedance Z, analogous to electrical impedance, can be assigned to each material; then, reflection and transmission can be approximated using standard impedance translation equations [83], as in electrical systems. From these, the reflection as a percentage($R_{\%}$) of amplitude of the incident wave can be obtained, again analogous to electrical theory. [84]

$$R_{\%} = \frac{|Z_1 - Z_2|}{Z_1 + Z_2} \tag{3.19}$$

The larger the mismatch in acoustic impedance, the larger the reflected energy(R) and therefore the less transmitted through the interface. This assumes that the interface is flat, and is a simple intersection of two materials.

Despite most interfaces being more complex in practice (i.e. glues or other adhesives), it gives a good estimate of the transmitted and reflected power.

Of course, not only will amplitude be affected, but also the phase and coherence of signals. The acoustic impedance of a material is defined as the product of its density, ρ, and acoustic velocity of the associated pressure wave through the material, v. For example, the impedance of a typical plastic-coated fibre jacket made of PVC is around $1.39 \times 10^6\,\mathrm{Pa\,s\,m^{-3}}$, much higher than the acoustic impedance of air at $420\,\mathrm{Pa\,s\,m^{-3}}$. For a solid insulation such as XLPE, it has an acoustic impedance of $2.14 \times 10^6\,\mathrm{Pa\,s\,m^{-3}}$, relatively close to PVC due to both being in the solid state rather than between a solid and a fluid. Acoustic waves travel well between too similar materials such as hard objects that are coupled together, but a large amount of energy is reflected on a boundary to air.

The amount of acoustic power that is transmitted across the interface between a cable's surface or fibre jacket (typically PVC or Polyethylene [85]) and air, such a scenario as if a fibre was mounted externally to a piece of equipment, can be found as the following from Equation 3.19:

$$\begin{aligned} R_{\%} &= \frac{|1.39e6 - 420|}{1.39e6 + 420} \\ &= 99.94\% \end{aligned} \tag{3.20}$$

Therefore approximately 0.05% of the overall emitted power can be expected to be transmitted into the fibre, or equivalently an attenuation of $-36\,\mathrm{dB}$. One must remember, however, that this transmission is on a single wavefront: the wave due to its repeating nature as well as reflections will have many chances of transmitting energy into the fibre. In extreme cases, such as violent total breakdown of a cable rather than small partial discharge, it could be expected that the acoustic emissions (AE) would be large enough to easily create measurable disturbances in the fibre even with this transmission loss. Within actual HV equipment such as a cable, there are many more internal boundaries. However, with all the components being in the solid state (ignoring oil filled cables), the transmission of acoustic waves is much higher, with a reflection percentage between PVC and XLPE of $\frac{|2.14e6-1.39e6|}{2.14e6+1.39e6} = 0.21$.

As mentioned by *Lundgaard* [47], the absorption of acoustic waves in solids is very complicated and varies massively [86, 87] from construction and variations of properties like elasticity in solid mediums. This can produce large amounts of scattering [88] and reflections [89], as well as other phenomenon like wave guiding [90]: especially in relatively small geometries. Other losses such as elasticity are also significant whereby a wave with acoustic energy will produce local displacement causing the material to stretch and loose energy through friction. This process typically has a hysteresis, and therefore is a function of frequency [91]. Despite losses, certain reflections can also provide benefits: if a very short impulse is scattered and reflected many times within a region, possibly due to many material changes, the original pulse will becomes lengthened, albeit with distortion of the source signal. This could allow for detection at lower frequencies where sample rates may be limited by equipment.

Furthermore, as a solid material compresses, it will induce other stresses and strains on the surrounding area; varying the properties and therefore propagation of waves. Therefore, simulation of attenuation, and more generally simulation of sound waves through a solid object and interactions can become extremely complicated. For example, pressure and shear waves in adjoining materials do not simply change their own cross section on wave fronts passing, but also change constraints of neighbouring materials requiring extension of the simple pressure and shear wave concepts [92]. Fluids tend to be more-Newtonian in nature as acoustic waves behave adiabatically, and therefore exhibit less hysteresis and are generally easier to simulate [93].

3.1.3 Stress and Strain

Transmission of acoustic waves in a solid do not simply travel as a pressure or displacement wave. This is because the encompassing material is not a fluid and does not experience pressure. Instead, within a solid, the wave-front is transferred through stress and strain. Specifically, strain is the most important in this research, as the mechanisms behind distributed acoustic sensing measure the changes in strain as opposed to more direct acoustic measurement methods.

Stress, σ, is defined as the force F applied to a material divided by the cross-sectional area A, across which the force is applied.

$$\sigma = \frac{F}{A} \tag{3.21}$$

It is measured in units of force per unit area (Nm^{-2}) or Pascals. Through the force applied to an elastic object, some compression will occur. Therefore, the local density of the area changes and as already discussed in the acoustic wave equation, this can allow for the propagation of a wave.

Strain, ε, is the deformation or change in length, Δl, of a material resulting from an applied force or stress across a length l. As apparent from its equation, the parameter is unitless and is can be considered a ratio.

$$\varepsilon = \frac{\Delta l}{l} \tag{3.22}$$

It follows from basic physics that modulus of elasticity, Y, is the relationship of Hooke's Law under the elastic region of a material and describes the stiffness of a material relating stress and strain by a linear relationship.

Through the spread of stress or strain over time, inside a solid material, acoustic waves propagate in either longitudinal, or transverse waves. Longitudinal waves exist through the movement of the waves in the same direction of motion, whereas transverse waves are supported through a shear wave: i.e. forces perpendicular to the direction of motion. Shear stresses also create moments on the material; further complicating dispersion. These differing displacement dir-

ections are also known as the polarisation of the wave[2] [94]. A diagram showing the differences between the two is demonstrated in Figure 3.2. Often, both wave types can exist at the same time [47]. The velocity of these waves can differ due to dispersion through the medium, and are determined from the density and elastic properties of the material [47, 95].

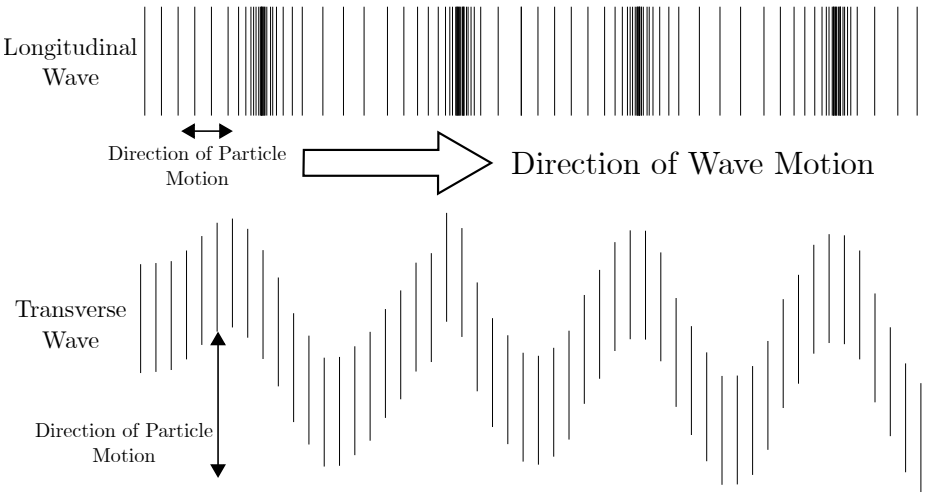

Figure 3.2: Diagram of Longitudinal and Transverse wave motion. Also shows difference in particle movements.

It is interesting to note that anisotropic materials, such as composite materials like pressboard, have different elastic properties along different axes, therefore propagation and wave velocities differ.

3.2 Scattering Processes

When light passes down an optical fibre, multiple processes scatter the light in different ways, each with different properties and returning energies. Of all these different scattering processes, Rayleigh and Raman provide the most-applied methods for DAS and Distributed temperature sensing (DTS) sensing. However, other scattering types do exist and are used for strain and temperature measurements in specific cases.

Rayleigh Scattering

A majority of light scattering within an optical fibre is caused by small inhomogeneities or random density fluctuations within the fibre core. It occurs when these variations are very small[3] such that the volume can be referred to as a particle. Incident light interacting with the particle results in the surface of the

[2] Not to be confused with optical polarisation of light

[3] Where the particle size is less than $\frac{1}{10}$ of the wavelength [96]; or more precisely $\frac{2\pi d}{\lambda} \ll 1$ [97], where d is the diameter of the particle or variation in refractive index

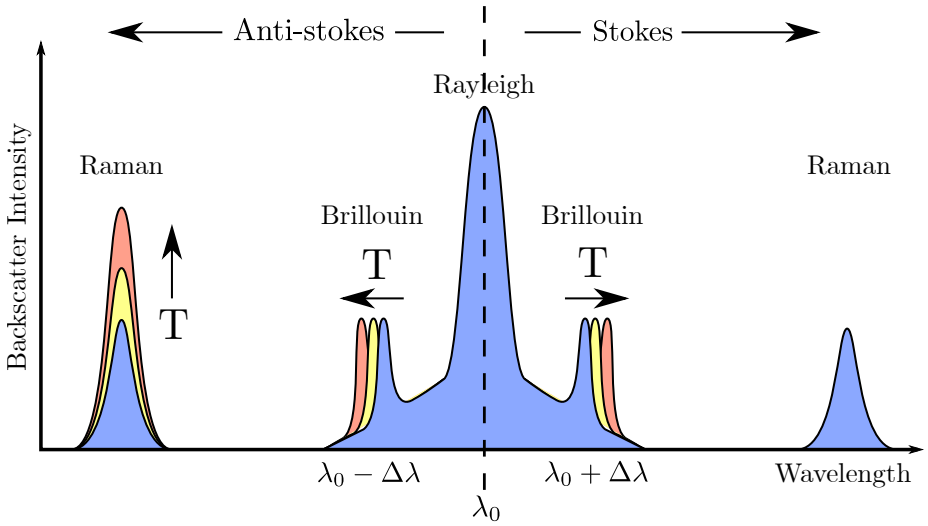

Figure 3.3: Rayleigh, Raman, and Brillouin scattering intensity in fibre-optics showing the symmetric components about the excitation wavelength λ_0 and change in wavelength $\Delta\lambda$. Colour skew represents change to higher temperature (towards red).

scattering point re-radiating with the same phase: a form of dipole scattering. Dipole scattering occurs when an electromagnetic wave, such as an interrogation pulse, interacts with a particle moving electrons back and forth creating an oscillating dipole. As this dipole is oscillating at the frequency of the incident wave, the dipole re-emits the same frequency. The re-radiation intensity of dipole scattering is dependent on the wavelength (λ) to the inverse fourth power: λ^{-4} [98]. This can be combined with the refractive index n of the particles of diameter d, at a distance R from the observing point, to give the intensity of light scattered by a single particle at angle θ from an incident wave I_0:

$$I = I_0 \frac{1 + \cos^2\theta}{2R^2} \left(\frac{4\pi}{\lambda}\right)^4 \left(\frac{n^2 - 1}{n^2 + 2}\right)^2 \left(\frac{d}{2}\right)^6 \tag{3.23}$$

As there will be a distribution of these particles, the collection of this scattering will be the summation of random phases resulting in an incoherent output.

The scattering as it is caused by an oscillating dipole, will radiate in an antenna-lobe pattern such as in Figure 3.4, allowing for the detection of this scattering from the same end that the fibre is interrogated from.

As light is being scattered, the original light is, of course, reduced in energy. This is one of the main reasons for a process known as "fading" down a long fibre [99], giving a finite length to a sensing fibre where the returning scatter signal must be above the noise floor.

Raman Scattering

When an electromagnetic wave interacts with a particle, instead of it resonating at the same frequency as the incident light, as in Rayleigh scattering, the photons are absorbed and later re-emitted at a different wavelength [100]. The spectrum

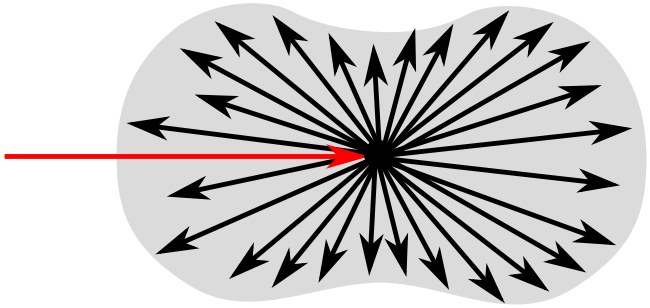

Figure 3.4: Scattering pattern from a single Rayleigh scattering event showing the radiation lobe and example paths of emitted light from the originating red incident light.

of these emitted photons are symmetric about the incident light. This is due to the difference in frequency corresponding to the difference in energy states between a ground and an excited vibrational, resonant state [101]. By absorbing a photon in either state, the energy level is increased and then drops to the other energy state by emitting a new photon as seen in Figure 3.5.

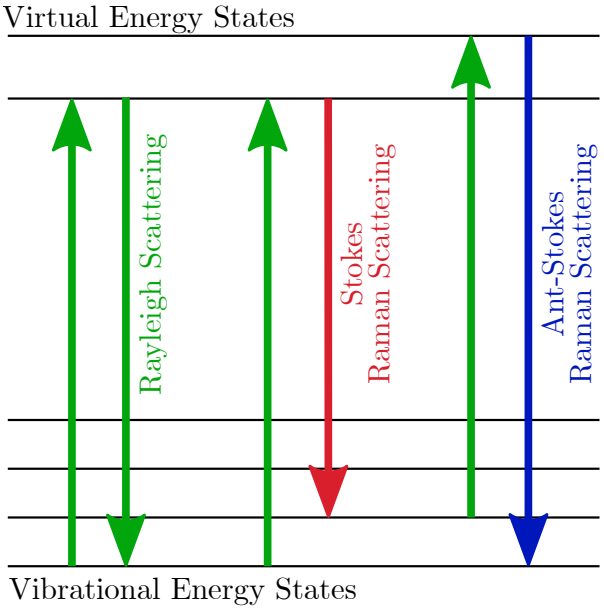

Figure 3.5: Diagram showing the transition between different energy levels during Raman scattering producing different wavelength photons. Red indicating an increase in wavelength, blue indicating a decrease in wavelength.

In thermodynamic equilibrium, more Stokes transitions will be witnessed in comparison to anti-Stokes transitions as the lower energy state will be more populated. Therefore, the resulting Stokes scattering peak will be stronger. As the temperature changes, the ratio between these two transitions changes, allowing for this change in temperature to be measured. This effect is used in Distributed temperature sensing (DTS) systems to measure absolute temperature by using

a known temperature gradients for reference and calibration [102].

Typically, the amount of Raman scattering is less than Rayleigh scattering, however by deliberately injecting Stokes photons (i.e. photons with the lower energy level), stimulated Raman scattering occurs where more interrogation light photons are converted into Stokes and anti-Stokes peaks.

DTS typically uses Optical time domain reflectometry (OTDR) techniques combined with spontaneous Raman scattering to measure the Stokes and anti-Stokes peaks across the distance of the Fibre under test (FUT) and then uses data processing and calibration to produce spatially binned temperature values for the fibre along the length [96]. The returning backscatter can be separated through use of a dichroic coupler which allows the launched pulse to transmit through, but backscatter is reflected into separate detectors for the Stokes (S) and Anti-stokes (AS) components. Due to the low intensity of the scattered light, there is a trade-off between spatial resolution, temperature resolution, measurement time and fibre length. For example, to increase the resolution, the fibre must be averaged over multiple readings and therefore the overall measurement time is increased (up to multiple minutes for sub-0.1 °C resolutions) [103] and/or fibre length reduced to speed up the individual measurements.

Using a laser pulse that is higher in power than a certain threshold causes non-linear effects within the fibre, resulting in the S/AS components distorting [104]. Therefore DTS systems can only use stimulation pulses up to that threshold. If a pulse that is higher than the threshold enters the fibre, after a certain distance due to the increased interactions producing the S/AS components so that the stimulation pulse is attenuated, the power will be reduced to below the non-linear threshold, and therefore the typical DTS procedure can occur after that distance. This is useful if the area of interest in the fibre is at a distance that a below-threshold pulse may typically be too attenuated to reach.

To derive accurate temperature measurements from the S/AS power levels reference sections of the fibre must be created that are kept at a known temperature. Typically, these are inserted at either end of the fibre optic to allow for assumptions of the light transmission properties down the fibre. However, this may be different due to damage or connection of different fibres giving rise to error [105]. Many instrument manufacturers rely on two references adjacent to the instrument at the start of the fibre relying upon known signal attenuation to eliminate the need for a remote reference.

In the general case, the S/AS components can be translated into absolute temperature using the following equation where γ is the shift in energy of a photon between the incident laser and scattered light, P is the received power across distance z of the Stokes and anti-Stokes peaks, C is a calibration constant, and $\Delta\alpha$ is the attenuation between the Stokes and Anti-Stokes signals within the fibre [103].

$$T(z) = \frac{\gamma}{\ln \frac{P_S(z)}{P_{aS}(z)} + C - \Delta\alpha z} \tag{3.24}$$

3.2.1 Brillouin Scattering

Brillouin scattering, as in Rayleigh scattering, occurs due to temporal fluctuations in density. However, whereas Rayleigh scattering relies on random, in-

coherent fluctuations of the transmitting medium, Brillouin scattering involves specifically periodic fluctuations (e.g. from standing acoustic waves, or *phonons*) [106]. When acoustic standing waves are generated within a medium, periodic conditions are generated across the medium so that incident light will be scattered according to the Bragg law [107]. This acoustic wave (known as a phonon) can be external, or generated by pressure on the material coming from radiation pressure or electrostriction[4] from the interference between optical modes in a waveguide such as a fibre under high powers [106]. This is known as stimulated Brillouin scattering. This interaction, unlike Rayleigh scattering, is non-elastic and causes a shift in energy, resulting in a frequency shift; although not as large a shift as Raman scattering. The shift is proportional to the relative velocity of the phonon. The shift can occur down: giving up energy to produce an Anti-Stokes photon and gaining energy to produce a Stokes photon. The photons are transmitted mostly in the reverse direction; however, some weak forward scattering is possible, especially during stimulation.

Brillouin scattering is much weaker than Rayleigh scatter, and therefore requires repeated interrogations to achieve the same sensitivity. This effect reduces maximum frequency at which strain changes can be measured: typically only in the tens of Hertz. Brillouin frequency shift is also dependent on temperature, making simple strain measurements more complicated. Therefore, Brillouin is typically not used in DAS systems.

3.3 Interferometers

An interferometer is a measurement instrument constructed of a single source of light being interfered with itself to create a very precise method of measuring changes in length. DAS uses this concept at its core to detect the minute changes in a fibre optic that it is capable of. In one of the simplest forms, a Michelson interferometer consists of a single coherent source of monochromatic light, shining into a splitter where the beam can be split to both a measurement arm and a reference arm [109]. When the light returns from being reflected in both arms, it interferes constructively or destructively into a photodetector. By measuring this change in intensity over time, the detector can measure the change in phase between the two arms. This change in phase represents a change in length of the detection arm, assuming the reference arm is fixed and that the source laser has a long enough coherence length, and can be used to determine length change down to partial wavelengths of the laser source. Larger changes will cause cycles of destructive and constructive interference, therefore by counting multiple cycles of dark and light detected by the photodetector, the system can measure multiple wavelengths of distance change. However, the Michelson interferometer has several downsides including the constant adjustment requirement of the mirrors in the system for optimum beam overlap to create the largest interference. By using fibre optics this problem can be reduced as mirrors can be permanently bonded onto fibre optics and do not require free-space alignment. However, Polarization maintaining (PM) fibre is required for the system to still work [109].

[4]Movement, or change of shape as a mechanical deformation, under the application of an electric field.

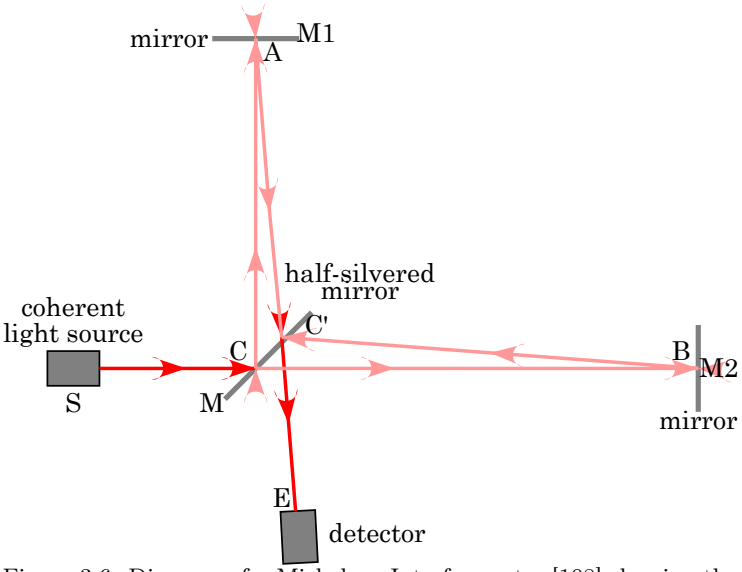

Figure 3.6: Diagram of a Michelson Interferometer [108] showing the splitting of a coherent light source at C and interference between the two paths on recombination at C‘ that is then reflected into the detector E.

Many other interferometer designs are available and in use for a plethora of applications, all with individual advantages and disadvantages. The Michelson described here was chosen for its simplicity in design and explanation. It is also one of the most similar interferometers to the techniques used in a DAS system.

3.4 DAS Theory

DAS works intrinsically like a distributed array of interferometers. Any length changes within each interferometer can produce an output with an associated location. This interrogation of the fibre is typically achieved by a method called Optical time domain reflectometry (OTDR). OTDR is a system normally used to characterize an optical fibre. It is advantageous as it is a single-ended, non-destructive technique: not requiring a full loop of fibre. By launching laser pulses into the fibre and measuring any reflected light from the same end in the time domain, information about the scattered light due to backscatter sources or discontinuities in the fibre can be collected. However, as the Rayleigh backscatter changes based on the strain that the optical fibre experiences, by use of a fast-repetitive scan of the fibre, acoustical signals that affect the fibre's backscatter can be reconstructed along the continuous length of fibre. This change of phase occurs due to two main processes: the mechanical changing of the optical path length, and photoelastic effects [96]. When strain is applied to a fibre optic, physically the length is stretched, therefore the optical path length is increased and a phase rotation is applied to light travelling through the extra length. Photoelastic effects are the additional changes in optical properties of a material when under mechanical deformation such as strain [110] which contributes to the total phase change as measured from the end of the fibre. Many methods

for this measurement of the backscatter, and therefore strain, have been demonstrated including Phase optical time domain reflectometry (φ-OTDR) [22, 77] where phase is directly measured rather than through interference, Coherent optical time domain reflectometry (COTDR) [111], Polarisation optical time domain reflectometry (POTDR) [112] as explained here, and also code-modulated versions of φ-OTDR. These variations on OTDR use different qualities about the returning scatter to measure wanted signals to improve SNR [113–115].

3.4.1 OTDR

Figure 3.7 shows an example layout of a simple OTDR system. The laser is triggered by a pulse generator to make a short (~10 ns) interrogation pulse that is then amplified and launched into the sensing fibre, known as the Fibre under test (FUT). Any backscatter within the fibre that returns to the start of the fibre is deflected into the detector by the circulator. From comparison between the time of launch to detected reflections, and the known speed of light down the fibre, the distance at which those scattered reflections came from can be determined. Often, additional fibre is positioned at the end of the fibre under test to inhibit large reflections from the un-terminated end of the fibre which could otherwise saturate the detector within the measurement region. Use of Angled physical contact (APC) connectors throughout the system also decreases unterminated reflections.

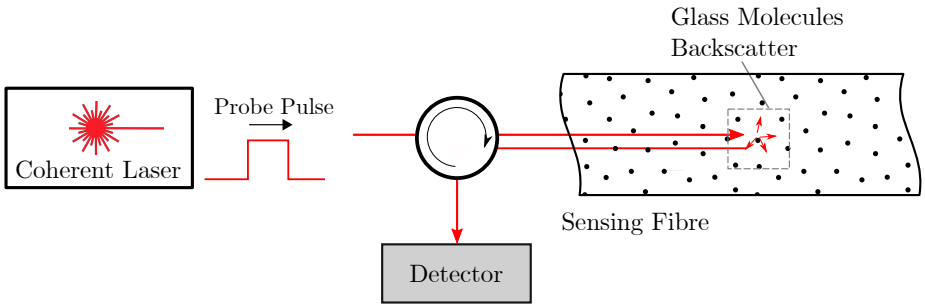

Figure 3.7: Example optical diagram of an OTDR system showing the laser path out to the fibre with backscatter being returned into the detector.

As the returning signal is of very low power, collection of this scattered light is amplified, and must be integrated over a period of time. These time slots in which the scattered light is measured, as well as the width of the laser pulse, gives an inherent "binning" of physical segments along the fibre known as spatial resolution or gauge length, and therefore this resolution is dependent on the sensitivity and SNR of the detection system. The measurement sections overlap by a length known as spatial sampling distance. Figure 3.8 shows the result of this binning, and how the smallest length between discernible signals can actually be less than the spatial resolution. The colours indicate successive sampling in time where the fibre is split into the gauge length segments: Sample 1 and 6 are the first to be measured. The sampling is then delayed slightly so

that the next gauge length periods are offset by the spatial sampling distance, allowing the measurement of sample 2 and 7. This is then repeated to produce a full overlap of measured segments. This overlap provides a higher precision than a simple splitting of the distance by gauge length. However, any measured values will still be the averaged across the gauge length.

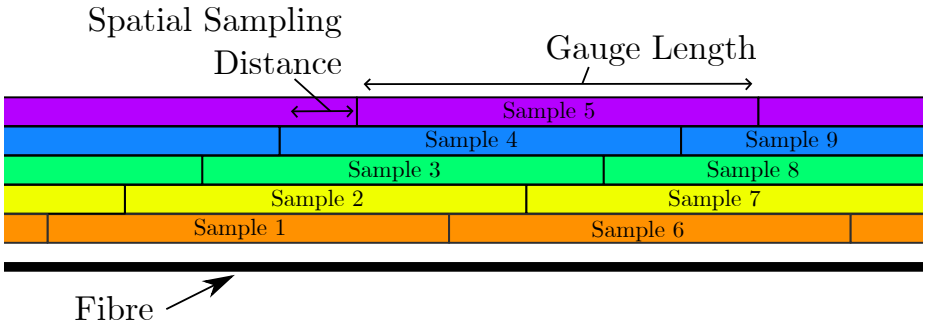

Figure 3.8: Diagram of the effective sampling positions along a fibre. Colours purely for distinction between differing sampling instances in time.

Whereas interferometers use a similarly sized reference arm for phase interference, this is not practical for a DAS system with very long sensing arms. There are a variety of ways this problem is avoided. As typically only the phase difference between samples is required, if the reference arm is constant between samples, the resultant phase change will be solely from the samples. This is the solution used by the APSensing system utilised within this research. Within measurement equipment, the phase of the interfered signal is measured using a 3x3 optical coupler at a higher sample rate than required to give the gauge length. The measurements are then integrated in the digital domain to allow for the overlapping gauge lengths as demonstrated above, giving an increased spatial resolution as opposed to other solutions. This also allows the gauge-length offsetting to be achieved with a single interrogation.

OTDR can provide a long measurement range but has the trade-off of reducing spatial resolution and repetition frequency. As the distance increases, the amplitude of the received backscatter decreases due to attenuation and the receiver must be more sensitive and therefore to achieve a decent SNR, the resolution must be decreased. The maximum repetition frequency f_{max} decreases simply due to the time that the light pulse takes to reach the end of the fibre before a new pulse can be launched. This can be expressed as $f_{max} = \frac{c_0/n}{2L}$, where c_0 is the speed of light in the fibre, n is the fibre refractive index, and L is the fibre length. Hence, the maximal sampling rate for a fibre of length 10 km is $\frac{c}{2e10*1.5}$ =10 kHz.

When the initial laser pulse is launched into the fibre, at the connections of optical components and connectors near the start of the DAS system, large Fresnel reflections are generated [116]. These reflections can then enter and

saturate the detector. Many OTDR systems include a launch fibre (also known as a send fibre) to move any dead zones due to this effect into distances of the fibre that are not within the FUT. Launch fibres can additionally be used for noise profiling.

To improve the scanning repetition speed of OTDR, Frequency division multiplexing (FDM) can be utilised. It is possible to launch a laser pulse down the FUT with a previous pulse still travelling as long as the pulses are distinguishable in some way such as frequency or coding. By sending n different pulses so that they are spaced equally at a higher repetition frequency, the sampling frequency can be improved by n times. This then requires further processing to align and rebuild the signal as shown in Figure 3.9, but can still be achieved in real time. This process may be repeated by using this method at both ends of the cable given that the received light from the other end of the fibre optic does not saturate the opposing detector, ensuring the probe encoding or frequency is different at either end to achieve greater sensing length at high-repetition frequencies.

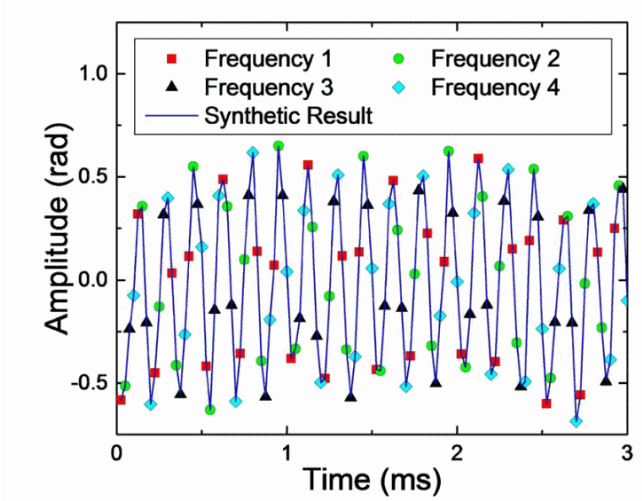

Figure 3.9: Reconstruction of a high-frequency signal using FDM-OTDR, from [117]

DAS typically is analysed using Frequency band energy (FBE) tools. This is where the time-based raw phase is translated into the frequency domain using Fourier transforms and then summed across frequency ranges. For example, by default the built-in tools of APSensing's provided DAS unit splits up the real-time data into 4 bands spread from 0 to the selected sample frequency of the DAS measurement. The frequency band energy E_{F} is calculated using the following equation where the raw phase $r(x,t)$ is representative of an array of distances x across time t. This is split into time segments given by the FFT window size W_{fft} which is by default set to the sampling rate divided by 4. The phase is unwrapped from its integer form and multiplied by a Blackman-Harris window $w[n]$ with the same size as the FFT ($n = W_{\mathrm{fft}}$) to prevent spectral leakage [118]. A Discrete Fourier transform (DFT) is taken, results squared and then normalised across the window. After which, the frequencies between the

min, f_{Min}, and max, f_{Max} of the frequency band in question are summed to produce the energy in the band. This equation is repeated for every multiple of the FFT window size across time, and also for every distance bin in the measurement data.

$$E_{\text{F}}(x) = \sum_{f=f_{\text{Min}}}^{f_{\text{Max}}} \frac{2}{W_{\text{fft}}} \left(\text{DFT}\Big((r(x,t)\frac{\pi}{2^{15}}) w[W_{\text{fft}}] \Big)_f \right)^2 \tag{3.25}$$

3.4.2 OFDR

The spatial resolution of OTDR methods is determined by the length of the interrogation pulse. As the interrogation pulse length decreases, the amount of returning backscatter decreases and thus OTDR methods are not currently able to resolve spatial resolutions of single meters due to the falloff of SNR. Optical frequency domain reflectometry (OFDR) solves this issue by providing a different method of interrogating the fibre. OFDR uses coherent light that is scanned in frequency during the interrogation period. Detection of the backscatter again occurs like in OTDR by mixing with a reference. The output signal of the detector will have a varying beat frequency over time due to the interrogation frequency scan; and this contains the spatial information [119]. By use of a Fourier-transform, the spatial information can be recovered and shown to only depend on the frequency sweep range of the initial interrogation pulse. Therefore, by using longer pulses that maintain the same frequency sweep, it is possible to increase SNR whilst maintaining spatial resolution [120].

However, OFDR is rarely used as a method in DAS due to the following reasons: the sweep frequency time is challenging to generate due to the high-repetition rate wanted in a DAS system. This is compounded by the drive signal. The theoretical best signal would be a ramp pulse; however, with the jump back to 0 offset it can be difficult to minimise transient oscillations [119]. Additionally, the range of OFDR methods is typically limited to much shorter ranges than OTDR [121]. Overall, OFDR is promising, however most commercially available DAS units use OTDR.

3.4.3 DAS for Discharge Localization

At the basic level DAS has inherent localisation down to a gauge length. If PD is detected, its location is trivial to find, as opposed to single-sensor methods that require triangulation given time or direction of arrival [5,10,122–126]. However, assuming the DAS system is sensitive enough to pick up signals, the acoustic emission will be picked up near-simultaneously and spread away from the original source, smearing the resulting location. As the acoustic wave spreads out, it will lose energy density. This is dependent on the shape and frequency spectra of the emission at the source, the surrounding materials and interfaces. Given a homogeneous region, the acoustic intensity will be attenuated at a rate that is inversely proportional to the distance [127]. Thus, the intensity of the acoustic wave decreases as distance increases from the originating point. Therefore in the DAS data a signal will be seen that should have an amplitude peak nearest the originating point of the AE, with symmetric side-lobes on either side of the

point source, and under most circumstances the point source could be located by an intersection of symmetrical distances. This ignores any reverberations that occur off of boundaries which would show as a series of time-delayed, reduced intensity reflections of the original signal that may also constructively and destructively interfere [128].

However, as will be explained in Section 4.1, the impulse-length of the source may be so small compared to the sampling interval, that a single DAS measurement may only sense the front of the acoustic emission wave front, a large portion of it, or even simply reverberations after the event has happened. This would result in a detection with a location that is not necessarily accurate to the original source. Nevertheless, given a high enough sample rate, over time multiple repeated signals, such as those from a PD event site, should average out across this propagated length to reveal a particular source point. However, the distance that such a high frequency signal could travel is very small and this phenomenon would likely just reduce the number of events detected.

Recent utilisations of DAS systems have been used to detect and locate discharges in Gas insulated lines [125]. The reported lengths of pulses were between 20 ms and 200 ms. As the length of the pulse is much greater than the time period between samples at a sample rate of 5 kHz, these discharges are easily captured and identified. Although, this does not apply to all discharges in other mediums, as the shown evidence is for amplitudes with many orders of magnitude higher than large PD. On the other hand, the lower amplitudes do not experience as much transmission and reflection of acoustic energy and therefore if a signal is detected, the uncertainty of its location is reduced.

3.5 DAS Uses

DAS is ideally suited to geophysics, specifically the application of seismic data acquisition [23]. This is because these data sources do not require high bandwidth, and can therefore achieve very long-distance sensing, making them perfect for sensing seismic events. This is used for detection of earthquakes [24], vertical seismic profiling [129–131], as well as other industrial uses such as monitoring oil and gas wells and hydraulic fracturing [132–134]. In these applications, the sample rates achieved are plenty high enough to properly sample the infra-sonic frequencies. There are not many applications for DAS that require high sample rates, possibly as the undersampling/aliasing process that occurs allowing detection of these higher frequencies is not fully realised. Otherwise, DAS has also been used for intrusion detection at secure sites [135, 136], and condition monitoring of pipelines such as leak detection [25]. In these scenarios, again only low frequency elements are required for these detections, and long detection distances can be achieved.

DAS has the capabilities to be a useful measurement device for any applications that require many distributed sensing elements across long distances. For example, real-time tracking of train and wagon locations on a railway only requiring a fibre to be non-intrusively added along the train track [137]. DAS has also started to be used for power cable monitoring for detection of failures or damages produced by mechanical impacts [138] across their lengths. However, this does not cover measuring or detecting any sort of electrical discharges within

the cable, but only external large-amplitude impulses that would be trivial to detect given the amplitude of said events.

3.6 Distributed Temperature Sensing

Although not a primary focus of this research, DTS contains very similar techniques to DAS but instead measures temperature. It can work on the same standard fibre optic cable as DAS measurement providing useful information on the temperature of the cable across the length. Most DTS systems utilise the Stokes and Anti-Stokes components of Raman scattering discussed in section 3.2. As the temperature at the scattering sites increases, the ratio of the Stokes to Anti-Stokes intensities changes (see Figure 3.10), thereby allowing measurement of temperature [139]. By having a section of temperature-controlled fibre within a DTS unit, this change in intensities can be calibrated to provide an accurate temperature reading.

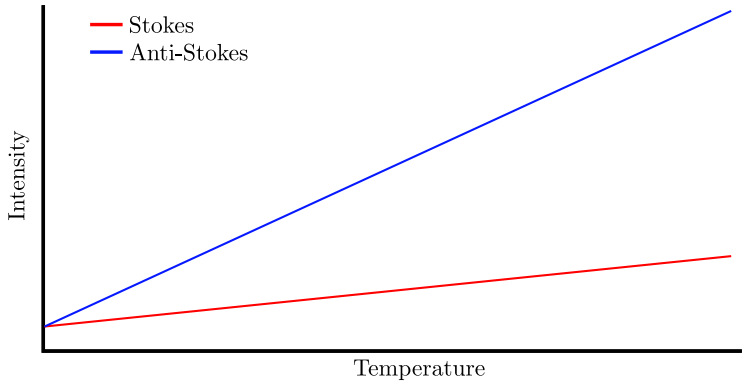

Figure 3.10: Comparison of the intensity of the Stokes and Anti-Stokes scattering peaks as temperature changes: the ratio between them increases as temperature increases.

DAS and DTS are able to be utilised at the same time on the same section of fibre, allowing for PD detection as well as hot spot / cable monitoring [140–142]. However, DTS is not able to be used for PD detection. The energy released during PD events can be calculated through the known charge transfer with the capacitor energy equation $E = \frac{1}{2}Q^2C$, where E is the energy, Q is the stored charge and C is the capacitance in which the charge is stored. In fact, the Omicron system already calculates this information given a known coupling capacitor. As previously mentioned, there can be inaccuracies with this method, especially at distance to a discharge source due to the measurement only measuring apparent charge movement. During an average discharge amplitude of 350 pC within a void event, the power dissipation is measured to be in the range 2 mW to 3 mW. Obviously, this will be concentrated in the partial discharge location produce a localised temperature rise. Assuming 2 grams of XLPE in the direct surrounding region, this temperature rise can be calculated to be 400 µK to 500 µK given the thermal resistance of the material. Even under much larger discharge producing 1 W of power dissipation, temperature would

only rise by an absolute maximum of 1 K to 2 K. Successive discharges at the same location would produce a cumulative effect raising temperature further, however any surrounding conductors would also act as heat-sinking spreading this temperature rise significantly therefore decreasing the peak value, as well as HV insulation likely blocking heat transfer between the site and measurement fibre. Even with commercially available DTS systems which can measure down to 100 mK, the measurable surface temperature / where the fibre could be installed will be insignificant, especially given the spatial averaging of a couple of meters on DTS systems [102]. Only under the most extreme of breakdowns discharges be detectable with DTS, at which point other protection systems would have likely engaged.

However, DTS is extremely well suited to adaptive cable ratings: by monitoring the temperature along different segments to dynamically calculate the maximum current ratings in order to maximise energy transfer; as well as hot spot monitoring. Hot spots can occur where cable routes pass through unfavourable conditions such as structures not allowing external cooling of the cable surface as the surrounding thermal resistivity is higher [11].

Figure 3.11 shows some example data from a DTS fibre within the Schwäbisch Gmünd tunnel, providing a fire detection system within a federal highway tunnel. A temperature rise is clearly seen in the 740 m to 1000 m section where the fibre is subjected to a hot air temperature rise simulating the initial conditions of a fire spreading within the tunnel.

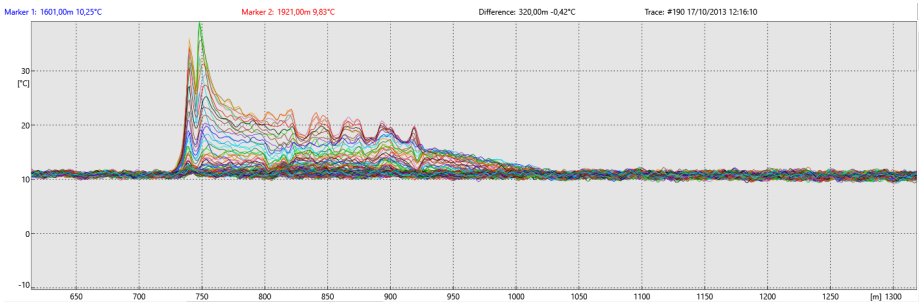

Figure 3.11: DTS output of a fibre installed in the ceiling of the Schwäbisch Gmünd tunnel during a hot-air fire test scenario. Different colour lines indicate the progression of time over a 5 minute period.

3.7 Conclusion

This chapter has covered a detailed exploratory view into the fundamentals of acoustics, how pressure and shear waves travel, and the interaction of these waves at interfaces of differing materials. Combined with the different scattering processes and interferometers, this has summarised a DAS system, its sampling details and how location data is recovered. The main problems with DAS are the available sample rates in commercial equipment, whilst maintaining a decent

detection range, and the possible sensitivity problem with the method itself. Other distributed technology such as DTS was briefly discussed and whilst it has a variety of uses such as dynamic cable rating and fire detection, it is not capable of sensing the minute temperature changes that can result from partial discharges.

Chapter 4

DAS Detection of Discharges

For DAS to be able to detect PD, a few criteria must be met. Firstly, the acoustic emission from the PD must be large enough in amplitude and the DAS to be sensitive enough to detect the created strain on the fibre optic. Acoustic models are created of various partial discharge scenarios to investigate the acoustic effects of materials between the source and sensing fibre, and how these would create the necessary strain to be measured. Secondly, there is still a large mismatch between the sample rates DAS is achievable of at a reasonable distance (20 kHz for the unit available in this research) and the accepted acoustic fundamental frequencies of PD of greater than 80 kHz [47, 50, 74]. As covered in Chapter 3, by limiting the maximum length of detection this frequency can be increased. However, 20 kHz gives a reasonable compromise between detection distance and sampling frequency. By using classical DAS processing techniques discussed in the previous chapter, these high frequency signals would easily be missed. However, the optical interrogation method of DAS has a useful side effect in attempting to sample these high frequency signals: most data sampling systems have a sample window on the order of the sampling frequency. DAS on the other hand has an extremely short sampling period in which high frequency signals can be aliased.

What follows in this chapter is an understanding of these processes and modelling them in a way that mimics a full distributed acoustic sensing system; allowing for a variety of scenarios to be tested and expected results generated. A proof of concept is also performed to ensure that DAS is at least capable of detecting breakdowns. If DAS is incapable of detecting these discharges larger than the wanted partial discharges, either some other direction is needed, or DAS would not be able to detect any smaller events. These larger discharges consist of multiple different sources: corona in air with the fibre separated and in contact with supporting insulator, and discharge under oil across an oil-impregnated pressboard. Given positive identification of these discharges in results, this alone is a useful result and shows that DAS is capable as an instant, location-aware breakdown detector for cables or other HV equipment.

4.1 Undersampling

Typically trying to detect a high frequency signal, such as the acoustic emission from PD, with a much lower sample rate would not be possible. The signal would be removed either through the effects of input averaging across the sampling window time period, or from anti-aliasing filters designed pre and post-measurement to specifically remove aliased components where a sampled signal is not fast enough to re-construct the original waveform. To reduce aliasing, typically an unwanted effect of sampling, the simplest methods are to either increase the sample rate, or apply suitable reconstruction filtering. But this is not valid in this case as sample rates are already at their limits, and the filtering would simply remove the aliased signals which contain hints of the acoustic emission. The pulse length used to interrogate the fibre in a DAS system is however, extremely short: on the order of nanoseconds. Therefore, the effective sample window of a singular position channel on the fibre is also this short, which would naturally cause aliasing artefacts. Signals with frequency content higher than the sample rate of the DAS system, if the signal occurs at the time of an interrogation, the source signal will produce an output in the measurement. For a constant wave source, this effect will give a sub-sampled frequency shifted output, much like a mixer [143], but for impulses, only short spikes are observed. To not remove these wanted effects, no anti-aliasing processing occurs during measurement, and minimal processing after capture is used: recording the raw phase samples so the distorted features of a higher frequency signal can still be detected.

The resultant signal will have several differences from the original: firstly, the waveform will be heavily distorted, possibly with only single numbers of samples covering the length of the original signal. Secondly, the maximum amplitude observed in the sampled data will not be respective of the original. This is down to where the sample window occurred in time, respective of the original waveform. Thirdly, the exact time information is therefore lost due to the lower time-resolution. The signal is only known to exist at the time of the sample window, not necessarily, and likely not, the start of the signal.

This means the acoustic emission from a partial discharge event could be observed given the random element of the detection, if, a stochastic in time PD event occurs during the sampling window (given as the sampling frequency is not locked to the applied voltage of the source of PD). Figure 4.1 illustrates how the timing of this window can affect the resulting sample amplitudes. The original spikes, created by summing varying sizes of impulses based upon the impulse response of a 5th order Butterworth lowpass filter to create a positive and negative-going dampened impulse, are sampled at a repeating time interval but with an extremely short window, resulting in the lower output graph. The outcome is that only a single impulse is seen, and with a reduced height peak. This is due to if the sampling window only happens to encompass the tail-end of the impulse rather than the front-edge of the spike. This effect could therefore give results where the amplitude of the original signal will correlate to the size of the discharge, but the sampled signal will not have this same correlation. Instead, the new sampled signal, as it is always a section of the original signal, has the property of never being larger than the original maximum amplitude of the originating signal.

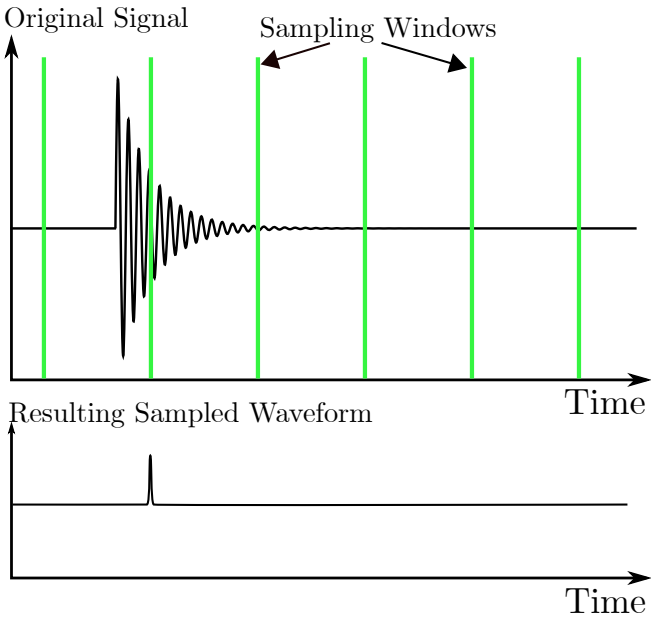

Figure 4.1: Diagram showing the random chance of detecting PDs with low sample rates. Top waveform is original signal, bottom is a resulting sampled waveform.

As PD is stochastic, a statistic approximation can be used to find a value for number of discharges one could expect to see given a certain time frame and rate of PD. The emission of PDs can be approximated as a rate per second, r_{pd} with an effective PD event width of $w_{\mathrm{PD,single}}$. The following assumes the sampling takes place at a lower rate, r_{s}, with a sample window size in seconds of w_{s}. Effective time windows of both the sensing and the PD events can be used to estimate the time taken before an event would be expected to be seen in DAS. This is computed by finding the chance of not taking a measurement and a PD event not occurring and then inverting the outcome to find the expected number of events in a period of 1 second. Without also compensating the number of PD events per second ($r_t exts$) by gating events with an amplitude below that that can be detected by the DAS system, the resultant expectant occurrence can only be taken as an upper limit, rather than a true expectancy of detected events.

$$\begin{aligned} \text{effective sensing window} \quad & w_{\mathrm{s}}^{\mathrm{eff}} = w_{\mathrm{s}} r_{\mathrm{s}} \\ \text{effective PD width} \quad & w_{\mathrm{PD}} = r_{\mathrm{pd}} w_{\mathrm{pd,single}} \end{aligned}$$

$$\begin{aligned} \text{Expected event occurrence} \quad E &= 1 - (1 - w_{\mathrm{s}}^{\mathrm{eff}})(1 - w_{\mathrm{pd}}^{\mathrm{eff}}) \\ &= 1 - (1 - w_{\mathrm{s}} r_{\mathrm{s}})(1 - r_{\mathrm{pd}} w_{\mathrm{pd}}) \end{aligned} \tag{4.1}$$

Therefore, the average number of seconds between an event being detected is $1/E$. The effective PD event width, $w_{\mathrm{PD,single}}$, can be quite large compared to

the normal impulse widths expected from a single point source as the width also considers any reflections or reverberations that a detection system may still pick up. This also means, as it is also an approximation, the value can only really be quoted by experiment. This figure can be used as a comparison between different solutions, giving a mean time between detected events.

4.1.1 Detecting Acoustic Emission with DAS

By using DAS techniques, an embedded fibre within a cable can be used as an array of microphones in order to pick up acoustic emission of PD. Fibre-based solutions for detecting partial discharge, other than *Che et al.* [144], have only been demonstrated that use discrete transducers that are coupled onto the fibre [145–149], and have only typically been used on transformers, therefore only making the measurement quasi-distributed at best. In a fully distributed sensing technique, whilst much better localisation and maximum length of measurement are obtained, certain physical limitations limit the maximum pick-up frequency, sensitivity, and length of the fibre. *Che et al.* [144] reported to have achieved PD recognition using a DAS system based upon a neural network, but required a weak Fibre Bragg grating (FBG) throughout to increase sensitivity to acoustic signals, as well as 1.5 km of fibre just to cover a very small section of power cable at unknown levels of PD. Sampling was achieved at a reported 25 kHz, with aluminium foil inadequately explained to improve sensitivity to the fibre. Classification used a neural network as well as wavelet decomposition, and spatial determination was not considered due to the large mismatch in sample and AE frequency making any determinations based on wave-shape impossible.

Assuming the detectable frequency range is not an issue, the acoustic amplitude of the AE is the next problem to address. The amplitude of acoustic signals from PD is very small, but proportional to the energy released in the discharge. The amplitude of which is reported to be in the range of 0.2 mPa of air pressure for approximately 100 pC discharges [150], so low as to be declared as impossible to sense in a plain optical fibre with a DAS method [147]. However, *Posada-Roman et al.* [148] managed to detect AE of 1.3 Pa with an optical fibre sensor which is equivalent to 96.26 dBSPL, which seems to be far in excess of numbers in literature and larger than what seems reasonable for PD sized events. Therefore, it is likely that the actual value lies somewhere between these upper and lower limits, and none of this previous work is in relation to creating strain on a fibre for detection.

4.2 Modelling

Modelling of a DAS system was used to create an environment to try early analysis techniques of large sets of data and to show how different sampling rates would affect high frequency acoustic signals measured by a DAS system. This encompasses both the acoustic effects from reverberations etc, but also modelling the strain applied on the fibre and how it is interrogated.

4.2.1 Theory

Consider an acoustic wave travelling in an elastic medium along an optical fibre. Ignoring effects of absorption and mechanical losses, and assuming the displacement is perfectly coupled between the medium and the optical fibre and that there is no directional sensitivity, the function of the change in displacement at a point is defined as $D_{\mathrm{A}}I(t)$ where $I(t)$ is the acoustic wave impulse itself, normalised, and D_{A} is the peak displacement of this impulse. Therefore, the strain applied to the fibre at a point x is linearly related where ε_0 is the peak strain relationship with the displacement:

$$\varepsilon(t) = \varepsilon_0 D_{\mathrm{A}} I(t) \tag{4.2}$$

For simplicity, these peak amplitude constants can be combined into an amplitude term A.

$$\varepsilon(t) = AI(t) \tag{4.3}$$

The optical phase change at a singular point, $\delta\phi(t)$ due to the strain applied can be found by another linear relationship [96,151], where K is a combined constant of mechanical and photo-elastic effects that affect the relationship between optical phase, ϕ, and strain. This constant contains the terms: n_{eff} the effective refractive index for the fibre (at the specific mode), L_{G} is the gauge length, ξ is the fibre length change, ν is Poisson's ratio, p_{ab} are the photo-elastic coefficients for the fibre in the corresponding directions specified by the 'a' and 'b' numbers according to standard spatial orientation nomenclature, and finally λ is the wavelength of light used for interrogation.

$$\delta\phi(t) = K\varepsilon(t) \tag{4.4}$$

$$K = \frac{4\pi n_{\mathrm{eff}} L_{\mathrm{G}} \xi}{\lambda} \tag{4.5}$$

$$\xi = 1 - \frac{n_{\mathrm{eff}}^2}{2}(p_{12} - \nu(p_{11} + p_{12})) \tag{4.6}$$

When ξ is combined into the combined constant K, the first term of ξ within the brackets indicates the phase change due to direct fibre length change, and the second negative term corresponds to the refractive index modulation of the segment due to the disturbance [96]. Equation 4.6 evaluates to approximately 0.79 using single-mode fibre at a standard DAS interrogation wavelength of 1550 nm.

Within a full DAS system, this strain is then integrated across a gauge length

L_{G} in the x axis along the fibre:

$$\varepsilon(x,t) = \frac{1}{L_{\mathrm{G}}} \int_{x}^{x+L_{\mathrm{G}}} \varepsilon_x(x,t)dx \tag{4.7}$$

However, for this phase change to actually be measured, light must be scattered and returned to the detector. For this, assuming there is a large number of natural scattering sites, these scattering points can be assumed to be uniformly distributed [151] so that a point x_{n} has a complex scattering coefficient: $\rho(x_{\mathrm{n}})$ where r_{n} is the amplitude, and ϕ_n is phase so that the combined coefficient is as follows:

$$\rho(x_{\mathrm{n}}) = r_{\mathrm{n}} e^{i\phi_{\mathrm{n}}} \tag{4.8}$$

Both r_n and ϕ_n can be modelled as 2 uncorrelated uniformly distributed number sets so that the mean and variance of each is equal. This results in a complex coefficient that is zero-mean, complex, Gaussian random number.

These described backscattering points reflect light defined as $A_{\mathrm{scat}}(t,x)$, incorporating a phase change according to the following equation where I_{s} is the source amplitude of light, γ is the complex propagation constant of the fibre, and $\phi(t,x)$ is the additional phase change added as specified in Equation 4.4.

$$A_{\mathrm{scat}}(t,x) = I_{\mathrm{s}}\rho(x)e^{2i(\gamma x+\phi(t,x))} \tag{4.9}$$

The factor of 2 comes from the fact that the incident light gets influenced by the phase change in the forward and reverse direction due to length changes (assuming that the velocity of the acoustic wave $\ll$ velocity of light in the fibre).

Therefore, using the above assumptions, the total complex amplitude U of the returning light within a gauge length, with n scattering points, can be found as:

$$U = \sum_{n=1}^{N_{\max}} I_{\mathrm{s}} r_{\mathrm{n}} e^{2i\phi(t,x_{\mathrm{n}})+\phi_{\mathrm{n}}} = I_{\mathrm{s}} U_0 \sum^{n} e^{2i\phi(t,x_{\mathrm{n}})} \tag{4.10}$$

where U_0 incorporates all the undisturbed phase and amplitude effects that should remain constant for a specific point across time. For modelling an OTDR/DAS system the wanted and measured property is phase change. By extracting just the measured phase from Equation 4.10 a simple solution is obtained containing the source signal and a random, constant phase noise component.

$$\phi_{\mathrm{meas}} = \phi(t,x_n) + \phi_n \tag{4.11}$$

4.2.2 Implementation

Simulations of this OTDR system were initially created using Python with a normal distribution used for the background scatter ϕ_n - see Equation 4.13.

This simulation was expanded upon for understanding of the DAS method and to attempt different de-noising techniques towards the improvement of SNR for detection of PD. The Rayleigh scattering intensity, I, within a continuous medium was approximated by a simplified Gaussian method [152] modelling the continuous, random distribution of imperfections in the fibre. A number of signals were created with a normal distribution $\mathcal{N}(\mu_{\mathrm{n}}, \sigma_{\mathrm{n}}^2)$, of amplitude A_{n}, centre μ_{n} and width σ_{n}^2 as to simulate the effect of vibrations propagating from a point source along the cable. These were then superimposed on top of a uniform, random background signal $\mathcal{U}(\min, \max)$ of maximum amplitude defined by the Rayleigh scattering constant implemented by updated python examples No.50 in [153], originating from the "*Textbook on Optical Fiber Communication and Its Applications*" [154] using the following equations:

$$I_{\mathrm{signal}} = \mathcal{N}(\mu_{\mathrm{n}}, \sigma_{\mathrm{n}}^2) \tag{4.12}$$

$$I = \mathcal{U}(0, \text{scattering constant}) + \sum_{\mathrm{n}} A_{\mathrm{n}} \frac{I_{\mathrm{signal,n}}}{\max(I_{\mathrm{signal,n}})} \tag{4.13}$$

By adjusting the scattering constant of the noise and amplitude of injected signals relative to the noise level, various scenarios can be created to describe different environments where noise signals could be greater, i.e. next to a busy road.

Figure 4.2 shows results of this modelling across a simulated 25 m section of fibre. The first pane shows the generated PD acoustic emission consisting of very short impulses (less than 1 ms in length) resulting in the fundamental frequency being below the sampling rate of the modelled DAS. The DAS modelling is set up with a sampling rate iof 20 kHz and a sampling window of 10 ns. The gauge length is 1 m. This is then added into the generated noise based upon the previous equations modelling backscatter (Equation 4.8 through 4.10). The PD AE is placed at a distance of 15 m. The data is processed across a 200 ms window to both reduce processing complexity, but also to ensure a presentable view in graphical format of the data.

The bottom pane of Figure 4.2 shows a line plot of the measured phase at the 15 m segment. A somewhat considerable noise level consisting of occasional, stochastic peaks higher than the average level are observed where the sampling of the DAS system happens to occur during a source AE impulse. As discussed in Section 4.1, these peaks are not representative of the original signals but do provide an indication of the presence of them. This resultant data from the corresponding distance bin is consistent with measured background data from a DAS system.

These results also clearly demonstrate the expected event occurrence statistics: across a given time window, only a fraction of events are seen: noted as $E_{\%}$ and defined as the number of events identified above the noise-floor in the DAS data per unit time as a fraction of total number of events (measured by a known reference system). Due to the nature of the PD events in the DAS data, many events are hard to distinguish from the noise floor and therefore this figure is yet to automatically be determined from data.

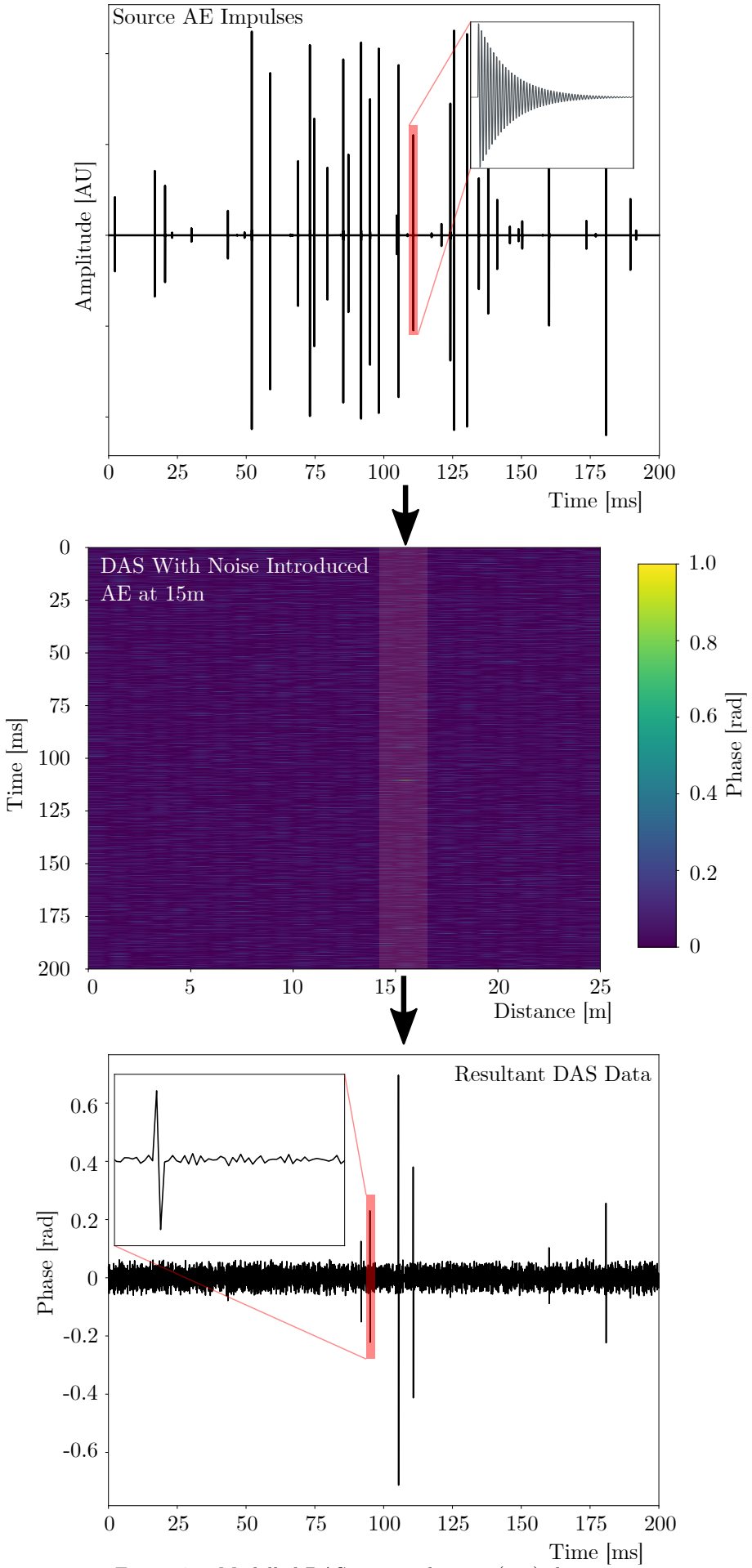

Figure 4.2: Modelled DAS system showing (top) the source high-frequency AE being sampled (greater in frequency than the DAS sampling frequency). Middle, the data at multiple modelled locations with the AE source placed at 15 m. Bottom, the resultant line chart of the undersampled data at 15 m showing the stochastic undersampling issues.

It could be initially assumed that the amount of correctly identified events would be the total sample window time per unit time coincident with the total time that an acoustic event is present per unit time:

$$\begin{aligned} E_{\%,\text{theoretical}} &= 1 - (1 - w_\text{s} r_\text{s})(1 - r_\text{pd} w_\text{pd}) \\ &= 1 - (1 - 10 \times 10^{-9} * 20 \times 10^{3})(1 - 200 * 0.9 \times 10^{-3}) \\ &= 0.1802 = 18.02\% \end{aligned} \tag{4.14}$$

However, this figure is only based on a binary representation of PD and DAS systems: one reason is due to both the acoustic reverberation extending the original impulse, but also the non-uniform modulation from reflected waves, the window in which detection would result in a positive identification is not a simple, singular time frame. This figure could be utilised as an upper bound, but comparing this to further results, it is shown that these assumptions are not accurate enough. Repeating the modelling with a new random source of AE, this time measured across 5 seconds rather than the earlier 200 ms, the $E_{\%,\text{theoretical}} = 18.02\%$ and $E_{\%,\text{measured}} = \frac{121 \text{ events}}{593 \text{ events}} = 20.40\%$. These models were then repeated, and swept across a multitude of DAS sample rates from 1 kHz to 200 kHz. From the initial equation, it would be expected that the expected percentage of correctly identified events would change at representatively linear rate. Therefore, the higher the sample rate, the greater chance of identifying events. Instead, two linear sections are observed with a curved transition between the regimes. Additionally sweeping the length of the acoustic PD impulse, this transition point between the two linear sections is moved towards the origin as the length is increased. Across this parameter sweep the fundamental AE frequency is kept constant. 3 repeats at each acoustic length are shown with an average response smoothed by a cubic Savitzky-Golay filter to reduce the oscillating response at higher frequencies.

The results of these sweeps are shown in Figure 4.3. From the curves of the data, it can clearly be seen that the response is not linear like the simple statistics from above presumed. Overall, the higher the sample rate, the higher the number of detected events. However, there is a point of diminishing returns that scales with the originating acoustic signal. For longer signals over 500 µs, this appears to occur around a sample rate of 25 kHz. For the shortest signals, 80 µs, this point does not reveal itself until around 100 kHz. The movement of this diminishing point also does not follow a simple trend: above 200 µs impulse lengths the point moves very little.

The regular drops in the detected events from the raw model data (shown as dotted lines), especially at longer impulse lengths, are from where the sampling window repeatedly lines up with the zero crossing of the PD acoustic impulse. In this case, at certain sampling frequencies, the impulse used happens to be a harmonic of the sampling frequency and therefore this comb filtering occurs. If the impulse was imperfect and contained a mixture of different frequency sources, this effect would be reduced.

Figure 4.4 shows the model output when changing the fundamental frequency of the source acoustic PD pulse to 50 kHz for impulse lengths of 50 µs and 500 µs.

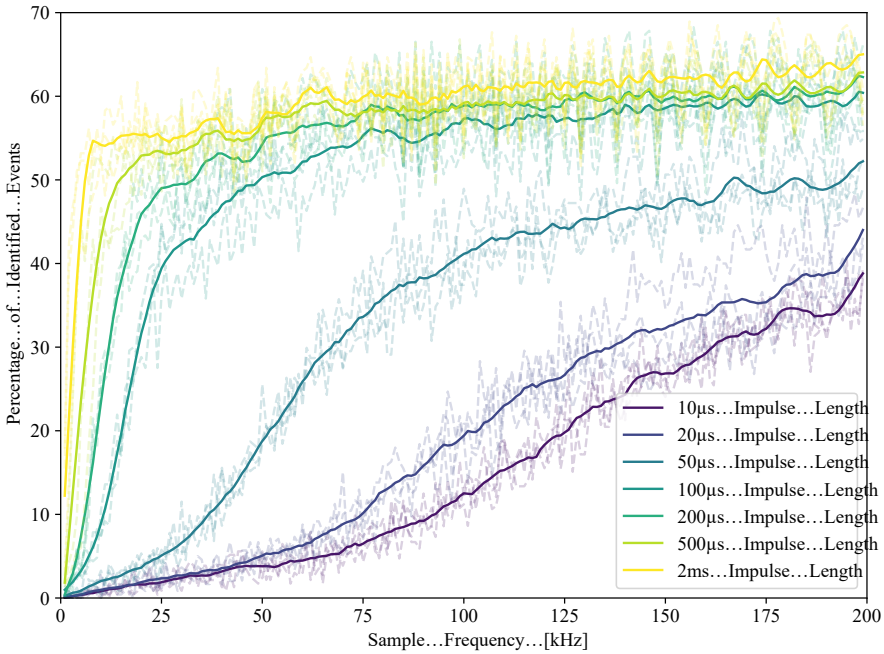

Figure 4.3: Percentage of PD events correctly identified above the noise floor compared to the DAS sampling frequency. This sweep was repeated at different PD impulse lengths from 10 µs to 2 ms. Dotted lines indicate raw samples from model with the solid line of the same colour showing the smoothed average.

These points are chosen to show the differences in the saturated region and below. At 50 µs, the number of detected events is severely reduced at the higher sample frequencies due to the reduced energy, whereas at the longer 500 µs length the result is unchanged bar a slight shift to the right. There is also a noticeable increase of the 500 µs line above the previous values in the range 100 kHz-150 kHz.

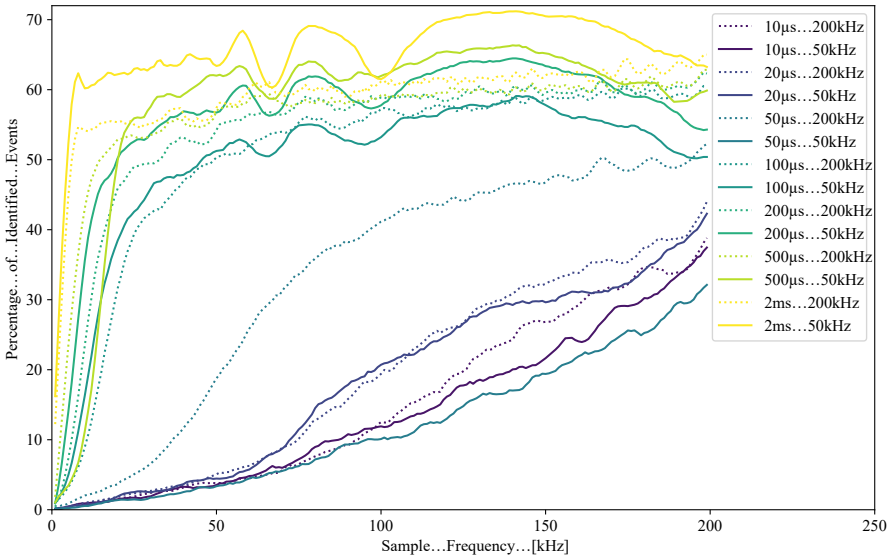

Figure 4.4: Percentage of PD events correctly identified above the noise floor compared to the DAS sampling frequency as in Figure 4.3, except with a lower PD fundamental frequency of 50 kHz. Dotted lines indicate raw samples from the previous model with the higher frequency AE.

4.2.3 Acoustic Wave Simulation

For simulating acoustic waves in air, there are a wide range of options; ranging from tools to aid speaker placements [155], to very complex, research orientated plugins to mathematical modelling software [156]. Unfortunately, many of these available packages are either unable to model acoustic waves in solids *and* fluids, including the boundary between them; or make the process very complicated. Either through difficult geometry editing tools, or custom algebraic expressions needed to bridge between solving systems that were beyond the scope of this work.

SimSonic [157], a tool that started development by *Emmanuel Bossy* during his PhD work, was discovered whilst looking for alternative options. It is an open source finite-difference time-domain simulator suite of elastodynamic equations, primarily designed for ultrasound propagation [158]. Input to the simulation is made extremely simple: a parameters file detailing simulation information such as boundary conditions and the properties of materials, the geometry specified as a bitmap image, and finally the signals. Therefore, creation of a setup to model both pressboard and void discharge, both which will be looked at later in the experimental chapters, was created.

SimSonic2D specifically uses central-difference approximations to the space and time derivatives of elastodynamic equations across a mesh of spatial steps, and a second mesh of time steps. These meshes are defined on staggered grids so that neither nodes overlap and are equally spaced [159]. This allows for the simplification of simulation by considering the velocity (time domain) components are constant during the stress parameter solving and vice-versa. The mesh

size conditions the accuracy of the results, and both the physical and time mesh must be chosen together as to obey a stability condition so that the solution converges where Δt and Δx are the inter-node mesh sizes, $c_{\max}$ is the maximum speed of sound in the simulation and d is the number of spacial dimensions (2 in this case):

$$\Delta t \leq \frac{1}{\sqrt{d}} \frac{\Delta x}{c_{\max}} \tag{4.15}$$

As the elastodynamic equations used are formulated based upon the rigidity tensor the tool can model both solid and fluid media. Absorption, however, is neglected as a simplification. Additional simplifications include that the rigidity tensor, the relationship between internal stresses and strains between all 3 spatial axes (i.e. with xyz as the 3 spatial directions, x to $x = c_{11}$, x to $y = c_{12}$, x to $z = c_{13}$ etc), is limited to a subset of crystal symmetries (as defined by only the c_{11},c_{12},c_{22},c_{66} stiffness tensors describing the relationship between force based stresses and resulting deformations). Additionally, the bulk movement or flow of fluid is ignored (only transient waves are considered). Multiple boundary conditions are provided: stress-free, rigid, mirror-symmetry and mirror-antisymmetry boundaries allowing the virtual placement of a system in a free or fixed environment. In the following simulations, perfectly matched layers are used on the boundaries in addition to defining the boundaries as stress-free to mimic the experiments sat at steady state in oil.

The geometry inputs to the SimSonic software are bitmaps in a specific "map2D" file with colours representing the different materials. This allows for very quick geometry creation and editing using simple image editing tools. Each pixel was defined as 0.1 mm. Figure 4.5 is the geometry used for the pressboard model demonstrated as the source image. The model is 2D, side-on taken as a cross-section of the pressboard. 3D simulations are also possible with SimSonic, but require much higher processing times and increased numbers of parameters of the material properties in all orthogonal directions, which can be hard to obtain. The purple coloured area shows the needle, in green the sense fibre positions, and in blue the bulk pressboard. Not shown is the surrounding tank walls at ± 300 mm from the centre of the pressboard. Other models are similarly constructed with colours representing individual materials with different acoustic properties. A singular Gaussian-impulse (Figure 4.6) was used for the initial acoustic signals to both to study the effects such as reverberation of the surrounding materials from a source impulse.

Unfortunately, paper is not the best medium to show the results of the simulation, as a full animated video is produced showing the acoustic pressures propagating through the various materials, ducting, and reflecting the pressure waves. Thankfully, SimSonic allows for the placement of receiver positions and arrays allowing the results in time to be plotted for a specific location, such as from the fibre positions.

Figure 4.7 shows the resultant strain change at the fibre position beneath the acoustic source (the other fibre position has a very similar response but is slightly delayed). The impulse is observed starts close to 0 ms, the time at which the acoustic signal originated, and rapidly decays to a more reverberant signal. The peak measured amplitude is much lower than the size of the initial strain change of course due to the absorption and spreading of energy. The fundamental

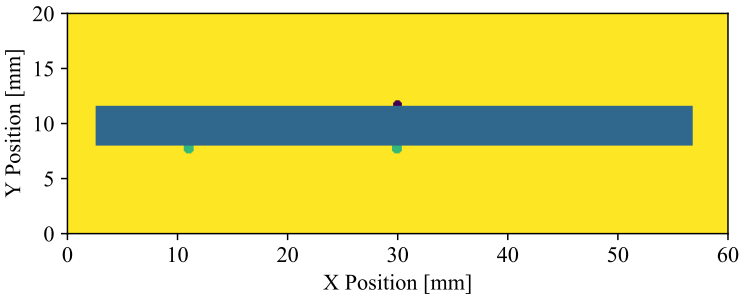

Figure 4.5: Source bitmap of a pressboard, for input into the SimSonic modelling software. Blue is the pressboard itself, whilst yellow is oil, purple is the source region of PD, and green the fibres on the bottom.

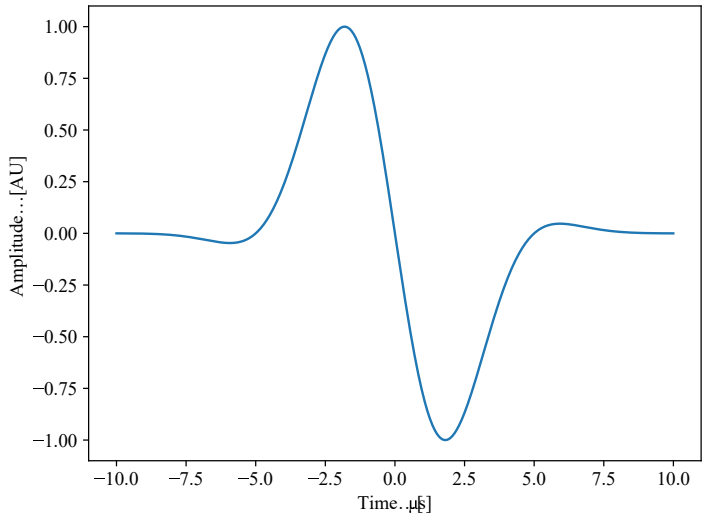

Figure 4.6: Gaussian impulse used as a simple acoustic signal.

frequency occurs from resonances across the thin cross-section of the pressboard with boundary conditions imposed by the oil-pressboard interface, whereas the modulation initially is from the acoustic energy spreading along the pressboard and causing interference, and later from the reflections of the tank walls from 0.5 ms onwards. This is more visible from the animations exported from the SimSonic tool but cannot be reproduced in this paper report. From this, it can be seen that a very short impulse of 1 µs is extended in length from even reverberations on a small cross-sectional area to more than 200 times the original pulse length.

The results of the void cell setup (using geometry in Figure 4.8, again a 2D cross-section model) producing the output in Figure 4.9, taken from Chapter 5, with a higher frequency impulse (250 kHz) shows again an impulse with ringing, but the impulse decays much faster. This is due to the different shape of the void model, smaller cross-sectional area creating less acoustic resonances. In the pressboard model, there was a long strip allowing for a singular wavefront to bounce back and forth between the two ends producing the even, regular

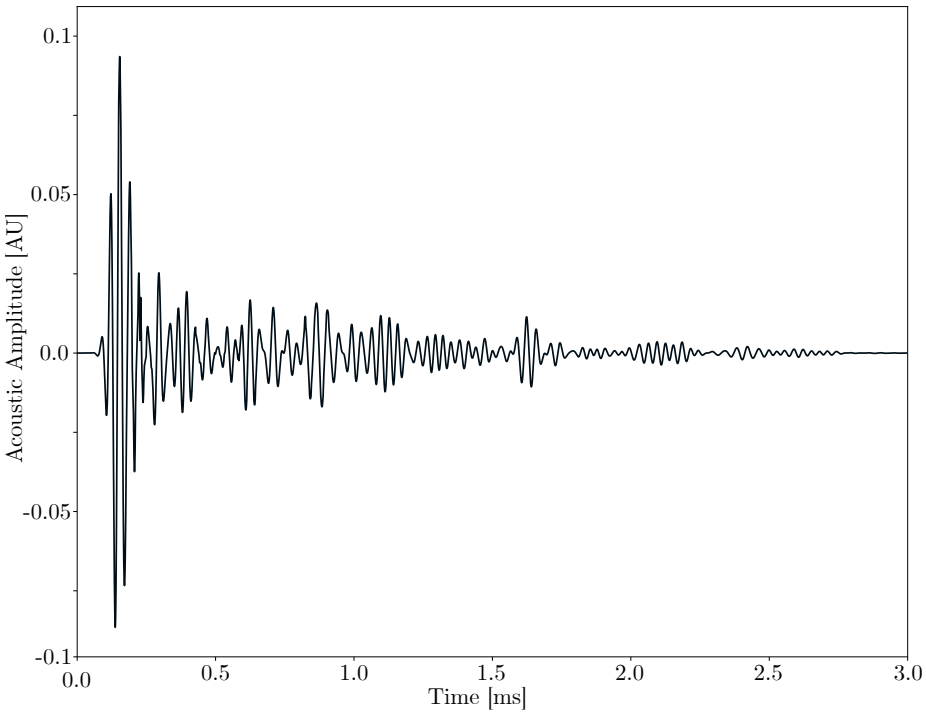

Figure 4.7: Plot of the strain in arbitrary units of a one-element receiver array at the fibre position beneath the acoustic source. Initial signal is detailed in Figure 4.6.

modulation. However, in the void model (Figure 4.8), the central mass is not a simple thin strip, and therefore a quicker-decaying but more chaotic waveform is observed. Modifying the base geometry of this void cell to introduce a triple junction at the electrodes with the surrounding oil, or splitting the void cell in two and adding an imperfect seam between the two halves produced slight variations in output, but the envelope and appearance remained the same. This shows that the bulk shape of the system defines the large reflections contributing to the decay of the signal after an impulse, whilst the source AE and area local to the source point defines the main fundamental frequencies. Of course, with a different, more elastic bulk material, the acoustic wave will experience more damping and therefore the reverberation tail will be reduced. This however could not be simulated due to lack of measured index densities and shear moduluses in the required spatial directions

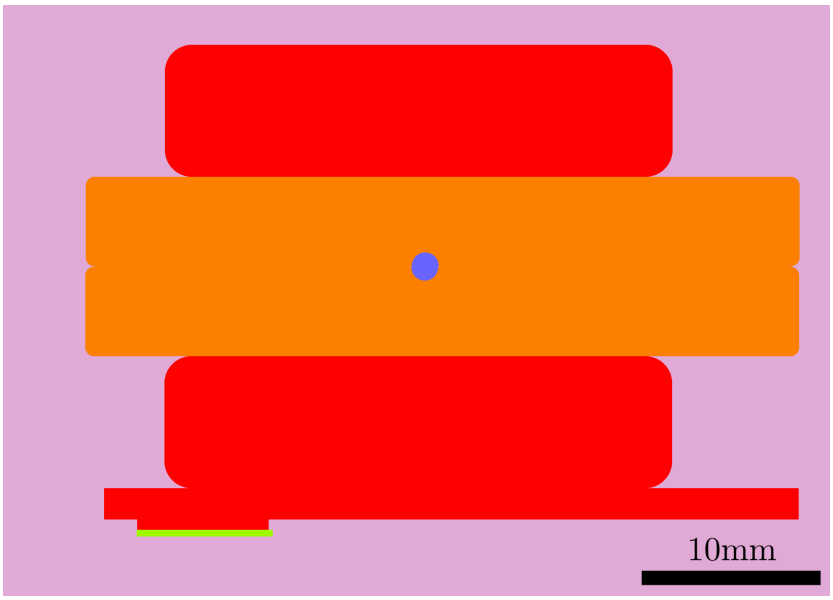

Figure 4.8: Source bitmap geometry of a void cell used later in Chapter 5. A section of insulation (orange) with a main air void is surrounded by electrodes (red) on both sides. The bottom electrode has a metal plate on which the sensor array (green) is placed. The entire setup is surrounded in mineral oil.

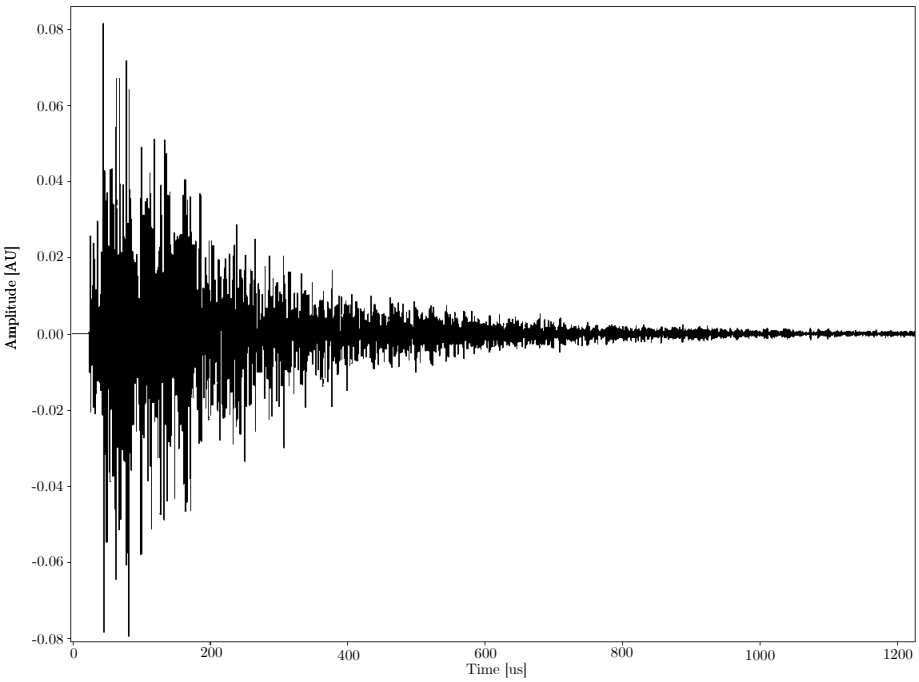

Figure 4.9: Line plot of the strain of a one-element receiver array at the fibre position of the void cell model.

4.3 Proof of Concept

4.3.1 Physical Setup

Figure 4.10: APSensing DAS System Picture showing the top optical unit, and bottom server components.

The DAS system is separated into 2 main components: the optics system and processing server. The optics component consists of the lasers, interferometer systems and an integrated reference coil for automatic noise measurement and reduction. The processing server contains the acquisition card for analog to digital conversion that is then fed into the APSensing software. As the optics system is very sensitive to vibrations, and any vibrations that are coupled in will appear as noise in the data across the whole fibre, the optics system is sat securely on vibration damping foam.

All control is handled by the software on the server, which can in turn control the optical components (such as laser tuning, fibre length information) via the use of a USB connection. The user-interface is run on a different computer, separated by a network. Therefore, this allows the DAS system to be placed in an isolated environment and controlled remotely with disturbing measurements. Data is recorded on the DAS server to an internal RAID in hdf5 [160] files split into 100 second sections. These contain a matrix of all sensing positions up to the maximum interrogation distance in an integer-version of the phase for every sample taken at the sample rate.

Often, external “quiet" or “reference" coils are placed on one, or either side of a Fibre under test (FUT). This is to aid extraction of useful data later by attempting to reduce coupled noise levels around the sample area. This quiet section is especially important before the sample, as large enough vibration events early in the fibre path can affect and cause measurable changes for all further distance bins.

By starting out using DAS to detect large acoustic signals and working to smaller and smaller levels, minimum sensitivities can be found. Breakdowns were chosen as the large acoustic signal trial of the DAS system. Full HV breakdowns where an arc is formed from one conductor of a cable or piece of equipment, to earth or another phase emit a large amount of energy. Compared

to a partial discharge, the acoustic energy dissipated is orders of magnitude greater. DAS must be able to detect these sized discharges in order for there to be a chance to detect the smaller PDs. Unlike the discharges seen in the partial discharge focussed chapters, the signals from these fault events are much larger and their acoustic spectra extends easily into the audible 20 kHz range. Location of breakdowns also has applications outside of a proof of concept across cables, transformers and air or gas insulated conductors. As the discharge consists of lower frequency components and large amplitudes, undersampling (Section 4.1) can be ignored for the most part, and the more classical methods of DAS analysis can be utilised such as frequency band analysis in addition to applying frequency-based filters to reduce noise.

Electrical measurements other than applied and breakdown voltage were not recorded for this initial proof of concept experiment due to the high energy breakdowns involved which would have damaged sensitive PD recording equipment.

4.3.2 Breakdown and Corona in Air

To create a source of corona and breakdowns, voltage was applied across a glass shed insulator up until the point of breakdown, as seen in the diagram in Figure 4.11 and picture in Figure 4.12. The base of the insulator was grounded whilst the top attached to an adjustable AC voltage supply. Voltage was ramped up to a maximum voltage of 56 kV at which point full breakdown occurred around the edges. Corona was visually and acoustically spotted starting at 25 kV. Increasing the applied voltage further resulted in large audible cracks until the sporadic arcs formed a continuous path, tripping the over-current detection on the power supply at 56 kV.

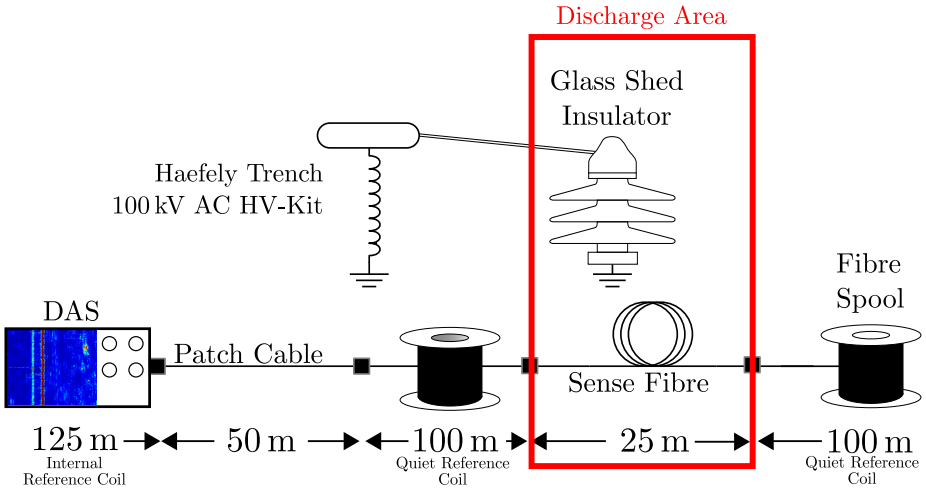

Figure 4.11: Diagram showing the fibre layout and basic connections for the breakdown experiment. Not pictured is the control electronics for measuring the applied AC voltage.

A Single-mode (SM) fibre used for the DAS measurement system was initially

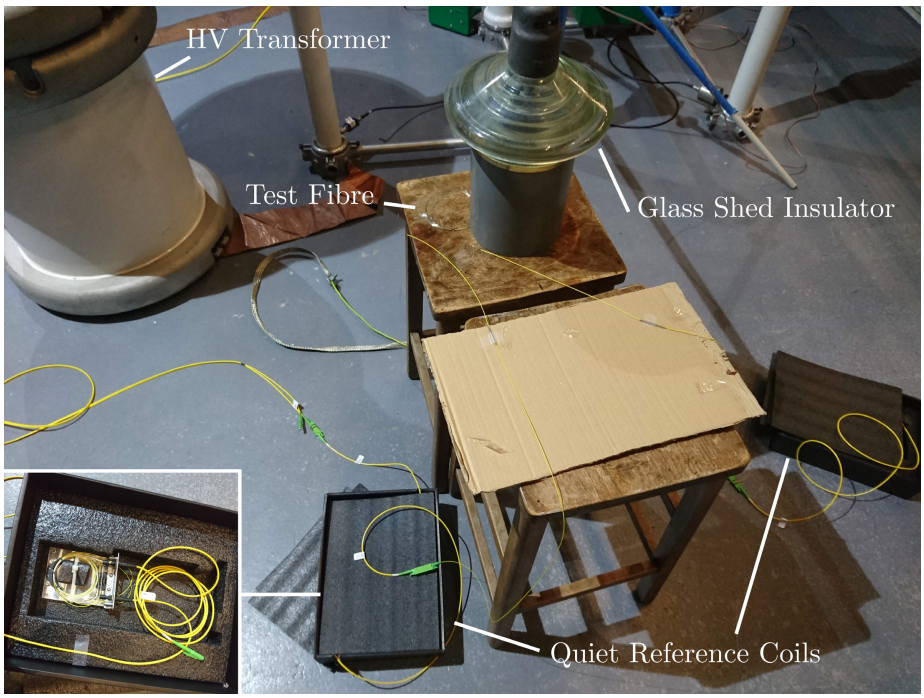

Figure 4.12: Picture showing the HV transformer, shed insulator and sense fibres. The test fibre is yet to be installed onto the plastic base of the glass shed insulator in this picture. The cardboard is supporting the fibre splices between the reference coils and test section.

located 1 meter away horizontally from the insulator. 5 m of fibre was coiled to increase sensitivity to begin with, corresponding with a 5 m gauge length, with the fibre separated in air. This positioning intimated the worst-case placement where fibre was a distance away from a discharge event, where acoustic coupling of energy as detailed in Section 3.1.2 is very low. This sense fibre was connected on either side to two quiet (also known as reference) coils to decrease noise in the detection region. These reference coils are 100 m of fibre vibrationally isolated from the environment through various layers of foam. This results in data in the discharge area only being from the fibre region itself, and not conducted vibrations from other sections. Additionally, this quiet section makes a useful source of decoupled background noise during analysis.

The data produced by the DAS system is analysed by looking at the frequency energy in specific bands. This is achieved by taking an FFT of the data across 1 second intervals, and then summating the components in the specified frequency band. As most background noise comes from low frequency vibrations such as people walking around or machinery with motors or compressors, the higher the frequency bands used, typically, the lower the noise floor becomes. However, there is a trade-off as the analysed frequency band increases, the less the wanted discharge AE couple into the fibre across the acoustic impedance change of air to fibre. By ignoring frequencies below 200 Hz, this removes most of the background sources: mainly from 50 Hz and related harmonics as well

as very low frequencies from general foot traffic around the lab without removing the important AE. The 500 Hz-1000 Hz frequency band was chosen as the demonstrated frequency band due to its highest signal to noise ratio for the following experiments.

Figure 4.13 shows the output of the DAS system in terms of the frequency band magnitude during a ramp of applied voltage up until breakdown of the insulator. In the test fibre section, no events can be detected during the corona build-up to the breakdown event at 250 s. The breakdown itself is clearly identified with a full deflection of the DAS scale for the duration of the breakdown.

At 130 m and 170 m, a continuous level of noise can be seen. This is attributed to the fibre couplers at that point joining the 50 m patch cable to the DAS and the 100 m coil being simply placed on the floor. Therefore, any and every vibration in the floor of the laboratory would couple into this point of higher reflection than general backscatter in the fibre[1]. Sadly, this data was taken before obtaining an acoustic measuring device such as the OptimAE system from Chapter 6 and 5, and before the more detailed analysis techniques in the later chapters, so there are no reference acoustic signals to compare to, as well as being outside the measurable range of discharge for the Omicron electrical measurement system without damaging the equipment. Evidence of the discharge event can also be seen at other locations other than the test fibre: namely in the 50 m patch cable - the only other section of fibre that is not vibrationally isolated from the environment.

The effect of the 5 m spread of the gauge length is visible within this data: any change in measured energy occupies a band of at least 5 m, or more if the energy propagated along the fibre. From the overlapping spatial sampling distance, these visible sections of above-background energy do not fall into a 5 m grid, but are offset from each other by the 1.27 m.

To improve the acoustic coupling into the fibre, a section of 1 m was wrapped directly around the grey plastic supporting base seen in Figure 4.12. This change allowed acoustic waves travelling through the solids of the insulator created by arcs and corona initiated across the glass surface to couple directly into the fibre rather than through the poorer conductor of sound: air. Voltage was ramped up from 0 kV to 15 kV at 100 s, increased to 30 kV at 200 s and reduced again to 20 kV and 0 kV at 410 s and 500 s. No breakdowns or direct arcs occurred during this test. With the test fibre attached directly to base of the insulator, corona discharge is clearly seen in Figure 4.14 starting at 200 s corresponding with the application of 30 kV across the same insulator. The resultant acoustic magnitude within the frequency band of 500 Hz to 1000 Hz, which had the highest signal to noise ratio, is smaller compared to the full discharge, as the corona acoustic emission is significantly lower in amplitude than a breakdown event. This discharge is not identified anywhere else other than the test fibre in vibrational contact with the surface on which the corona discharge is occurring on, corroborating with the initial air barrier attenuating small AE. With the voltage reduced to 20 kV, the corona discharge is still observed in the DAS data, but at a reduced amplitude of 0.2 rad to 0.6 rad, much closer to the noise floor.

[1] At points of coupling: where a connector is present, as there must be a physical way of detaching the two halves, there will always be some slight misalignment when brought together making the connection. Therefore, this discontinuity will lose some amount of light into the surrounding medium and reflections.

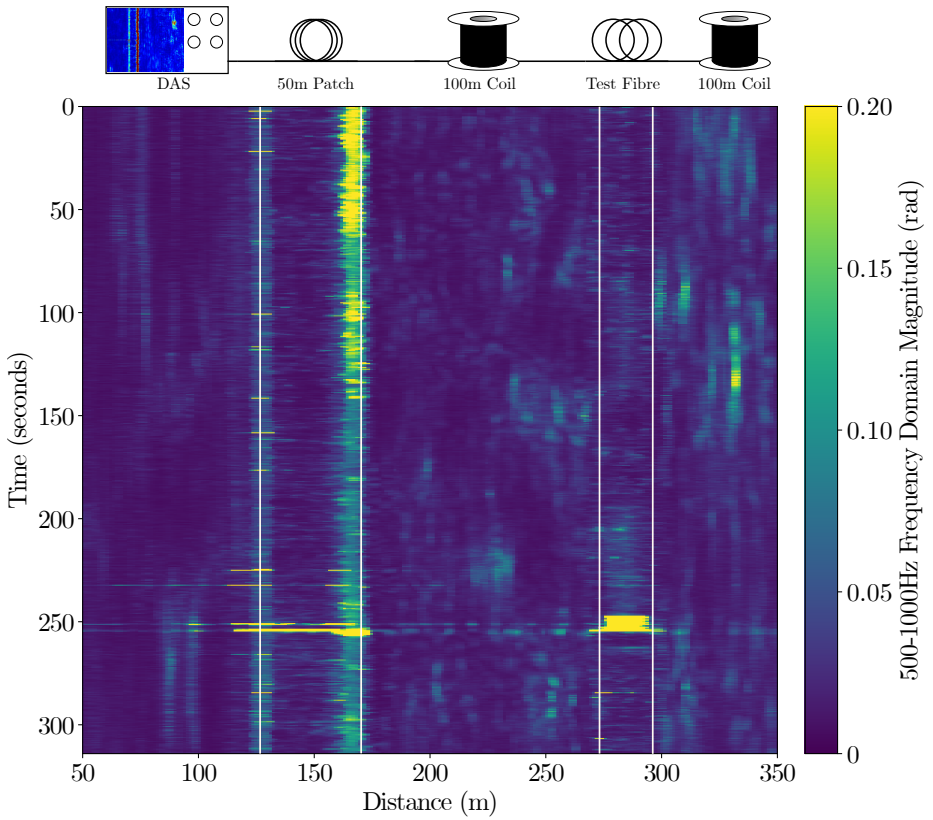

Figure 4.13: Frequency energy plot of the 500 Hz to 1000 Hz band during a ramping voltage test of a glass shed insulator. Breakdown occurs at 250 s. White vertical lines indicate the different sections of the fibre under test. Final discharge size measured at 0.8 rad.

Within the test fibre, vibrations from other sources such as the HV transformer are not coupled in as repeating the experiment without the glass shed insulator resulted in no increase of frequency band energy in correlation with the applied voltage or whether the transformer was energised or not.

Figure 4.15 shows the frequency content of the corona discharge from the DAS system. 50 Hz and higher harmonics are clearly seen outside the general noise floor at 0.1 rad. Only certain odd and even harmonics are seen, not a series of mostly odd, or mostly even. This is an odd result, but simply demonstrates that the main energy detected by the DAS are these harmonics which differs from expected PD events where the fundamental frequencies were well above the sample rate of the system, resulting in aliasing effects.

As the acoustic sources are relatively large in amplitude, the acoustic energy spreads down the incoming and outgoing fibre, creating additional responses in the DAS data in the surrounding distance bins, not just the primary detection area. Even though the transmission through air is extremely lossy, again due to the high amplitude: specifically in the full breakdown events, the energy is enough to spread through the air and still be easily detected.

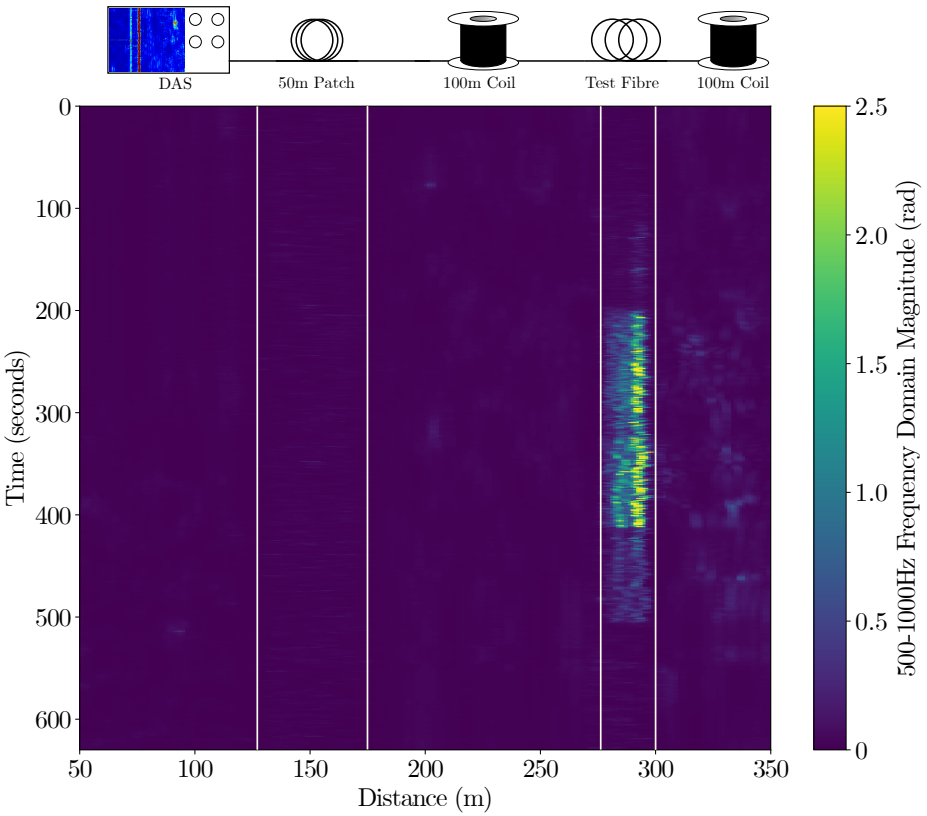

Figure 4.14: Frequency energy plot of the 500 Hz to 1000 Hz band during corona across a glass shed insulator. 15 kV applied at 100 seconds, 30 kV at 200 s, reduced to 20 kV at 410 s and 0 kV at 500 s. Test fibre in contact with the base of the shed insulator.

4.3.3 Breakdown under Oil

Breakdowns were also recorded under oil at a lower breakdown voltage at 28 kV. Breakdowns under oil will naturally have different characteristic acoustic properties such as frequency spectra and a different source impulse shape due to how the oil quenches an arc quicker than in a gas [17, 161]. Two processes generate the acoustic wave in liquid dielectrics: cavitation near electrodes surfaces at lower discharge levels, and from streamers causing a shockwave throughout the fluid [21, 162].

A gap of 20 mm was set up between a needle electrode and a grounded bar immersed under Nytro Gemini X mineral oil. Some contamination was present in the oil including small hair-like whiskers likely from previous pressboard experiments. These were attracted to the electric field produced across the gap thereby resulting in bridging where a rapid build-up of discharges was observed across a few seconds up until full breakdown of the gap, at which point voltage was automatically removed by over-current protection. The system was monitored by use of an Omicron MPD600 system for measurement of the amplitude of PDs. PRPD analysis of the discharges was ignored at this stage due to lack of synchronisation between the different measurement systems and data

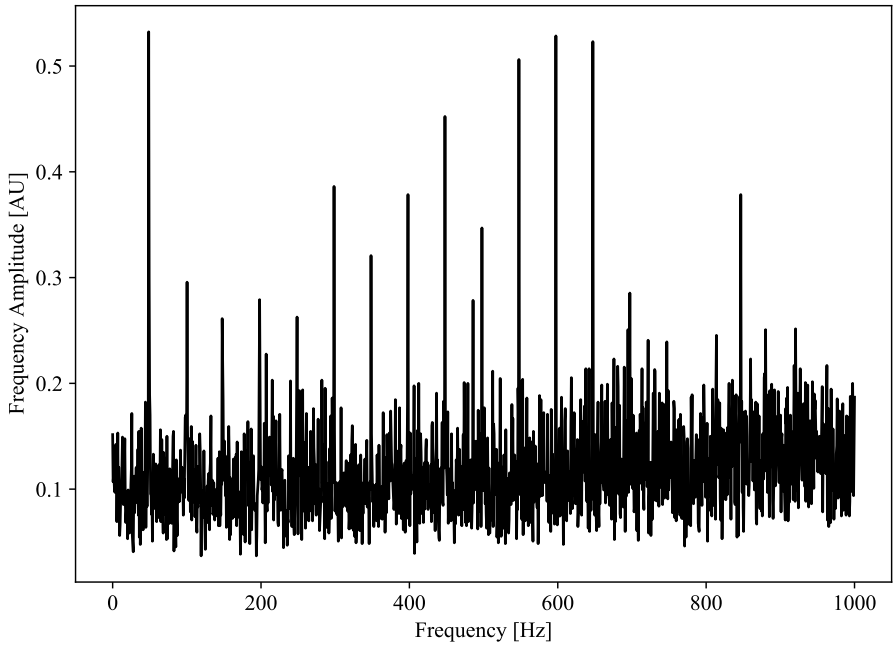

Figure 4.15: Frequency content of multiple discharges at 280 m-290 m during corona discharge from Figure 4.14. 50 Hz and harmonic peaks are observed.

processing. HFCT measurements were not taken due to the large amplitude size tripping the measurement system into protection, and the events easily being detected on the coupling-capacitor method. Recording a single continuous capture with the HFCT equipment available, synchronised with the other measurements, was additionally not possible for the length of the experiment.

Figure 4.16 shows the output of the Omicron (bottom) and DAS system amplitude (top) measured as the optical phase change caused by the strain on the fibre, during the discharge build-up and breakdown. Large amounts of discharges between 10 pC and 600 pC are seen in the Omicron data up until 2000 ms where the bridging starts to occur. The final breakdown clips the front-end of the Omicron system at 10 nC and are much larger in amplitude than shown. The DAS data at the position of the discharge (shown in purple) shows a set of small spikes from the smaller PDs, and then large spikes at each of the breakdowns. All identified large discharges by the Omicron can be observed to line up with a spike in the DAS data. The second position shown in a more saturated red that corresponds with a section of fibre not submerged in the oil shows that these discharges contained in the oil can only be detected with a fibre in direct contact with the fluid. This trace also demonstrates the noise floor of the experiment of $<\pm 0.1$ rad. These discharges were able to be heard by the human ear with the final discharge which tripped an over-current condition resembling a loud "pop".

The experiment shows evidence of partial discharge events under 1 nC being identifiable using the DAS system. Figure 4.17 is a snippet of data from the larger dataset showing 5 events less than 500 pC. Other than the first discharge at 214 pC, the other discharges all produce obvious output in the phase data.

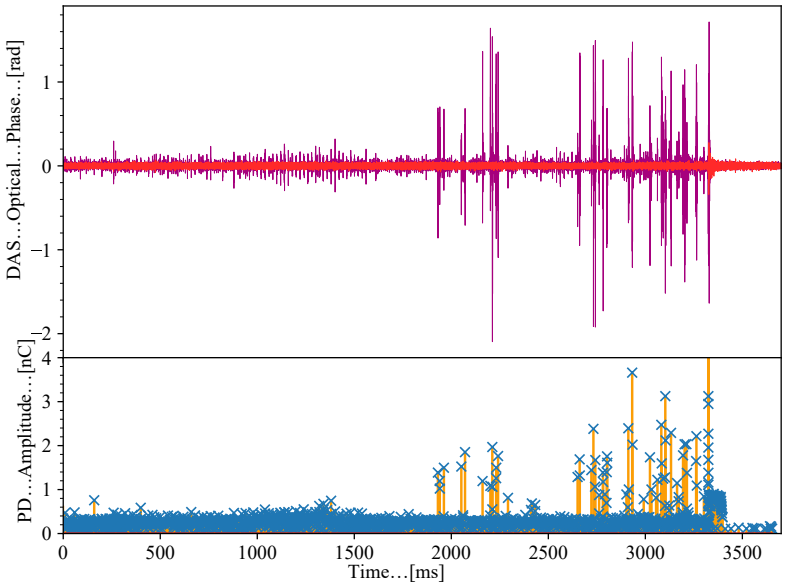

Figure 4.16: DAS (top, purple: within void cell, red: 5 m away from void cell) and Omicron (bottom) output during the build-up and breakdown of an oil gap. Omicron events are shown as blue Xs with a vertical yellow line for better identification of time. Breakdown occurred at 28 kV. Final discharge at 3300 ms is off scale of the Omicron system in excess of 10 nC. Omicron discharge events shown as crosses with vertical stems for identification purposes.

Rather than the single outlying point as expected from the earlier modelling, the data has a linear phase style impulse response where there is a slight pre and post ringing. This results in the system having a mean of zero: i.e. no permanent stress change, whereas the modelling result did not have this property. However, these points are still at the extreme end of the sampling frequency meaning that extraction techniques such as wavelet transforms despite the appearance of waveform, would not work. This is because wavelet denoising requires many samples describing the wavelet image whereas in these datasets, typically only 1 or 2 samples make up the PD events.

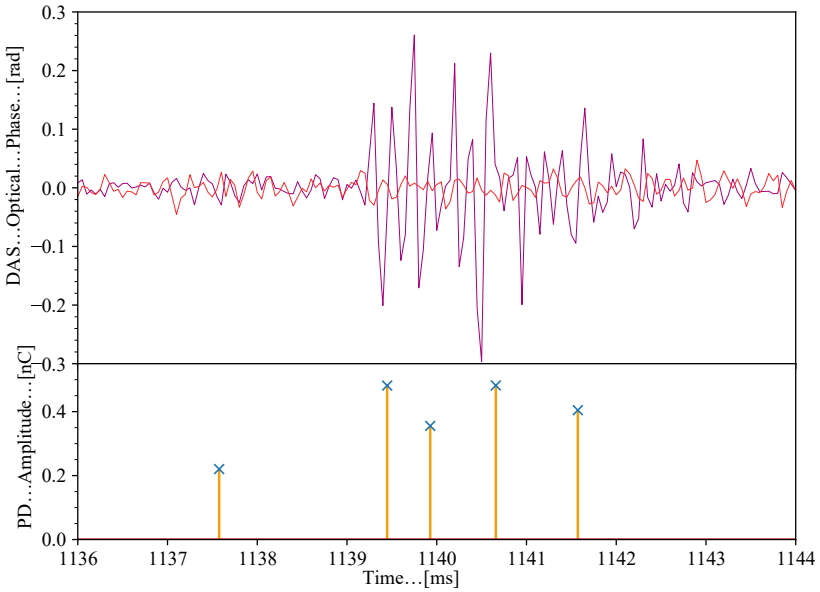

Figure 4.17: Zoomed version of Figure 4.16 detailing one set of discharges in the build-up to the breakdown. Discharges of between 340 pC and 500 pC measured by the Omicron system (bottom) are observed to generate spikes in the resultant DAS data (top). Purple: within void cell, red: 5 m away from void cell.

4.4 Conclusions

DAS can easily detect large breakdowns at large signal to noise ratios, and inherently their locations. The exact amount of energy released in these breakdowns was not able to be calculated correctly due to clipping of the electrical measurement devices. However, the amplitude is definitely more than tens of nanocoloumbs. Therefore, as DAS is able to easily detect these signals, and the evidence in the pressboard breakdown of sub 1 nC partial discharge events, it follows that DAS should be able to detect events smaller than these. Given the measured amplitudes of the discharges in this proof of concept experiment being in the range of 1 rad to 3 rad, partial discharges on the order of hundreds of picocoloumbs and below would, by linear extension, be beneath the current noise floor. However, as the acoustic events become smaller in amplitude, as well as the acoustic length of the events becoming shorter (higher frequency), the undersampling effects such as aliasing become more important. In these breakdown events, the detection was mostly obtained by sensing large, lower frequency components (below 2 kHz) of the breakdowns; whereas, for smaller partial discharges, the undersampling effect from is more significant due to the smaller amplitude, but higher frequency AE, and relies upon seeing the presence of discharges over time rather than immediately seeing a single large event.

Models were also completed for the complex acoustic reverberations resulting in impulse-lengthening as well as a whole system model. Using large partial discharges before breakdown across a pressboard under oil, there is experimental evidence that the generated models closely match real-world measurements.

Therefore, progressing experimental designs to look for smaller discharges from a wider array of sources is the next step for determining the usefulness of DAS as a PD detection system.

Chapter 5

Partial Discharge within a Void

Partial discharge due to presence of voids in dielectric materials, is a common phenomena in HV plant such as polymeric cable, fluid filled cables, transformers and ancillary equipment [18, 20]. It occurs when the electric field across a void or cavity exceeds the dielectric strength of the constituent gases in the void. PD then occurs generating heat and acoustic emissions that can then be detected. This PD generates heat, light, mechanical stress, chemical changes along with currents, magnetic and acoustic waves [163–165]. Presented in this chapter is an alternative detection system using DAS techniques, with peak detection achieved down to 18.55 pC with the sense fibre directly in contact with the insulation medium. Alongside DAS and coupling capacitor electrical measurements, a single-ended high sample rate acoustic sensor provided by Optics11 is used allowing comparisons with similar acoustic measurement techniques. Custom synchronisation tools are developed to allow a multitude of existing electrical and acoustic sensing solutions to be compared and aligned on a sample-by-sample basis: even across differing sample rates and data formats. A time-linearity check is also completed between the different measurement systems to confirm synchronisation over time.

The sources of void discharges are fabricated as singular test cells described in Figure 5.1 through the use of rapid prototype 3D-printing and epoxy casting, rather than attempting to create reliable sources in an already-existing insulation system such as a cable. The goal of this PD source is simply to create a reliable single source of PD of which the emitted energies can be measured. These analogues can then be customised through void size to create a range of different sized discharge and AE sources.

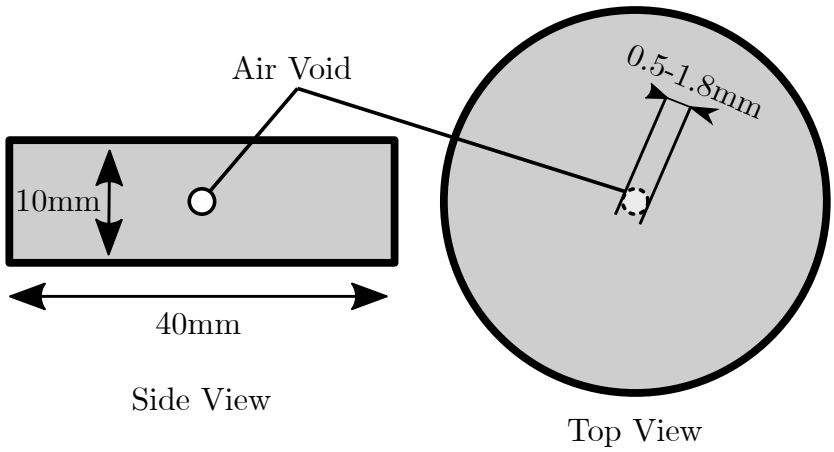

Figure 5.1: Side and plan view of a void discharge cell, showing the dimensions for the final fabricated cells.

5.1 Experimental Design

To simulate void discharge, a suitable analogue consists of a single air-gap void surrounded by insulating material so that discharge can only occur from one known position in the source. From these requirements, two types of void cell were constructed: the first, a rapid prototyping method for generating a wide range of void sizes and with high customisability for mating with other sensors; and a second epoxy-cast cell with better defined characteristics in literature [36, 166]. To complicate matters, coils of test fibre (5 m and under) were required to be directly attached in some way to the cells, in order to provide adequate acoustic coupling for measurement of AE. For both methods, the cells are submersed under oil to stop discharge from tracking across the surfaces as well as prevention of corona. The cells are sandwiched between two flat-surface electrodes as shown in Figure 5.2 - one connected to a variable high voltage supply as in pressboard experiment, and one connected to ground. Voltage was applied until partial discharge inception and then increased a further 10% to maintain a mostly continuous series of PD events.

5.1.1 Rapid Prototyping Method

Rapid prototyping, or in this case more specifically: resin 3D printing, was the basis for this void cell construction. Other 3D printer methods such as Fused deposition modelling (FDM), where plastics such as ABS or PLA are melted through an extrusion nozzle and placed in layers to create objects, are not suitable for this sort of test cell. Due to the nature of the layers, small voids are created throughout the entire printed object seen between layers and would therefore create large amounts of unwanted PD. Additionally, the layers are not liquid-tight and would let oil easily permeate into the central areas. A resin 3D printer instead uses a liquid polymer that is cured using UV light and can create homogeneous solid objects eliminating voids in unintended places.

The PD test cell was created utilising 3D resin printing (SLA) using an

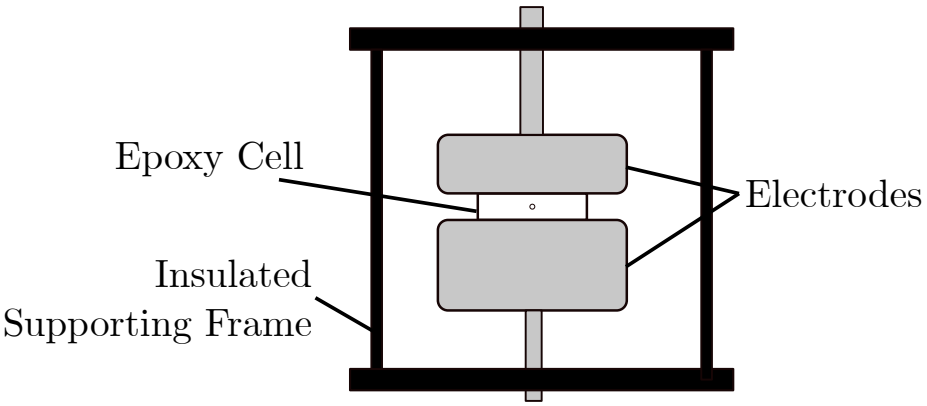

Figure 5.2: Side-view diagram of the void cell construction. Entire assembly is connected to a high voltage supply identical to Figure 6.1, and immersed under oil to stop surface tracking and corona.

AnyCubic Photon 3D Printer [167] and AnyCubic UV Resin. The properties of the printer and resin can be found in Appendix A.3. The cell was split in two as 3D printing voids in the middle of an object with this SLA method is difficult, and in some cases requires small temporary structures to be created to print over the void. As the void is fully encased in resin, this structure would not be able to be removed. This design could be improved to enable singular printing of the entire cell without these issues, but for simplicity and ease of adding in sensors such as the fibre, the two halves were printed separately. Each half is a 40 mm diameter cylinder standing 1.5 mm tall with a 1 mm spherical void removed from the centre. By printing the halves of the test cell individually, a fibre can be clamped in between the two halves as well as providing access to the void to inspect damage over time. Two small groves were cut into the inner surfaces of the two halves to facilitate this fibre clamping without stopping the two sides from properly touching and forming the single void. The constructed cell was finally exposed to an additional UV curing session of 10 minutes to ensure that the resin material was fully cured.

Due to the printing process, any trapped air bubbles during the printing process show on the flat surfaces. Figure 5.3b identifies these holes on the bottom and top surfaces. These voids should not be a problem as they are immersed in oil, however light sanding was used to smooth the surfaces. In addition, the mating surfaces (Figure 5.3a) between the two halves were also sanded to ensure a liquid tight contact once the two halves were offered up to each other.

5.1.2 Epoxy Casting Method

The epoxy casting method consists of pouring 2-part epoxy into a cylindrical mould and incorporating an air bubble in the middle of the cast. A silicone mould pictured in Figure 5.4b was constructed around a FPD 3d-printed cylindrical form: Figure 5.4a, dimensions 40 mm and 10 mm tall. To create the

(a) Void sides of the printed cell showing the central void and a much flatter surface

(b) Flat sides of the printed cell showing voids from trapped air bubbles

Figure 5.3: Pictures of the void cell using the Rapid Prototyping method

void, a hybrid approach was taken to both inject the air bubble with a needle and also cast in two halves due to the very narrow window in which the viscosity would be perfect to allow a bubble to remain centred in the epoxy. The mould was filled just over halfway with 2-part epoxy that had been degassed in a vacuum chamber for 15 minutes. Fibres were also immersed in this epoxy with slits cut in the mould to allow entrance and exit of the fibre path. Care was taken to ensure no trapped air bubbles remained from the assembly and pushed-in fibre and application of flame was used to pop surface bubbles. The epoxy was then cured by placing in an oven at 60 °C until its viscosity increased enough that an air bubble could be injected with a syringe without the bubble popping. The increased temperature also aided removal of trapped air bubbles due to thinning of the liquid before curing occurred.

After 5 minutes of additional curing at heat, more uncured epoxy was poured on top to the final height of the cell; encasing the air bubble.

A completed cell can be seen in Figure 5.5a, the cells is mostly transparent from top to bottom allowing inspection of the voids. The main 0.5 mm void can

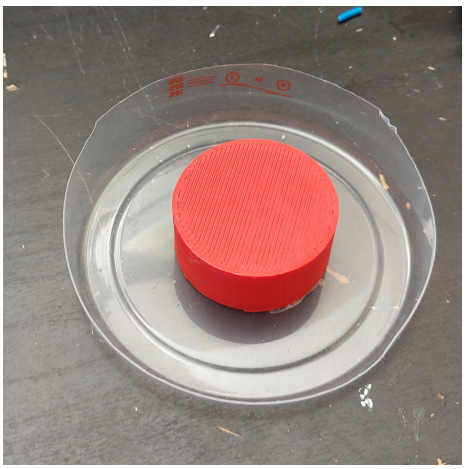

(a) Original form used to fabricate the silicone mould pictured in (b)

(b) The completed silicone mould with visible cuts for entrance and exit of the fibre optic cable. Pictured with an epoxy mould in progress.

Figure 5.4: Pictures from the epoxy casting method

be clearly seen slightly off centre, with an additional unwanted void below. The centrality of the void is not of concern as discharge will still occur within the void. The pattern seen on the surface of the cells is from the FDM method of fabricating the original mould and makes no difference to the operation of the cell. Figure 5.5b has a larger void of 2.5 mm with the goal of generating higher amplitudes of discharge. Figure 5.5c shows a manufacturing failure during the void-injection process; the epoxy had cured too much when trying to inject the air bubble resulting in the epoxy not being unable to form back together into a uniform puck leaving the gouge of the needle behind. This cell is still able to produce PD, however, the discharge is irregular and less repeatable, producing odd PRPD patterns at sporadic intervals.

(a) Small void (0.5 mm)

(b) Large void (2.5 mm)

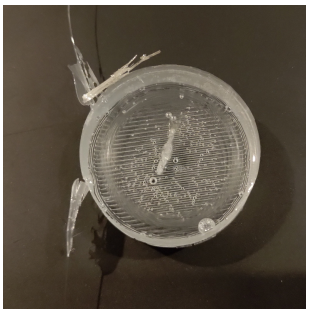

(c) Failed cell with gouge instead of void

Figure 5.5: Pictures of the formed Epoxy-cast void cells showing different void sizes as well as a failed cell (c) due to letting the epoxy cure too much before injecting the void.

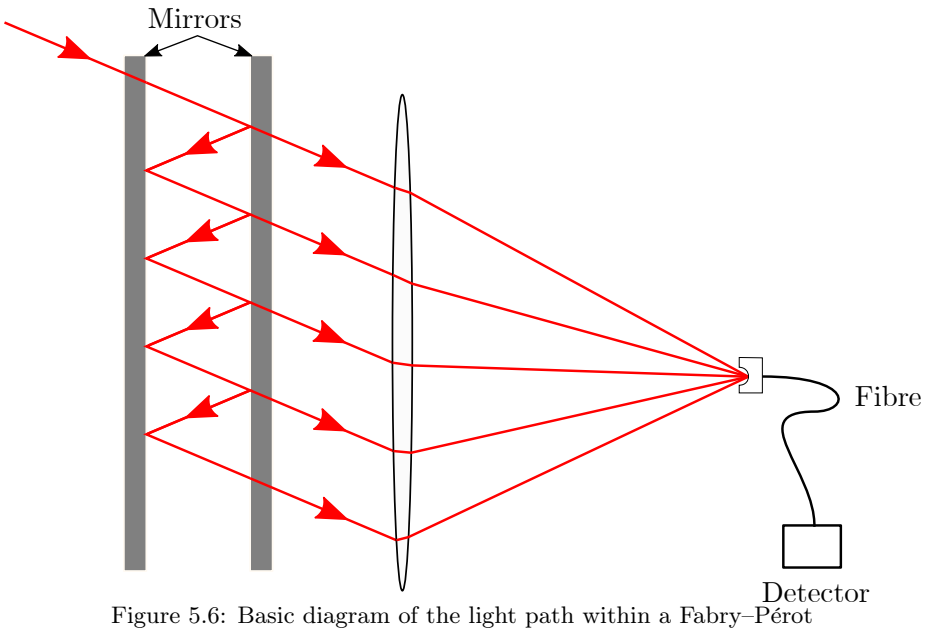

Figure 5.6: Basic diagram of the light path within a Fabry–Pérot cavity showing the repeated splitting of the light and combination at the focussing lens producing

5.1.3 High Sample Rate Acoustic Sensors

For an acoustic comparison at high sample rates, an Optics11 OptimAE system was employed. The system consists of a central measurement system and multiple discrete sensors attached by fibre optics rather than electrical pickup devices such as a piezo element. These sensors contain a Fabry–Pérot cavity and are intended to be mounted onto surfaces such as a transformer tank [5, 146]. The fact they are optical only allows for installation in adverse environments as well as being immune to electrical interference. As this system is not a DAS method, and is simply an interferometer, it allows for sensors to be polled at a very high rate: in this case, a sample rate of $1\,\mathrm{MS\,s^{-1}}$ is achieved.

A Fabry–Pérot cavity is pair of two partially reflective flats so that light entering from one side will bounce between the two flats many times [96] as is demonstrated in Figure 5.6. Laser light is injected from one fibre optic into the cavity. The transmissive light is collected from each of the bounces and focussed with lenses to couple back into a different fibre optic. This fibre couples the light back to a detector where the self-interference producing repeated dips in intensity can be measured giving both temporary and static displacements. The measurement is measured in nanometres of movement of the cavity walls. Therefore, each sensor in the OptimAE system connects back to the measurement unit on APC-LC fibre connectors. The laser is tuned in power during a calibration process to achieve the best possible signal levels. In practice, if this calibration procedure with no acoustic signals present is not undergone, then the resultant amplitude of PD events and other signals is typically in the noise floor of $<0.2\,\mathrm{nm}$. The noise floor of the OptimAE system, once calibrated, is the data's 2 least significant bits, or in output units of nanometres of effective movement of the sensor head: $0\,\mathrm{nm}$ to $0.03\,\mathrm{nm}$.

As the sensors comprise of solely optics components, and are separated by fibre optics, much like the DAS system, they are unaffected by electrical and magnetic noise sources. Only the acquisition and measurement system could introduce systematic noise from these sort of sources. Therefore, any signals detected by this source must be from movement in the Fabry–Pérot cavity[1].

Sensors with 2 cavity resonances were provided by Optics11: one at 50 kHz, and another at 200 kHz. Acoustic frequencies coinciding with these resonances experience a higher measurement gain. However, frequencies outside this resonance have some attenuation. The frequency response is shown in Figure 5.7 for the 200 kHz sensor. The 50 kHz sensor's frequency response was unavailable, as it was a custom prototype. Both sensors with different resonant frequencies were used for measurement of partial discharge. These sensors were attached on the plastic tank wall with ultrasonic gel as a coupling interface in between. An additional 200 kHz resonance sensor was used on the Piezo-electric transducer (PZT) attached to the DAS system for synchronisation purposes. The difference between the two sensors can also be seen in their physical size shown in Figure 5.8.

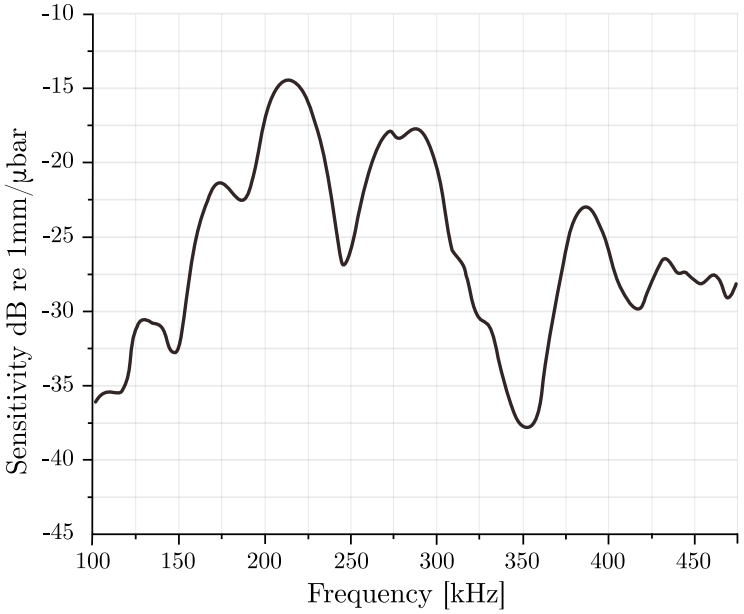

Figure 5.7: The frequency response of the 200 kHz resonant OptimAE sensor as stated in the Optics11 datasheet.

5.1.4 Electrical Measurement

A conventional capacitive-divider system from Omicron was used for the basis of discharge monitoring and as a primary comparison source following the relevant IEC60502 and IEC60270 standards. The Omicron system comprises of an

[1] If noise was injected at the measurement end, this noise would appear in all 3 channels of measurement as they are handled by the same acquisition card within the OptimAE interrogation unit.

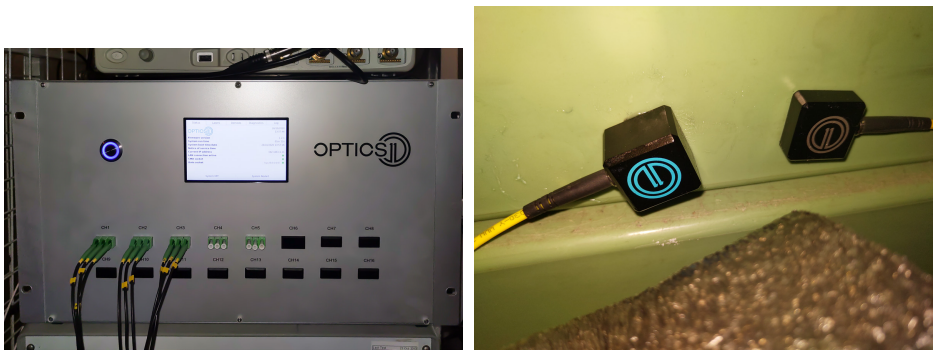

(a) Picture of the OptimAE interrogation unit with up to 5 sensor connections provided - 3 of which are used

(b) Picture of the two sensor heads with differing cavity resonances: the larger left sensor at 50 kHz, and the smaller sensor on the right at 200 kHz

Figure 5.8: Pictures of the OptimAE system by Optics 11

HV coupling capacitor, a CPL542 quadripole used to separate the PD measurement signal from the synchronising voltage waveform, and a MPD600 combined with a USB interface MCU502 used for acquisition of the voltage and PD waveforms. The MPD system has a software-selectable frequency window to help suppress noise. For the presented results, the window was set to the standard of 250 kHz±150 kHz. Before each measurement session, the system was calibrated using a Omicron CAL542 calibrator and separate voltage standards. Phase, amplitude, and voltage data was recorded in the proprietary Omicron format and then exported later to MATLAB compatible files for processing in Python.

5.1.5 DAS Fibre Placement

The fibre layout consists of the fibre segments under test, quiet reference coils, and patch cables to connect everything together. A schematic diagram of the connections is shown in Figure 5.9. This consists of a 50 m patch cable between the DAS interrogation unit and reference coil. Then, two sections of test fibre are laid out: the first is the one in physical contact with the void cell, either embedded or glued depending on the construction. This is limited to a single coil due to space constraints. The second test section is located at the oil tank wall, directly next to the OptimAE sensor heads allowing for better comparison between the acoustic methods. Multiple length fibre coils within each of the void cells are used for comparison; and with correlation between the different FUTs at the tank wall, positive identification of events versus noise can be achieved. These comparisons will be made in the next chapter as to not be repeated across two different discharge sources. Between each measurement fibre, 5 m-10 m of patch fibre is used to separate the test sites within the measurement data, and to reduce coupled vibrations as well as ensuring at least one gauge length between the sites. By placing fibre at the tank wall, directly next to the OptimAE acoustic sensors, this allows for better comparison between the high sample rate measurement and the DAS.

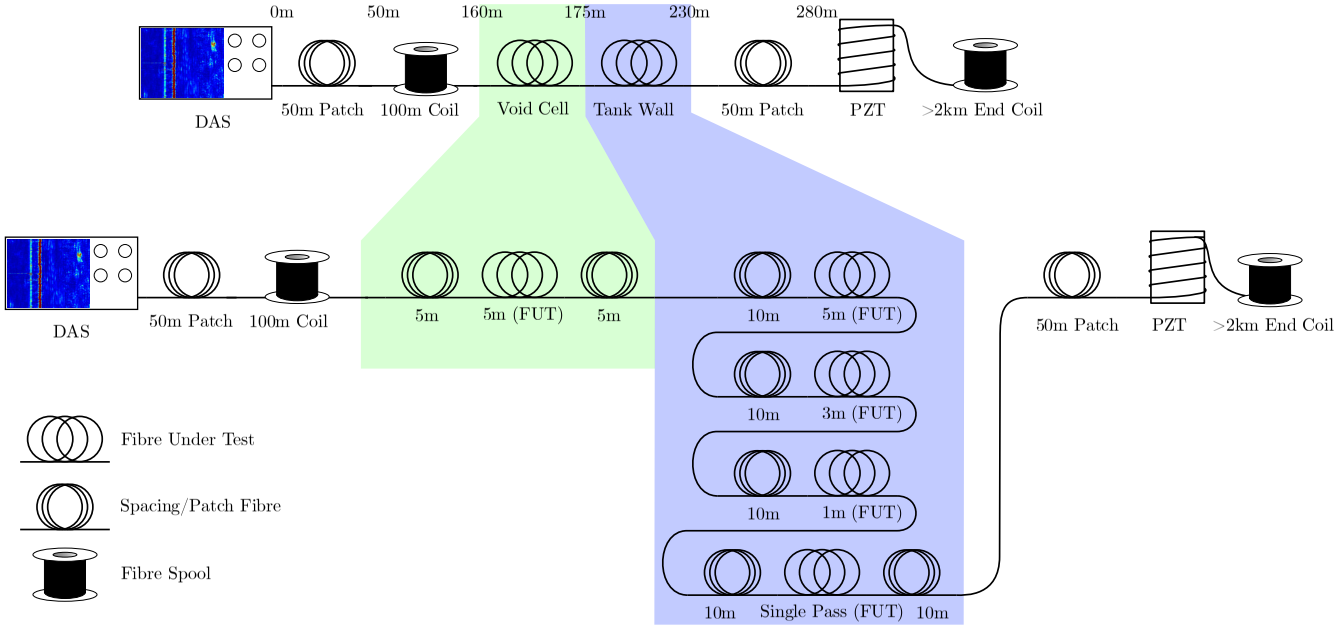

Figure 5.9: Schematic diagram showing the simplified (top), and detailed (bottom) fibre connections from the DAS unit through the fibres under test to the PZT.

5.2 Characterisation of Discharge

The void cells in these experiments are not designed to progress over time. Rather, they are intended to create a static, mostly repeatable source of void discharge. Figure 5.10 shows PRPD plots of the two cell constructions under an applied voltage of 16.35 kV and 24.71 kV, just above the observed PD inception point for the respective cells that produced continuous discharge over a 3 minute period. Looking firstly at the 3D printed void Figure 5.10a, multiple different voids can be seen from the many different patches of PD in the symmetric positive and negative sections. These unintentional voids are most likely due air trapped either in the seam between the two halves: as the material itself is homogeneous from inspection. The PD has an average figure of 142.3 pC and a peak of 309.6 pC with an average rate of 192 PDs/s.

The epoxy cell's PRPD plots in Figure 5.10b contrastingly do not contain the numerous separate voids as seen in the 3D print. Instead, a rising amplitude is seen to match the higher applied voltage (due to the higher inception voltage), alongside a cluster of discharges at a constant amplitude in the positive and negative half-cycle. These observations are indicative of a single large void in early stages of progression, and possibly a number of significantly smaller voids (likely due to very small amounts of trapped air). The average discharge size is higher at 523.9 pC with a peak of 1.13 nC and a higher rate of 470 PDs/s. Some possible triple-junction discharges can be observed as the small discharge near the below 50 pC.

Over time with the 3D printed void cell, oil seeped into the central void through the seam between the two halves. Additionally, the fabrication material appeared to change properties over time becoming more supple. This is possibly due to the oil impregnating the material, or the cell being improperly cured. Although this impregnation would increase the dielectric strength of the material over time, as observed the mechanical strength was decreased as well as unintentionally changing the partial discharge patterns; even in some cases to stopping discharge entirely. A difference is also seen in the MPD plots after 60 minutes of discharge whereas the epoxy void cell does not change significantly. After 60 minutes (Figure 5.11), spurious discharges are reduced with more defined tight void-like groupings in the negative half-cycle. In the positive half-cycle, the initial groupings merge into a cloud close to the start of the half-cycle as well as discharges following the voltage curve rather than tighter groups seen in the negative cycle. The average PD amplitude did not change significantly from 163 pC initially, to 169 pC. The number of discharges per second also increased to 538 PDs/s, compared to the initial rate of 391 PDs/s. The epoxy cell, due to its sealed construction, did not significantly change discharge patterns over time other than natural degradation from the repeated discharge events and both cells experienced similar number of discharges across the same time period. Therefore, the epoxy cast cell was chosen as the preferred discharge source for a more consistent, and reliable design for later results.

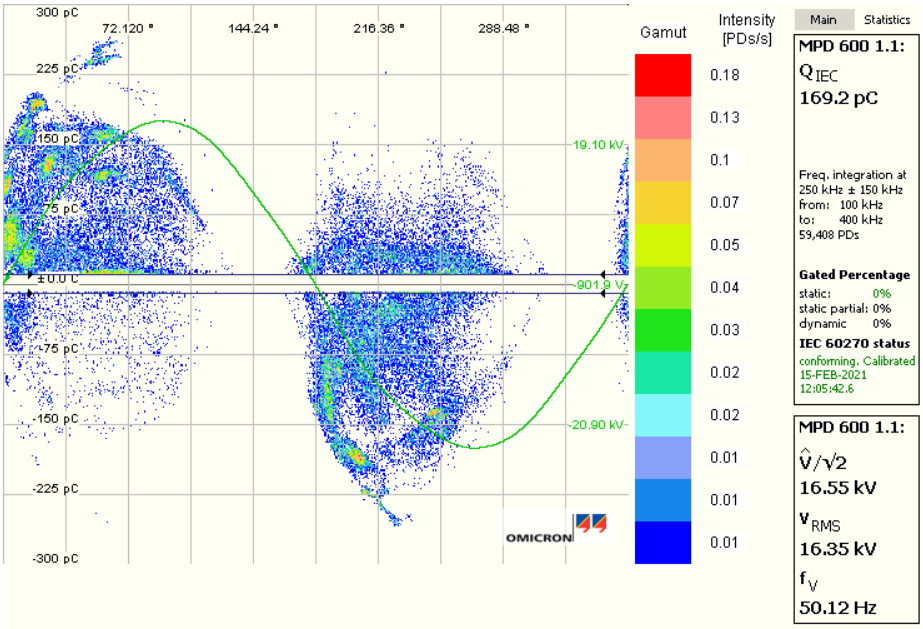

(a) Initial discharge from the 3D printed cell. Average applied voltage: 22 kV.

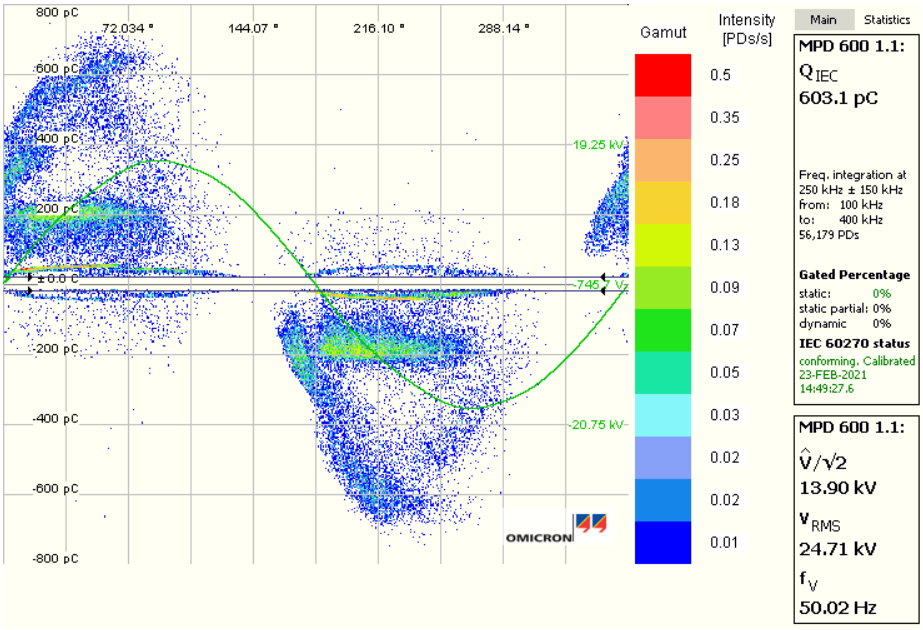

(b) Initial discharge from an epoxy cast cell. Average applied voltage: 28 kV.

Figure 5.10: Omicron PRPD example plots for the 3D printed cells(a), and the Epoxy cast cell (b). Void type discharge can be identified in all plots, with multiple discharge sources identified as separate groupings in (a).

5.3 Synchronisation Method

The Omicron system records a timestamp with every PD event it sees. However, these timestamps are not absolute, and are relative to the first event detected: which could be at any random time due to background noise. Additionally, the trend file that can be generated by the MPD software only records the average PD amplitude and voltage level every 300 ms. The timestamp tends to slip back to the start of the file whenever the MPD is disconnected, or the system is left recording for a long time without any events making later analysis arduous. Therefore, a separate synchronisation system was developed.

A Piezo-electric transducer (PZT) was used to inject synchronisation signals into the DAS system. This meant that the same DAS interrogation pulses used for scanning the test region of fibre were used for synchronisation, and no additional time delay was added. The synchronisation signals were created and conditioned using the following method. A MSO6034A Agilent Oscilloscope is used to trigger on and switch between the following different synchronisation sources: Line 50 Hz, PD thresholding, synchronisation pulse generator. To obtain PD thresholding on the oscilloscope, the PD output of the Omicron quadripole is split into Omicron measurement unit and an input on the scope. Provided on the rear of the unit, the trigger out connection is used to provide a TTL-level square wave whenever a trigger event occurs. The scope's trigger level is set to a threshold above the noise level of 0 pC to 15 pC and therefore triggers on any events greater than this threshold. The trigger time delay between a signal passing the threshold value on an input channel of the oscilloscope to the trigger output going high was measured to be under 60 ns.

The signal is then passed through a TTi TGP110 Pulse Generator to widen the short pulse from the oscilloscope up to 500 µs primarily for the PZT. 500 µs was chosen as at the sampling rate used on the fibre of 20 kHz, the pulse will be seen as a short spike in the PZT region of connected fibre. The output is additionally split off into the PD sense input of the Omicron system, which is normally connected to the quadripole and HV coupling capacitor allowing injection of sync pulses.

The synchronisation pulse generator consisted of a Cyclone II EP2C5 FPGA board that was manually triggered, to inject a specific timing sequence. This sequence was designed to ensure even with large background noise, this timing reference can be found and uniquely decoded even if multiple sequences are accidentally fired. This is achieved by appending an increasing 3-bit binary code at the end of the synchronisation pulse train, creating 8 unique codes. After each pulse sequence, this sequence is increased so that the following sequence is different and differentiable. During the processing of the relevant data, this sequence is searched for to find the time offset between the multiple sources and allow for correction. Figure Figure 5.12 shows the various connections and pathways to each piece of equipment.

Unfortunately, the pulse generator does not have a tri-state output. Therefore, signals originating from the quadripole will be attenuated, as measured by the MPD600 when this cable is connected. To allow for unimpeded measurements whilst also allowing synchronisation, the cable is manually connected and disconnected from the pulse generator whenever a synchronisation pulse is required. The Omicron system was tested for distortion of pulses with a stub-

ended BNC cable (as in disconnected from the pulse generator) in-circuit: no variation was found at the standard measurement range of 250 kHz±150 kHz.

The outputs of two synchronisation trains from the DAS, OptimAE and Omicron system are shown in Figure 5.13, each from their respective measurement systems. The synchronisation impulses are easily detected in both the DAS and Omicron; well above the noise floor. In fact, the Omicron MPD600 clips the signal due to its amplitude, however this is acceptable as the amplitude is not required and the timestamp is maintained. The OptimAE has more difficulty detecting the pulses, although this is because the sensor is indirectly coupled to the PZT used by the DAS system. These impulses are threshold-detected and checked for the correct timing sequence before creating an offset file tied to the data. This method would allow for multiple measurements to be made across systems at significant distances, assuming that at least one of the measurement methods has a fixed known time reference (e.g. GPS).

Linearity of time was a concern in the Omicron data, as it does not claim any time accuracy between PD events. Therefore, to measure any time drift, synchronisation pulses were generated every 10 seconds for a period of 30 minutes and fed into both the Omicron and DAS. The resultant delta between the DAS and Omicron is shown in Figure 5.14. A slow negative trend is seen equating to approximately a time-slip of $7.08\,\mathrm{ms\,h^{-1}}$ or $1.96\,\mathrm{\mu s\,s^{-1}}$. The OptimAE system was unable to be checked with such a large sample set due to amount of data generated, however, as each capture using this system is typically under 5 minutes and the system is network time synchronised, the timestamps are assumed to be accurate.

The jitter in Figure 5.14 is from two sources: the MPD system and the sample rate of the DAS system. As the DAS's sample rate is only 20 kHz in this case, the large jumps seen correspond to the lowest time resolution period of 0.5 ms. The jitter from the timing accuracies, presumably from the less accurate PC-based timing of the Omicron MPD system, is less than 0.1 ms. Overall, the synchronisation over time between the two systems is close, although over longer recordings this effect would become more of an issue. With a continuous recording with no resynchronisations, after 10 minutes the difference between Omicron MPD and the other measurements would be 1.18 ms or a 50 Hz phase angle of 21 degrees. This limits the maximum length of data capture and measurement periods of 2 minutes are used to keep this error below 235 µs and therefore below 4 degrees on a PRPD diagram. As the trend is linear, synchronisation at both the start and end of measurements could be used to fit the Omicron MPD data to the correct timebase removing the effect of time slip. This however was not achieved due to the large amount of post-processing required, and instead data captures were maintained short.

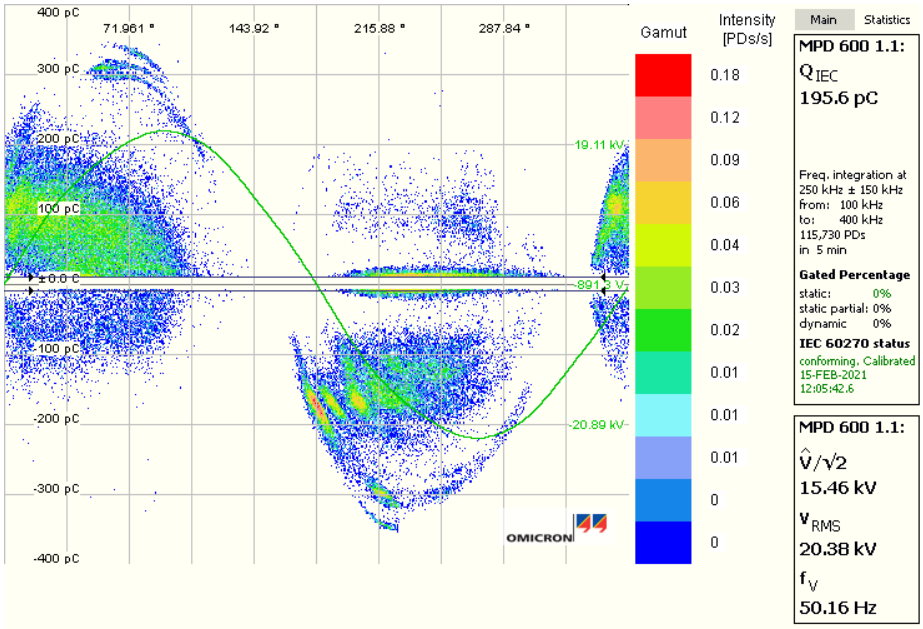

Figure 5.11: Omicron PRPD progression for the 3D printed cells, discharge after 60 minutes. Average applied voltage: 22 kV.

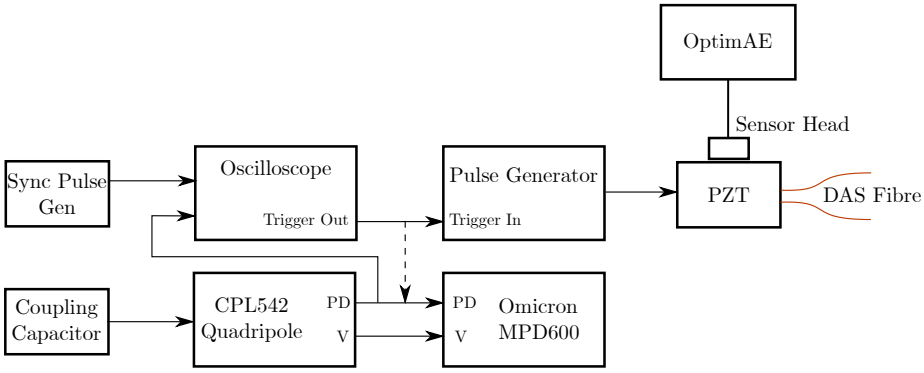

Figure 5.12: Diagram showing the synchronisation connections and signal flow from the FPGA pulse generator to the Omicron, OptimAE, and DAS systems. Dashed lines indicate optional links for use during a synchronisation event.

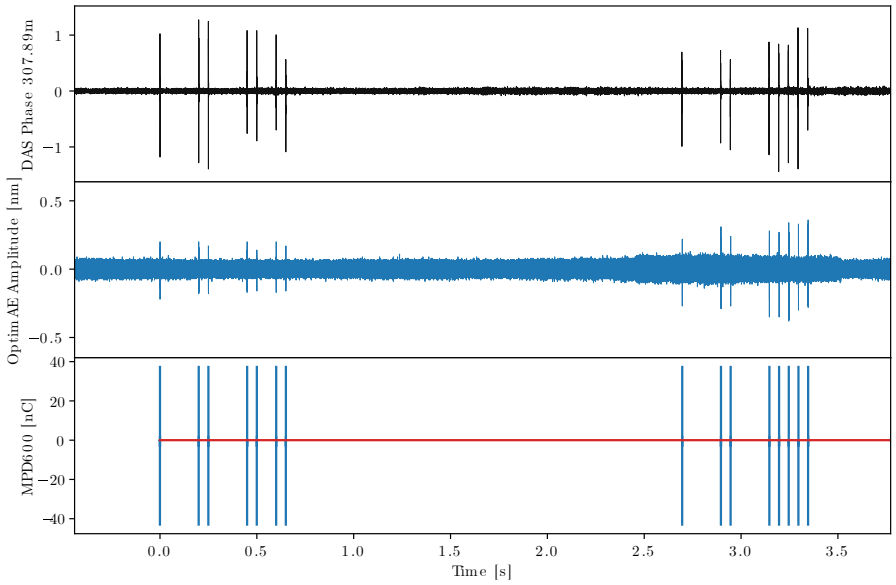

Figure 5.13: Output of two synchronisation pulse trains (sequence number 3 and 7) in the DAS data (Top), OptimAE system (Middle), and Omicron MPD system (Bottom).

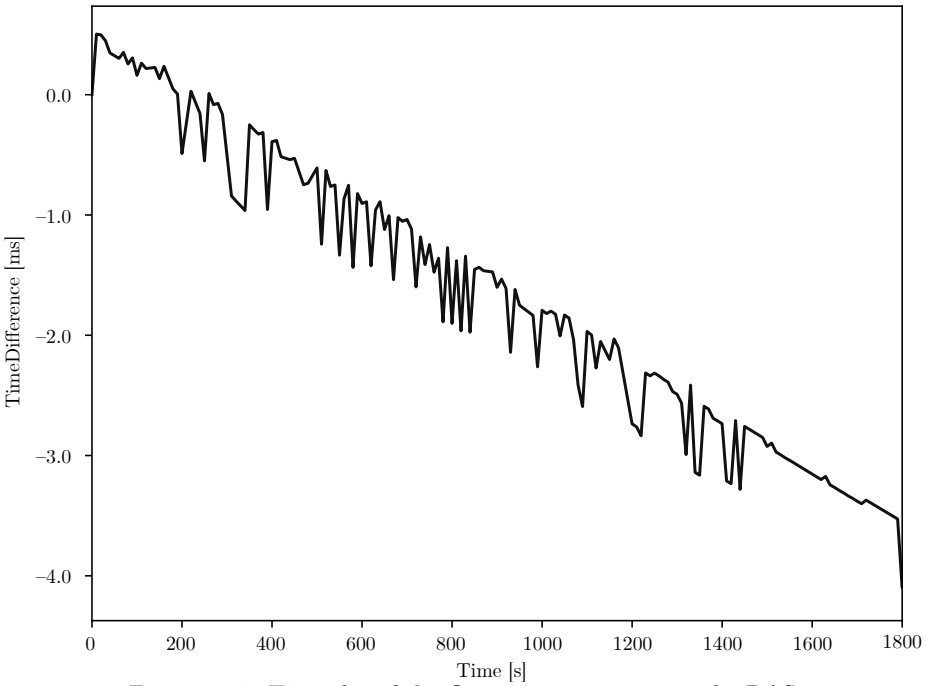

Figure 5.14: Time slip of the Omicron system versus the DAS system. The DAS system in this case is used as the reference source. A slight negative trend is visible with additional least-significant-bit jitter.

5.4 Results

The following results start with the high-sample rate acoustic sensors demonstrating the typical AE seen at high frequencies as well as including the time-synchronised electrical measurement ensuring that the systems are tightly aligned. Then DAS is introduced detailing the initial problems in detection from the poor coupling of the 3D printed cell, and then moving on to the epoxy cell with much better results.

5.4.1 Acoustic Sensors

Starting with the acoustic results from the OptimAE sensors in Figure 5.15 and Figure 5.16, respectively for a 3D printed void and an epoxy cast void, the data shows large spikes on the 50 kHz sensor. Similar signals are also present on the 200 kHz sensor for the epoxy void, but at a reduced amplitude. The lack of signal detected in the 3D printed void is attributed to a bad acoustic coupling, and less overall sensitivity than the 50 kHz sensor. The same colour scheme is applied to all graphs containing acoustic, electrical and DAS measurements: dark blue and purple for acoustic measurements made by the OptimAE system, red and a lighter magenta for DAS traces at different positions, and a stem plot for the discharge events seen by the electrical Omicron measurement shown as a blue x and a yellow stem drawn to the y origin for clarity and better identification of the time of the event. The impulse-like signals match up within 1 ms with discharge events detected by the electrical Omicron measurement are shown at the bottom of the figures. The events detected are confirmed to be partial discharge originating from the cells, and only occur with voltage present past an inception point and do not occur without the cell being present. The discrepancy between the two different acoustic sensors is from two sources: firstly, the frequency spectra of the void discharges in this particular setup appear to better suit the larger sensor cavity of the 50 kHz sensor; and secondly, the difference of the positioning, even by a few centimetres, of the two sensors could with resonance effects cause the measured amplitude to be reduced. However, both sources show similar multiple millisecond tail offs from reverb as observed in the detail of a single discharge in Figure 5.17.

Despite being within 1 ms of each other, a variable delay is noticed between the electrical Omicron measurement and the start of the impulse measured by the acoustic sensors. As discharge is initiated in the gas internal to the void, acoustic energy then must pass through the interface of the air void and the epoxy (or resin in the case of the 3D printed) cell, then through the cell-oil interface and finally to the tank edges where it can be picked up by the sensors. Therefore, the amplitude is reduced over distance, as well as creating a delay dependent on the acoustic path, and the multiple reflections causing interference, additionally producing the modulation seen on the envelope of the AE signal in Figure 5.17. This observed signal is again very similar to the modelling completed in Section 4.2.3. This phenomena is also likely why even though many of the discharges seen by the Omicron are the same amplitude, their received acoustic emissions vary. Section 6.3.2 looks at correlating the integrated acoustic emission with the size of PD amplitude which produces a

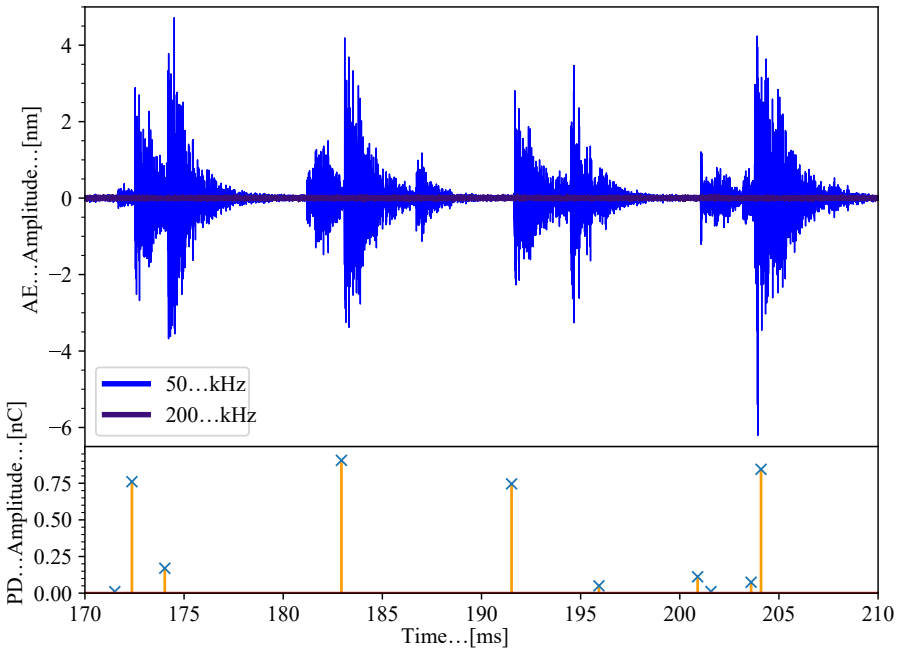

Figure 5.15: Output of the OptimAE sensors (of resonant frequency 50 kHz and 200 kHz) attached to the tank wall during void discharge of the 3d printed cell. Time-synchronised electrical measurement shown in the bottom panel measured from the Omicron MPD system. 200 kHz OptimAE sensor shows only noise for the duration of the experiment.

better likeness compared to simple peak value comparison. However, the peak information is more relevant when comparing with the DAS method, as it does not have the luxury of capturing the full acoustic pulse and therefore cannot be accurately integrated. The measured expectancy of a discharge detection event across this window of time is approximately 58%.

The frequency content of this discharge shown in Figure 5.18. It can be seen that AE produced by void discharge produces a pronounced peak in the 20 kHz to 70 kHz range but drops down to the background level quickly after 150 kHz. This frequency content is derived by cutting each discharge event back-to-back in time and then taking an DFT of the data, zero padded using the Python library SciPy. Only the amplitude is considered to show the harmonic content of the signal. The higher frequency 200 kHz sensor appears to only pick up certain peaks, possibly due to bad acoustic coupling or positioning. These peaks do not occur at regular intervals: and therefore, are not harmonics of a fundamental signal. Instead, they are as already inferred, resonances of various surfaces and cavities. These frequencies are well above the measurement range of DAS, however the aliasing processes should allow detection. As the sensors used were prototypes containing new resonant cavities, their frequency response was not reliably measured and can not be used to normalise the measured frequency domain energies. Therefore, overlap of signals between the two sensors in the frequency domain is more reliable than peaks in just one of the sensors as the frequency pick up patterns of the two heads will be different.

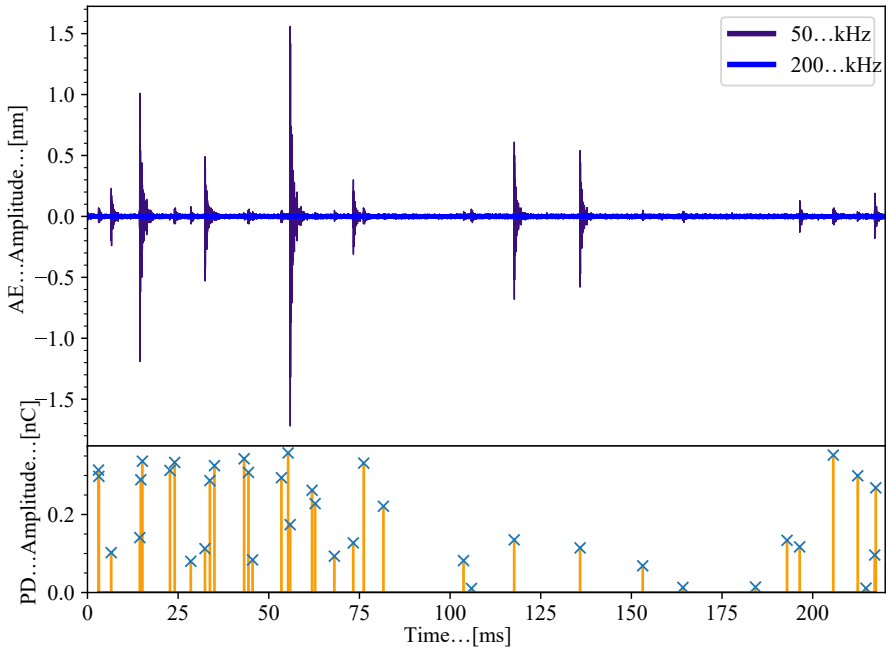

Figure 5.16: Output of the OptimAE sensors (of resonant frequency 50 kHz and 200 kHz) attached to the tank wall during void discharge of the epoxy cell. Time-synchronised electrical measurement shown in the bottom panel measured from the Omicron MPD system.

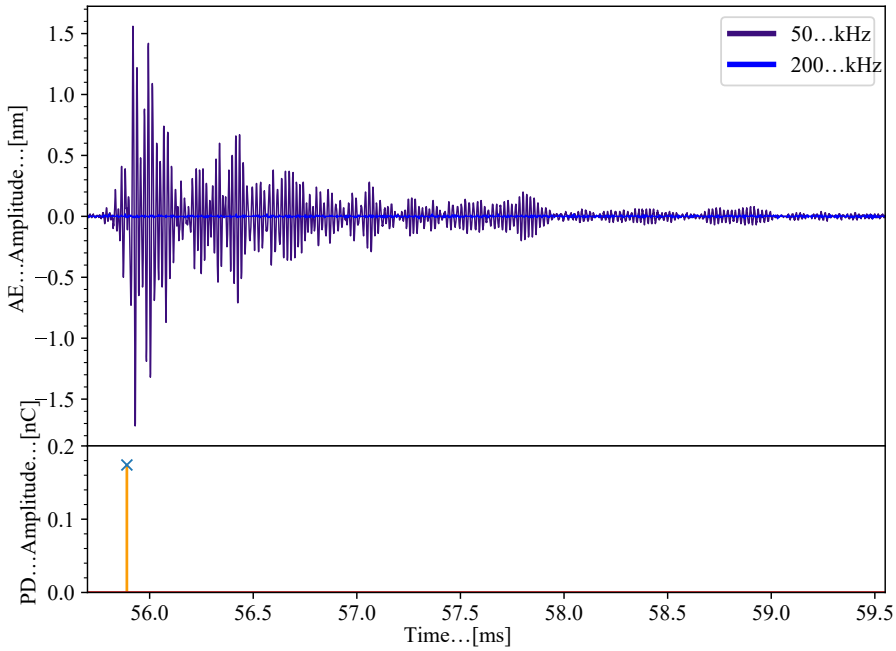

Figure 5.17: Zoomed section of Figure 5.16 during a 180 pC partial discharge event. Time-synchronised electrical measurement shown in the bottom panel measured from the Omicron MPD system.

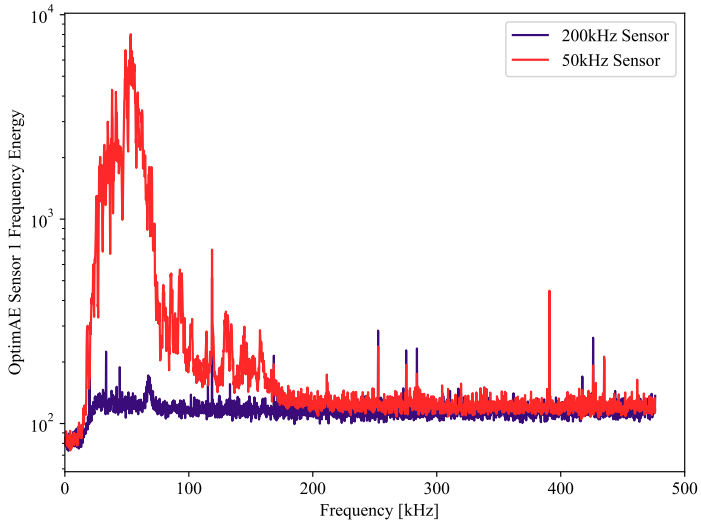

Figure 5.18: Frequency content of the acoustic OptimAE sensors during void discharge.

5.4.2 DAS

The noise floor of the DAS, as it is extremely sensitive, can suffer from periods of high noise. Unfortunately, the noise floor of the DAS unit in the laboratory is not constant. Noise from vibrational sources is somewhat obvious, such as footsteps or machinery nearby; but coupled 50 Hz can be an issue from transformers as well as loose fibres. Loose fibres are a fibre optic in the path of the DAS system, where any minute air currents can push the fibre around: which, for an acoustic system would not be an issue, but as the DAS measures strain, the fibre optic flexing can produce quite large signals that come and go as air currents change without obvious causes. These sources stimulate various resonance modes in the fibre adding to the slow modulations of the noise observed in Figure 5.19. The figure for the noise level is taken from a quiet period before each experiment with no applied voltage on the void cell, in this example 0.12 rad. The peak optical phase seen in the raw DAS data within this period compared to an outlying point corresponding to a PD event gives the SNR. If a PD event can not be distinguished if its signal to noise ratio is 1, i.e. it's peak value was the same as the peak level of noise observed. Although the background levels seen in Figure 5.19 are usually consistent and mostly flat, there are a few spikes outside of this usual profile making distinguishing PD events within this noise floor impossible.

The noise floor was reduced experimentally by isolating different components on vibrational damping pieces of foam and rubber. It was found that air currents on loose-hanging pieces of fibre, usually between the connectors and reference coils up to the on-test sections of fibre, were the largest cause of noise. Additionally, despite DAS's method of separating distance channels in measurement and the quiet reference coils placed in-line, large vibrations like those caused by footsteps, could easily influence early sections of fibre running out of the DAS, and would additionally add the same noise to proceeding channels. Therefore, it was imperative to keep early portions of fibre that required crossing

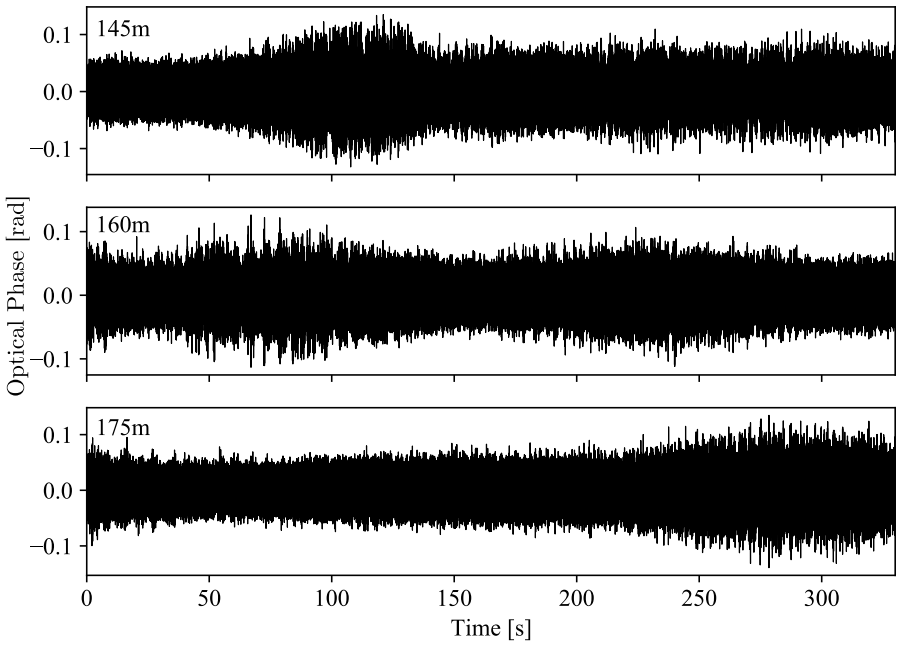

Figure 5.19: DAS noise amplitude showing the various sources of noise coming and going due to suspended fibres in air. Data from 3 locations on the same fibre (top) placed on the ground, (middle) and (bottom) suspended in air.

the laboratory as vibrationally isolated as possible. This was achieved through minimising direct contact with the floor and storing any excess fibre with the quiet reference coils. The DAS unit contains the most vibrationally sensitive parts in the form of a miniature optics bench providing the necessary functions to construct a DAS system. The unit already contains damping systems for reducing coupled noise, but by introducing extra absorbent foam between the server underneath, and the optical DAS unit, noise was further reduced.

Starting with the initial 3D printed cell, whilst the OptimAE acoustic sensor showed spikes for all of the PD events, the DAS trace at the location of the fibre clamped within the cell contains almost no signs of events above the noise floor. Two spikes are seen that do line up with events from the electrical and acoustic measurement at 183 ms and 961 ms. Similar single events are seen sporadically for the rest of the measurement. This gives a successful detection rate of approximately 2.3%, putting the result well below expected values from the previous modelling. However, as explained below, this is not due to the DAS technique itself and still presents a positive identification of PD occurring. Due to the nature of the spikes in the DAS data being single outlying points, and the proximity to the similar noise floor, this figure cannot be automatically determined with a good degree of accuracy, and must be filtered by hand after a peak detection step. Figure 5.21 shows the event at 183 ms, the electrical event is detected, and within 200 µs the spike is seen in the DAS trace and the acoustic sensor. Compared to the void discharge seen in the DAS system, there is little ringing seen, possible below the noise floor, and only a single outlying

point plus returning negative point to maintain 0 mean (no permanent stress change).

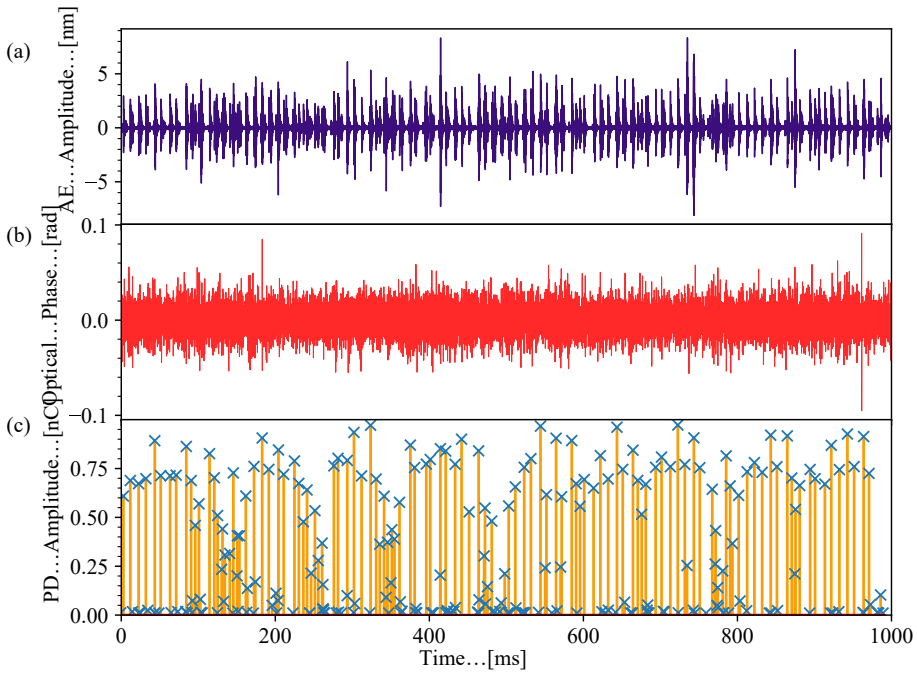

Figure 5.20: Synchronised OptimAE acoustic (a), DAS (b), and Omicron (c) electrical results of a 3D printed void cell under a steady 29.27 kV over a 1 second period.

The lack of events seen in the DAS trace above the noise floor presents several problems with the 3D printed cell methodology. Firstly, the fibre mounting mechanism, whether clamping as originally intended, or via glues did not provide a satisfactory acoustic coupling, resulting in attenuated or absent events in the DAS systems.

Beginning with the embedded fibre in the epoxy cast cell in Figure 5.22, the DAS system picks up more discharges than the OptimAE system. The fibre external to the cell, shown in magenta overlaid on top of the red trace corresponding to the embedded fibre, does not show any evidence of picking up events. This means, as previously seen for void discharge such as this to be detected with a DAS system, the fibre must be in primary contact with, or at least connected with similar acoustic property materials, to the solid insulation region. Although ideal for DAS, the fibre would likely not want to be extruded into the insulation of the cable as the permittivity of the glass fibre will be different to the surrounding insulation possible raising concerns of generating PD itself. Therefore, the fibre could be placed within the outer grounding and strengthening layers of the cable whilst still being bonded to the main mass for acoustical coupling. Additionally, the OptimAE system sees less of, and much smaller amplitude, events due to many differing surface boundaries attenuating the AE as compared to the previous void source. This positioning provides a much better detection rate at around 72% across 5 minutes. The OptimAE

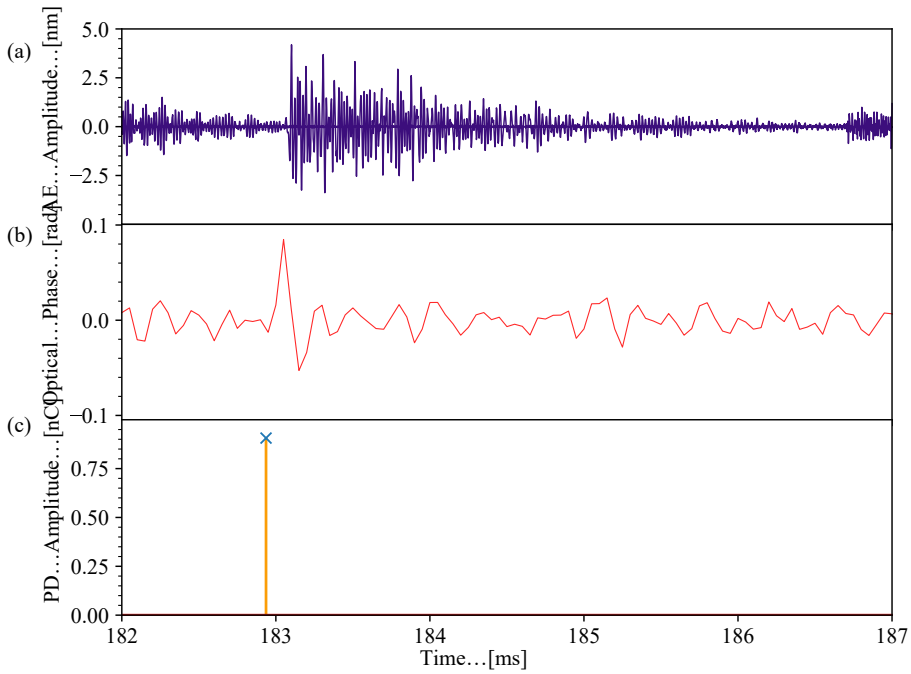

Figure 5.21: Zoomed single event from Figure 5.20. Synchronised OptimAE acoustic (a), DAS (b), and Omicron (c) electrical results of a 3D printed void cell under a steady 29.27 kV.

system only sees less than 50% with many signals being very close to the noise floor.

Malformed epoxy cells where the injection to make a central void was not successful, and instead air gaps were made on the edges of the cell, produced discharges that coupled AE better into the oil than the embedded fibres. In a failed epoxy cell where the epoxy had cured before injecting the air bubble, similar to Figure 5.5c, a crevice was instead created on the bottom surface, exposed to the oil. Voltage was again applied and void PD occurred in this gap. In Figure 5.23, impulses are seen in the fibre positioned at the tank edge in oil (shown in light magenta) rather than the embedded fibre (shown in red). Likewise, larger impulses can be seen in the OptimAE data than in previous data such as Figure 5.22 where the PD was in the central void. This shows that the AE has a better coupling into the oil rather than the solid epoxy due to its positioning. Furthermore, as the dielectric surrounding the discharges is a fluid, has some compressibility and can also be pushed out the way, it is likely that the peak AE is significantly reduced from a fully encased void in a solid as the pressure wave cannot build so high. This results in a detection rate of less than 1.5% for the tank wall fibre, and below 0.8% for the embedded fibre. Altogether, this shows that the coupling of AE is one of the main limiting factors in detecting PD, especially as real-world implementations would likely contain many more barriers and a greater physical separation between PD and fibre.

In Figure 5.24, multiple discharges in the same half-cycle can be differentiated in the observed DAS signal, although events closer than 1 ms cannot be told apart. This presents the problem where events are shaded by other larger

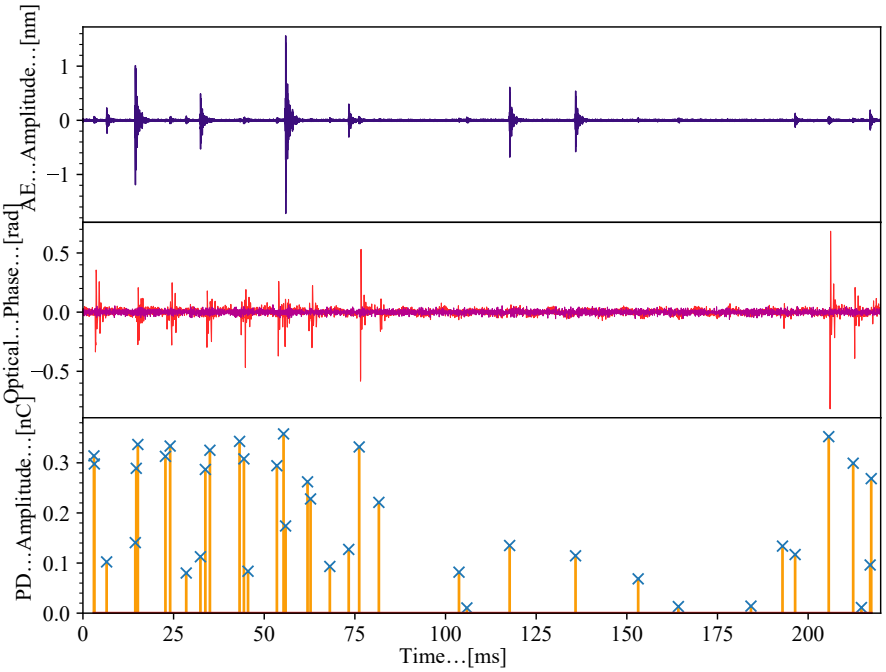

Figure 5.22: Synchronised OptimAE acoustic, DAS, and Omicron electrical results during discharge from the epoxy void cell. DAS output in red corresponding to the embedded fibre coil in the cell, purple corresponds to the fibre coil at the tank edge.

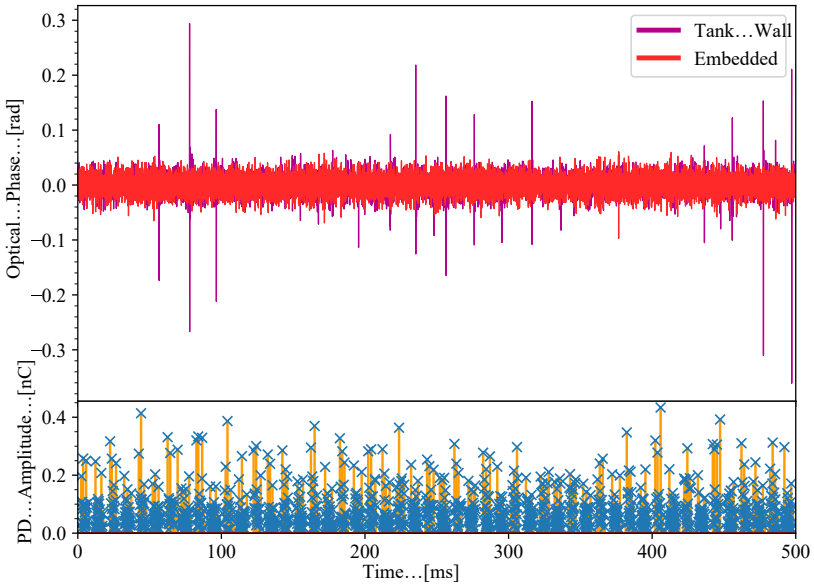

Figure 5.23: DAS data (top) and electrical Omicron measurement (bottom) during discharge in a failed epoxy cell where the void was not surrounded by epoxy, but rested underneath the cell, in contact with oil.

events happening within a small time window in which ringing is still occurring which along with the statistical chance of seeing an event not being 100% means that analysis methods relying on timing between pulses such as PSA are not usable for this sort of measurement. For the 3 similarly sized discharges seen in the Omicron, the OptimAE system only has a response to the last despite 2 clear events are observed in the DAS. This is because the DAS sensor position shown in red is within the cell itself, and little AE makes it outside the cell for that discharge.

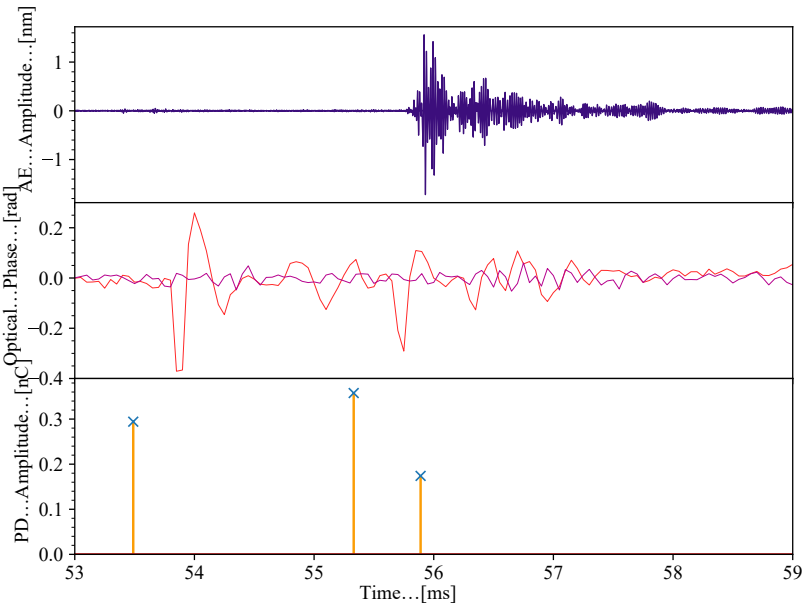

Figure 5.24: Zoomed detail from Figure 5.22. (a) Amplitude of AE (b) Optical phase of the DAS, red corresponding to the embedded cell fibre, and magenta corresponding to the coil at the tank wall. (c) Amplitude of PD events

Changing the void cell for a smaller void of 0.5 mm in Figure 5.25, a record detection of 0.170 rad for an PD amplitude of 18.55 pC achieved at 781.40 ms. Generally during this test, the discharge is maintained below 80 pC with almost all discharges showing in the OptimAE 50 kHz sensor. Hence due to the low discharge amplitudes, an average detection rate for the session is only achieved at 8% in the DAS. This figure was calculated through comparison of detected peaks in the DAS, OptimAE, and electrical data with a tolerance window of 1 ms (below the synchronisation error during the experiment). Additional small value signals are seen at 201.10 ms: 0.187 rad at 23.6 pC. As these peaks are close to the noise floor in this experiment, the 50 Hz from the transformer and other equipment in the laboratory can also be seen superimposed on the DAS trace.

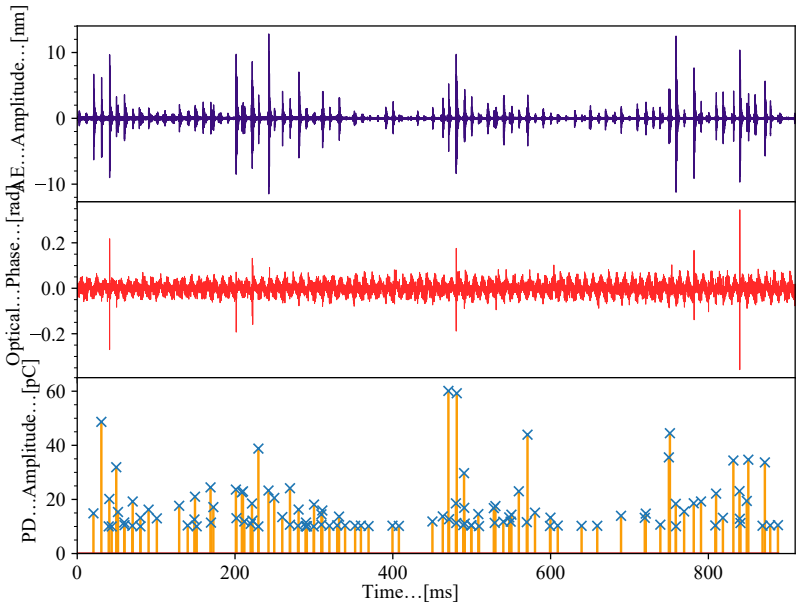

Figure 5.25: Lowest measured amplitudes in the DAS system. Discharge from a 1 mm epoxy-void cell. (a) Amplitude of AE in purple (b) Phase output of the DAS system in red, embedded cell fibre (c) amplitude of PD events in amber

5.5 Conclusion

DAS has been shown to be able to detect void partial discharges, down to a PD events with a minimum electrical amplitude of 18.55 pC. This is, however, with a wrapped length in very close proximity to the discharges. Outside the laboratory, the fibre would likely be located physically further away, and not be directly embedded in the insulation, therefore any AE would be attenuated. Discharges of greater than 100 pC are much more reliably seen and would be more likely to be detectable in such environments. Significant noise is an issue, making small AEs appear below the noise floor. However, the laboratory is a relatively bad environment for acoustic noise, espically low frequencies coupled from machinery, and therefore DAS fibres installed in HV plant would be expected to have decreased noise and thus detect even lower levels of PD. The detection method in its current form still requires some amount of repeated fibre sections (e.g. coiling) to increase the chance of detection enough to reliably sense discharges, but detection rates do not linearly increase with coiled length. With improvements made to decreasing the gauge length and sensitivity improvements such as through FBGs, this limitation could be reduced. This relationship of sensitivity versus coiled length will be revisited in Section 6.3.

The system can only detect the presence of PD in its current form: it is not an in-depth measurement system leading to higher level analysis like others, but it has the capability of detection at much longer ranges with the inherent location and ranging. Overall, the DAS method is well suited to applications such as large transformer tanks, where fibre is easily wound in coils across the windings of a transformer. The upper allowable limits for PD in an oil filled transformer

are also within detectable ranges of the DAS system: up above 100 pC, compared to far lower limits (<10 pC) for plant such as extruded cables [168].

Synchronisation between different systems is an issue, especially with data captures over 5 minutes. The time slip due to the Omicron PC-based system is significant enough that if PRPD comparisons were carried out across the systems, then a phase error of more than 10 degrees would be likely. By using short captures and ensuring that at the beginning of each dataset a synchronisation pulse is injected, this error is currently maintained below 5 degrees.

Chapter 6

Partial Discharge Detection of a Discharge at the Oil-Pressboard Interface

Pressboard is a solid cellulose-based composite insulation used in a variety of insulation applications such as HV transformers. This composite is composed of a light porous and fibrous board which is then impregnated with mineral oil, typically under a vacuum and at an elevated temperature. This removes moisture and gasses from the fibrous structure whilst increasing the dielectric strength of the material. Composite insulations such as pressboard suffer from creeping partial discharges, or treeing, where a carbonised path can grow across a large gap spanning conductors, eventually causing failure [67].

This chapter focuses on the application of DAS onto treeing partial discharges at the oil pressboard interface, using similar analysis as used with void discharge. Undersampling is still a significant factor due to the sample rates involved, allowing the higher frequency AE to be detected. Applications of this type of sensing include oil filled transformers. Many new transformers containing pressboard insulation in fact already have integrated fibres wound on the cores for testing at the factory for finding hotspots and temperature profiles utilising DTS and other methods [169, 170]. These unused fibres after installation could easily be re-purposed by a DAS system for PD measurements providing detection of partial discharges whilst on-line and requiring no additional sensors.

6.1 Experimental Design

5mm thick Weidmann "Transformerboard TIV' pressboard was cut into squares of dimensions 100mm x 100mm. 5mm was chosen due to availability and that the pressboard was from the same stock as previous experiments witnessed in literature [171]. The discharge source stemmed from a 70 µm needle facing

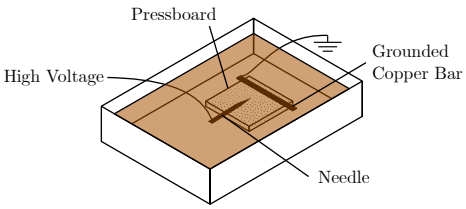

(a) Diagram of the pressboard experiment construction. The pressboard assembly is entirely immersed under oil.

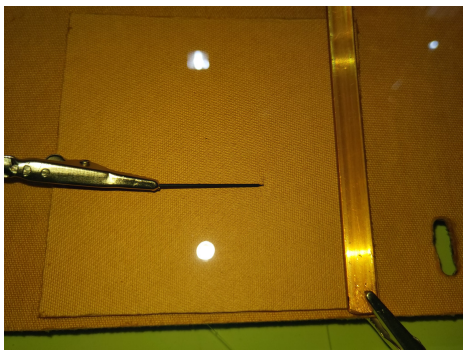

(b) Picture of the pressboard experiment construction showing needle at an acute angle to the pressboard underneath, and perpendicular to the earth bar.

Figure 6.1: Pressboard experimental setup showing needle and ground bar positioning

a grounded copper bar, clamped to the edge of the pressboard as shown in Figure 6.1. This setup is typically known as a point-bar configuration, and is used where an extreme electric field is required; in this case to initiate treeing from the point.

The needle-bar configuration builds charges around the needle tip that are spread or pushed across the pressboard surface, rather than penetrating the underlying bulk material [172]; therefore discharges preferentially occur across the surface initially leading to a tree forming from the tip, and eventually full breakdown. In the event of significant discharges originating from the needle tip, or complete breakdowns, the arcs and streamers cause significant erosion and ablation of the needle tip. Such damage is not seen on the grounded side due to the larger solid copper bar. After enough damage, the needle-tips no longer maintain their sharpness and increases the inception point of PD due to the decreased peak electric field. At this point the needles are either reconditioned to recover the sharp point or replaced with a fresh needle. This PD system allows for a varying discharge source over time, allowing the DAS system to be characterised against different amplitude and typed sources within one experiment.

Moisture levels of the pressboard contribute significantly to the start and progression of PD. Specifically, the pressboard must contain some water in order to initiate PD. A too dry board (0.5 % moisture content by weight, or lower) [173] makes it extremely difficult to initiate PD, however a too wet board risks significantly increasing the time of progression as a greater content of water must be dried out by the discharge to spread. Therefore, the pressboard was conditioned to 6 % moisture content by weight as a compromise on progression time and ease of initiating the treeing process. The samples were placed into an oven at 110 °C for a minimum period of 24 hours, and then tested hourly for a weight change of under 0.5 % between measurements, at which point they were considered dry with no water content. Extra samples were then stored in sealed plastic pouches with their dry weight recorded. When ready to be used in an experiment, these samples were then exposed to ambient conditions of 16 °C to

20 °C, RH 60 % to 85 %, to absorb moisture from the air. Once the weight of the samples achieved the target moisture content by weight, they were immersed under oil in the oil bath.

After the pressboard has sat immersed in the oil bath for a period of days, the moisture content in the pressboard and oil reach an equilibrium state, often different from the initial conditioning. This was discovered after periods of particularly dry conditions within the laboratory (RH <60 %), partial discharge would be particularly hard to initiate; even with new sharp needles and prepared pressboard. This is due to the oil bath releasing water content within the oil, and by migration of water, also within the pressboard, to the surrounding atmosphere when there is a significant humidity differential between the mediums.

6.1.1 Comparison Methods

As in Chapter 5, an Omicron MPD600 coupling capacitor system is used as the primary comparison source and for monitoring the progression of discharge from the pressboard. This again was connected with the developed synchronisation system to allow for sample-by-sample comparisons with the other measurement methods. The Optics11 OptimAE solution is set up almost identically to the void experiment with the 2 different sensor heads attached to the tank wall of the plastic oil tank, and one attached to the PZT on the fibre path for synchronisation.

6.1.2 DAS Setup

DAS sensing fibres were attached in multiple ways to the pressboard: firstly, in direct contact underneath the board. This was so the fibre was not in the way of the progressing discharge, and so that additional tracking paths along the fibre itself were not created. Multiple various lengths of fibre: a single pass of fibre, 1 m, and 5 m coils were glued in place to provide good acoustical contact and as to provide data on comparing different lengths of fibre on sensitivity. Later on 3 m was also added as an in-between. This also provided repeat measurements for ensuring observed data was indeed from the PD source and not noise. Specifically, cyanoacrylate was used due to its brittle nature giving better transmission and coupling of strain than other compatible glues [174]. Secondly, another set of fibre coils were positioned at the wall of the tank, under oil for a more direct comparison with the external acoustic sensors. The fibre connections to and from the various fibres under test are detailed in appendix A.2. Again, a 100 m quiet coil is used before the experimental sections. Following that, the glued pressboard sections are connected end-to-end with 5 m spacer fibres, then the separated by oil coils behind the pressboard, and at the tank wall in the same position as the OptimAE solution. Finally the same PZT synchronisation system as in Chapter 5 is used.

The setup is pictured in Figure 6.3 showing the coupling capacitor system, patch and reference fibres, as well as the pressboard under oil in the tank. The OptimAE system is not shown as at the time that the picture was taken, the OptimAE system was not available.

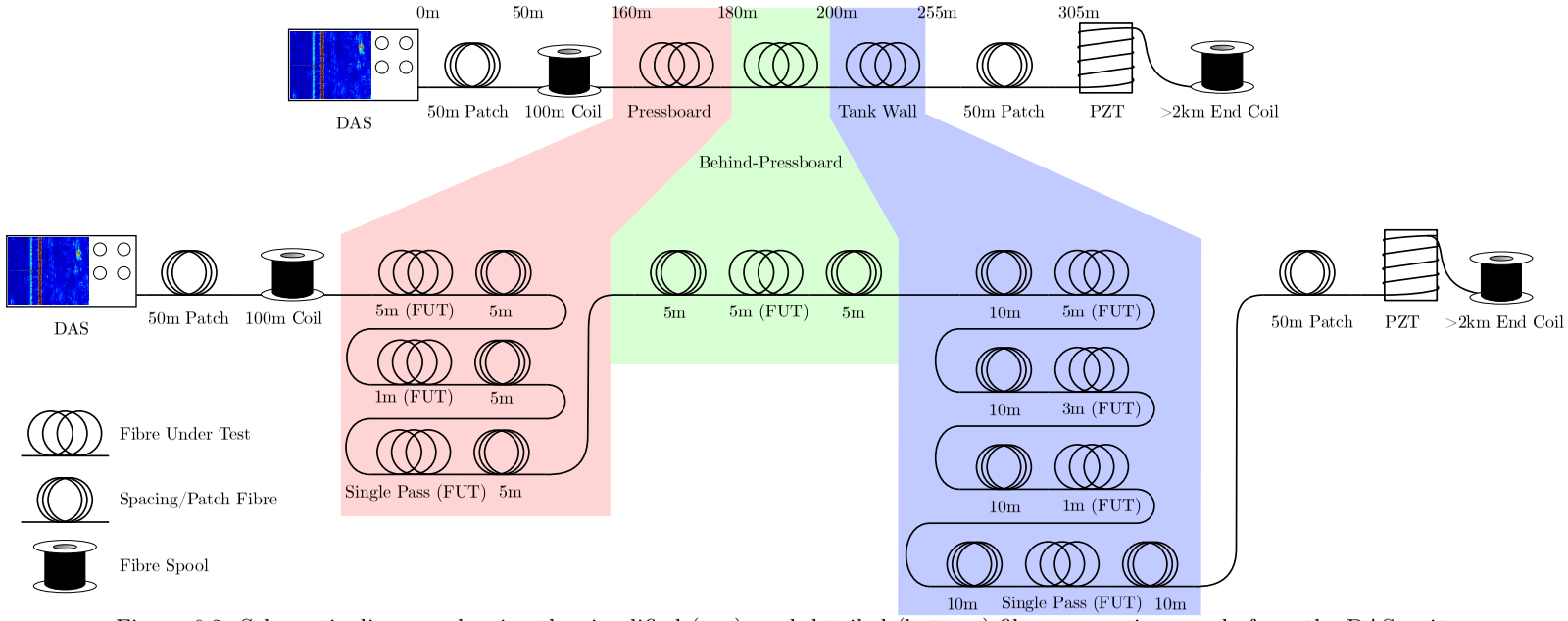

Figure 6.2: Schematic diagram showing the simplified (top), and detailed (bottom) fibre connections made from the DAS unit, through the fibres under test to the PZT. The bottom detailed view shows how different lengths of FUT are separated in distance channels.

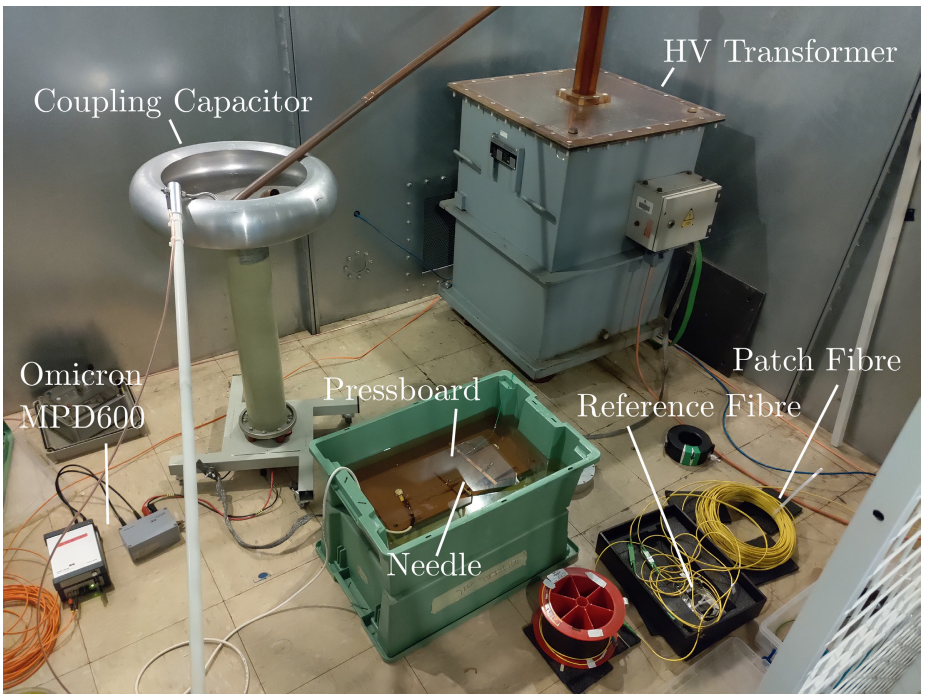

Figure 6.3: Picture of the pressboard experiment showing the coupling capacitor, DAS fibres and the pressboard itself. OptimAE system missing due to availability at the time of picture.

6.2 Characterisation and Progression of Discharge

Characterisation was principally achieved through analysis of the PRPD plots from the Omicron MPD system along with comparison to previous work into investigation of discharge at the oil-pressboard interface [175]. Discharge initially starts with surface discharge with the PRPD plots showing large cones of discharge on both half cycles: Figure 6.5a and Figure 6.5b. The small discharges can be seen by eye racing across the surface from the needle tip. After 15-20 minutes of this intense discharge, visible arcs cease, and the PD instead starts to occur within the pressboard surface and starts to dry out slowly producing white marks across the surface (as in Figure 6.4). This concurrently occurs whilst the discharge PRPD decreases in peak magnitude but builds in number of lower amplitude events in line with [175] - Figure 6.5c and Figure 6.5d. Slowly, the amplitude of this discharge tends to both increase into the nanocoulomb range as the larger discharges occur along non-fully conductive tree branches, but also many more smaller discharges per second where the increased electric field at the tip of the tree is slowly progressing (Figure 6.5e). Eventually, the drying process produces an increased gap between the electric field and ground as well as no more large discharges within the branches themselves, resulting in a sudden drop in discharge levels to single digit pico-coulombs that continue until the treeing and carbonisation process from the needle tip can get close enough to different sections to initiate further large discharges.

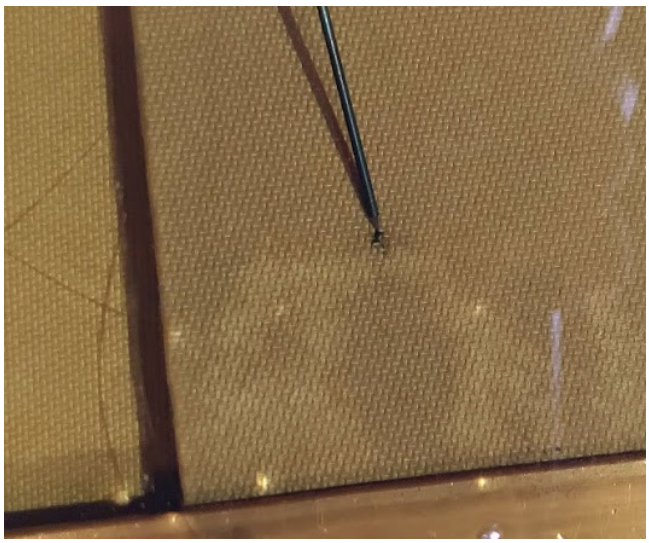

Figure 6.4: Detail of arcing progression at needle tip after approximately 1 hour. Dried tracks within the pressboard can be observed as well as black carbonisation at the needle tip.

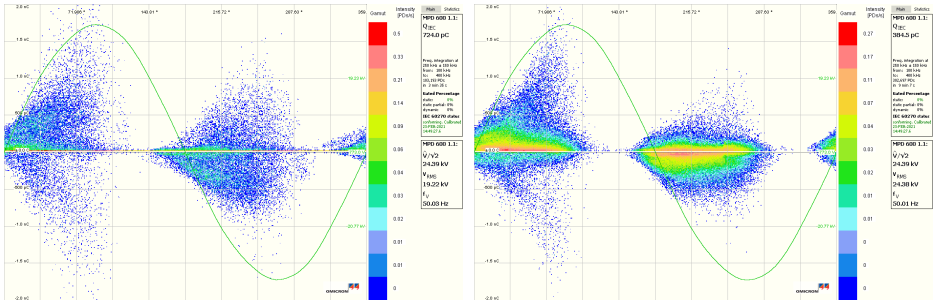

(a) Initial, ±2 nC max scale

(b) After 15 minutes, ±2 nC max scale

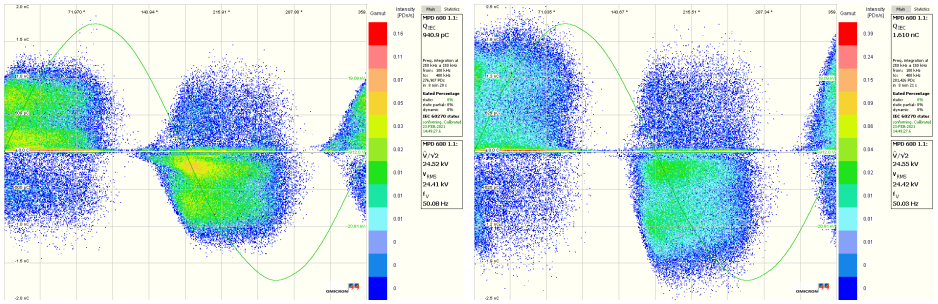

(c) After 30 minutes, ±2 nC max scale

(d) After 60 minutes, ±2.5 nC max scale

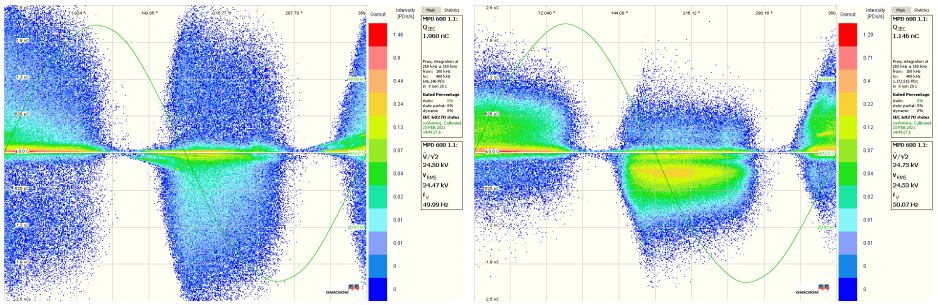

(e) After 90 minutes, ±2.5 nC max scale

(f) After 120 minutes, ±2.5 nC max scale

Figure 6.5: PRPD plots from the Omicron MPD system showing the progression of discharge at various states. (a) and (b) show mainly surface discharge, whereas (c-f) show mostly internal treeing and drying of the pressboard

6.3 Results

The following results start with the output of the high sample rate acoustic sensors from Optics11 showing the correlation of electrical-detected events to observed acoustic emission and then moving on to compare this with the DAS results. These initial results use the 3 m section of fibre at the tank edge for comparison to the OptimAE and conventional methods as this has the best SNR out of the different fibre lengths measured. Events seen as spikes in the DAS data as previously seen and modelled show up synchronised in the other measurements. Comparison of the other fibre lengths and locations in relation to the source PD are completed in the later Section 6.4.

6.3.1 Acoustic Sensors

During the initial phases of surface discharge across the pressboard surface, the OptimAE system captures many events at large signal to noise ratios. Figure 6.6 details the output of both sizes of sensors for just over a 300 ms period, in which all 25+ discharges that are seen in the electrical measurement produce corresponding acoustic spikes within 1 ms. The peak amplitudes of these spikes vary widely between single-digit nanometres of movement of the sensor head, to the largest seen movements of 182 nm. A rough observable correlation can be seen between the amplitude of the electrical discharge, and the peak amplitude of the acoustic emission as detected by the OptimAE system.

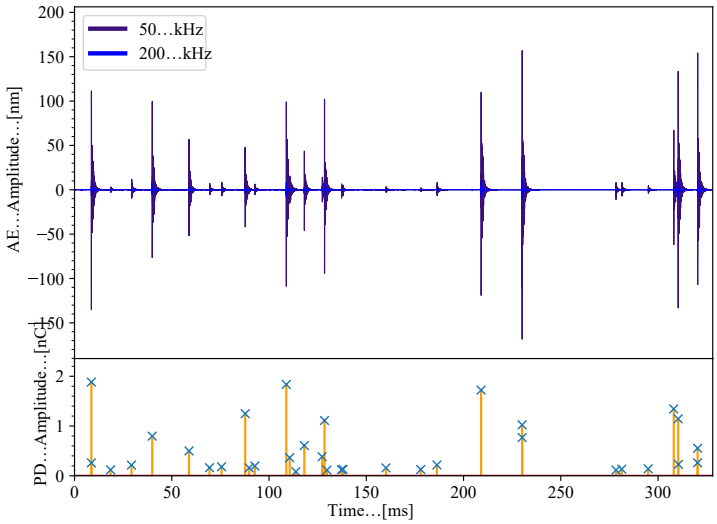

Figure 6.6: Top: Output of the OptimAE sensors (of resonant frequency 50 kHz and 200 kHz) attached to the tank wall during surface discharge across the pressboard. Bottom: Time-synchronised electrical measurement shown in the bottom panel measured from the Omicron MPD system.

Looking at a single PD event in more detail in Figure 6.7 shows the initial, large impulse which rapidly decays to a much lower amplitude ringing, lasting

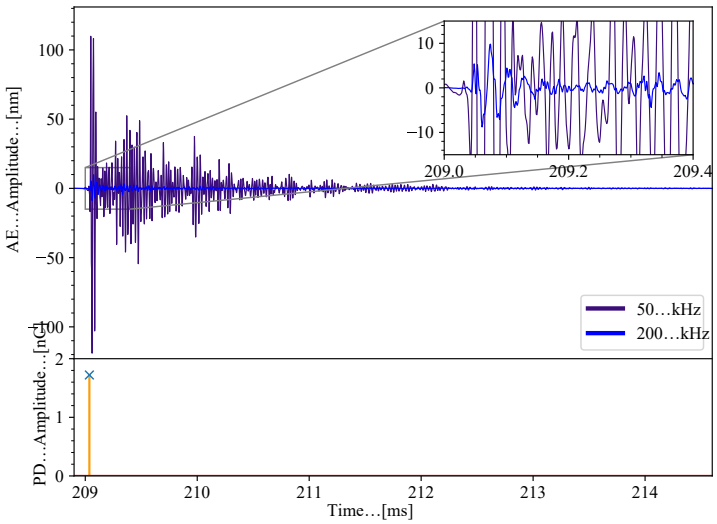

Figure 6.7: Zoomed section of Figure 6.6 during a 1.8 nC partial discharge event during the surface discharge phase of the pressboard progression. Time-synchronised electrical measurement shown in the bottom panel measured from the Omicron MPD system. Zoomed panel for detail of the 200 kHz sensor at the impulse event.

multiple milliseconds. The 200 kHz sensor has a greatly reduced amplitude in comparison to the 50 kHz and fails to see the initial impulse. As the sensors are located within 5 centimetres of each other, this difference in response is attributed to the different frequency characteristics of each sensor. This variation between the sensors is seen throughout this experiment.

In order to correlate and plot the acoustic energy seen by the OptimAE system as compared to the conventional PD amplitude, SciPy's peak detection function in python was used to create a time-series list of events. The precise start and end of the impulse was then found by iterating over the data in the reverse and forward direction respectively for each side until 25 successive samples (a period longer than the observed ringing frequency) were below a noise threshold value of 0.3 nm. This produced the time windows shown in Figure 6.8. The total equivalent acoustic energy seen by the OptimAE system during each event was then calculated by squaring the signal and integrating over the time window producing a value proportional to the energy in an event. This figure is then normalised between 0 and 1 for the whole data for comparison.

By plotting the acoustic energy against conventional PD amplitude in Figure 6.9, a reasonable correlation is observed with some scatter due to the variation in PD source location. This variance in location provides a different acoustic path length to the sensor head, with differing amounts of absorbtion and reflections summing to the total energy measured, resulting in the scatter. Events under 150 pC begin to lose this positive correlation. Although these events maintain detectable low OptimAE amplitudes above the noise, they no longer fit a linear line. This is most likely due to small PD events occurring deeper within the pressboard at the tree branch tips meaning that the produced AE is significantly reduced by the surrounding bulk material compared to discharges closer to the pressboard surface.

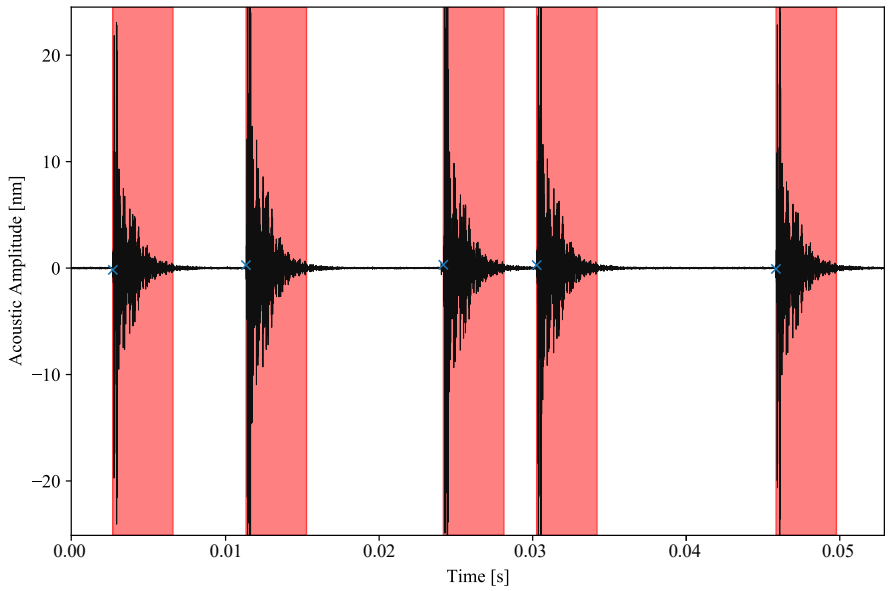

Figure 6.8: High sample rate acoustic sensor output of 5 PD events with a red window showing the detected start and end of each impulse-like signal.

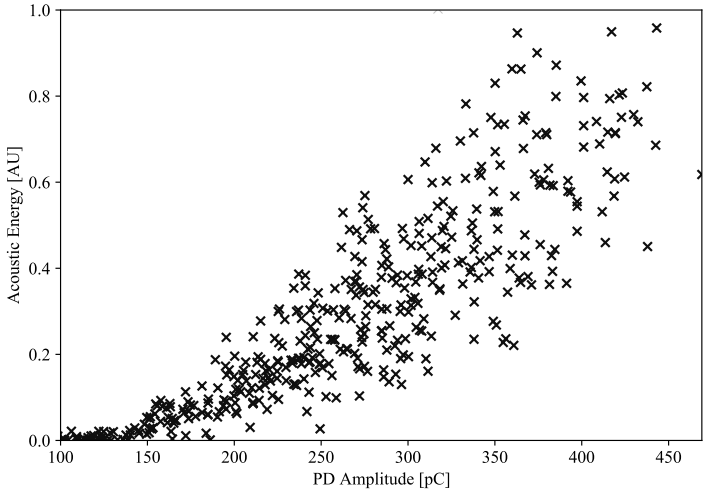

Figure 6.9: Correlation between amplitude of events seen by the electrical MPD measurement, and the acoustic energy measured by OptimAE across 10 s of internal treeing discharge.

Plotting multiple single impulse events on the same axes across different repeats of the experiments with the same sensor locations gives the result seen in Figure 6.10. A common fundamental frequency and modulation of said fundamental[1] is present in all 3 examples. Calculating the frequency of this primary wave based on the repeated wavelength comes out at approximately 36 kHz with an impulse tail length of greater than 1 ms. This waveform looks very similar to the modelled acoustic and DAS system from Section 4.2.3. The results of which are repeated in Figure 6.11 for ease of comparison. The two traces share many similarities: both have an initial large spike that is immediately followed by a damped oscillatory response: and both have a similar fundamental frequency to ringing length ratio, even if the time scales do not match. From this, it can be deduced that the modelling is a good analogue of the complex acoustic processes and given the correct fundamental parameters, the model can closely match experimental results.

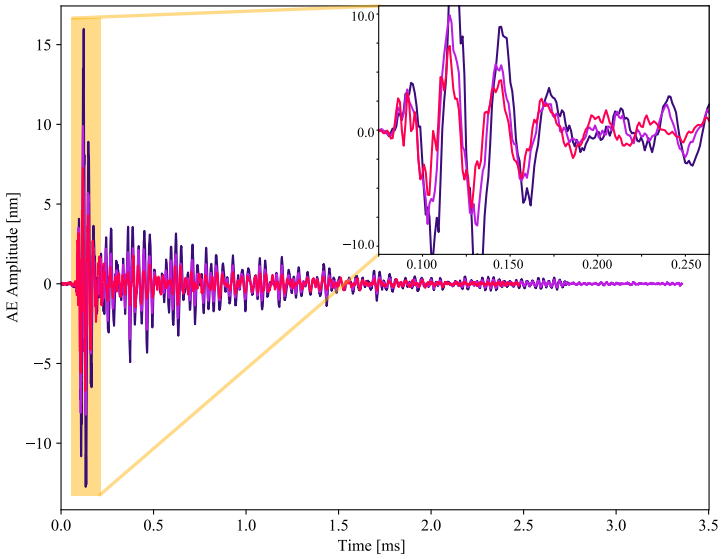

Figure 6.10: Detailed graph of the acoustic impulse as seen by an OptimAE sensor of multiple PDs synchronised by the first large rising edge during pressboard discharges. Similar details of the fundamental frequency and modulation are seen. Samples (differentiated by colour) were taken from the same pressboard sample, but across different experimental repeats.

[1] Highly dependent of course on the surrounding geometry and materials as presented in Section 4.2.3

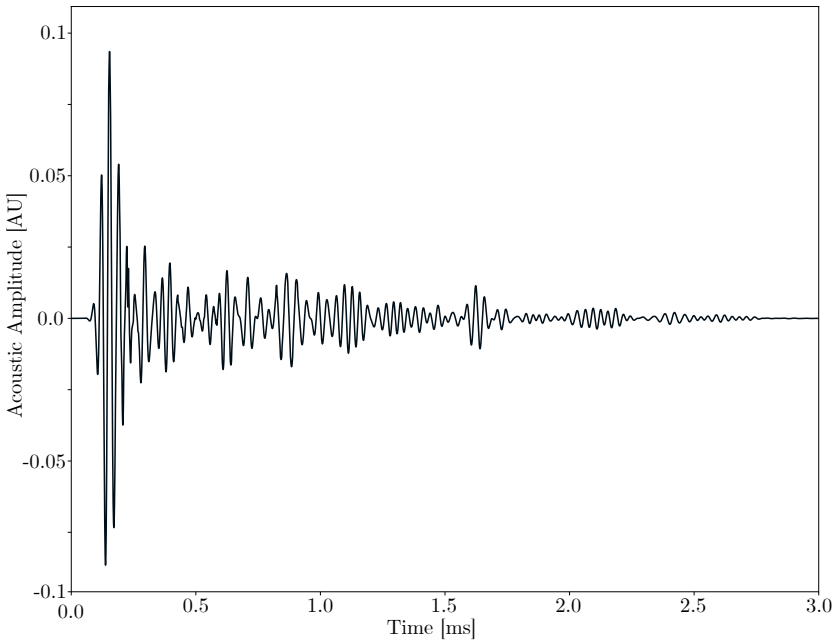

Figure 6.11: Repeat of Figure 4.7: Modelled acoustic emission plot of the strain in arbitrary units of a one-element receiver array at the fibre position beneath the pressboard source.

Frequency Spectra

Figure 6.12 shows the frequency spectrum of recorded OptimAE data from both sensors during a 100 second window. Even despite the two differing resonant frequencies of the sensors, a significant amount of frequency band energy is seen in the 35 kHz to 70 kHz region. Additional spikes are seen above 200 kHz. There is very limited content under 20 kHz where the fundamental acoustic range of the DAS system lies. Of course, the sensing is not limited to this due to the undersampling effect as mentioned. The resonance of the 50 kHz sensor clearly makes a large difference in the amplitude of detected events around that frequency band: an order of magnitude or larger at the 45 kHz peak.

The multiple spikes seen, and harmonics thereof, above 200 kHz are constant throughout the discharge progression. Therefore, these frequencies are likely related to the environment and size of acoustic cavities such as the pressboard itself rather than the source discharge. An attenuation would be expected for the higher frequencies as the sensors are mounted on the outside of the tank wall (whereas the DAS fibre is placed internally).

Reducing Data

As the OptimAE system generates $1\,\mathrm{MS\,s^{-1}}$ of data, and each sample of each channel is stored as a 24-bit number; the system produces $6\,\mathrm{MB\,s^{-1}}$ that need to be stored. Over a typical measurement period of discharge of 60 s to 120 s, the resultant data size, including metadata and overheads, is 490 MB to 980 MB. This size of data is fine in terms of storage, considering today's easily available bulk storage, but plotting data of this size into readable graphs is difficult and

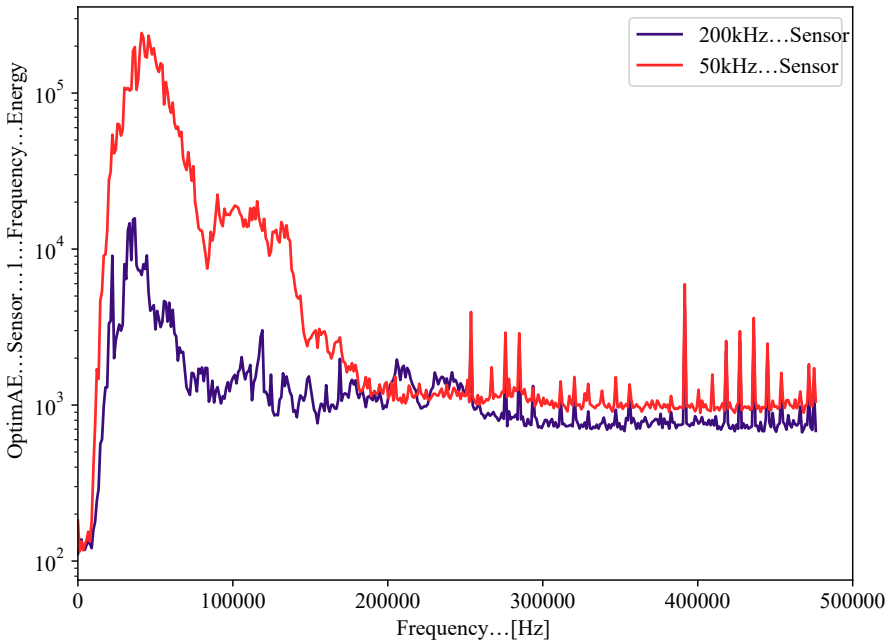

Figure 6.12: Frequency spectra of the OptimAE sensors during treeing discharge with resonant frequency 200 kHz shown in purple, and resonant frequency 50 kHz in red. FFT window taken across 100 seconds.

time consuming due to the graphics processing involved. Therefore, a method of reducing the data set size, whilst keeping the important features was enacted: a form of down-conversion.

The data, D of size n, is chopped into chunks of size S, derived from the down-conversion ratio which is a ratio defined against 1 (i.e. 4:1 compression makes $S = 4$). For every chunk of data $D[i : i + S]$[2], the chunk is reduced to a single sample defined as the maximum of the data in that period using the function[3]:

$$D = \text{И}_{i=0}^{\frac{n}{S}}\big(D[i]_{\text{Reduced}}\big) = \text{И}_{i=0}^{\frac{n}{S}}\big(\max(D[iS : (i+1)S])\big) \tag{6.1}$$

This down-sampling is applied when viewing data on graphs where single samples are invisible to the eye and the raw data size would be immense. Typical down-sampling ratios are 100:1 or 1000:1 depending on the time scale of the graph. On figures with more detailed information, the original data is instead used as the graph limits are much closer together and allow for viewing of the detailed data. A similar type of dynamic conversion is often implemented in computer images, known as mipmaps, giving the same bonuses of increasing rendering speed, and reducing aliasing artefacts [177].

[2]Where $D[x : y]$ is the Python slicing syntax meaning the values of D between the indexes of x and y.

[3]$\text{И}_{i=0}^{\frac{n}{S}}$ is used here as an iterator symbol, proposed by [176] from 0 to $\frac{n}{S}$

6.3.2 DAS

Starting with data from Figure 6.13 in the 3 m coil next to the OptimAE sensors in Figure 6.13, with direct line-of-sight to the top of the pressboard, spikes show up that correlate to both the OptimAE and electrical measurement. The discharges in this data are a mix of larger discharges in amplitude corresponding to surface discharges and across partially non-conductive already existing tree structures as well as much smaller discharges (below 50 pC) at the tips of the trees slowly drying and forming new branches. The shape of each of the acoustic events can be seen in better detail in Figure 6.14; with a profile like those seen by the OptimAE: a larger impulse at the front, and then ringing. However, distortion from the much lower sample rate is clearly visible. The ringing that is observed, is at the Nyquist frequency of the data and is not indicative of that frequency being present in the originating acoustic signal. As previously discussed in Section 4.1, this distortion and warping is from the mismatch between sampling and original frequencies, coupled with the very small sampling window of the DAS. DAS achieves 63% detection rates with this setup and is repeatable even with varying the position of detection. Comparisons of different fibre sensing lengths will be detailed later in Section 6.4.

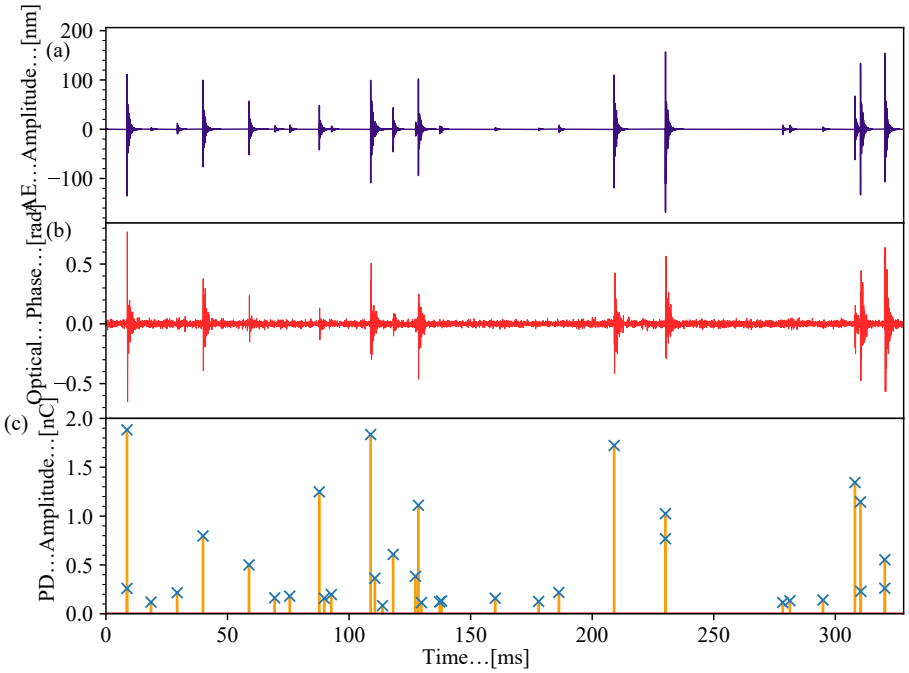

Figure 6.13: Data taken during surface and treeing discharge of the pressboard experiment. (a) Amplitude of AE in purple, as measured by the Optics11 OptimAE sensor. Measured in displacement of sensor element. (b) Phase output of the DAS system in red, corresponding to the 3 m coil of fibre suspended in oil next to the OptimAE sensor. (c) Absolute amplitude of PD events in amber, as measured by the Omicron MPD600 system. As the events recorded by the Omicron system are not continuous, the crosses indicate partial discharge events with the vertical lines added for better clarity.

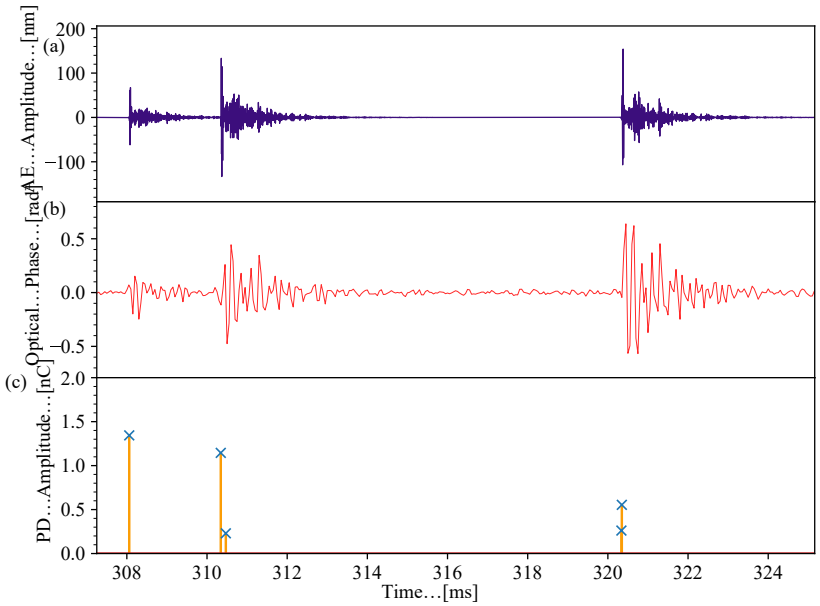

Figure 6.14: Zoomed in detail of a PD event from Figure 6.13. (a) Amplitude of AE in purple, as measured by the Optics11 OptimAE sensor. Measured in displacement of sensor element. (b) Phase output of the DAS system in red, corresponding to the 5 m coil of fibre suspended in oil next to the OptimAE sensor. (c) Absolute amplitude of PD events in amber, as measured by the Omicron MPD600 system.

At first glance, the peak amplitude of these spikes appears to have a correlation with the high sample rate acoustic and conventional PD amplitude. This is also more apparent looking at a longer-format figures in Section B where greater time-spans are shown: Figure B.1 and Figure B.2. Plotting the correlation between OptimAE and the DAS measurement, Figure 6.15 shows that a rough correlation is developed. The method for estimating the energy seen in each event used for the OptimAE system cannot be reused for the DAS data due to the lost information from undersampling. So instead, peak amplitude for each event was used as obtained by a peak-detect algorithm shown first in Section 5.4.2. The grouping is not as good as between the electrical measurement and OptimAE, but still demonstrates an increase peak DAS amplitude for a given acoustic energy from the AE which makes sense given both methods are measuring the acoustic signal. The increased scatter as compared to the original AE/Omicron correlation is due to the undersampling process removing important acoustic information. Given a DAS system with a better sampling frequency, this correlation would be expected to tighten more towards a straight line, providing better single-event information. As it stands, the DAS is able to provide a definitive detection ability as well as an estimation of PD size given a time period long enough to capture significant number of individual events.

As alluded to, the spread of events seen, even at higher electrical discharge, sometimes falls below the noise floor. The reasons why this occurs has already been covered in Section 4.1 and is due to the sampling of non-periodic impulses (the acoustic emission from the PD). Additionally, the noise floor in the lab fluctuates from the various machinery turning on and off, as well as footsteps

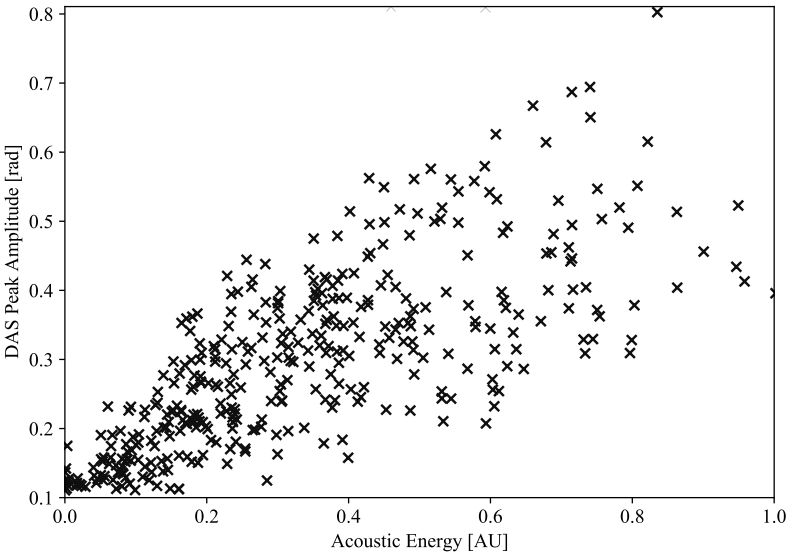

Figure 6.15: Correlation between amplitude of events seen by the high sample rate acoustic sensor, and the DAS system across the same 10 s period as in Figure 6.9.

and external vibrations from traffic outside. This noise of below 0.05 rad is the main source of error within these measurements, other than issues caused by undersampling. Figure 6.16 is a good example of events dropping below the noise floor. In the first event the starting impulse is still visible, but the ringing previously demonstrated is hidden in the noise. The later events are almost totally below the noise floor, with only tiny changes to the trace that can be observed given the time information from the other measurements. Without the comparison, these events would likely be dismissed as noise.

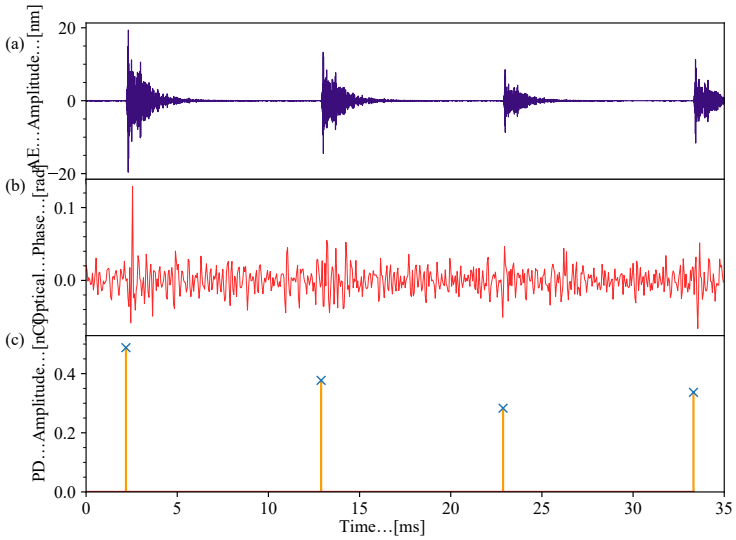

Figure 6.16: Detail of PD events at a lower electrical (280 pC to 480 pC) and acoustic amplitude. Deviation in the DAS data at the time of each event can be observed, however is very close or below the average noise floor.

6.4 DAS Position Comparison

Previously, the main data presented was at the position corresponding to the 3 m fibre section by the tank wall. The reason behind choosing this position for analysis was that that position gave the best SNR out of all surrounding positions, as well as providing better like-for-like comparison with the OptimAE high sample rate acoustic sensors due to proximity. Figure 6.17 shows several PD events consisting of the different lengths bonded the pressboard and the different lengths at the tank wall separated in oil. First, the fibres with mechanical contact underneath the pressboard: the signal is significantly lower than fibre simply suspended in oil at a greater distance from the pressboard, but with line-of-sight to the top surface. This reinforces how absorbent the pressboard material is for acoustic signals; the AE from the PD events are attenuated as they travel through the material, resulting in a lower amplitude. Secondly, by examining the data in all positions, the largest peak amplitudes are seen in the coils of 3 m and 5 m. The 1 m sections, and especially the single passes of fibre, have increasing reductions of amplitude resulting in the events falling beneath the noise floor. This is believed to be caused by the increasing lengths having an increasing proportion of the spatial samples in each gauge length of the DAS system. Thereby AE introducing strain in across a region producing a larger amplitude. If the gauge length was able to be decreased without significantly increasing noise, given this hypothesis, the shorter lengths of test fibre should have amplitude similar to that of the current, longer pieces. This finding is consistent throughout all of the tests undertaken with the DAS system, and shows that a single pass of fibre, at this time, is not usable as a detection method except under breakdown events.

The 3 m sections as shown in Figure 6.17 have greater amplitude than the 5 m sections. Even comparing the cumulative sum of the square of the amplitude

giving the total of energy measured, shows that the 3 m sections outperform both the longer and shorter test fibres. Given that the gauge length effectively averages out the spatial samples, a maximum length of fibre being in contact with the acoustic signal should therefore generate the largest signal. Two potential explanations are either the coil of fibre is cancelling itself out, or the larger coil in the longer sections imposes a greater acoustic-impedance inconsistency causing an attenuation.

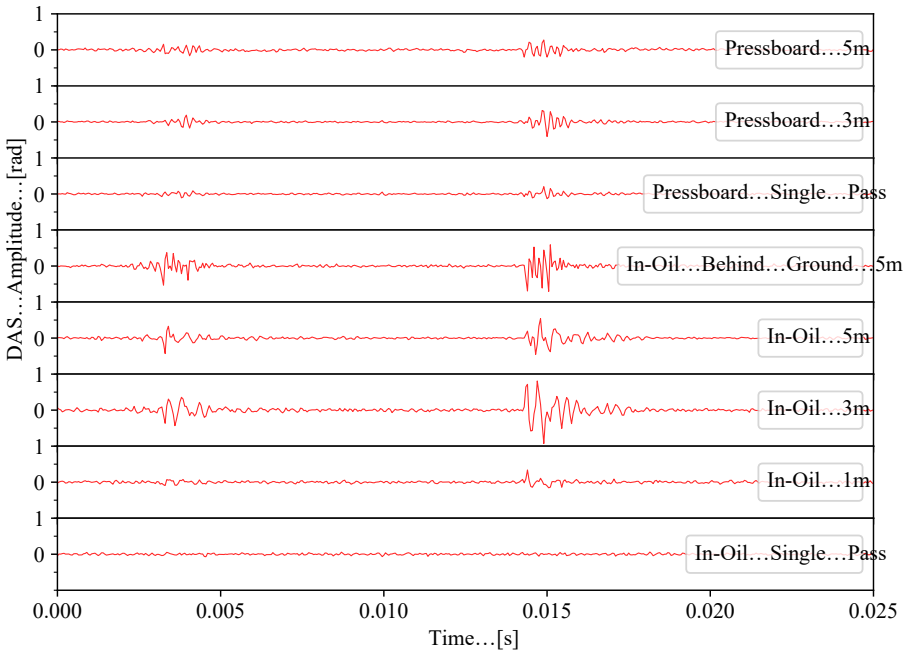

Figure 6.17: Comparison of different DAS fibre positions and lengths. 2 PD events seen. Single pass refers to a length of around 15 cm, enough for the fibre to enter and exit the oil at the specified position. See Figure 6.2 for how the fibre positions relate to each other.

If an acoustic wave is imagined passing across a coil of fibre, depending on the wavelength of the approaching signal, the wave will impart multiple additional positive and negative displacements onto the fibre. When the fibre is interrogated, these positive and negative strains will somewhat cancel each other out across the gauge length. Specifically, the wavelength of a signal with a frequency of 60 kHz, the recorded peak of the AE, in 20 °C oil with a wave velocity of 1480 $\mathrm{m\,s^{-1}}$ will be 24.7 mm [178]. This is approximately half the diameter of the coils in the experiment and could likely be the fundamental cause. If not necessarily because of the cancellation, but perhaps also due to different resonance modes getting excited as the coils are close to this integer 2× wavelength.

The other hypothesis is that the increased number of turns required in the coil to achieve the longer lengths could cause a change in the effective acoustic impedance, resulting in less acoustic transmission into the fibres. However, this effect is much less likely to produce such a drastic effect than what is observed.

PRPD

By utilising a zero-crossing detector on the high voltage supply and the PZT used for initial synchronisation of the various systems, a reference was injected in DAS and OptimAE from the voltage waveform. This allows the common analysis technique of PRPD, already utilised on the electrical Omicron system, but instead applied to the acoustic methods. To achieve this, the voltage output of the CPL542 quadripole shown in Figure 5.12 was connected to the oscilloscope (still triggering the pulse generator for the PZT) and triggered on the rising-edge zero crossing. By searching and recording the sample position of each 50 Hz trigger, the remaining samples are segmented into sections: each referring to one cycle of the AC waveform. These sections are then folded onto a scatter plot resulting in an x-axis of electrical phase in reference to the trigger. Figure 6.18 shows the resultant graph in comparison to the Omicron-generated PRPD graph. The colour representing density of events was calculated by calculating the distance between each point and every other point, increasing the colour scale when the distance was below a threshold value. Other analysis methods such as PSA do not work for DAS data due to the system not detecting every sequential pulse.

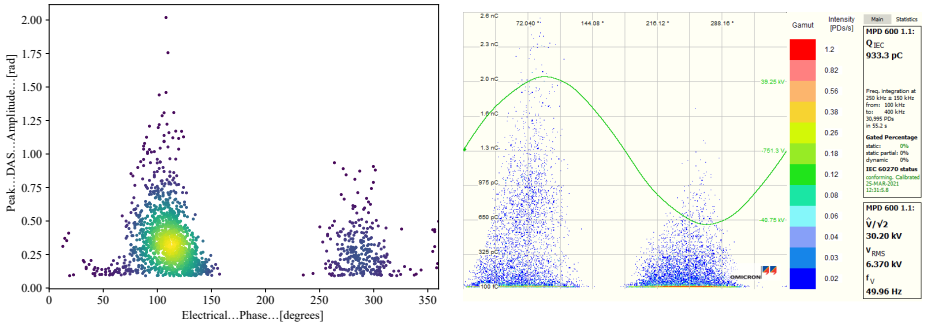

(a) DAS (b) Omicron

Figure 6.18: Comparison of PRPD plots using data from just the DAS system in (a), and the Omicron system in (b). Similarities can be seen with a larger number of events seen in the positive half cycle of the DAS. Colour indicates the density of points.

During this 1 minute capture, PD rates were approximately 160 PD/s with an average PD amplitude of 934 pC and a peak of 2.9 nC. The DAS positively identified 70% of these PDs as compared to the electrical measurement. Both plots clearly have the same patterns of increased amplitude discharge on the positive half-cycle, a gap during the positive / negative transitions, and decreased amplitude discharge on the negative cycle. Due to the higher amplitude peaks in the positive half-cycle, more events in DAS are recorded, resulting in the higher density of points. This shows that given a reference trigger, PRPD analysis can be applied to DAS data allowing possible classification of events and removal of noise shown by points uncorrelated to the voltage phase angle. An example of this is in Figure 6.19, where a band of points is seen at the bottom uncorrelated with the voltage phase. This data is from a different pressboard sample but shows the same 2 groups of points.

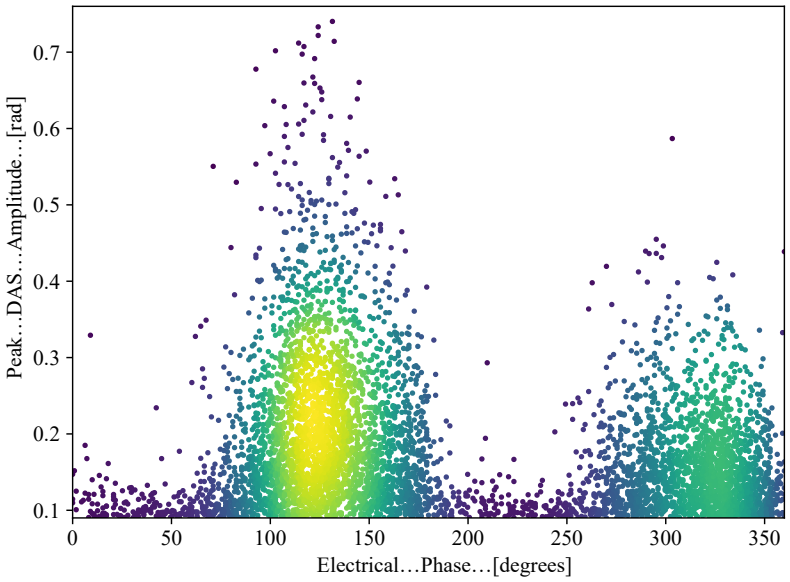

Figure 6.19: DAS PRPD plot where the noise floor of the DAS can be seen as a continuous band of points. Colour indicates the density of points where yellow is the highest.

From Figure 6.18 and 6.19, a delay can be observed that is constant between the DAS plots but offset from the electrical measurement in Figure 6.18. The peaks and tightest group of points should occur at approximately 70° and 260°, but instead shows at 120° and 320°: an offset of approximately 50° to 60°. This is equivalent to a 3 ms time delay, and is partially from the acoustic transmission delay (contributing as previously seen below 1 ms) and primarily from a synchronisation delay not from the original system in Section 5.3, but from the zero-crossing detector used. With calibration, as this delay is shown to be constant, the correct phase information can be obtained.

6.5 Conclusion

DAS has been shown to detect partial discharges across the oil-pressboard interface in excess of 100 pC. This detection still requires a coil, or repeated section of fibre with a preferred size of approximately half the gauge length, in order to gain acceptable signal above the noise floor. Compared to void discharges, there is also an increased percentage of identified events within the DAS system. Correlation between the DAS, high sample rate acoustic, and electrical measurements was shown with decent relationship between the high sample rate acoustic and electrical, and a similar but more scattered version between DAS and acoustic. This increased scatter would be expected to decrease given a higher sample rate DAS system in future. This ability for the DAS system to reliably pick up the acoustic signals is very dependent on the position of the fibre in relation to the PD source: fibres must be placed in positions that are acoustically transparent to the released acoustic emission from partial dis-

charge events (i.e. not shaded by acoustically absorptive materials such as the pressboard itself as demonstrated in this experiment).

The evidence provided in this chapter highlights the current best application of DAS: PD detection within HV transformers, specifically as a trend monitoring system. This is because void and creeping treeing partial discharges, both important lifetime indicators [179], have been shown to be successfully detected and the acceptable limits during online operation is within the current detection range [168]. The fibre is easily wrapped around the existing electrical coils providing good acoustic coupling and the required lengths of fibre to achieve the shown sensitivity. Some transformers, as already mentioned, already contain a suitable fibre installed at the factory for hotspot detection as part of the build process. Through a mix of DAS and DTS, hotspots and overall temperature profiles can also be simultaneously measured. With an integrated zero-crossing voltage signal, the DAS output can be resolved using a PRPD plot which closely matches that of standard electrical measurements, despite not identifying all PDs that the electrical method sees. As each zero crossing was recorded on each system respectively, the earlier time slip issues do not have an effect on this analysis method.

Chapter 7

Concluding Remarks

This work presents for the first time DAS as a fully distributed detection system for partial discharge. DAS was shown to be able to correctly identify partial discharge events at any position along the length of the fibre, given a reasonable source PD amplitude of at least approximately 100 pC. Introduction of a synchronisation system to the applied voltage also enables this method to employ PRPD analysis for better understanding of the discharges occurring as well as synchronisation with other measurement systems. A correlation of peak DAS size and acoustic energy was shown to exist between the high frequency AE and the reported DAS data. Given the trend in development of DAS systems pushing the maximum sample rate of a section of fibre, the performance gap between discrete acoustic sensing and a DAS measurement for a specific location should converge; furthering the ability to estimate PD size given an observed peak DAS amplitude.

Undersampling was a key feature of the mechanisms behind DAS detection of PD, and is often mis-represented in systems in which short sample windows are employed leading to erroneous conclusions of DAS not being suitable for partial discharge detection. This inherent feature of DAS systems has been explored in this research, where the ability of low sample rate DAS systems can detect high frequency AE from PD. Modelling of both the surrounding acoustic environment as well as the complicated DAS processes were completed and found to closely match experimental results, confirming the assumptions during creation.

Under void discharge, detection was achieved down to 18.55 pC with the void very close to the sense fibre. PD over 150 pC was detected more easily with a higher signal-to-noise ratio, even at lower discharge rates. For pressboard treeing discharges across the oil-pressboard interface, AE was found to be better picked up with direct sight of the area through oil, achieving a minimum detection figure of 120 pC due to the effects from the acoustic properties of the pressboard material readily absorbing acoustic energy. The In addition, as compared to void discharge, a higher percentage of PD events were correctly identified. The minimum sensitivities found are extremely useful for on-line detection of PDs that may be occurring in high voltage infrastructure. Given the inherent localisation features of DAS and distributed nature, these combined features in a single package produce a very unique and useful measurement system. As the

DAS technique demonstrated the highest, repeatable sensitivity with treeing discharges, and need for a coiled section, the best-suited application for this method is in HV transformers. With a fibre wound within the windings of a transformer, PD within acceptable limits can be detected and located, and the fibre can also be used for other measurements such as DTS. Within an HV substation or similar site, multiple items of HV plant could be connected in series with the same optical fibre using the inherent positional localization mechanism of DAS to separate signals from different items; thus requiring only a single DAS unit.

A number of current limitations are identified with utilising DAS as a PD tool at this time. Namely, the requirement of a coiled section of at least a 2-3 m to gain the discussed sensitivities. In the best case situation, the detection rate of PD events is less than 100% due to the under-sampling nature of the DAS technique. For the majority of applications this does not represent a problem: sampling over a period of at least a few minutes is sufficient given sporadic discharge to provide information on the occurrence and location of PD, as well as size trends. Shadowing of acoustic emission by absorbative materials, combined with the current need for a coiled section leads DAS to be more application limited in its uses. The best scenario for this technology currently seems to be within transformers.

Time-domain analysis such as PSA cannot be applied to DAS due to the high chance of missing sequential pulses either through randomness, or by shading of pulses within a short time-frame. Synchronisation issues, specifically time-slip, is problematic between multiple measurement systems. However, it is unlikely for real-world measurements to require such tight synchronisation between differing systems for analysis. The DAS method is unlike many existing PD detect systems as in its current for. Although it is not the best method for measuring absolute size of PD, its omnipotent technique allows thousands of measurement locations to be simultaneously sampled with immunity to electromagnetic interference and inertness to chemicals.

Advanced processing routines for accumulating and reducing data set sizes from the large, raw files produced by the DAS system were designed and can be found in Section C alongside the synchronisation utility for finding the specific pulse train used for synchronising the different measurements together.

Additional uses of the DAS measurement technique were identified as instant detection of faults and breakdowns within a multitude of scenarios such as cables, transformers, and substations. This presents many benefits over classical fault detection and pinpointing, massively reducing time and costs spent in the normal process. DTS was also mentioned to provide additional metrics on cable runs for dynamic load calculations and hot spot detection. DTS combined with DAS could provide a powerful combination for both fault/PD locating as well as hotspot/fire detection at the same time only requiring a single fibre and measurement equipment.

Further Research

Further research into the use of DAS as a PD tool splits into two main sections: the sensitivity of the system, and the validation of applications. By performing

experiments on specimens of transformers and other applications, comparison can be made between these initial lab conditions and real-world scenarios. An initial expectation with these experiments would be a similar result from the comparison of different sensing locations in Section 6.4, where sensing fibres with an acoustic path without absorbative materials seeing good amounts of PD events.

Further work into improving the sensitivity should be considered covering not only the signal to noise ratio of the system itself, but also decreasing the need for coiled fibre. Fibres used as part of a cable assembly typically are not a single strand, but contain many fibres bundled together to provide multiple avenues of communication. By applying DAS on multiple fibres in the same bundle, and through similar digital processing to the gauge-length stacking used in the APSensing system, sensitivity could be increased compared to a single fibre pass by using the additional fibres as more sensing fibre length.

Work utilising higher DAS sampling frequencies would give indications to where sensitivity issues lie: whether by undersampling of fundamental DAS technology. Increasing the DAS's sample rate to higher frequencies would also produce a higher number of detected PD events by a linear relationship in addition to aiding characterisation of PD and increased accuracy of PD size estimation.

Fault detection was not a focus of this research, but the DAS technology leads itself very well to obvious detection and location of such events. So far there is lack of published papers on the use of DAS for these kinds of protection systems, and results shown in this thesis present evidence that DAS has the potential for providing this service but has yet to be proved in real world conditions. If successful, it would greatly reduce time taken to locate and detect faults including possibly a speed and accuracy in finding high resistance faults due to PD detection.

Appendix A Additional Experimental Procedures and Data

A.1 Synchronisation Procedure

Precise synchronisation across different systems is quite difficult to achieve. The following is the utilised checklist during the various experiments to ensure as tight timing between the systems as possible.

1. Connect all systems to synchronisation source
    - For omicron system, tee in the synchronisation source to the PD input from the quadrature splitter
    - For DAS, as the sync pulses are shorter than the sample rate, a gated frequency source is used to excite a Piezo-electric transducer (PZT) located at the end of the fibre
2. Start all systems recording
3. Trigger two synchronisation pulses with a spacing of 2 seconds
4. Reconnect any swapped cables with the proper sources
5. <Run the experiment>
6. Run each dataset through the synchronisation program (detailed in Appendix C) to generate the offset file detailing the time difference between the start of the data, and the sync pulse.
7. These offsets are then used when combining data to correctly match up the datasets

A.2 Pressboard Fibre Layout

Item	Actual Length [m]	Cumulative Position [m]	Point of Interest Measurement Location [m]
DAS		0	
Patch Fibre	50	50	
100m Quiet Coil	110	160	
FUT Under Pressboard	5	165	162
5m Separator Fibre	5	170	
FUT Under Pressboard	1-2	172	171
5m Separator Fibre	5	177	
FUT Under Pressboard	<1	178	177
5m Separator Fibre	5	183	
FUT Behind Pressboard	5	188	185
5m Separator Fibre	5	193	
5m Separator Fibre	7	200	
FUT At Tank Wall	5	205	203
10m Separator Fibre	10	215	
FUT At Tank Wall	3	218	217
10m Separator Fibre	12	230	
FUT At Tank Wall	1	231	232
10m Separator Fibre	10	241	
FUT At Tank Wall	<1	242	242
10m Separator Fibre	10	250	
Patch Fibre	50	300	
PZT	10	310	308
End Fibre Spool	>2km	>2km	

Table 1: Detailed list of fibre connections and positions in the DAS chain, in order of connection

A.3 Anycubic Printer and Resin Data

Parameter	Value
Printing Technology	LCD-based SLA 3D Printer
XY DPI	47 µm (2560 * 1440)
Y Axis Resolution	1.25 µm
Layer Resolution	25 µm to 100 µm
Max Printable Volume	115 mm * 65 mm * 155 mm

Table 2: Specifications for the Anycubic Photon LCD-based SLA 3D printer [167]

Parameter	Value
Solidify Wavelength	405 nm
Hardness	79.0
Solid Density	1.184 g cm^{-3}
Tensile Strength	23.4 MPa
Colour	Aqua-Blue
Composition	Polyurethane Acrylate: 30-60%
	Acrylate Monomer: 10-40%
	Photoinitiator: 2-5%
	Colour Pigment: <2%

Table 3: Specifications for the Anycubic Basic Aqua Blue Coloured UV Resin [180]

Appendix B Extra Results

The following extra results on the next pages consist of longer-format data: i.e. similar presentation to those found in the main sections but covering a wider period of time where details may not easily be seen, but overall trends are more straightforwardly identified.

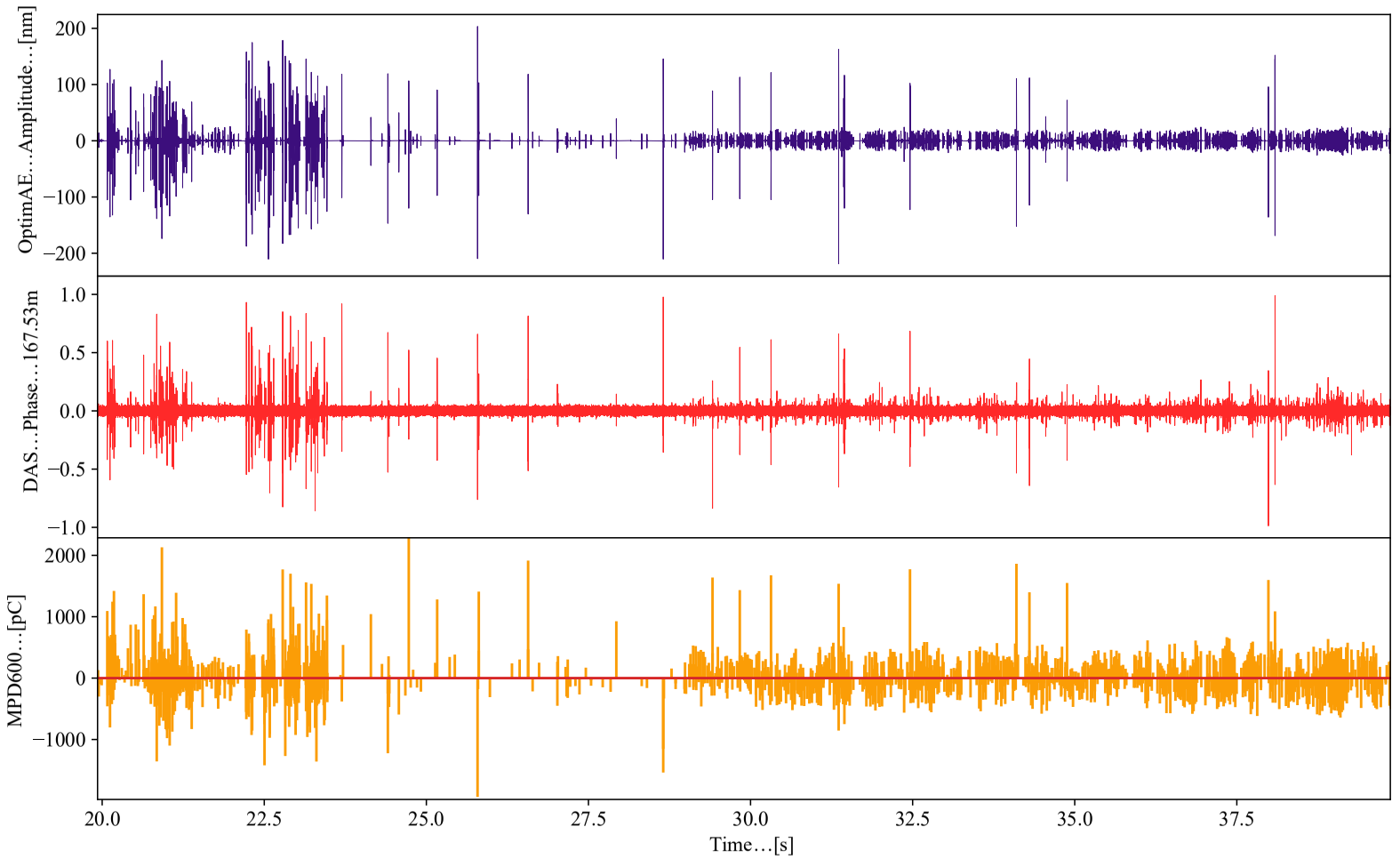

Figure B.1: OptimAE, DAS and Omicron measurements during pressboard discharge across 20 seconds. A good correlation between amplitude of detected events can be seen. The Omicron electrical measurement is shown without X's as in previous figures due to the density of data.

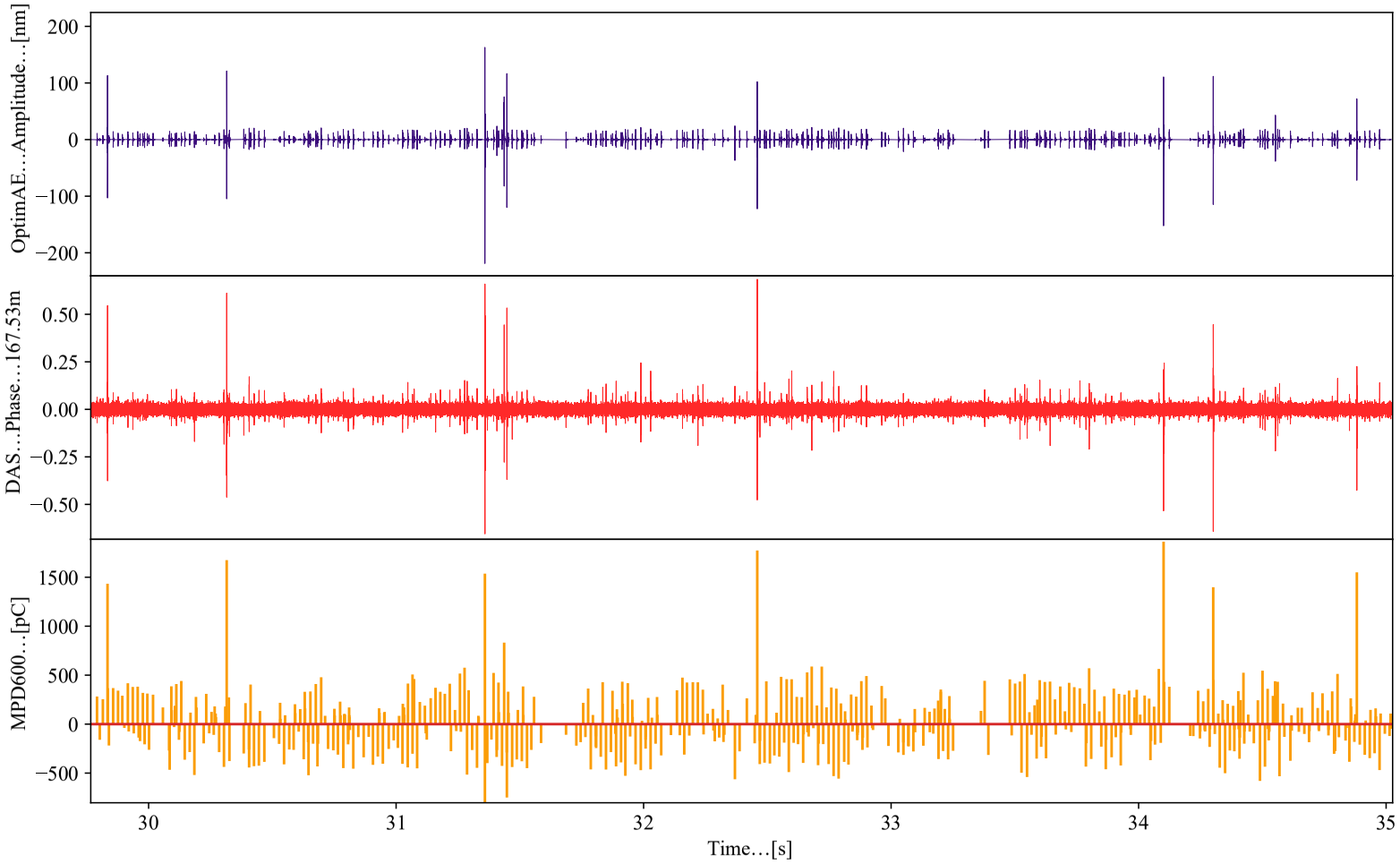

Figure B.2: More OptimAE, DAS and Omicron measurements during pressboard discharge across 5 seconds. A good correlation between amplitude of detected events can be seen. The Omicron electrical measurement is shown without X's as in previous figures due to the density of data.

Appendix C Code Segments

Most of the Python code uses pandas DataFrames for data storage and manipulation. This enables the use of many SciPy and NumPy functions to achieve the required data processing. As Python is a implied-type language, assume DataFrames are used where arrays are observed.

```
def downConvertPeak(data, order):
  # down converts data by using peak detection (think oscilloscope peak detect)
    ↪ by an order
  if not isinstance(data, pd.DataFrame):
    data = pd.DataFrame(data)
  print("Downconverting data...")
  df = pd.DataFrame(columns = data.columns)
  index = data.index
  max = int(len(index)/order)
  for i in range(max):
    if i % 50==0:
      print("Downconverting "+str(i)+"/"+str(max))
    df.loc[index[i*order]] = data.iloc[i*order:(i+1)*order,:].max()
  print("Finished")
  return df
```

Listing 1: Peak-maintaining down conversion used to decrease large datasets without removing peak information as seen with OptimAE data.

```
def findSyncPulses(self):
  tryAgain = True # for if we want to try tighter constraints
  tryAgainUndo = False # for stepping back in max range (from FUDGEFACTOR) as we
    ↪ might have tried to sync too tightly, and lost the pulses
  FUDGEFACTOR = 0.005 / 2  # number in seconds of the max distance we should try
    ↪ to find the pulses

  while tryAgain:
    offsets = []

    # the following assumes pulses in the format: | <-200ms-> | <-50ms-> | <-200
    ↪ ms-> | <-50ms-> |
    print("--------- Attempting Sync attempts-----------")
    for i in range(len(self.gatedIndex)-4):
      offset = self.gatedIndex[i]  # offset in index of sample points of where we
    ↪  are trying to find sync pulses
      # start by assuming where the pulses should be
      assumedTime = [offset+(0.200),offset+(0.200+0.050),offset
    ↪ +(0.200+0.050+0.200),offset+(0.200+0.050+0.200+0.050)]

      # for each pulse in sync train, try to find it in the data in our fudged
    ↪ range (as close as possible)
      for j in range(4):
        if len(findWithinRange(self.gatedIndex, assumedTime[j] - FUDGEFACTOR,
    ↪ assumedTime[j] + FUDGEFACTOR)) > 0:
          found = True
        else:
          found = False
          break
      if found:
        offsets.append(offset)
        print("Found sync pulses that line up. Offset (seconds): %f, FUDGEFACTOR:
    ↪  (s): %f" % (offset,FUDGEFACTOR))

    if len(offsets)>1:
      if (tryAgainUndo):
```

```
        tryAgain = False
      else:
        print("Multiple offsets detected, trying with smaller FUDGEFACTOR")
        FUDGEFACTOR = FUDGEFACTOR * 0.8
        if FUDGEFACTOR < (1 / samplingrate):
          tryAgain = False
          print("FUDGEFACTOR is now <1, so stopping")
    elif len(offsets)<1:
      print("Unable to get any closer than the ones we had last round")
      tryAgainUndo = True
      FUDGEFACTOR = FUDGEFACTOR * (1/0.8) # undo the last fudgefactor as we've
    ↪ removed ALL our points
    else:
      tryAgain = False

def findWithinRange(list, lowerBound, upperBound):
  lowerBoundi = bisect.bisect_left(list, lowerBound)
  upperBoundi = bisect.bisect_right(list, upperBound, lo=lowerBoundi)
  return list[lowerBoundi:upperBoundi]
```

Listing 2: Synchronisation Processing: For a given input pre-filtered by gating attempt to find a set of outlying pulses that line up with the synchronisation timings with a decreasing error margin. FUDGEFACTOR is the margin of error allowed between pulses which decreases with sucessive iterations.

Appendix D Published Papers

The following pages show the latest versions of the published and in-review papers written during this research.

- Jicable 2019 Conference: 123-128
- IEEE Sensors Applications Symposium Conference 2021: 129-132, (© 2021 IEEE. Reprinted, with permission)
- IEEE Transactions on Dielectrics and Electrical Insulation (*In Review*): 133-138, (© 2022 IEEE. Reprinted, with permission)

Distributed Acoustic Sensing of Partial Discharge: Initial Findings

Laurie **KIRKCALDY**, James **PILGRIM;** University of Southampton, (United Kingdom), laurie.kirkcaldy@soton.ac.uk, jp2@ecs.soton.ac.uk
Rosalie ROGERS, Gareth **LEES,** AP Sensing, (United Kingdom), rosalie.rogers@apsensing.com, gareth.lees@apsensing.com

ABSTRACT

This report investigates novel, initial experimentation in detecting and measuring Partial Discharge along an insulated cable using a fibre-optic-based Distributed Acoustic Sensing system. Initial detection of in-air corona and discharge has successfully been observed with a high signal-to-noise ratio, thus more sensitive signals will be able to be measured towards the goal of detecting partial discharge. This method could present numerous advantages over conventional Partial Discharge measurement techniques including accurate positional information, greater detection distance and immunity from electrical noise.

KEYWORDS

Distributed Acoustic Sensing (DAS), Partial Discharge (PD), measurement, detection, void discharge, distributed measurement, fibre-optic, power cable monitoring

INTRODUCTION

Power cable PD detection and location is now a necessary part of operating and maintaining a cable system and is routinely used for condition monitoring. Conventional test methods do not allow for the location of PD along cable circuits to be determined accurately. This work presents an optical fibre-based detection system that uses the minute vibrations caused by Partial Discharge which disturb the fibre, providing location and possible characterisation about the event. A Distributed Acoustic Sensing (DAS) system allows for precise localisation of PD without electrical signal degradation at great distances. Other measurements could be taken using the same system using multiplexing, such as detection of mechanical damage or larger discharges such as break-down events.

Present online detection methods such as high frequency (HF) current and single-point acoustical emission monitoring only provide very limited range and have no ability to provide accurate localisation data other than through time of flight between multiple sensors. By knowing the location and size of discharges, it is possible to make more informed asset management decisions.

Currently as far as the authors are aware, DAS systems have not been used for fully distributed detection or location of discharge activity. Therefore, this research is required to investigate whether DAS is suitable for the detection of discharge activity within a cable. Further research can demonstrate whether discharge characterisation is possible from DAS measurements alone.

OUTLINE OF DAS SYSTEMS

DAS typically uses a method called c-OTDR for detection of vibrations that can be reconstituted into an acoustic signal. Coherent Optical Time Domain Reflectometry (c-OTDR) is a well understood technique used to measure the Rayleigh backscatter along an optical fibre. A highly coherent laser pulse is launched into the sensing fibre which generates scattered light that is then collected on a detector. The returning scatter then constructively and destructively interferes with each other, as in an interferometer, causing a change in the phase relation and/or amplitude that is measured. However, as this Rayleigh backscatter changes based on the strain that the optical fibre experiences, by use of a fast-repetitive scan of the fibre acoustical signals can be reproduced along the continuous length of fibre. From comparison between the time of launch to detected reflections and the known speed of light down the fibre, the distance at which those scattered reflections originate from can be determined.

As the returning signal is of very low power, collection of this scattered light has to be taken over a measurable amount of time. These time slots in which the scattered light is measured, gives an inherent “binning” of physical segments along the fibre known as spatial resolution or gauge length. The sensitivity and SNR (Signal to Noise Ratio) of the system is affected by the selection of this spatial resolution. The measurement sections overlap by a length known as “spatial sampling distance” thereby allowing the spatial resolution to be accurately sampled.

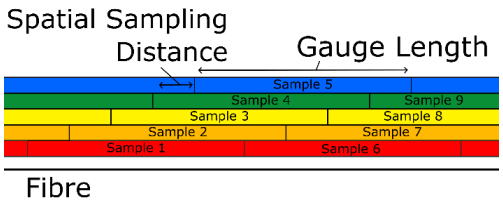

Figure 1: Graphical drawing of sampling terms used in DAS

c-OTDR techniques are able to provide a long measurement range, however longer ranges do provide a limitation in that the spatial resolution and repetition frequency are often impacted. A DAS system has recently been reported with a measurement range of 125km, with a spatial resolution of 8m [1]. As the measurement range increases, the amplitude of the received backscatter decreases due to fibre attenuation and therefore increased light should be launched into the fibre to maintain a good SNR. This can be achieved by increasing the optical pulse width which therefore decreases the spatial resolution. The

repetition frequency decreases simply due to the time that the light pulse takes to reach the end of the fibre before a new pulse can be launched. Therefore, experiments in lab conditions can achieve much greater sampling frequency than real-world cable lengths. For example, a 50km length fibre optic can only achieve a theoretical maximum of $f = \frac{c}{2.n.d} = \frac{2.998e8\ (\frac{m}{s})}{149820\ (m)} = 2001Hz$ where n is the refractive index, which for single mode fibre is 1.4982. Frequency division multiplexing (FDM) techniques could be used to increase the sampling rate in a linear fashion.

ACOUSTIC EMISSION (AE) OF PD

Partial discharge creates acoustic signals by exerting force on the surrounding materials of the void discharge due to the rapidly expanding gases. These materials are elastic and therefore oscillate at ultrasonic frequencies producing the acoustic emissions [2]. As the exciting vibration is dependent on the size and shape of the void, it can be seen that different void types create different emission spectra and also that due to the force applied to the surrounding material, the magnitude of the AE is proportional to the magnitude of the PD. Between the AE and where a fibre may be installed, surrounding insulation layers within a cable will distort and reflect the AE due to the differing acoustical properties of the material making the signal less defined. A sensor such as a fibre optic installed inside the cable however, would detect a much better signal than a sensor mounted externally to the cable. The intensity of PD signals is very small and is proportional to the energy released in the discharge. The peak amplitude is reported to be lower than -68dB ref. VµBar which approximately equals 5.979dBSPL, so low that some researchers declare as impossible to sense in a plain optical fibre with a DAS method [3]. However, *Posada-Roman et al.* [4] discusses the detection of AE of 1.3Pa with an optical fibre sensor which is equivalent to 96.26dBSPL, which seems far too large in amplitude for a PD event.

Acoustic detection is normally only carried out on transformers, using discrete sensors and relying on the ultrasonic transmission through the oil within the transformer tank. With a distributed fibre-optic based system, this solution of acoustic sensing can be applied on any power cable that contains, or is mechanically joined to, a fibre optic cable.

From the spectra that can be obtained from acoustic sensors it is possible given enough measurement bandwidth to classify the observed discharge into the different PD types. Other work [5-7] shows that with a high bandwidth of 400kHz, it is possible to characterize AE into different shaped cavity/void discharges and treeing. *Boczar et al.* [8] also demonstrates that the supply voltage at which the PD occurs, does not influence the frequency or time waveforms of the AE. However, this bandwidth is only available to very short OTDR systems or ones that use FDM techniques to improve sampling frequency.

ACOUSTIC ABSORBTION INTO SURROUNDING MATERIAL

As the fibre used for DAS is not directly embedded within the insulation of the cable where discharge may occur, the vibrations must travel through various layers. Also, if the fibre is mounted externally to the cable such as at a cable joint, likewise, vibrations detected by the fibre must pass through the surrounding air.

By using equivalent equations to power transfer in an electrical system, using the acoustic impedance of a material it is possible to approximate the reflected and transmitted power of these vibrations. The larger the mismatch in impedance, the larger the reflected energy and therefore the less energy transmitted, and the smaller the signal detected.

From acoustic theory [9,10]:

$$Reflection_{\%} = \frac{|Z_1 - Z_2|}{Z_1 + Z_2} \quad (1)$$

The acoustic impedance of a material (Z) is defined as the product of its density and acoustic velocity of a pressure wave through the material. The acoustic impedance of the various materials used in the construction of a power cable, as they are all solids, are on the order of MPaSm^{-3}, and are relatively constant. This results in the losses due to reflection being low within the cable. In contrast, air has a very low impedance at 420PaSm^{-3}, therefore at an interface between the cable and air such as at a joint site where the two are separated, only around 0.05% of the overall acoustic power is transmitted. Therefore, for good results of a DAS system applied to a cable, the fibre must be in solid vibrational contact.

Due to this high mismatch in acoustic impedance, detection is unlikely other than in perfect conditions with extremely high sensitivity. In these extreme cases, such as violent breakdown, the vibrations could be detected and act as a method to quickly locate a fault site. The reflection between layers inside the cable construction between the dielectric and where the fibre may be mounted is significant at up to 90% reflection.

For cables where the detection fibre may be buried next to the cable, the acoustical transmission varies greatly due to inconsistencies in soil packing and the different constituents. An estimated typical transmission is on the order of 10-20% [11] with additional attenuation of around 0.2-0.8dB/cm-kHz [12] through the soil.

EXPERIMENTAL SETUP

An initial experiment was carried out as to determine the viability of detection of discharge using a DAS system. It is assumed that if a DAS system is unable to detect large discharge that is much higher in amplitude of sound levels than PD, it is extremely unlikely that the system will be able to detect PD when embedded within a cable despite the increased coupling between the insulation and fibre optic.

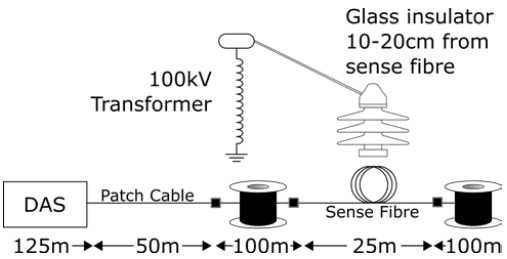

A 25m loop of bare single-mode fibre was initially placed at a distance of 30cm in air, from a glass insulator. A 50m patch cable was connected between the DAS instrument and the beginning of a 100m vibration-isolated spool. Another vibrationally isolated 100m spool was connected after the fibre under test to provide a low-noise section of fibre either side to increase signal to noise ratio. Figure 2 shows the background noise with no voltage applied to the insulator.

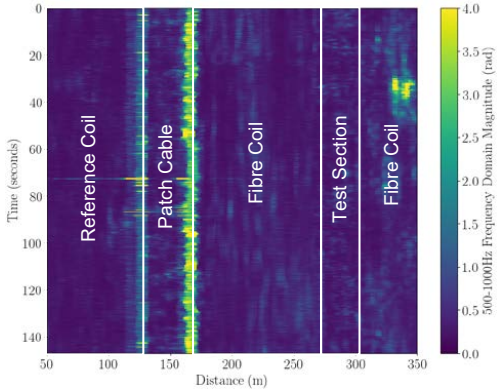

Figure 2: DAS background noise between 500-1000Hz.

Down the entire length of fibre, the two large responses in the 100-500Hz region correspond to the distance where the 50m patch cable is coupled on. These large signals (as compared to other coupling sites between the isolating boxes) is attributed to the E2000 fibre connectors acting as an in-line reflector, providing a much higher reflection signal than the normal backscatter. The patch cable had a thicker jacket and therefore was more rigid than the rest of the isolated reels and sense fibre, and therefore might be conducting more vibrations into the connectors than the thinner, more flexible single-mode fibre that was used as other interconnects. Compared with the HV equipment not energised, the amplitude of detected vibrations is significantly increased at a distance of 160m. This is physically the closest point where a sensitive part of the fibre (the connectors) is to the HV transformer and variac and thereby can be concluded that this was the measurement of 50Hz harmonics.

From basic OTDR simulations and the acoustic reflection between air and other materials, it was expected that large discharges could be seen with the fibre in air but anything smaller than catastrophic breakdown would likely not be seen. By moving the fibre so it would be physically attached to the point of acoustic emission, or to something vibrationally coupled, the high acoustic impedance mismatch could be reduced thereby allowing the overall sensitivity to increase by orders of magnitude. This was tested by attaching the fibre to the base of the insulator.

DISCHARGE EXPERIMENT

Measurements were taken with an initial sampling rate of 2kHz, Gauge length of 5m and spatial sampling of 1.25m. Figure 3 shows increasing and decreasing voltage applied

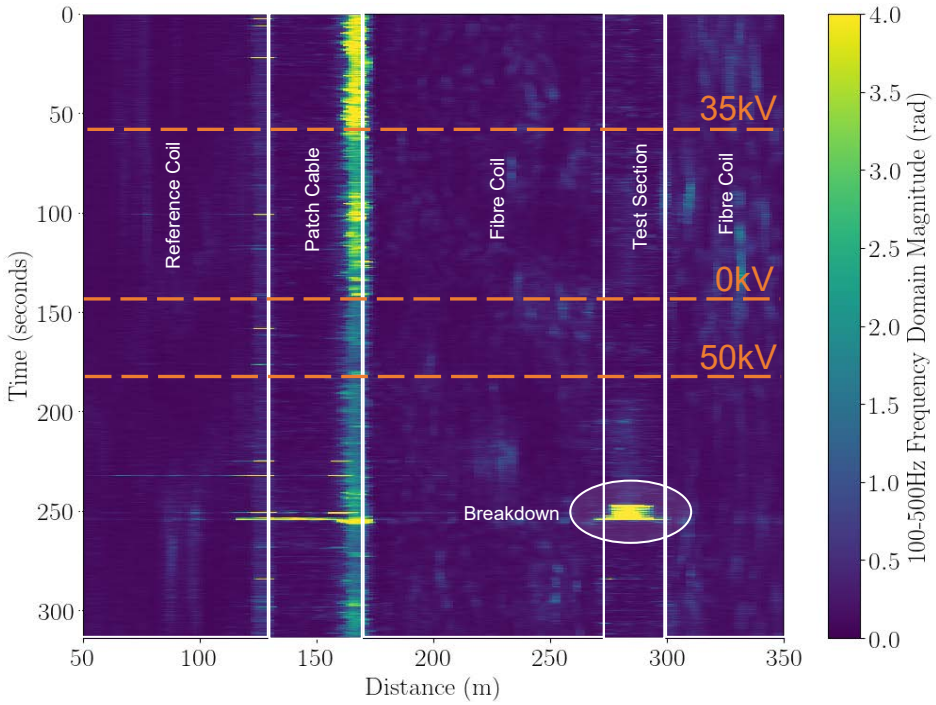

Figure 3: DAS 100-500Hz output with fiber in air at a distance of 30cms from insulator. Voltage ramped up at 70 seconds to 47kV, down to 0 at 150s. Ramped up again at 180s through to breakdown at 250s

to the insulator eventually up to the full in-air breakdown of the insulator at 69.1kV. At the location of the fibre near the discharge (275-300m), the decrease in detected vibrations is almost imperceptible; likely not extractable given no knowledge of the timing or position of the event. The nearby E2000 connector has a much more pronounced response due to a higher reflection. This reinforces the prediction from acoustic impedance previously calculated, showing that detection of small discharges through air is unlikely except in the worst case of discharges.

By comparing the different frequency bands of the build-up to the discharge, it was found that 100-500Hz output gave the best signal at the point of discharge of any frequency bands at the known sense fibre location. However, compared to the surrounding noise in any of the frequency bands it was extremely difficult to identify the discharge's acoustic emission.

By moving the fibre in contact with part of the insulator, vibrations are then directly coupled rather than attenuating through air and the boundaries into the fibre optic core. The bare single mode fibre was wrapped circumferentially around the outside of a PVC tube supporting the insulator.

As shown in Figure 4, there is a much greater signal and when corona starts to occurs, the signal is clearly visible above all other noise in the same 500-1000Hz frequency bin with a SNR of up to approximately 60:1 or 17.8dB. This reflects an equivalent scenario with an embedded fibre optic in a cable where the fibre optic is coupled through solid insulation to the places where Partial Discharge may occur. The experimental setup due to its non-perfect mounting methods are likely reducing the signal more than what could be expected in a cable. Thus, it can be expected with this higher coupling ratio, a greater sensitivity can be achieved and therefore PD would be able to be detected.

Previously identified noise such as at the connector locations is still present, but the wanted signal is now at a much higher amplitude that within Figure 4 it is not visible.

Most of the energy is detected as broadband across the entire measurement spectrum with tail-off sub-500Hz and above 9kHz. 50Hz harmonics are very strong in the received data when corona discharge is occurring. From this, it can be deduced that the fibre is picking up the fundamental frequency of the discharge rather than the HF components that most AE sensors detect (usually greater

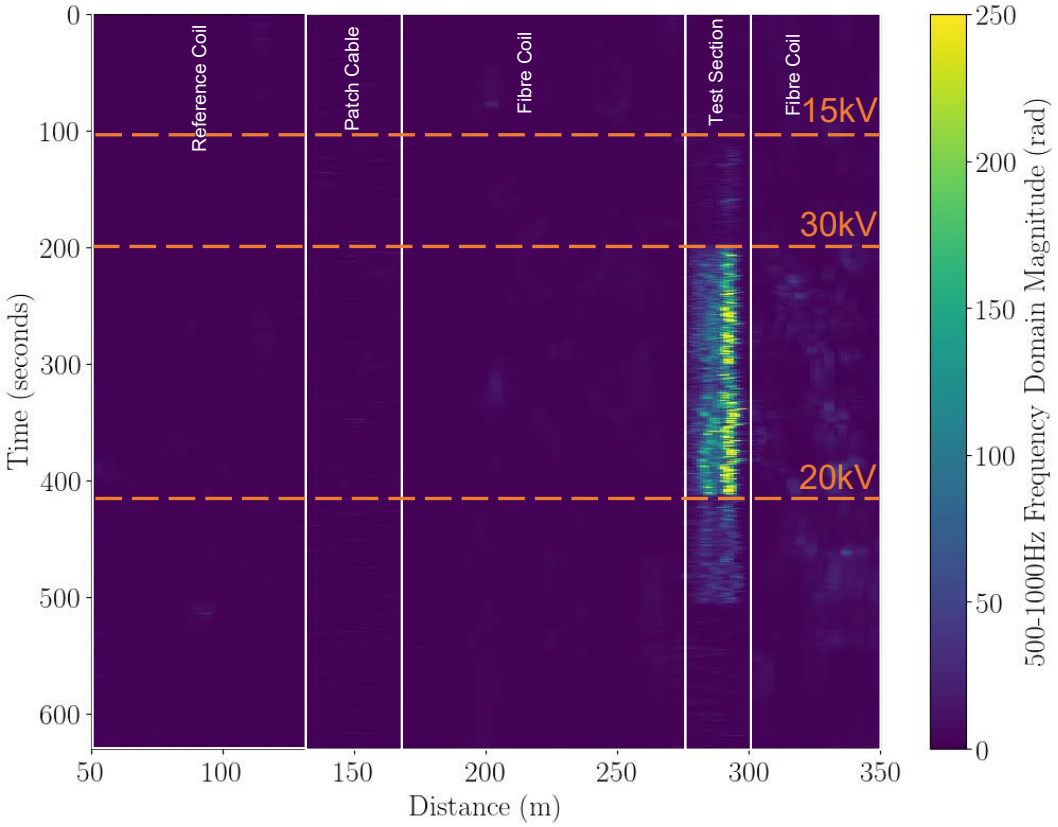

Figure 4: 500-1000Hz output with fibre vibrationally attached to insulator. Max amplitude increased to 250 Voltage increased at 100s up to 15kV, 30kV at 200s and 20kV at 420s.

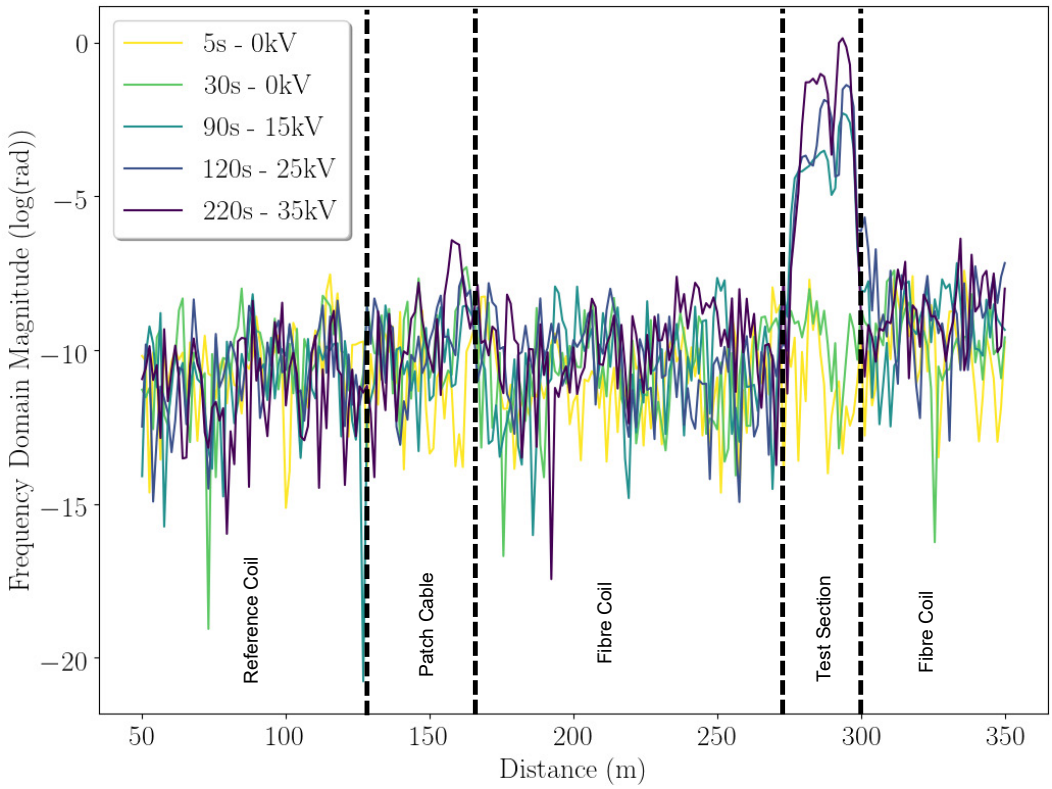

Figure 5: 50Hz intensity against distance for different discharge conditions. Fibre attached to insulator at 275-300m

than 5kHz). By looking at the 50Hz intensity along the length of the fibre in Figure 5, the location of the discharge can be easily found with a decent SNR considering no de-noising has been applied.

This is identified as an easy way of filtering out and automating the detection of discharge from a DAS system assuming a cable does not produce excess 50Hz vibrations that could swamp the desired signals. 50Hz is also well within the typical sample rate expected on a long length of fibre optic so no advancement on present detection methods would need to take place to implement this on existing cables. Fundamentals of the 50Hz signal (e.g. 100Hz, 150Hz, 200Hz etc.) were also examined and showed similar results but decreased in SNR above the 4th-5th harmonic. For isolation against default cable vibrations, these higher fundamentals may be useful. The fibre couplers that presented large reflections in previous measurements are present in the 50Hz signals, however they are much lower in amplitude than the discharge.

CONCLUSION

This report has shown that fibre in equivalent conditions to one mounted inside of a cable that experiences vibrations from partial discharges of reported values from literature, could be able to both detect and sense the amplitude of the discharges with a good signal to noise ratio. Due to the sense fibre being common single-mode communications fibre, DAS systems can be retro-fitted to any cables that already contain compatible and spare fibre optics. For cables installed in more ideal conditions where external vibrations are minimal e.g. subsea, the measured SNR may be further improved.

The fibre is also able to detect any large breakdowns external to the cable or other disturbances such as excavation activities along with the location. Due to vibrations transmitting along the cable, the precise location is hard to ascertain but within 25m localisation is considered adequate. Classification has not yet been achieved due to the low maximum sample frequency expected on long cable lengths. More research is required in this area for detection of PD types from data only in the low frequency spectrum.

Acknowledgements

The support of Advanced Photonic Sensing (APSensing) for both sponsoring this work as well as providing support and the hardware necessary for all the DAS experiments. is gratefully acknowledged.

Thanks also to *J.D. Hunter* for providing the Python library MatPlotLib, used for a majority of the graphing and data visualisation within this paper.

REFERENCES

[1] G. Cedilnik *et al*, 2019, “Pushing the Reach of Fiber Distributed Acoustic Sensing to 125 km Without the Use of Amplification”, IEEE Sensors Lett., vol. 3-3, 1-4

[2] L. Yanqing *et al*, 2005, “Study on Ultrasonic Generation Mechanism of Partial discharge”, Proceedings International Symposium on Electrical Insulating Materials, vol. 2, 467-471

[3] P. Rohwetter et al, 2015, “Distributed acoustic sensing: towards partial discharge monitoring”, Proceedings
International Conference on Optical Fibre Sensors, vol 9634, 96341C

[4] J. Posada-Roman *et al*, 2012, “Fiber optic sensor for acoustic detection of partial discharges in oil-paper insulated electrical systems”, Sensors, vol 12, 4793-4802

[5] Y. Tian *et al*, 2004, “PD characterization using short duration fourier transform of acoustic emission signals”, Proceedings
IEEE International Conference on Solid Dielectrics, vol 2, 695-698

[6] Y. Tian *et al*, 2000, “Acoustic emission techniques for partial discharge detection within cable insulation”, Proceedings
Dielectric Materials, Measurements and Applications, 503-508

[7] T. Bocazar, 2001, “Identification of a specific type of PD from acoustic emission frequency spectra”, IEEE Trans. Dielectr. Electr. Insul, vol 8 no 4, 598-606

[8] T. Boczar *et al*, 2015, “Comparative Studies of Partial Discharge Using Acoustic Emission Method and Optical Spectroscopy”, Proceedings
IEEE International Conference on the Properties and Applications of Dielectric Materials , 740-743

[9] S. Rienstra, *et al*, 2018, An Introduction to Acoustics

[10] L. Kinsler *et al*, 2000, Fundamentals of acoustics, Wiley

[11] K. Attenborough, 1985, “Acoustical impedance models for outdoor ground surfaces”, JSV, vol 99-4, 521-544

[12] W.D. O’Brien *et al*, 1996, “Acoustic Characterization of Soil”, US Army Construction Engineering Research Report

GLOSSARY

AE: Acoustic Emission
c-OTDR: Coherent Optical Time Domain Reflectometry
DAS: Distributed Acoustic Sensing
FDM: Frequency Division Multiplexing
HF: High Frequency
OTDR: Optical Time Domain Reflectometry
PD: Partial Discharge
PVC: Polyvinyl Chloride
SNR: Signal to Noise Ration

Partial Discharge Detection Using Distributed Acoustic Sensing at the Oil-Pressboard Interface

Laurie Kirkcaldy and Paul Lewin
School of Electrical and Computer Science
University of Southampton
University Road, Southampton, SO17 1BJ
Email: laurie.kirkcaldy@soton.ac.uk

Gareth Lees and Rosalie Rogers
AP Sensing UK Ltd
Basingstoke, Hants, RG21 4EB
Email: info@apsensing.com

***Abstract*—This paper investigates novel, initial experimentation in detecting and analysing Partial Discharge at the Oil-Pressboard interface using a continuous fibre-optic-based Distributed Acoustic Sensing (DAS) system. Discharge was successfully detected at a minimum of 223 pC despite the sample rate of DAS being lower than the spectra of acoustic emission. DAS presents multiple advantages over conventional Partial Discharge techniques including inherent localisation, immunity to electrical and magnetic noise, as well as much greater detection distances.**

***Index Terms*—Distributed Acoustic Sensing, Partial Discharge, Pressboard, High Voltage, Oil-Pressboard Interface**

I. Introduction

Ageing of insulation systems within High-Voltage equipment during operational life is natural [1]; however, it is established that ageing is accelerated when the systems are under increased electrical, mechanical or thermal stresses [2]. This then contributes heavily increases chances of breakdown or failure [3]. Partial Discharge (PD) is a localised electrical discharge that adds to these stresses, and is known to degrade insulation [3]. Therefore, as partial discharges are known to be a cause and symptom of degradation across many different types of insulation systems, detection and monitoring are of key importance [4].

Typical detection methods for monitoring partial discharge within a transformer include transient voltage [5], Ultra High Frequency (UHF) [6], Acoustic Emission (AE) [7] and Dissolved Gas Analysis(DGA) [8]. Electrical measurements looking for transients are not easily able to distinguish between different discharge sources. UHF however, can even provide triangulation of discharges, but relies on many high bandwidth sensors; which can be expensive and hard to install [8], [9]. DGA does not provide location information and can only be sampled periodically [10]. Conversely, AE can provide all of these benefits with the main drawback of being sensitive to external vibrations and mechanical noise.

Fibre optic sensors have been used to detect AE [11]–[13], however these are single discrete sensors mounted at the end of fibre optic cable, as opposed to using the fibre itself as a sensor. Distributed Acoustic Sensing (DAS) provides a continuous, distributed set of vibration sensors along a fibre optic cable [14] that are able to detect and locate possible PD events whilst being inherently immune to electrically or magnetically induced noise [15]. DAS has previously been utilised on high voltage systems for detection of breakdown events [16]: much greater in amplitude than PD events.

This paper presents the first stage of experimental results and initial analysis for continuous on-line detection of pressboard-based partial discharge using DAS, focussing on the techniques required to detect AE at much lower sample rates than standard techniques [17].

A. Principle of Distributed Acoustic Sensing

Coherent Optical Time Domain Reflectometry (c-OTDR) is a well understood technique used to measure the Rayleigh backscatter along an optical fibre. A highly coherent laser pulse is launched into the sensing fibre which generates Rayleigh backscatter due to random imperfections in the fibre [18]. The returning scatter interferes constructively and destructively, as in an interferometer, causing a change in the phase that is measured. However, as this Rayleigh backscatter changes based on the strain of the optical fibre; by interrogation of the Rayleigh backscatter generated by periodic pulsing of a coherent laser down the fibre, the acoustic signal disturbing the fibre can be reproduced. From comparison between the time of launch to detected reflections and the known speed of light down the fibre, the distance at which those scattered reflections originate from can be determined.

The fibre distance channels at which positions of reflections can be determined are separated by "spatial sampling" distances. The measurement at each spatial sample distance represents the average measurement of all spatial samples within a fixed spatial resolution. The spatial sampling and spatial resolution are both fixed values, so that as the position increases in number of spatial samples, the fibre distance channel always represents the average measurement of the surrounding samples within the spatial resolution. By increasing the repetition of interrogation, time resolution can be increased. However, without additional methods [19], the maximum speed that can be achieved is the light round-trip time along the fibre. To achieve the 20 kHz sampling rate used in this paper, the longest length of fibre that can be achieved at this time is 5.1 km with 1.27 m spatial sampling and a gauge length of 5 m.

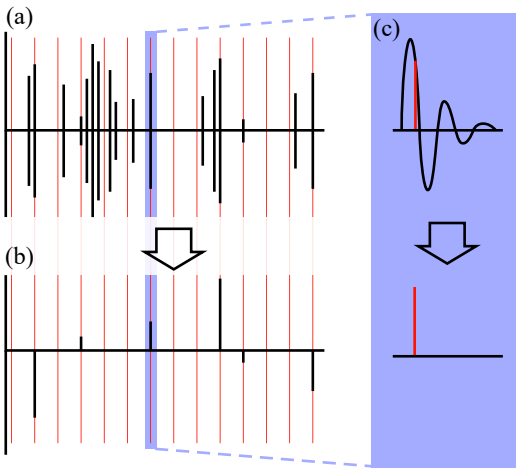

Fig. 1. Exaggerated example of how high-frequency events are sampled, missed and distorted from being sampled at a lower rate. (a) example high-frequency events in the time domain to be observed occurring randomly with random amplitude. The regular red lines indicate the intervals at which these events are sampled with a very short interrogation. (b) shows the resultant data producing events only when the interrogation happens to line up with an event. Zoomed inset (c) details the effect of the interrogation sample being much shorter than width of the event causing distortion of the resultant amplitude.

B. Undersampling

At sample rates that DAS is currently capable of [20], at longer distances (i.e. >5 km) there is a mismatch between this sampling rate and the time scale of individual PD acoustic events. It may be construed that under normal sampling, these events would be aliased removing all but the largest amplitudes of acoustic impulses due to inherent time-averaging between sampling points. However, DAS sampling relies on a very short (<10 nS) interrogation pulses that can allow the detection of higher-frequency signals than the sampling rate, albeit with distortion-causing aliasing.

As demonstrated in Figure 1, when a high-frequency signal or impulse interacts with the fibre at the same time as that fibre-section being interrogated, a very short impulse-like event will be observed in the results. In Figure 1c, it can be seen that the interaction between the high frequency acoustic signal and fibre interrogation has to occur within the sampling window. Therefore, there is a chance the event may be missed, as well as the recorded data not being representative of the original signal other than detection of existence. As originating PD acoustic emission comprises of mostly impulse-like discharge, it is most likely that the DAS will sample the reverberant ringing and not the highest peak value. By decreasing the length of fibre, the sample rate can be increased as the round-trip time of the fibre is less, thereby increasing the chance of detecting events; but the detection range is shortened.

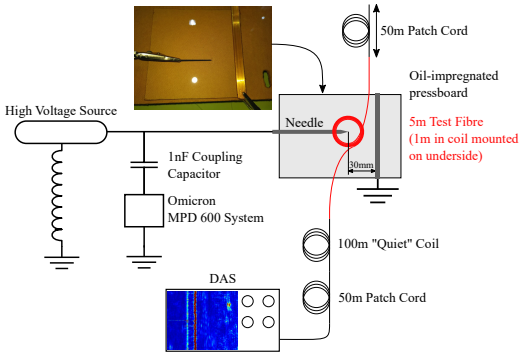

Fig. 2. Mixed electrical and optical schematic of the pressboard setup compromising of the DAS firing through the patch and quiet coils into the 5 m of test section of which 1 m is mounted to the pressboard; as well as electrical omicron measurement connected in parallel with the HV source. Needle is set at 30mm from the grounded bar at an angle of 10°.

II. Experiment

A. Setup

A needle-bar setup (Figure 2) is used as a discharge source across an oil-pressboard interface, allowing for easy attachment of fibre-optic components. The construction is the same as in [21] with the bar grounded, and the needle elevated to between 20 and 25 kVrms, reliably initiating partial discharge. The needle is positioned at a shallow angle (10°) to the 5 mm thick pressboard to induce tracking along the interface. The pressboard was conditioned to 6% moisture by weight, achieved by 48 hours of drying in an oven at 90 °C and then allowing re-absorption from the ambient air. 1m of bare SMF28e unbuffered fibre in a loose coil is clamped to the underside of the pressboard.

The pressboard and close fibre assembly was immersed in Nitro Gemini X mineral oil, with the setup sat on high-density foam to reduce direct-coupled environmental noise. As shown in Figure 2, an APSensing DAS system is connected to the fibre in the test area through a 50 m patch cable and then through a 100 m acoustically-decoupled reference coil. The repetition rate of the DAS system was set to the maximum 20 kHz with a gauge length of 1.27 m, spatial resolution 5 m.

The system was monitored electrically with an Omicron MPD600 system, though a 1 nF coupling capacitor connected in parallel to the experiment. The system was tested to be PD free (<5 pC) up to 35 kV with no needle.

As most PD events are missed due to the sampling mechanism, as well as lack of synchronisation methods with the Omicron system, single discharge events can not be individually compared and therefore the envelope of the events are compared other a greater time period.

B. Processing

As events in the DAS data takes the form of spikes, most standard denoising techniques [22], such as wavelet or spectral

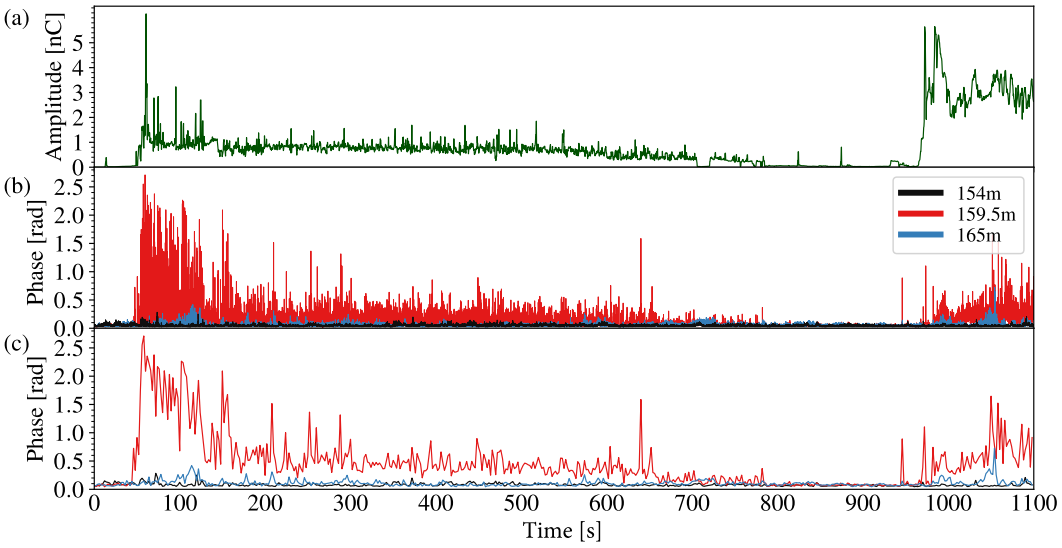

Fig. 3. (a) Amplitude trend of PDs electrically measured with Omicron MPD system. (b) Phase output of the DAS system at 3 different locations: 154m before pressboard in black, 159m within pressboard in red, 165m after pressboard in blue. (c) Data from (b) has been downconverted using the peak-detect method as described above with a ratio of 100:1; peak values are maintained whilst reducing data.

subtraction, do not show any SNR improvement at this time. Furthermore, the amount of data recorded per minute can be in excess of gigabytes, therefore the data must be reduced before analysis. The data from each location bin is segregated into chunks: the highest value in the absolute values of each chunk is taken as a new point in an output array at that location and starting time. This allows for downsampling the data whilst maintaining any peak values that may exist. Unfortunately, processing data in this form may also pronounce and mask signals along with the events. Results in this report are above the noise level and therefore not an issue in presented data.

III. Results and Discussion

Figure 3a shows the amplitude trend of the Omicron PD measuring system, starting with large discharge averaging 1 nC to 2 nC, peaking at 6 nC; and then decreasing to a steady 0.9 nC to 1.5 nC at 150 s until 600 s. The discharge then peters out to below 50 pC until at 970 s in discharge rapidly climbs to above 2 nC. The output of DAS system in Figure 3b, at the pressboard location 159.5 m shown in red, closely follows this trend seen by the electrical measurements with peak values of 2.72 rad at 1.8 nC of discharge. During the steady 0.9 nC to 1.2 nC range, average spikes are seen in the DAS of 0.73 rad. Noise floor was measured without voltage applied at 0.056 rad(rms) across a period of 30 seconds.

As expected, the occurrence of these spikes is, like the originating discharge, stochastic; but loosely correlated with the amplitude and number of discharges. Locations surrounding the pressboard, shown at 154 m and 165 m, only background

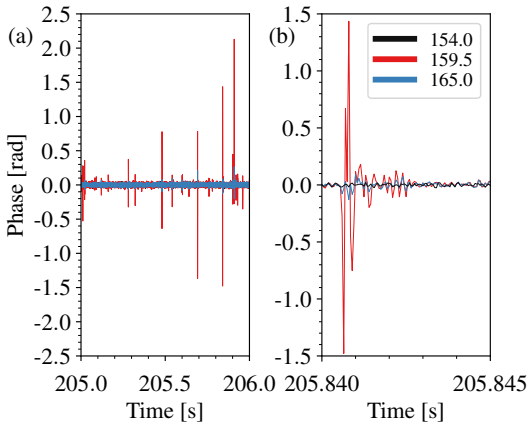

Fig. 4. Greater detail of single events between 205 and 206 s; same data as in Figure 3 without any downconversion. (a) 1 second of DAS data, distances: 154m before pressboard in black, 159m within pressboard in red, 165m after pressboard in blue. (b) Greater detail across time frame of 5 ms showing an impulse-like single PD event in DAS data at pressboard location.

noise is observed, and does not correlate with PD events. The increased resolution of a single event in Figure 4 shows acoustic events are picked up as a major peak and then ringing causedby the elasticity of the materials and acoustic reverberations of the system.

Due to undersampling, the majority of the DAS data shows amplitudes less than peak value of the originating acoustic

emission; as due to chance, this highest impulse peak is missed and instead the remaining reverberation is sampled. Peaks at 150 s and 640 s, however, show events during which this is not the case, and produce an uncharacteristically high peak in the data.

Figure 3c shows the peak-detect downsampled data, producing a more similar plot to the trend given by the Omicron allowing for easier visual comparisons between the datasets. As PD amplitude decreases over time, the overall envelope of the resultant DAS data at that location decreases until at 800-950 s, the spikes are within the noise floor giving a minimum sensitivity of 0.147 rad at 223 pC.

IV. Conclusion

The purpose of this study was to analyse whether a DAS system was capable of detecting partial discharges, specifically in the case of oil-pressboard interfaces. Based upon the tests carried out, DAS is able to detect discharges of larger levels given that the acoustic coupling between the fibre and discharge source is good enough.

These results are early in the development of DAS for PD detection and show promising results. The data described in this report due to the effect of undersampling of events, and the stochastic nature of the PD itself, means that recorded minimum sensitivities may not be the best achievable. Additionally, the noise floor of the DAS system in this report is within a working laboratory environment, and therefore is not typically representative of a permanent fixture. Thus, it would be expected that in such a system, high sensitivities of PD detection would be achieved.

Acknowledgment

The authors would like to thank APSensing for their generous funding of this project as well as providing useful input and comment on many aspects. Thanks also goes to the technicians of the Tony Davies High Voltage Laboratory Alan Welford and Charlie Reed.

References

[1] J. Kuffel and P. Kuffel, *High Voltage Engineering Fundamentals*, 2nd ed. Newnes, 2000.

[2] V. Sokolov, "Understanding failure modes of transformers," Tech. Rep., 2005.

[3] P. H. Morshuis, "Degradation of solid dielectrics due to internal partial discharge: Some thoughts on progress made and where to go now," *IEEE Transactions on Dielectrics and Electrical Insulation*, vol. 12, no. 5, pp. 905–913, oct 2005. [Online]. Available: https://doi.org/10.1109/TDEI.2005.1522185

[4] I. Sadeghi, H. Ehya, R. N. Zarandi, J. Faiz, and A. A. S. Akmal, "Condition Monitoring of Large Electrical Machine under Partial Discharge Fault - A review," in *2018 International Symposium on Power Electronics, Electrical Drives, Automation and Motion (SPEEDAM)*. IEEE, jun 2018, pp. 216–223. [Online]. Available: https://doi.org/10.1109/SPEEDAM.2018.8445261

[5] R. Bartnikas, "Partial discharges their mechanism, detection and measurement," *IEEE Transactions on Dielectrics and Electrical Insulation*, vol. 9, no. 5, pp. 763–808, oct 2002. [Online]. Available: https://doi.org/10.1109/TDEI.2002.1038663

[6] S. Tenbohlen, D. Denissov, S. M. Hoek, and S. M. Markalous, "Partial discharge measurement in the ultra high frequency (UHF) range," *IEEE Transactions on Dielectrics and Electrical Insulation*, vol. 15, no. 6, pp. 1544–1552, dec 2008. [Online]. Available: https://doi.org/10.1109/TDEI.2008.4712656

[7] L. E. Lundgaard, "Partial Discharge - Part XIII: Acoustic Partial Discharge Detection -Fundamental Considerations," *IEEE Electrical Insulation Magazine*, vol. 8, no. 4, pp. 25–31, jul 1992. [Online]. Available: https://doi.org/10.1109/57.145095

[8] M. M. Yaacob, M. A. Alsaedi, J. R. Rashed, A. M. Dakhil, and S. F. Atyah, "Review on partial discharge detection techniques related to high voltage power equipment using different sensors," pp. 325–337, dec 2014. [Online]. Available: https://doi.org/10.1007/s13320-014-0146-7

[9] Y. Tian, P. L. Lewin, A. E. Davies, S. G. Swingler, S. J. Sutton, and G. M. Hathaway, "Comparison of on-line partial discharge detection methods for HV cable joints," *IEEE Transactions on Dielectrics and Electrical Insulation*, vol. 9, no. 4, pp. 604–615, aug 2002. [Online]. Available: https://doi.org/10.1109/TDEI.2002.1024439

[10] S. S. Ghoneim and I. B. Taha, "A new approach of DGA interpretation technique for transformer fault diagnosis," *International Journal of Electrical Power and Energy Systems*, vol. 81, pp. 265–274, oct 2016. [Online]. Available: https://doi.org/10.1016/j.ijepes.2016.02.018

[11] J. Posada-Roman, J. A. Garcia-Souto, and J. Rubio-Serrano, "Fiber optic sensor for acoustic detection of partial discharges in oil-paper insulated electrical systems," *Sensors*, vol. 12, no. 4, pp. 4793–4802, 2012. [Online]. Available: https://doi.org/10.3390/s120404793

[12] P. Casals-Torrens, A. González-Parada, and R. Bosch-Tous, "Online PD detection on high voltage underground power cables by acoustic emission," in *Procedia Engineering*, vol. 35, jan 2012, pp. 22–30. [Online]. Available: https://doi.org/10.1016/j.proeng.2012.04.161

[13] P. Rohwetter, R. Eisermann, and K. Krebber, "Distributed acoustic sensing: towards partial discharge monitoring," H. J. Kalinowski, J. L. Fabris, and W. J. Bock, Eds., vol. 9634. International Society for Optics and Photonics, sep 2015, p. 96341C. [Online]. Available: https://doi.org/10.1117/12.2194850

[14] A. Masoudi and T. P. Newson, "Contributed Review: Distributed optical fibre dynamic strain sensing," *Review of Scientific Instruments*, vol. 87, no. 1, p. 011501, jan 2016. [Online]. Available: https://doi.org/10.1063/1.4939482

[15] A. K. A. K. Ghatak and K. Thyagarajan, *An introduction to fiber optics*. Cambridge University Press, 1998.

[16] S. T. Sorensen, H. Bookey, A. Shanks, and E. Buck, "Simultaneous distributed temperature and disturbance sensing in single-mode fibre for power cable monitoring," in *Fiber Optic Sensors and Applications XV*, H. H. Du, A. Mendez, and C. S. Baldwin, Eds., vol. 10654. SPIE, may 2018, p. 34. [Online]. Available: https://doi.org/10.1117/12.2304379

[17] Y. Tian, P. L. Lewin, S. J. Sutton, and S. G. Swingler, "PD characterization using short duration fourier transform of acoustic emission signals," in *Proceedings of the 2004 IEEE International Conference on Solid Dielectrics, 2004. ICSD 2004.*, vol. 2. IEEE, 2004, pp. 695–698. [Online]. Available: https://doi.org/10.1109/ICSD.2004.1350526

[18] A. Masoudi, M. Belal, and T. P. Newson, "A distributed optical fibre dynamic strain sensor based on phase-OTDR," *Measurement Science and Technology*, vol. 24, no. 8, p. 085204, aug 2013. [Online]. Available: http://stacks.iop.org/0957-0233/24/i=8/a=085204?key=crossref.d2d69f90ea4fcef40ab2889e74795108

[19] D. Iida, K. Toge, and T. Manabe, "Distributed measurement of acoustic vibration location with frequency multiplexed phase-OTDR," *Optical Fiber Technology*, vol. 36, pp. 19–25, jul 2017. [Online]. Available: https://doi.org/10.1016/j.yofte.2017.02.005

[20] G. Yang, X. Fan, Q. Liu, and Z. He, "Increasing the frequency response of direct-detection phase-sensitive OTDR by using frequency division multiplexing," Y. Chung, W. Jin, B. Lee, J. Canning, K. Nakamura, and L. Yuan, Eds., Jeju, South Korea, apr 2017, p. 103238F. [Online]. Available: http://proceedings.spiedigitallibrary.org/proceeding.aspx?doi=10.1117/12.2265632

[21] P. M. Mitchinson, P. L. Lewin, B. D. Strawbridge, and P. Jarman, "Tracking and surface discharge at the oilpressboard interface," *IEEE Electrical Insulation Magazine*, vol. 26, no. 2, pp. 35–41, mar 2010. [Online]. Available: https://doi.org/10.1109/MEI.2010.5482553

[22] R. Hussein, K. B. Shaban, and A. H. El-Hag, "Denoising of acoustic partial discharge signals corrupted with random noise," *IEEE Transactions on Dielectrics and Electrical Insulation*, vol. 23, no. 3, pp. 1453–1459, jun 2016. [Online]. Available: https://doi.org/10.1109/TDEI.2015.005532

Time Synchronised Distributed Acoustic Sensing of Partial Discharge at the Oil-Pressboard Interface

Laurie Kirkcaldy, Gareth Lees, Rosalie Rogers, Paul Lewin

***Abstract*— Distributed Acoustic Sensing (DAS) is a well-established technology used across a variety of industries. Due to its inherently low sample rates at detection ranges of a couple hundred metres or more, at face value, it appears ineffective for Partial Discharge (PD) detection and therefore has not been previously used. However, in this publication, we show that aliasing effects due to the DAS sampling methods successfully down-sample the higher frequency acoustic emissions and can provide detection of PD above 120 pC under treeing discharge across an oil-pressboard interface. This is supported with comparisons between DAS, high-sample rate acoustic sensors, as well as industry standard electrical measurements. Synchronization between the different measurement systems is achieved allowing for sample-to-sample comparison as well as a more statistical approach. We additionally show Phase Resolved Partial Discharge (PRPD) analysis can be applied to the DAS results with an additional voltage zero-crossing synchronisation signal, with a clear resemblance to electrical methods.**

***Index Terms*— Partial discharge (PD), distributed acoustic sensing (DAS), void discharge, treeing, high voltage, acoustics, acoustic emission.**

I. Introduction

Partial discharge is known to be a prominent indicator, and contributing factor, of insulation failure within high voltage equipment [1]. Many methods for detection are used today including electrical, acoustic, radio and chemical [2], [3]. However, none of these methods are able to provide long detection ranges or exact localisation of Partial Discharge (PD) events without the use of multiple costly discrete sensors [3], [4]. Fibre systems which have these long ranges of kilometres or more have been previously used for PD detection using Bragg Gratings [5] or single-ended sensors [6], typically using an interferometer system for measurement. However, this does not provide a continuous detection array and requires these sense regions to be specifically placed where detection is required.

Distributed Acoustic Sensing (DAS) provides an acoustic based method of detection, whilst also providing exact location and continuous detection distances up to many kilometres. DAS does not require a specific sensor element, it instead utilises cheap, standard single mode telecommunication fibres that may already be embedded in HV plant. As the sensing element is simply a glass fibre, it is also inherently immune to electrical or magnetic noise.

DAS, however, does have a limited sample rate, primarily due to the round-trip time of light down the fibre. Because of the sampling techniques of DAS, we demonstrate that higher frequencies like those emitted from Acoustic Emissions (AE) of PD are still able to be successfully detected, despite when the sample rate is as low as 20 kHz, achieving 5.1 km of usable detection range. The use of DAS also allows for mechanical damage detection [7] as well as fault detection [8], [9] utilising the same strain data.

DAS works on the same principles of other acoustic sensors by looking for minute vibrations and therefore strain caused by AE originating from PDs, but instead has a continuous sensing array provided by the fibre optic itself. Therefore, multiple separated sources of PD can be detected across the length of measurement simultaneously. Following on from initial proof-of-concept work with DAS as a detection method [10], this paper displays results and individual event comparisons of electrical, high bandwidth acoustic and DAS systems of treeing discharge at the oil-pressboard interface primarily used in transformers.

II. Distributed Acoustic Sensing

DAS measures the strain along a fibre optic using Rayleigh backscatter using the well understood technique of Coherent Optical Time Domain Reflectometry (c-OTDR) [11]. A highly coherent laser is pulsed launching light pulses down a single-mode fibre optic cable. Rayleigh backscatter occurs within the fibre, causing some reflection of the launched pulse back-towards the source. The backscatter is then measured by constructing an interferometer with the laser and the returning light. By measuring how this backscatter changes over successive interrogations of the fibre, strain on the fibre over time can be recorded [12], and therefore an acoustic signal is extracted. Distance information of a vibration event can be determined by comparing the time of launch to detected reflections, given the known speed of light down the fibre.

The strain changes measured for each channel or "distance bin" of measurement are not a point measurement but are integrated over a distance known as the spatial resolution or gauge length. Given the phase data from the backscatter, gauge lengths can be overlapped on top of each other for the same fibre interrogation by a distance known as the spatial sampling

Manuscript received May 03, 2022; revised May 03, 2022.

distance or channel spacing, increasing the resultant distance resolution. The gauge length is required to be long enough to obtain an optimal Signal to Noise Ratio (SNR) [13] whereas the spatial sampling distance only need to be longer than the duration of the laser pulse [14]. The DAS channel spacing used in these experiments was 1.27 m, and the gauge length was 5 m. This means for an acoustic event, the detected energy will be spread across a gauge length, but the closest channel will have the highest peak energy thereby giving a more-accurate location than the gauge length.

The sample rate of a DAS system without additional methods [15] is the round-trip time of light to the end of the fibre. Therefore, the distance limit, D, of a required sample rate, f, is given by $D = \frac{v}{2f}$, where v is the speed of light within the fibre and can be determined from the refractive index: $v = \frac{c}{n}$. $n \approx 1.47$ for a Single-Mode (SM) glass fibre. For example, at a rate of 100 kHz the maximum distance achievable is 1.02 km; at the sample rate used in these experiments of 20 kHz, the maximum distance is 5.10 km.

A. Undersampling

Whilst the DAS' sample rate is only 20 kHz, it is possible for the system to detect the presence of higher frequency acoustic signals. This occurs as, due to the interrogation of the fibre by a short laser pulse, the sample window is on the order of 10 ns [14]. Therefore, if a DAS sample window occurs during an AE signal of higher frequency, the recorded optical phase will approximately correlate to the envelope of the high frequency signal, given the window did not occur at a zero-crossing. The high frequency information of the original signal will be lost, but identification of the event occurring will be recorded [10]. This phenomenon is described as an aliasing or undersampling effect and is typically unwanted by many low-sample rate systems [16].

Additionally, due to this distortion of the originating signal, many de-noising techniques such as bandpass filtering or discrete wavelet transforms applied to other PD measurement methods are unsuitable in this application.

III. Experiment Setup and Procedure

A 5 mm thick 100x100 mm section of Weidmann Transformerboard TIV pressboard was prepared to 6% moisture content by weight and placed in an oil bath to reduce further moisture absorption. The thickness of pressboard was selected to ensure that surface discharge was the dominant degradation mechanism and the board would not mechanically fail during the experiment. The setup and procedure was designed to replicate experiments from [17] and [18], reproducing types of discharge observed within power transformers and other devices containing similar pressboard insulation. The moisture content drives how fast the degradation of the pressboard progresses and therefore is not critical in this experiment other than limiting the experiment time-frame. A needle was placed at a shallow angle to the pressboard and connected to a variable high voltage source. An earthed copper bar was perpendicularly attached 30 mm from the tip of the needle as shown in Fig. 1. This needle-bar configuration ensures that built-up charges around the needle tip are spread across the pressboard surface, rather than penetrating into the underlying bulk material [19]; therefore, preferring discharges across the surface leading to tracking discharge.The voltage was increased to the inception point of PD and allowed to progress through initial corona and surface discharge up to treeing as described in [18]. Electrical measurement was continued throughout as to monitor discharge progression. DAS, and AE were sampled at various points during the progression as to provide a variety of sampled discharge sizes.

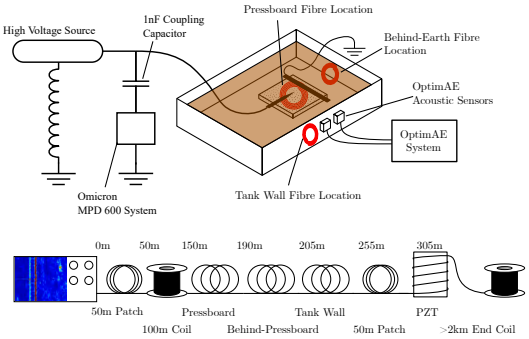

Fig. 1. Diagram of the pressboard experiment detailing fibre positions and electrical connections. The 3 fibre positions shown are: mechanically attached underneath the pressboard, suspended in oil near the tank wall and OptimAE sensors, and behind the grounding bar.

A. Electrical Partial Discharge Measurement

An industry standard Omicron MPD600 system was utilised for recording electrical events, as well as resolving the PD patterns for use of condition monitoring under IEC60270. This was also used as a measurement of the applied voltage and for analysing inception points for the PD. The maximum measured noise level up to 30 kV of the HV setup without the needle present was 12 pC, and as most discharges studied in this experiment are above 100 pC, a threshold level of 20 pC was chosen below which events were discarded. This method was chosen over a direct recording into, for example, a digital oscilloscope due to the duration of data captures required for comparison to acoustic methods.

B. Acoustic Measurement

For the measurement of acoustic signals at a high sample rate and sensitivity, an Optics11 OptimAE system was used. This was chosen over other methods as the optical measurements ensure immunity to electric and magnetic fields, and also provided a better comparison of distributed optical methods versus discrete. The OptimAE system consists of a central measurement unit and multiple sensor heads. Each measurement head is sampled separately to allow for multiple channels of independent measurement. Each chanel acts as an optical interferometer, with a Fabry–Pérot cavity [20] at the sensing end. This allows for extremely small disturbances to be measured, down to below single nanometres of movement

of the sensor head, at sample rates of one mega-sample per second (1 MS/s). A total of 3 sensors were utilised, 2 for measurement of PD, and one extra sensor for synchronisation.

C. DAS Fibre Layout

The DAS fibre layout consisted of a 100 m launch coil internal to the DAS unit, 50 m of patch cable to bring the fibre to the experimental area, an acoustically decoupled 100 m coil to reduce the background noise of the experimental section, and then alternating sections of measurement and spacing fibre. 10 m of spacing fibre were placed between measurement sections to ensure that different areas did not influence each other.

The first measurement sections bonded to the pressboard with cyanoacrylate consisted of: 5 m, 3 m and a single pass of fibre. In addition, 5 m, 3 m, 1 m and a single pass of fibre were submerged in the oil tank against the wall; next to which the high-sample rate sensors were held in place on the outside of the tank with a clamp stand and mated using ultrasonic coupling gel. This allowed for comparison event amplitudes from different fibre lengths in contact with, and separated in oil. An additional 5 m of fibre was placed behind the pressboard, still submerged in oil, but without direct line of sight of the top side of the discharge area to investigate acoustic shading effects from the pressboard compared with the other sensing areas.

The fibre path then consisted of another 50 m patch fibre into a Piezo-Electric Transducer (PZT) allowing injection of custom pulses into the DAS data at its location. Finally, a long coil (greater than 2 km in length) was used as a receive coil to ensure end reflections did not affect any measurement sections. All fibres used were SMF-28 and interrogated simultaneously with the DAS system. The coils of fibre used in measurement sections were used to increase the sensitivity at these specific points as well as provide a comparison for the different lengths of bundled fibre. An overview of the fibre connections can be found in Fig. 1.

D. Synchronisation

Synchronising the different measurement systems was achieved through manually triggered synchronisation pulses, rather than timestamp-alignment as the Omicron system does not support absolute timestamps of data. The synchronisation pulses were injected into the PD input of the electrical system and split into a pulse generator to form correctly shaped driving signals to the PZT. This also provided synchronisation to the high sample rate acoustic sensors through a mounted sensing element on the PZT.

After capture of data, these synchronisation pulses are scanned for and used to generate an offset per data capture system. These time offsets can then be subtracted lining up an absolute zero point across all data. Without this custom synchronisation, the widely different sample rates and data formats would not be able to be compared at the individual PD event level. The synchronisation achieved between systems is <1 ms and obtains a drift of less than $15\,\mathrm{ms\,h^{-1}}$. This is mostly limited by the PC-based timing jitter of the Omicron system and therefore data captures are kept under 2 minutes with synchronisation completed before each data capture to reduce the effects of this drift.

IV. Results

Partial Discharge was initiated at the needle tip causing initial surface discharges at an inception voltage of 19 kV. The pressboard was then allowed to progress through to drying stages and finally treeing under the same applied voltage after a period of an hour. Indication of the progression was monitored through the electrical system as well as observable changes on the pressboard surface: black tracking and evidence of drying seen as lighter regions of the pressboard, shown in Fig. 2. The average PD amplitude decreased to 600 pC after these observations, with peaks of 2.2 nC and rates of 120 PDs per second.

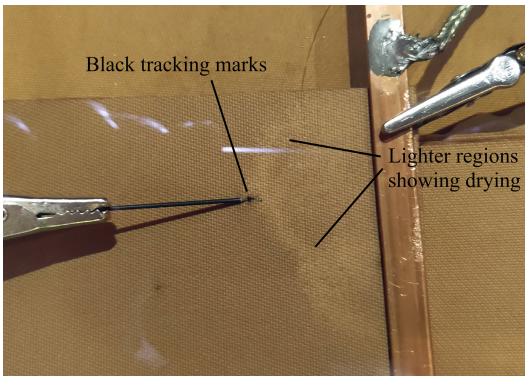

Fig. 2. Picture of the needle-bar setup on the pressboard after 1 hour of applied voltage. Black tracking marks are seen emanating from the needle tip and lighter branching regions showing drying of the pressboard.

Fig. 3 shows the high sample rate acoustic sensors, DAS output of the 3 m coil of fibre suspended in the oil near the tank wall and the reference electrical system synchronised together. The 3 m measurement section was used as it contains the best signal to noise ratio as detailed in Section IV-B. Spikes from PD events can be seen clearly to line up in all systems. A rough correlation can be observed between the amplitude of the PD and the size of the AE in the high sample rate system and DAS. Many events in this period of discharge are significantly lower in amplitude for both acoustic methods compared to the high levels seen during surface discharge [10]. This is mostly due to the position of the discharge, as well as the original AE size difference. During surface discharge the arcs form across the surface, easily transferring acoustic energy into the surrounding oil. However, for treeing discharge, most of the acoustic energy is contained in the bulk of the material. Pressboard due to its composite composition is an excellent damping material, absorbing acoustic energy and therefore attenuating the resultant acoustic amplitude.

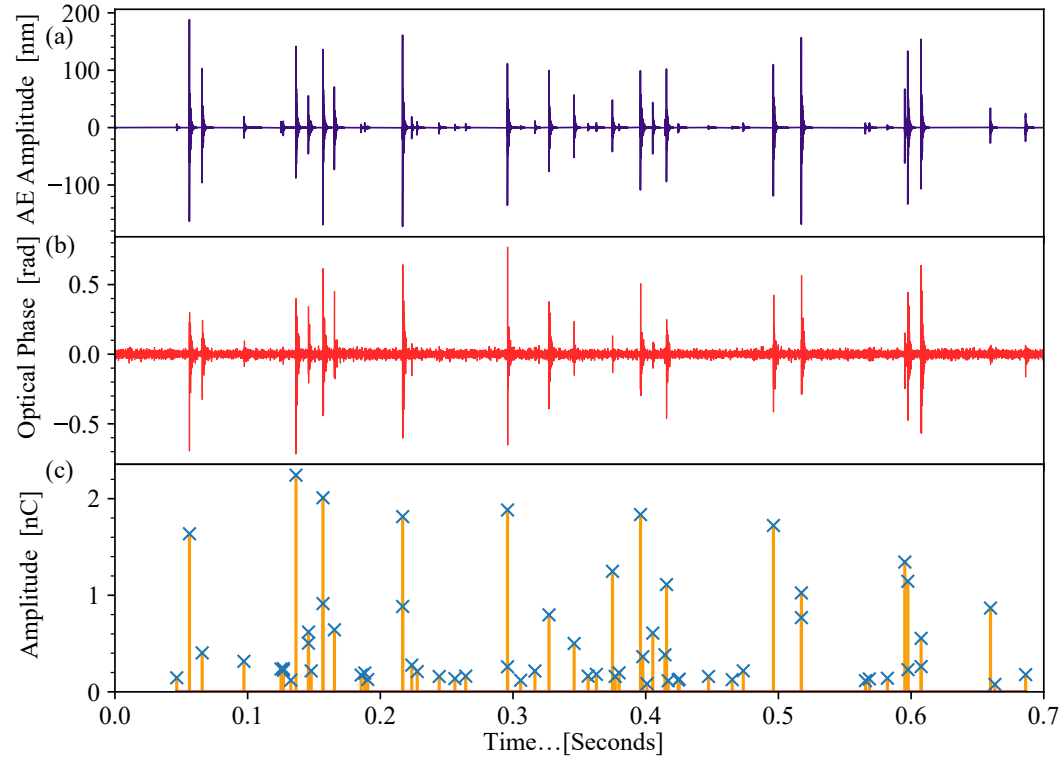

Fig. 3. Amplitude of Acoustic Emissions in purple, as measured by the acoustic sensor. Measured in displacement of sensor element. (b) Optical phase output of the DAS system in red, corresponding to the 5 m coil of fibre suspended in oil next to the OptimAE sensor. (c) Absolute amplitude of PD events in amber, as measured by the electrical system. As the events recorded by the electrical system are not continuous, the crosses indicate partial discharge events with the vertical lines added for better clarity.

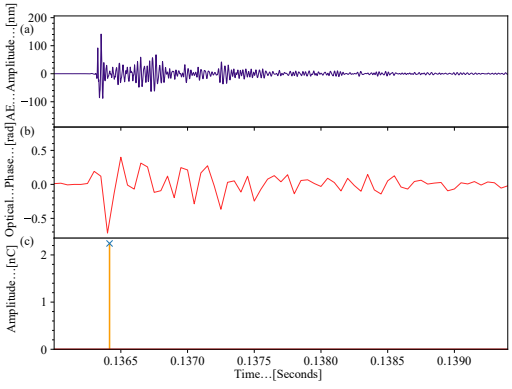

Fig. 4. Zoomed in detail of a PD event from Figure 3. (a) Amplitude of Acoustic Emissions in purple, as measured by the Optics11 OptimAE sensor. Measured in displacement of sensor element. (b) Optical phase output of the DAS system in red, corresponding to the 5 m coil of fibre suspended in oil next to the OptimAE sensor. (c) Absolute amplitude of PD events in amber, as measured by the Omicron MPD600 system.

Looking at a single event from Fig. 3 at 136.4 ms in more detail (Fig. 4), the AE impulse followed by ringing is seen by both acoustic systems, albeit with distortion in the DAS due to undersampling. The damped ringing after the initial impulse is from reflections off the geometry of the surrounding materials. The lower sample rate DAS maintains following the envelope of the source AE and picks up the initial higher amplitude spike.

In this initial data capture, PDs under 500 pC in amplitude are rarely seen in the DAS data, and corresponding peaks in the AE sensors are orders of magnitude smaller. After 30 minutes of further treeing discharge, the larger PDs of over 500 pC stop occurring as the surrounding area from the needle dries out and tracking at the branch tips becomes the primary discharge. During the following discharge, lower amplitude events that were not previously seen in the DAS increase in number. Fig. 5 shows these events with similar features to the previous PDs.

The peak amplitude of these events in the DAS data is much closer to the noise floor due to the AE being smaller in amplitude as seen by the discrete sensors, with the smallest repeatable event with a noticeable change in strain of a PD

amplitude of approximately 120 pC. These peaks dropping below the noise floor, however, do not constitute the minimum sensitivity. For example, at 70 ms and 150 ms in Fig. 5 PD events of 200 pC and 300 pC both register the same peak DAS amplitude of 0.9 rad. This is because the sampling window of the DAS misses the initial spike and only picks up later ringing. As the size of the AE is quite small, only the first few microseconds of the impulse are large enough to produce a measurable DAS output, and therefore DAS can detect these smaller events but only if the sampling window happens to line up with the initial spike. This demonstrates an important undersampling effect resulting in the DAS amplitude not always representing the true AE size, and therefore the origin PD amplitude. By taking multiple events into account rather than focussing on individual events, a trend can be established from the peaks of DAS data.

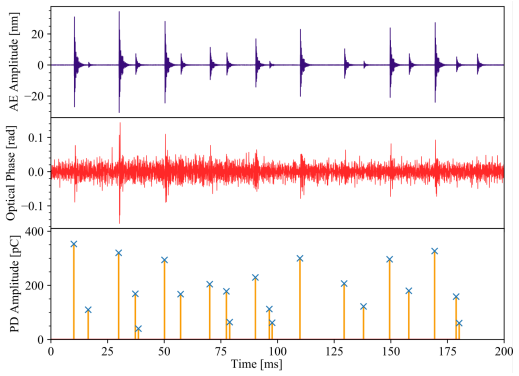

Fig. 5. Amplitude of PDs from the acoustic sensors, DAS and electrical systems during later treeing discharge, time synchronized. Peak PD amplitudes of 380 pC and rates of 95 PDs/s.

A. PRPD Analysis of DAS

By triggering the PZT used for synchronisation from a zero-crossing detector referenced to the high voltage source during data capture, the voltage phase can be determined for each spike seen in the DAS. This turns the DAS data from a continuous-time optical phase data capture into a list of PD events with associated time and voltage phase. By plotting these events in a scatter plot, the DAS-detected PD events can have PRPD analysis applied.

Fig. 6 shows the PRPD plot generated from the DAS data for a 100 second data capture of pressboard discharge. In comparison, an Omicron generated plot of the same measurement period generated from the electrical measurement is shown on the right. Both plots clearly show similar patterns with increased intensity of lower amplitude discharge in the positive half-cycle in addition to higher peak values, and less amplitude of discharge on the negative cycle. PRPD analysis also allows for some separation of noise and discharge events: noise will appear with no correlation across the plot, whereas discharge events tend to occur in specific patterns relative to the AC waveform.

B. Comparison of Sensing Locations

As previously mentioned, data was also recorded from different lengths of test fibre in contact with the pressboard and submerged in the oil tank to investigate the effect of fibre shorter than the gauge length on the resultant event amplitude. Fig. 7 shows PD events from all fibre sections during treeing discharge. All 3 positions of fibre (in contact with, behind pressboard and by tank wall) detect the incident AE, with the highest amplitudes observed in the fibre by the tank wall. This is again due to the AE being absorbed within the pressboard, and therefore the fibres mechanically mounted on the bottom of the pressboard experiencing less strain change.

Regions consisting of less than 3 m of sense fibre have a significantly reduced maximum amplitude compared to other

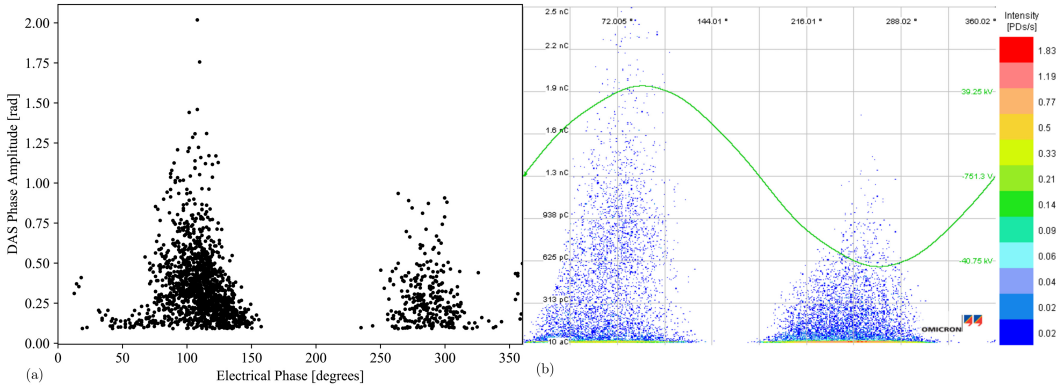

Fig. 6. PRPD plots of the DAS (a) and electrical (b) systems. A strong correlation between the two graphs can be seen with higher amplitude events occurring in the positive half-cycle. The DAS shows fewer detected events in the negative half-cycle, possibly due to reduced PD amplitude resulting in more events below the noise floor.

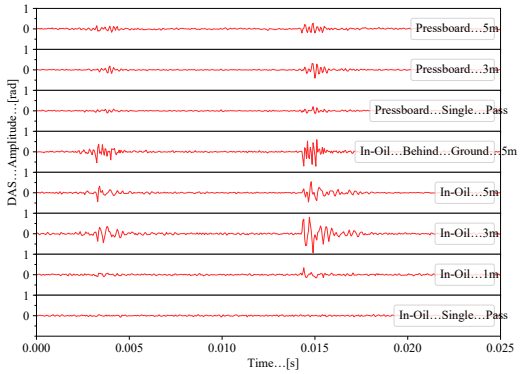

Fig. 7. Comparison of different DAS amplitude at different fibre positions and lengths of sense fibre. 2 Partial Discharge events seen. A single pass refers to a length of around 15 cm, enough for the fibre to enter and exit the oil at the specified position.

locations, with the 3 m sections appearing to experience the highest strain change. The significant reduction in amplitude appears to occur at the transition between 3 m and below, at approximately half the gauge length (2.5 m). The 5 m sections, despite having the greatest coiled length covering exactly a gauge length, shows a lower amplitude than the 3 m. This is either due to the larger coil of fibre creating a larger acoustic impedance change, or cancellation effects from the averaging across the gauge length.

The position of fibre behind the pressboard was not in line of sight to the top surface of the pressboard. Therefore as a significant strain change is observed, this demonstrates AE can still be detected from the diffraction and reverberation off surrounding materials without a clear line of sight, given no absorptive materials are in the wave path from source to sensing fibre.

V. Conclusion

This research has demonstrated that partial discharge detection can be achieved using DAS down to PD amplitudes of 120 pC during treeing discharge. Due to the fibre interrogation method, locations of these events are inherently known. The unique undersampling processes with DAS are shown to allow low sample rate DAS systems to be able to detect the high frequency AE produced by PDs. Given the current requirement for a repeated segment of fibre, at least half the gauge length, and the range of detectable PD, the authors believe this DAS method is currently best suited for application of detection of PDs within high voltage transformers. As no discrete sensors are required, continuous fibres could easily be wound within windings, or utilise existing temperature sensing fibres, providing useful detection and pinpointing within the transformer of partial discharge events despite tank reverberations due to the continuous fibre optic providing proximity to possible discharge sites. Analysis techniques such as PRPD can also be utilised given a zero-crossing synchronisation signal is also recorded alongside the optical data.

Acknowledgments

The support from APSensing and the lab technicians at the Tony Davies High Voltage Laboratory is greatly appreciated, along with thanks given to Optics11 for the generous loan of an interferometer based acoustic sensing solution: OptimAE.

References

[1] S. A. Boggs, "Partial Discharge: Overview and Signal Generation," *IEEE Electrical Insulation Magazine*, vol. 6, no. 4, pp. 33–39, 1990. [Online]. Available: https://doi.org/10.1109/57.63057

[2] Y. Tian, P. L. Lewin, J. S. Wilkinson, S. J. Sutton, and S. G. Swingler, "Continuous on-line monitoring of partial discharges in high voltage cables," in *Conference Record of IEEE International Symposium on Electrical Insulation*, 2004, pp. 454–457. [Online]. Available: https://doi.org/10.1109/elinsl.2004.1380640

[3] M. M. Yaacob, M. A. Alsaedi, J. R. Rashed, A. M. Dakhil, and S. F. Atyah, "Review on partial discharge detection techniques related to high voltage power equipment using different sensors," *Photonic Sensors*, vol. 4, no. 4, pp. 325–337, dec 2014. [Online]. Available: https://doi.org/10.1007/s13320-014-0146-7

[4] N. Saravanakumar and K. Sathiyasekar, "Circular Array of Ultrasonic Sensor based DOA estimation: Location of multiple Partial Discharge in Transformer oil," *Journal of Electromagnetic Waves and Applications*, vol. 32, no. 12, pp. 1569–1585, aug 2018. [Online]. Available: https://doi.org/10.1080/09205071.2018.1456365

[5] M. R. Hussain, S. S. Refaat, and H. Abu-Rub, "Overview and Partial Discharge Analysis of Power Transformers: A Literature Review," pp. 64 587–64 605, 2021. [Online]. Available: https://doi.org/10.1109/ACCESS.2021.3075288

[6] J. Deng, H. Xiao, W. Huo, M. Luo, R. May, A. Wang, and Y. Liu, "Optical fiber sensor-based detection of partial discharges in power transformers," *Optics and Laser Technology*, vol. 33, no. 5, pp. 305–311, jul 2001. [Online]. Available: https://doi.org/10.1016/S0030-3992(01)00022-6

[7] K. Hicke and K. Krebber, "Towards efficient real-time submarine power cable monitoring using distributed fibre optic acoustic sensors," in *25th International Conference on Optical Fiber Sensors*, vol. 10323. SPIE, apr 2017, p. 1032390. [Online]. Available: https://doi.org/10.1117/12.2267474

[8] G. Ma, W. Qin, C. Shi, H. Zhou, Y. Li, and C. Li, "Electrical Discharge Localization for Gas Insulated Line Based on Distributed Acoustic Sensing," in *Lecture Notes in Electrical Engineering*. Springer, 2020, vol. 598 LNEE, pp. 606–614. [Online]. Available: https://doi.org/10.1007/978-3-030-31676-1{_}57

[9] S. Cherukupalli and G. J. Anders, "Use of Distributed Sensing for Strain Measurement and Acoustic Monitoring in Power Cables," in *Distributed Fiber Sensing and Dynamic Rating of Power Cables*, 1st ed. Wiley, sep 2019, ch. 11, pp. 185–209. [Online]. Available: https://doi.org/10.1002/9781119487739.ch11

[10] L. Kirkcaldy, P. Lewin, G. Lees, and R. Rogers, "Partial Discharge Detection Using Distributed Acoustic Sensing at the Oil-Pressboard Interface," in *IEEE Sensors Applications Symposium*, Virtual, 2021.

[11] A. Masoudi and T. P. Newson, "Contributed Review: Distributed optical fibre dynamic strain sensing," *Review of Scientific Instruments*, vol. 87, no. 1, p. 011501, jan 2016. [Online]. Available: https://doi.org/10.1063/1.4939482

[12] A. Masoudi, M. Belal, and T. P. Newson, "A distributed optical fibre dynamic strain sensor based on phase-OTDR," *Measurement Science and Technology*, vol. 24, no. 8, p. 085204, aug 2013. [Online]. Available: https://doi.org/10.1088/0957-0233/24/8/085204

[13] H. Gabai and A. Eyal, "On the sensitivity of distributed acoustic sensing," *Optics Letters*, vol. 41, no. 24, p. 5648, dec 2016. [Online]. Available: https://doi.org/10.1364/ol.41.005648

[14] A. Mateeva, J. Lopez, H. Potters, J. Mestayer, B. Cox, D. Kiyashchenko, P. Wills, S. Grandi, K. Hornman, B. Kuvshinov, W. Berlang, Z. Yang, and R. Detomo, "Distributed acoustic sensing for reservoir monitoring with vertical seismic profiling," *Geophysical Prospecting*, vol. 62, no. 4, pp. 679–692, jul 2014. [Online]. Available: https://doi.org/10.1111/1365-2478.12116

[15] G. Yang, X. Fan, Q. Liu, and Z. He, "Increasing the frequency response of direct-detection phase-sensitive OTDR by using frequency division multiplexing," in *25th International Conference on Optical Fiber Sensors*, Y. Chung, W. Jin, B. Lee, J. Canning, K. Nakamura, and

L. Yuan, Eds., vol. 10323, Jeju, South Korea, apr 2017, p. 103238F. [Online]. Available: https://doi.org/10.1117/12.2265632

[16] V. Lesnikov, T. Naumovich, A. Chastikov, and D. Garsh, "Unaliasing of undersampled spectra," in *2016 Mediterranean Conference on Embedded Computing*. Institute of Electrical and Electronics Engineers Inc., jul 2016, pp. 124–127. [Online]. Available: https://doi.org/10.1109/MECO.2016.7525719

[17] H. Zainuddin, P. L. Lewin, and P. M. Mitchinson, "Partial discharge characteristics of surface tracking on oil-impregnated pressboard under AC voltages," in *Proceedings of IEEE International Conference on Solid Dielectrics, ICSD*, 2013, pp. 1016–1019.

[18] P. M. Mitchinson, P. L. Lewin, G. Chen, and P. N. Jarman, "A new approach to the study of surface discharge on the oil-pressboard interface," in *2008 IEEE International Conference on Dielectric Liquids, ICDL 2008*, 2008.

[19] P. M. Mitchinson, P. L. Lewin, B. D. Strawbridge, and P. Jarman, "Tracking and surface discharge at the oilpressboard interface," *IEEE Electrical Insulation Magazine*, vol. 26, no. 2, pp. 35–41, mar 2010. [Online]. Available: https://doi.org/10.1109/MEI.2010.5482553

[20] G. Hernandez, *Fabry-Perot interferometers*, 1st ed. Cambridge University Press, 1988.

References

[1] E. C. R. Bascom, M. J. Von Herrmann, T. Zhao, M. J. V. Herrmann, and Tiebin (Tom) Zhao, "Power cable failure modes and fault location methods, practices and strategies," in *IEEE PES T&D Conference and Exposition*. Institute of Electrical and Electronics Engineers Inc., jul 2014, pp. 1–5. [Online]. Available: https://doi.org/10.1109/TDC.2014.6863514

[2] M. Bawart, M. Marzinotto, and G. Mazzanti, "Diagnosis and location of faults in submarine power cables," *IEEE Electrical Insulation Magazine*, vol. 32, no. 4, pp. 24–37, jul 2016. [Online]. Available: https://doi.org/10.1109/MEI.2016.7528987

[3] V. Sokolov, "Understanding failure modes of transformers," Tech. Rep., 2005.

[4] I. Sadeghi, H. Ehya, R. N. Zarandi, J. Faiz, and A. A. S. Akmal, "Condition Monitoring of Large Electrical Machine under Partial Discharge Fault - A review," in *2018 International Symposium on Power Electronics, Electrical Drives, Automation and Motion (SPEEDAM)*. IEEE, jun 2018, pp. 216–223. [Online]. Available: https://doi.org/10.1109/SPEEDAM.2018.8445261

[5] M. M. Yaacob, M. A. Alsaedi, J. R. Rashed, A. M. Dakhil, and S. F. Atyah, "Review on partial discharge detection techniques related to high voltage power equipment using different sensors," *Photonic Sensors*, vol. 4, no. 4, pp. 325–337, dec 2014. [Online]. Available: https://doi.org/10.1007/s13320-014-0146-7

[6] Y. Tian, P. L. Lewin, A. E. Davies, S. G. Swingler, S. J. Sutton, and G. M. Hathaway, "Comparison of on-line partial discharge detection methods for HV cable joints," *IEEE Transactions on Dielectrics and Electrical Insulation*, vol. 9, no. 4, pp. 604–615, aug 2002. [Online]. Available: https://doi.org/10.1109/TDEI.2002.1024439

[7] P. Casals-Torrens, A. González-Parada, and R. Bosch-Tous, "Online PD detection on high voltage underground power cables by acoustic emission," in *Procedia Engineering*, vol. 35, jan 2012, pp. 22–30. [Online]. Available: https://doi.org/10.1016/j.proeng.2012.04.161

[8] F. Álvarez, F. Garnacho, J. Ortego, and M. Á. Sánchez-Urán, "Application of HFCT and UHF sensors in on-line partial discharge measurements for insulation diagnosis of high voltage equipment," *Sensors (Switzerland)*, vol. 15, no. 4, pp. 7360–7387, mar 2015. [Online]. Available: https://www.mdpi.com/1424-8220/15/4/7360/htmhttps://www.mdpi.com/1424-8220/15/4/7360

[9] M. Tozzi, "Department of Electrical Engineering Partial Discharges in Power Distribution Electrical Systems : Pulse Propagation Models and," Ph.D. dissertation, University of Bologna, 2010. [Online]. Available: https://core.ac.uk/download/pdf/11012459.pdf

[10] Z. Li, L. Luo, N. Zhou, G. Sheng, and X. Jiang, "A novel partial discharge localization method in substation based on a wireless UHF sensor array," *Sensors (Switzerland)*, vol. 17, no. 8, p. 1909, aug 2017. [Online]. Available: https://doi.org/10.3390/s17081909

[11] K. Wang and K. Kopsidas, "Modelling Network Reliability Considering Underground Cable Hot Spot Failures," in *2020 International Conference on Probabilistic Methods Applied to Power Systems, PMAPS 2020 - Proceedings*. Institute

of Electrical and Electronics Engineers Inc., aug 2020. [Online]. Available: https://doi.org/10.1109/PMAPS47429.2020.9183388

[12] J. Downes and H. Y. Leung, "Distributed temperature sensing worldwide power circuit monitoring applications," in *2004 International Conference on Power System Technology, POWERCON 2004*, vol. 2, 2004, pp. 1804–1809.

[13] M. Harbaji, K. Shaban, and A. El-Hag, "Classification of common partial discharge types in oil-paper insulation system using acoustic signals," *IEEE Transactions on Dielectrics and Electrical Insulation*, vol. 22, no. 3, pp. 1674–1683, jun 2015. [Online]. Available: https://doi.org/10.1109/TDEI.2015.7116364

[14] R. E. James and Q. Su, *Condition assessment of high voltage insulation in power system equipment*, 2008. [Online]. Available: https://doi.org/10.1049/PBPO053E

[15] S. Karmakar and S. Mishra, "Detection of partial discharges and its effect on solid insulation used in high voltage cable," in *2015 International Conference on Condition Assessment Techniques in Electrical Systems, CATCON 2015 - Proceedings*, 2016, pp. 204–208. [Online]. Available: https://doi.org/10.1109/CATCON.2015.7449535

[16] B. Howarth, M. Coates, and L. Renforth, "Fault Location Techniques for One of the World's Longest AC Interconnector Cables," *8th IEE International Conference on AC and DC Power Transmission*, pp. 14–18, 2006. [Online]. Available: https://doi.org/10.1049/cp:20060004

[17] G. Koperundevi, M. K. Goyal, S. Das, N. K. Roy, and R. Sarathi, "Classification of incipient discharges in transformer insulation using acoustic emission signatures," in *Proceedings of the 2010 Annual IEEE India Conference: Green Energy, Computing and Communication, INDICON 2010*, 2010. [Online]. Available: https://doi.org/10.1109/INDCON.2010.5712640

[18] M. Wu, H. Cao, J. Cao, H. L. Nguyen, J. B. Gomes, and S. P. Krishnaswamy, "An overview of state-of-the-art partial discharge analysis techniques for condition monitoring," *IEEE Electrical Insulation Magazine*, vol. 31, no. 6, pp. 22–35, nov 2015. [Online]. Available: https://doi.org/10.1109/MEI.2015.7303259

[19] S. A. Boggs, "Partial Discharge: Overview and Signal Generation," *IEEE Electrical Insulation Magazine*, vol. 6, no. 4, pp. 33–39, 1990. [Online]. Available: https://doi.org/10.1109/57.63057

[20] R. Bartnikas, "Partial discharges their mechanism, detection and measurement," *IEEE Transactions on Dielectrics and Electrical Insulation*, vol. 9, no. 5, pp. 763–808, oct 2002. [Online]. Available: https://doi.org/10.1109/TDEI.2002.1038663

[21] R. J. Van Brunt, "Stochastic Properties of Partial-discharge Phenomena," *IEEE Transactions on Electrical Insulation*, vol. 26, no. 5, pp. 902–948, 1991. [Online]. Available: https://doi.org/10.1109/14.99099

[22] A. Masoudi and T. P. Newson, "Contributed Review: Distributed optical fibre dynamic strain sensing," *Review of Scientific Instruments*, vol. 87, no. 1, p. 011501, jan 2016. [Online]. Available: https://doi.org/10.1063/1.4939482

[23] B. G. Gorshkov, K. Yüksel, A. A. Fotiadi, M. Wuilpart, D. A. Korobko, A. A. Zhirnov, K. V. Stepanov, A. T. Turov, Y. A. Konstantinov, and I. A. Lobach, "Scientific Applications of Distributed Acoustic Sensing: State-of-the-Art Review and Perspective," *Sensors*, vol. 22, no. 3, p. 1033, jan 2022. [Online]. Available: https://doi.org/10.3390/S22031033

[24] I. Lior, A. Sladen, D. Rivet, J. P. Ampuero, Y. Hello, C. Becerril, H. F. Martins, P. Lamare, C. Jestin, S. Tsagkli, and C. Markou, "On the Detection Capabilities of Underwater Distributed Acoustic Sensing," *Journal of Geophysical Research: Solid Earth*, vol. 126, no. 3, p. e2020JB020925, mar 2021. [Online]. Available: https://doi.org/10.1029/2020JB020925

[25] C. Wang, M. Olson, B. Sherman, N. Dorjkhand, J. Mehr, and S. Singh, "Reliable Leak Detection in Pipelines Using Integrated DdTS Temperature and das Acoustic

Fiber-Optic Sensor," in *Proceedings - International Carnahan Conference on Security Technology*, vol. 2018-Octob. Institute of Electrical and Electronics Engineers Inc., dec 2018. [Online]. Available: https://doi.org/10.1109/CCST.2018.8585687

[26] H. Illias, G. Chen, and P. Lewin, "Partial discharge behavior within a spherical cavity in a solid dielectric material as a function of frequency and amplitude of the applied voltage," *IEEE Transactions on Dielectrics and Electrical Insulation*, vol. 18, no. 2, pp. 432–443, apr 2011. [Online]. Available: https://doi.org/10.1109/TDEI.2011.5739447

[27] R. J. Van Brunt, "Physics and Chemistry of Partial Discharge and Corona: Recent Advances and Future Challenges," *IEEE Transactions on Dielectrics and Electrical Insulation*, vol. 1, no. 5, pp. 761–784, 1994. [Online]. Available: https://doi.org/10.1109/94.326651

[28] V. O'Byrne, D. Kokkinos, D. Meis, D. Piehler, F. Coppinger, and L. Pender, "UPC vs. APC Connector Performance in Passive Optical Networks," in *Optical Fiber Communication Conference and Exposition and The National Fiber Optic Engineers Conference*. Optical Society of America, 2005, p. NTuF3. [Online]. Available: http://www.osapublishing.org/abstract.cfm?URI=NFOEC-2005-NTuF3

[29] M. Kannan and P. P. Sreejaya, "Partial Discharge Detection in Solid Dielectrics," *International Journal of Scientific & Engineering Research*, vol. 4, no. 8, p. 6, 2013.

[30] M. Pompili, C. Mazzetti, and E. O. Forster, "Partial Discharge Distributions in Liquid Dielectrics," *IEEE Transactions on Electrical Insulation*, vol. 27, no. 1, pp. 99–105, 1992. [Online]. Available: https://doi.org/10.1109/14.123445

[31] J. C. Devins, "The Physics of Partial Discharges in Solid Dielectrics," in *Conference on Electrical Insulation and Dielectric Phenomena (CEIDP), Annual Report.* IEEE, 1984, pp. 15–31. [Online]. Available: https://doi.org/10.1109/eidp.1984.7683959

[32] J. Deng, S. Matsuoka, A. Kumada, and K. Hidaka, "The influence of residual charge on surface discharge propagation," *Journal of Physics D: Applied Physics*, vol. 43, no. 49, p. 495203, nov 2010. [Online]. Available: https://doi.org/10.1088/0022-3727/43/49/495203

[33] G. Callender, I. O. Golosnoy, P. Rapisarda, and P. L. Lewin, "Critical analysis of partial discharge dynamics in air filled spherical voids," *Journal of Physics D: Applied Physics*, vol. 51, no. 12, p. 125601, mar 2018. [Online]. Available: https://doi.org/10.1088/1361-6463/aaae7c

[34] H. A. Illias, G. Chen, and P. L. Lewin, "The influence of spherical cavity surface charge distribution on the sequence of partial discharge events," *Journal of Physics D: Applied Physics*, vol. 44, no. 24, p. 245202, jun 2011. [Online]. Available: https://doi.org/10.1088/0022-3727/44/24/245202

[35] T. Bai, "Degradation Processes of Voids in Solid Dielectrics under AC Applied Fileds," Ph.D. dissertation, University of Southampton, 2013. [Online]. Available: https://eprints.soton.ac.uk/361731/1/Bai.pdf

[36] F. Gutfieisch and L. Niemeyer, "Measurement and Simulation of PD in Epoxy Voids," *IEEE Transactions on Dielectrics and Electrical Insulation*, vol. 2, no. 5, pp. 729–743, 1995. [Online]. Available: https://doi.org/10.1109/94.469970

[37] N. G. Trinh, "Partial Discharge XIX: Discharge in Air Part I: Physical Mechanisms," *IEEE Electrical Insulation Magazine*, vol. 11, no. 2, pp. 23–29, 1995. [Online]. Available: https://doi.org/10.1109/MEI.1995.1025997

[38] H. Illias, Teo Soon Yuan, A. H. A. Bakar, H. Mokhlis, G. Chen, and P. L. Lewin, "Partial discharge patterns in high voltage insulation," in *PECon 2012 - 2012 IEEE International Conference on Power and Energy*, 2012, pp. 750–755. [Online]. Available: https://doi.org/10.1109/PECON.2012.6450316

[39] N. Fujimoto, S. Rizzetto, and J. M. Braun, "Partial Discharge - Part XV: Improved PD Testing of Solid Dielectrics Using X-Ray Induced Discharge Initiation," *IEEE Electrical Insulation Magazine*, vol. 8, no. 6, pp. 33–41, 1992. [Online]. Available: https://doi.org/10.1109/57.168890

[40] C. Hudon and M. Bélec, "Partial discharge signal interpretation for generator diagnostics," *IEEE Transactions on Dielectrics and Electrical Insulation*, vol. 12, no. 2, pp. 297–319, apr 2005. [Online]. Available: https://doi.org/10.1109/TDEI.2005.1430399

[41] T. Okamoto and T. Tanaka, "Novel partial discharge measurement computer-aided measurement systems," *IEEE Transactions on Electrical Insulation*, vol. EI-21, no. 6, pp. 1015–1019, 1986. [Online]. Available: https://doi.org/10.1109/TEI.1986.349017

[42] N. H. Ahmed and N. N. Srinivas, "On-line partial discharge detection in cables," *IEEE Transactions on Dielectrics and Electrical Insulation*, vol. 5, no. 2, pp. 181–188, 1998. [Online]. Available: https://doi.org/10.1109/94.671927

[43] E. Gulski, "Digital Analysis of Partial Discharges," *IEEE Transactions on Dielectrics and Electrical Insulation*, vol. 2, no. 5, pp. 822–837, 1995. [Online]. Available: https://doi.org/10.1109/94.469977

[44] Y. Tian, P. L. Lewin, J. S. Wilkinson, S. J. Sutton, and S. G. Swingler, "Continuous on-line monitoring of partial discharges in high voltage cables," in *Conference Record of IEEE International Symposium on Electrical Insulation*, 2004, pp. 454–457. [Online]. Available: https://doi.org/10.1109/elinsl.2004.1380640

[45] Y. Tian, P. L. Lewin, A. E. Davies, and G. M. Hathaway, "Acoustic emission techniques for partial discharge detection within cable insulation," in *Dielectric Materials, Measurements and Applications, 2000. Eighth International Conference on (IEE Conf. Publ. No. 473)*, vol. 2000. IEE, 2000, pp. 503–508. [Online]. Available: https://doi.org/10.1049/cp:20000560

[46] A. S. Deshpande, H. A. Mangalvedekar, and A. N. Cheeran, "Partial discharge analysis using energy patterns," *International Journal of Electrical Power and Energy Systems*, vol. 53, no. 1, pp. 184–195, 2013. [Online]. Available: http://doi.org/10.1016/j.ijepes.2013.04.015

[47] L. E. Lundgaard, "Partial Discharge - Part XIII: Acoustic Partial Discharge Detection -Fundamental Considerations," *IEEE Electrical Insulation Magazine*, vol. 8, no. 4, pp. 25–31, jul 1992. [Online]. Available: https://doi.org/10.1109/57.145095

[48] L. E. Lundgaard and Norweigian Electric Power Research Institute, "Partial Discharge - Part XIV: Acoustic Partial Discharge Detection - Practical Application," *IEEE Electrical Insulation Magazine*, vol. 8, no. 5, pp. 34–43, sep 1992. [Online]. Available: https://doi.org/10.1109/57.156943

[49] P. Kundu, N. K. Kishore, and A. K. Sinha, "Classification of acoustic emission based partial discharge in oil pressboard insulation system using wavelet analysis," in *Annual Report - Conference on Electrical Insulation and Dielectric Phenomena, CEIDP*, 2010. [Online]. Available: https://doi.org/10.1109/CEIDP.2010.5724085

[50] Y. Tian, P. L. Lewin, S. J. Sutton, and S. G. Swingler, "PD characterization using short duration fourier transform of acoustic emission signals," in *Proceedings of the 2004 IEEE International Conference on Solid Dielectrics, 2004. ICSD 2004.*, vol. 2. IEEE, 2004, pp. 695–698. [Online]. Available: https://doi.org/10.1109/ICSD.2004.1350526

[51] E. A. Cherney, "Partial Discharge - Part V: PD in Polymer-type Line Insulators," *IEEE Electrical Insulation Magazine*, vol. 7, no. 2, pp. 28–32, 1991. [Online]. Available: https://doi.org/10.0.4.85/57.75766

[52] G. Paoletti and A. Golubev, "Partial discharge theory and applications to electrical systems," *IEEE Conference Record of Annual Pulp and Paper Industry Technical Conference*, pp. 124–138, 1999. [Online]. Available: https://doi.org/10.1109/PAPCON.1999.779355

[53] G. J. Paoletti, "Partial discharge theory and technologies related to medium-voltage electrical equipment," *IEEE Transactions on Industry Applications*, vol. 37, no. 1, pp. 90–103, jan 2001. [Online]. Available: https://doi.org/10.1109/28.903131

[54] W. G. Moore and A. Khazanov, "Insulation degradation in Generator stator bars due to spark erosion and partial discharge damage," in *Conference Record of IEEE International Symposium on Electrical Insulation*, 2010. [Online]. Available: https://doi.org/10.1109/ELINSL.2010.5549794

[55] P. H. Morshuis, "Degradation of solid dielectrics due to internal partial discharge: Some thoughts on progress made and where to go now," *IEEE Transactions on Dielectrics and Electrical Insulation*, vol. 12, no. 5, pp. 905–913, oct 2005. [Online]. Available: https://doi.org/10.1109/TDEI.2005.1522185

[56] M. Farahani, H. Borsi, E. Gockenbach, and M. Kaufhold, "Partial discharge and dielectric response behaviour of insulation systems for high voltage rotating machines under electrical stress," in *Annual Report - Conference on Electrical Insulation and Dielectric Phenomena, CEIDP*, 2004, pp. 271–274. [Online]. Available: https://doi.org/10.1109/ceidp.2004.1364240

[57] British Standard, "High-voltage test techniques-Partial discharge measurements BS EN 60270:2001+A1:2016," Tech. Rep., 2001.

[58] T. Tanaka, "Internal partial discharge and material degradation," *IEEE Transactions on Electrical Insulation*, vol. EI-21, no. 6, pp. 899–905, 1986. [Online]. Available: https://doi.org/10.1109/TEI.1986.348999

[59] K. Wu, Y. Suzuoki, T. Mizutani, and H. Xie, "Model for partial discharges associated with treeing breakdown: III. PD extinction and re-growth of tree," *Journal of Physics D: Applied Physics*, vol. 33, no. 10, pp. 1209–1218, may 2000. [Online]. Available: https://doi.org/10.1088/0022-3727/33/10/312

[60] Y. Ehara, M. Naoe, K. Urano, H. Kishida, M. Matsuyama, and T. Ito, "Fractal analysis of the treeing process from luminous discharge image and measurement of discharge magnitude," *IEEE Transactions on Dielectrics and Electrical Insulation*, vol. 5, no. 5, pp. 728–733, 1998. [Online]. Available: https://doi.org/10.1109/94.729695

[61] R. Vogelsang, B. Fruth, T. Farr, and K. Fröhlich, "Detection of electrical tree propagation by partial discharge measurements," in *European Transactions on Electrical Power*, vol. 15, no. 3. John Wiley & Sons, Ltd, may 2005, pp. 271–284. [Online]. Available: https://doi.org/10.1002/etep.60

[62] L. Niemeyer, "A Generalized Approach to Partial Discharge Modeling," *IEEE Transactions on Dielectrics and Electrical Insulation*, vol. 2, no. 4, pp. 510–528, 1995. [Online]. Available: https://doi.org/10.1109/94.407017

[63] F. Grum and L. F. Costa, "Spectral emission of corona discharges," *Applied Optics*, vol. 15, no. 1, p. 76, jan 1976. [Online]. Available: https://doi.org/10.1364/ao.15.000076

[64] D. A. Nattrass, "Partial Discharge Measurement and Interpretation," *IEEE Electrical Insulation Magazine*, vol. 4, no. 3, pp. 10–23, 1988. [Online]. Available: https://doi.org/10.1109/57.830

[65] A. A. Mas'ud, R. Albarracín, J. A. Ardila-Rey, F. Muhammad-Sukki, H. A. Illias, N. A. Bani, and A. B. Munir, "Artificial neural network application for partial discharge recognition: Survey and future directions," p. 574, jul 2016. [Online]. Available: https://doi.org/10.3390/en9080574

[66] H. A. Illias, G. Chen, and P. L. Lewin, "Partial discharge measurements for spherical cavities within solid dielectric materials under different stress and cavity conditions," in *Annual Report - Conference on Electrical Insulation and Dielectric Phenomena, CEIDP*, 2009, pp. 388–391. [Online]. Available: https://doi.org/10.1109/CEIDP.2009.5377831

[67] X. Zhou, P. Werle, E. Gockenbach, H. Shi, and M. Kuhnke, "Study of Oil/Pressboard Creeping Discharges under Divergent AC Voltage - Part 1: Fundamental Phenomena and Influencing Factors," *IEEE Transactions on Dielectrics and Electrical Insulation*, vol. 28, no. 2, pp. 355–363, apr 2021. [Online]. Available: https://doi.org/10.1109/TDEI.2020.009196

[68] M. M. Mohsin, M. N. Narayanachar, and R. S. Nema, "Study of partial discharge characteristics in oil impregnated pressboard insulation," in *Conference Record of IEEE International Symposium on Electrical Insulation*, vol. 1. IEEE, 1996, pp. 79–82. [Online]. Available: https://doi.org/10.1109/ELINSL.1996.549287

[69] M. Hoof and R. Patsch, "Analyzing partial discharge pulse sequences - a new approach to investigate degradation phenomena," in *Conference Record of IEEE International Symposium on Electrical Insulation*. IEEE, 1994, pp. 327–331. [Online]. Available: https://doi.org/10.1109/elinsl.1994.401501

[70] R. Patsch and F. Berton, "Pulse sequence analysis - A diagnostic tool based on the physics behind partial discharges," *Journal of Physics D: Applied Physics*, vol. 35, no. 1, pp. 25–32, dec 2002. [Online]. Available: https://doi.org/10.1088/0022-3727/35/1/306

[71] Y. Tian, P. L. Lewin, A. E. Davies, S. J. Sutton, and S. G. Swingler, "Partial discharge detection in cables using VHF capacitive couplers," *IEEE Transactions on Dielectrics and Electrical Insulation*, vol. 10, no. 2, pp. 343–353, apr 2003. [Online]. Available: https://doi.org/10.1109/TDEI.2003.1194121

[72] B. A. Fruth and D. W. Gross, "Partial discharge signal conditioning techniques for on-line noise rejection and improvement of calibration," in *Conference Record of IEEE International Symposium on Electrical Insulation*, vol. 1. IEEE, 1996, pp. 397–400. [Online]. Available: https://doi.org/10.1109/elinsl.1996.549365

[73] T. Boczar, "Identification of a specific type of PD from acoustic emission frequency spectra," *IEEE Transactions on Dielectrics and Electrical Insulation*, vol. 8, no. 4, pp. 598–606, aug 2001. [Online]. Available: https://doi.org/10.1109/94.946712

[74] T. Boczar, D. Zmarzly, and P. Fracz, "Comparative Studies of Partial Discharge Using Acoustic Emission Method and Optical Spectroscopy," *IEEE 11th International Conference on the Properties and Applications of Dielectric Materials 2015 (ICPADM)*, pp. 740–743, jul 2015. [Online]. Available: https://doi.org/10.1109/ICPADM.2015.7295378

[75] S. S. Ghoneim and I. B. Taha, "A new approach of DGA interpretation technique for transformer fault diagnosis," *International Journal of Electrical Power and Energy Systems*, vol. 81, pp. 265–274, oct 2016. [Online]. Available: https://doi.org/10.1016/j.ijepes.2016.02.018

[76] O. H. Waagaard, E. Rønnekleiv, A. Haukanes, F. Stabo-Eeg, D. Thingbø, S. Forbord, S. E. Aasen, and J. K. Brenne, "Real-time low noise distributed acoustic sensing in 171 km low loss fiber," *OSA Continuum*, vol. 4, no. 2, p. 688, feb 2021. [Online]. Available: https://doi.org/10.1364/OSAC.408761

[77] A. Masoudi, M. Belal, and T. P. Newson, "A distributed optical fibre dynamic strain sensor based on phase-OTDR," *Measurement Science and Technology*, vol. 24, no. 8, p. 085204, aug 2013. [Online]. Available: https://doi.org/10.1088/0957-0233/24/8/085204

[78] W. Matson, "Wave motion and propagation," in *Earthquakes The sound of multi-modal waves*. IOP Publishing, 2016, ch. 3, pp. 3–1 to 3–20. [Online]. Available: https://doi.org/10.1088/978-1-6817-4329-5ch3

[79] D. Russell, "Longitudinal and Transverse Wave Motion," 2016. [Online]. Available: https://www.acs.psu.edu/drussell/Demos/waves/wavemotion.html

[80] W. Elmore and M. Heald, *Physics of Waves*. New York: Dover Publications, 1985.

[81] D'Alembert, *Histoire de l'Académie royale des sciences et des belles lettres de Berlin*, A. Haude, Ed. Deutsche Akademie der Wissenschaften zu Berlin, 1749, vol. 3. [Online]. Available: https://books.google.co.uk/books?id=lJQDAAAAMAAJ&pg=PA214&redir_esc=y#v=onepage&q&f=false

[82] S. Rienstra and A. Hirschberg, *An introduction to acoustics*, revised ed., Eindhoven, 2021. [Online]. Available: https://www.win.tue.nl/~sjoerdr/papers/boek.pdf

[83] H. Kuttruff, *Acoustics : An Introduction*, 1st ed. CRC Press, nov 2006. [Online]. Available: https://www.taylorfrancis.com/books/9780367807696

[84] C. Zwikker and C. Kosten, *Sound absorbing materials*. Elsevier Publishing, 1949.

[85] Shanghai Tarluz Telecom Tech Co. LTD., "What you should know about Fiber Optic Cable Jacket Material - TARLUZ - FIBER OPTIC SUPPLIERS." [Online]. Available: http://www.tarluz.com/fiber-optic-cable/know-fiber-optic-cable-jacket-material/

[86] N. Totaro, C. Dodard, and J. L. Guyader, "SEA coupling loss factors of complex vibro-acoustic systems," *Journal of Vibration and Acoustics, Transactions of the ASME*, vol. 131, no. 4, pp. 0 410 091–0 410 098, aug 2009. [Online]. Available: https://doi.org/10.1115/1.3086929

[87] G. B. Thomas, "US7263028B2 - Composite acoustic attenuation materials," pp. 8–15, 2006. [Online]. Available: https://patents.google.com/patent/US7263028B2/en

[88] M. Kafesaki and E. N. Economou, "Multiple-scattering theory for three-dimensional periodic acoustic composites," *Physical Review B - Condensed Matter and Materials Physics*, vol. 60, no. 17, pp. 11 993–12 001, nov 1999. [Online]. Available: https://doi.org/10.1103/PhysRevB.60.11993

[89] C. Payan, V. Garnier, J. Moysan, and P. A. Johnson, "Determination of third order elastic constants in a complex solid applying coda wave interferometry," *Applied Physics Letters*, vol. 94, no. 1, p. 011904, jan 2009. [Online]. Available: https://doi.org/10.1063/1.3064129

[90] A. I. Beltzer, *Acoustics of solids*. Springer, 2012. [Online]. Available: https://doi.org/10.1016/0020-7225(90)90067-s

[91] A. Bhatia, *Ultrasonic Absorption: An Introduction to the Theory of Sound Absorption and Dispersion in Gases, Liquids, and Solids*. Dover Publications, 1985. [Online]. Available: https://doi.org/10.1126/science.158.3807.1441

[92] E. Manoha, R. Guenanff, S. Redonnet, and M. Terracol, "Acoustic scattering from complex geometries," in *Collection of Technical Papers - 10th AIAA/CEAS Aeroacoustics Conference*, vol. 2, 2004, pp. 1543–1551. [Online]. Available: https://doi.org/10.2514/6.2004-2938

[93] J. Allard and N. Atalla, *Propagation of Sound in Porous Media: Modelling Sound Absorbing Materials*, 2nd ed. Wiley, 2009.

[94] K.-y. Hashimoto, "Bulk Acoustic and Surface Acoustic Waves," in *Surface Acoustic Wave Devices in Telecommunications*. Berlin, Heidelberg: Springer, 2000, ch. Bulk Acous, pp. 1–23. [Online]. Available: https://doi.org/10.1007/978-3-662-04223-6_1

[95] V. Bucur and I. Böhnke, "Factors affecting ultrasonic measurements in solid wood," *Ultrasonics*, vol. 32, no. 5, pp. 385–390, sep 1994. [Online]. Available: https://doi.org/10.1016/0041-624X(94)90109-0

[96] A. Hartog, *An Introduction to Distributed Optical Fibre Sensors*, 2017. [Online]. Available: https://doi.org/10.1201/9781315119014

[97] R. Acharya, "Interaction of waves with medium," in *Satellite Signal Propagation, Impairments and Mitigation*. Academic Press, jan 2017, pp. 57–86. [Online]. Available: https://doi.org/10.1016/b978-0-12-809732-8.00003-x

[98] X. Bao and L. Chen, "Recent Progress in Distributed Fiber Optic Sensors," pp. 8601–8639, jun 2012. [Online]. Available: https://doi.org/10.3390/s120708601

[99] F. Uyar, I. T. Ozdur, E. Ozbay, and T. Kartaloglu, "Field test and fading measurement of a distributed acoustic sensor system over a 50 km-long fiber," in *Fiber Optic Sensors and Applications XV*, H. H. Du, A. Mendez, and C. S. Baldwin, Eds., vol. 10654. SPIE, may 2018, p. 12. [Online]. Available: https://doi.org/10.1117/12.2304735

[100] N. B. Coltup, L. H. Daly, and S. E. Wiberley, *Introduction to Infrared and Raman Spectroscopy*. Academic Press, 1990.

[101] D. J. Gardiner, "Introduction to Raman Scattering," in *Practical Raman Spectroscopy*. Springer, Berlin, Heidelberg, 1989, pp. 1–12. [Online]. Available: https://doi.org/10.1007/978-3-642-74040-4_1

[102] A. Ukil, H. Braendle, and P. Krippner, "Distributed temperature sensing: Review of technology and applications," *IEEE Sensors Journal*, vol. 12, no. 5, pp. 885–892, 2012. [Online]. Available: https://doi.org/10.1109/JSEN.2011.2162060

[103] F. Suárez, J. E. Aravena, M. B. Hausner, A. E. Childress, and S. W. Tyler, "Assessment of a vertical high-resolution distributed-temperature-sensing system in a shallow thermohaline environment," *Hydrology and Earth System Sciences*, vol. 15, no. 3, pp. 1081–1093, 2011. [Online]. Available: https://doi.org/10.5194/hess-15-1081-2011

[104] G. Bolognini, J. Park, M. A. Soto, N. Park, and F. Di Pasquale, "Analysis of distributed temperature sensing based on Raman scattering using OTDR coding and discrete Raman amplification," *Measurement Science and Technology*, vol. 18, no. 10, pp. 3211–3218, sep 2007. [Online]. Available: https://doi.org/10.1088/0957-0233/18/10/S24

[105] S. W. Tyler, J. S. Selker, M. B. Hausner, C. E. Hatch, T. Torgersen, C. E. Thodal, and S. G. Schladow, "Environmental temperature sensing using Raman spectra DTS fiber-optic methods," *Water Resources Research*, vol. 46, no. 4, pp. 0–23, apr 2009. [Online]. Available: https://doi.org/10.1029/2008WR007052

[106] C. Wolff, M. J. A. Smith, B. Stiller, and C. G. Poulton, "Brillouin scattering—theory and experiment: tutorial," *Journal of the Optical Society of America B*, vol. 38, no. 4, p. 1243, apr 2021. [Online]. Available: https://doi.org/10.1364/JOSAB.416747

[107] H. Moseley, "XCIII. The high-frequency spectra of the elements," *The London, Edinburgh, and Dublin Philosophical Magazine and Journal of Science*, vol. 26, no. 156, pp. 1024–1034, dec 1913. [Online]. Available: https://doi.org/10.1080/14786441308635052

[108] Krishnavedala, "Michelson interferometer with labels.svg - Wikimedia Commons," 2014. [Online]. Available: https://commons.wikimedia.org/wiki/File:Michelson_interferometer_with_labels.svg

[109] M. Lucki, L. Bohac, and R. Zeleny, "Fiber Optic and Free Space Michelson Interferometer — Principle and Practice," in *Optical Sensors - New Developments and Practical Applications*. InTech, mar 2014. [Online]. Available: https://doi.org/10.5772/57149

[110] H. Mueller, "Theory of the photoelastic effect of cubic crystals," *Physical Review*, vol. 47, no. 12, pp. 947–957, jun 1935. [Online]. Available: https://doi.org/10.1103/PhysRev.47.947

[111] M. Tateda and T. Horiguchi, "Advances in optical time domain reflectometry," *Journal of Lightwave Technology*, vol. 7, no. 8, pp. 1217–1224, 1989. [Online]. Available: https://doi.org/10.1109/50.32386

[112] X. Wang, Z. Yan, F. Wang, Z. Sun, C. Mou, X. Zhang, and L. Zhang, "SNR enhanced distributed vibration fiber sensing system employing polarization OTDR and ultraweak FBGs," *IEEE Photonics Journal*, vol. 7, no. 1, pp. 1–11, feb 2015. [Online]. Available: https://doi.org/10.1109/JPHOT.2015.2396010

[113] M. A. Soto, G. Bolognini, F. Di Pasquale, and L. Thévenaz, "Simplex-coded BOTDA fiber sensor with 1 m spatial resolution over a 50 km range," *Optics Letters*, vol. 35, no. 2, p. 259, jan 2010. [Online]. Available: https://doi.org/10.1364/OL.35.000259

[114] M. Taki, Y. Muanenda, C. J. Oton, T. Nannipieri, A. Signorini, and F. Di Pasquale, "Cyclic pulse coding for fast BOTDA fiber sensors." *Optics letters*, vol. 38, no. 15, pp. 2877–80, aug 2013. [Online]. Available: https://doi.org/10.1364/OL.38.002877

[115] M. D. Jones, "Using Simplex Codes to Improve OTDR Sensitivity," *IEEE Photonics Technology Letters*, vol. 5, no. 7, pp. 822–824, jul 1993. [Online]. Available: https://doi.org/10.1109/68.229819

[116] R. Feced, M. Farhadiroushan, and V. A. Handerek, "Zero dead-zone OTDR with high-spatial resolution for short haul applications," *IEEE Photonics Technology Letters*, vol. 9, no. 8, pp. 1140–1142, aug 1997. [Online]. Available: https://doi.org/10.1109/68.605529

[117] G. Yang, X. Fan, Q. Liu, and Z. He, "Increasing the frequency response of direct-detection phase-sensitive OTDR by using frequency division multiplexing," in *25th International Conference on Optical Fiber Sensors*, Y. Chung, W. Jin, B. Lee, J. Canning, K. Nakamura, and L. Yuan, Eds., vol. 10323, Jeju, South Korea, apr 2017, p. 103238F. [Online]. Available: https://doi.org/10.1117/12.2265632

[118] National Instruments, "Understanding FFTs and Windowing Overview." [Online]. Available: https://download.ni.com/evaluation/pxi/UnderstandingFFTsandWindowing.pdf

[119] E. Leviatan and A. Eyal, "High resolution DAS via sinusoidal frequency scan OFDR (SFS-OFDR)," *Optics Express*, vol. 23, no. 26, p. 33318, dec 2015. [Online]. Available: https://doi.org/10.1364/OE.23.033318

[120] G. Li, P. Zhao, and Y. Li, "Spatial-Resolution Improvement in Optical Frequency Domain Reflectometry System Based on Tunable Linear Fiber Laser," *Journal of Physics: Conference Series*, vol. 276, no. 1, p. 012022, feb 2011. [Online]. Available: https://doi.org/10.1088/1742-6596/276/1/012022

[121] X. Fan, Y. Koshikiya, and F. Ito, "Centimeter-level spatial resolution over 40 km realized by bandwidth-division phase-noise-compensated OFDR," *Optics Express*, vol. 19, no. 20, p. 19122, sep 2011. [Online]. Available: https://www.osapublishing.org/oe/abstract.cfm?uri=oe-19-20-19122

[122] N. Saravanakumar and K. Sathiyasekar, "Circular Array of Ultrasonic Sensor based DOA estimation: Location of multiple Partial Discharge in Transformer oil," *Journal of Electromagnetic Waves and Applications*, vol. 32, no. 12, pp. 1569–1585, aug 2018. [Online]. Available: https://doi.org/10.1080/09205071.2018.1456365

[123] C. Thomas, *Array Signal Processing*. New York, NY: Springer New York, 1985. [Online]. Available: https://doi.org/10.1049/pbew015g_ch13

[124] L. G. Taff, "Target localization from bearings-only observations," *IEEE Transactions on Aerospace and Electronic Systems*, vol. 33, no. 1, pp. 2–10, 1997. [Online]. Available: https://doi.org/10.1109/7.570703

[125] G. Ma, W. Qin, C. Shi, H. Zhou, Y. Li, and C. Li, "Electrical Discharge Localization for Gas Insulated Line Based on Distributed Acoustic Sensing," in *Lecture Notes in Electrical Engineering*. Springer, 2020, vol. 598 LNEE, pp. 606–614. [Online]. Available: https://doi.org/10.1007/978-3-030-31676-1_57

[126] T. Kundu, "Acoustic source localization," *Ultrasonics*, vol. 54, no. 1, pp. 25–38, jan 2014. [Online]. Available: https://doi.org/10.1016/j.ultras.2013.06.009

[127] L. E. Kinsler, A. R. Frey, A. B. Coppens, and J. V. Sanders, *Fundamentals of acoustics*, 4th ed. Wiley, 1999, vol. 1. [Online]. Available: https://doi.org/10.1002/9780470612439

[128] J. Hensman, R. Mills, S. G. Pierce, K. Worden, and M. Eaton, "Locating acoustic emission sources in complex structures using Gaussian processes," *Mechanical Systems and Signal Processing*, vol. 24, no. 1, pp. 211–223, jan 2010. [Online]. Available: https://doi.org/10.1016/j.ymssp.2009.05.018

[129] A. Mateeva, J. Lopez, H. Potters, J. Mestayer, B. Cox, D. Kiyashchenko, P. Wills, S. Grandi, K. Hornman, B. Kuvshinov, W. Berlang, Z. Yang, and R. Detomo, "Distributed acoustic sensing for reservoir monitoring with vertical seismic profiling," *Geophysical Prospecting*, vol. 62, no. 4, pp. 679–692, may 2014. [Online]. Available: https://doi.org/10.1111/1365-2478.12116

[130] K. Miah and D. K. Potter, "A review of hybrid fiber-optic distributed simultaneous vibration and temperature sensing technology and its geophysical applications," *Sensors (Switzerland)*, vol. 17, no. 11, pp. 1–25, 2017. [Online]. Available: https://doi.org/10.3390/s17112511

[131] J. Correa, R. Pevzner, A. Bona, K. Tertyshnikov, B. Freifeld, M. Robertson, and T. Daley, "3D vertical seismic profile acquired with distributed acoustic sensing on tubing installation: A case study from the CO2CRC Otway Project," *Interpretation*, vol. 7, no. 1, pp. SA11–SA19, feb 2019. [Online]. Available: https://doi.org/10.1190/INT-2018-0086.1

[132] K. Johannessen, B. Drakeley, and M. Farhadiroushan, "Distributed acoustic sensing - A new way of listening to your well/reservoir," in *Society of Petroleum Engineers - SPE Intelligent Energy International 2012*, vol. 1. OnePetro, mar 2012, pp. 95–103. [Online]. Available: https://doi.org/10.2118/149602-ms

[133] S. K. Bakku, P. Wills, M. Fehler, J. Mestayer, A. Mateeva, and J. Lopez, "Vertical seismic profiling using distributed acoustic sensing in a hydrofrac treatment well," in *SEG Technical Program Expanded Abstracts*, vol. 33. Society of Exploration Geophysicists, 2014, pp. 5024–5028. [Online]. Available: https://doi.org/10.1190/segam2014-1559.1

[134] J. J. Xiao, M. Farhadiroushan, A. Clarke, R. A. Abdalmohsen, E. Alyan, T. R. Parker, J. Shawash, and H. C. Milne, "Intelligent distributed acoustic sensing for in-well monitoring," in *Society of Petroleum Engineers - SPE Saudi Arabia Section Technical Symposium and Exhibition*. OnePetro, apr 2014. [Online]. Available: https://doi.org/10.2118/172197-ms

[135] X. Fan, Z. He, Q. Liu, D. Chen, S. Wang, and G. Yang, "Fiber-optic distributed acoustic sensors (DAS) and applications in railway perimeter security," vol. 10821. International Society for Optics and Photonics, oct 2018, p. 1. [Online]. Available: https://doi.org/10.1117/12.2505342

[136] G. L. Duckworth and E. M. Ku, "OptaSense distributed acoustic and seismic sensing using COTS fiber optic cables for infrastructure protection and counter terrorism," in *Sensors, and Command, Control, Communications, and Intelligence (C3I) Technologies for Homeland Security and Homeland Defense XII*, vol. 8711. International Society for Optics and Photonics, jun 2013, p. 87110G. [Online]. Available: https://doi.org/10.1117/12.2017712

[137] C. Wiesmeyr, M. Litzenberger, M. Waser, A. Papp, H. Garn, G. Neunteufel, and H. Döller, "Real-time train tracking from distributed acoustic sensing data," *Applied Sciences (Switzerland)*, vol. 10, no. 2, p. 448, jan 2020. [Online]. Available: https://doi.org/10.3390/app10020448

[138] K. Hicke and K. Krebber, "Towards efficient real-time submarine power cable monitoring using distributed fibre optic acoustic sensors," in *25th International Conference on Optical Fiber Sensors*, vol. 10323. SPIE, apr 2017, p. 1032390. [Online]. Available: https://doi.org/10.1117/12.2267474

[139] Z. Amira, M. Bouyahi, and T. Ezzedine, "Measurement of Temperature through Raman Scattering," in *Procedia Computer Science*, vol. 73. Elsevier, jan 2015, pp. 350–357. [Online]. Available: https://doi.org/10.1016/j.procs.2015.12.003

[140] K. Miah and D. K. Potter, "A review of hybrid fiber-optic distributed simultaneous vibration and temperature sensing technology and its geophysical applications," *Sensors (Switzerland)*, vol. 17, no. 11, p. 2511, nov 2017. [Online]. Available: https://doi.org/10.3390/s17112511

[141] W. Zou, Z. He, and K. Hotate, "Demonstration of Brillouin Distributed Discrimination of Strain and Temperature Using a Polarization-Maintaining Optical Fiber," *IEEE Photonics Technology Letters*, vol. 22, no. 8, pp. 526–528, apr 2010. [Online]. Available: https://doi.org/10.1109/LPT.2010.2041922

[142] S. M. Maughan, H. H. Kee, and T. P. Newson, "Simultaneous distributed fibre temperature and strain sensor using microwave coherent detection of spontaneous brillouin backscatter," *Measurement Science and Technology*, vol. 12, no. 7, pp. 834–842, jul 2001. [Online]. Available: https://doi.org/10.1088/0957-0233/12/7/315

[143] Y. Rolain, J. Dunsmore, J. Schoukens, W. Van Moer, and G. Vandersteen, "Wave distorsion in multiplying, switching or sampling mixers," in *73rd ARFTG Microwave Measurement Conference Spring 2009 - Practical Applications of Nonlinear Measurements*, 2009. [Online]. Available: https://doi.org/10.1109/ARFTG.2009.5278081

[144] Q. Che, H. Wen, X. Li, Z. Peng, and K. P. Chen, "Partial Discharge Recognition Based on Optical Fiber Distributed Acoustic Sensing and a Convolutional Neural Network," *IEEE Access*, pp. 1–1, 2019. [Online]. Available: https://doi.org/10.1109/ACCESS.2019.2931040

[145] J. Deng, H. Xiao, W. Huo, M. Luo, R. May, A. Wang, and Y. Liu, "Optical fiber sensor-based detection of partial discharges in power transformers," *Optics and Laser Technology*, vol. 33, no. 5, pp. 305–311, jul 2001. [Online]. Available: https://doi.org/10.1016/S0030-3992(01)00022-6

[146] B. Yu, D. W. Kim, J. Deng, H. Xiao, and A. Wang, "Fiber Fabry-Perot sensors for detection of partial discharges in power transformers," *Applied Optics*, vol. 42, no. 16, p. 3241, jun 2003. [Online]. Available: https://doi.org/10.1364/ao.42.003241

[147] P. Rohwetter, R. Eisermann, and K. Krebber, "Distributed acoustic sensing: towards partial discharge monitoring," in *24th International Conference on Optical Fibre Sensors*, vol. 9634. SPIE, sep 2015, p. 96341C. [Online]. Available: https://doi.org/10.1117/12.2194850

[148] J. Posada-Roman, J. A. Garcia-Souto, and J. Rubio-Serrano, "Fiber optic sensor for acoustic detection of partial discharges in oil-paper insulated electrical systems," *Sensors*, vol. 12, no. 4, pp. 4793–4802, apr 2012. [Online]. Available: https://doi.org/10.3390/s120404793

[149] D. Siebler, M. Hohberg, P. Rohwetter, R. Brusenbach, and R. Plath, "Elastomeric fluorescent POF for partial discharge detection: recent progress," in *24th International Conference on Optical Fibre Sensors*, vol. 9634. SPIE, sep 2015, p. 96343W. [Online]. Available: https://doi.org/10.1117/12.2194875

[150] Y. Tian, P. L. Lewin, A. E. Davies, and Z. Richardson, "Acoustic emission detection of partial discharges in polymeric insulation," in *Eleventh International Symposium on High Voltage Engineering*, vol. 1, no. 467. IEE, 1999. [Online]. Available: https://doi.org/10.1049/cp:19990513

[151] A. E. Alekseev, B. G. Gorshkov, V. T. Potapov, M. A. Taranov, and D. E. Simikin, "Dual-pulse phase-OTDR response to propagating longitudinal disturbance," *Laser Physics*, vol. 30, no. 3, p. 035107, feb 2020. [Online]. Available: https://doi.org/10.1088/1555-6611/AB70B0

[152] M. Nakazawa, "Rayleigh backscattering theory for single-mode optical fibers," *Journal of the Optical Society of America*, vol. 73, no. 9, p. 1175, sep 1983. [Online]. Available: https://doi.org/10.1364/JOSA.73.001175

[153] Free Libre and Open Source Software in Education, "Python Optical Fibers & Fiber Cables." [Online]. Available: https://tbc-python.fossee.in/convert-notebook/Textbook_on_Optical_Fiber_Communication_and_Its_Applications_by_S._C._Gupta/Chapter2.ipynb

[154] S. C. Gupta, *Textbook on Optical Fiber Communication and Its Applications*. Prentice-Hall of India, 2004. [Online]. Available: https://books.google.co.uk/books/about/Textbook_on_Optical_Fiber_Communication.html?id=isk67iZ847MC

[155] D. Audiotechnik, "ArrayCalc | d&b audiotechnik," 2021. [Online]. Available: https://www.dbaudio.com/global/en/products/software/arraycalc/https://www.dbaudio.com/global/es/products/software/arraycalc/#tab-downloads

[156] Comsol Inc., "Simulation Software for Analyzing Acoustics and Vibrations," 2019. [Online]. Available: https://uk.comsol.com/acoustics-modulehttps://www.comsol.com/acoustics-module#acoustic-behavior

[157] E. Bossy, "SimSonic: free fdtd software for the simulation of ultrasonic waves propagation." [Online]. Available: http://www.simsonic.fr/index.php

[158] E. Bossy and Q. Grimal, "Numerical methods for ultrasonic bone characterization," in *Bone Quantitative Ultrasound*. Springer, Dordrecht, 2011, pp. 181–228. [Online]. Available: https://doi.org/10.1007/978-94-007-0017-8_8

[159] E. Bossy, "SimSonic Suite User's guide for SimSonic3D," pp. 1–28, 2012. [Online]. Available: https://www.simsonic.fr/downloads/SimSonic2D_UserGuide.pdf

[160] HDF Group, "HDF5 File Format Specification Version 3.0," 2016. [Online]. Available: https://support.hdfgroup.org/HDF5/doc/H5.format.html

[161] T. Sakoda, T. Arita, H. Nieda, and K. Ando, "Analysis of acoustic emissions caused by the partial discharge in the insulation oil," *IEEE International Conference on Conduction and Breakdown in Dielectric Liquids, ICDL*, pp. 483–486, 1999. [Online]. Available: https://doi.org/10.1109/icdl.1999.798977

[162] R. T. Harrold, "Acoustic Theory Applied to the Physics of Electrical Breakdown in Dielectrics," *IEEE Transactions on Electrical Insulation*, vol. EI-21, no. 5, pp. 781–792, 1986. [Online]. Available: https://doi.org/10.1109/TEI.1986.348925

[163] G. Paoletti and A. Golubev, "Partial discharge theory and applications to electrical systems," in *Conference Record of 1999 Annual Pulp and Paper Industry Technical Conference (Cat. No.99CH36338)*. IEEE, pp. 124–138. [Online]. Available: http://ieeexplore.ieee.org/document/779355/

[164] R. J. Densley, "An investigation into the growth of electrical trees in XLPE cable insulation," *IEEE Transactions on Electrical Insulation*, vol. EI-14, no. 3, pp. 148–158, 1979. [Online]. Available: https://doi.org/10.1109/TEI.1979.298215

[165] P. H. F. Morshuis, "Partial Discharge Mechanism: Mechanism leading to breakdown, analyzed by fast electrical and optical measurements," Ph.D. dissertation, Delft University, 1993. [Online]. Available: https://resolver.tudelft.nl/uuid:5e39ece9-bcb1-40e0-8501-cfb963873a78

[166] M. Hikita, M. Kozako, H. Takada, M. Higashiyama, T. Hirose, S. Nakamura, and T. Umemura, "Partial discharge phenomena in artificial cavity in epoxy cast resin insulation system," in *Conference Record of IEEE International Symposium on Electrical Insulation*, 2010. [Online]. Available: https://doi.org/10.1109/ELINSL.2010.5549549

[167] Anycubic, "Anycubic Photon LCD/DLP/SLA 3D Printer," 2020. [Online]. Available: https://www.anycubic.com/collections/3d-printers/products/anycubic-photon-3d-printer

[168] Cigre Working Group D.129, "Partial discharges in transformers," 2017.

[169] CIGRE Study Committee A2, "Dynamic Thermal Behaviour of Power Transformers," CIGRE, Tech. Rep. 1, 2017.

[170] E. Gockenbach, P. Werle, and H. Borsi, "Monitoring and diagnostic systems for dry type transformers," in *IEEE International Conference on Conduction and Breakdown in Solid Dielectrics*, 2001, pp. 291–294. [Online]. Available: https://doi.org/10.1109/icsd.2001.955628

[171] H. Zainuddin, P. L. Lewin, and P. M. Mitchinson, "Partial discharge characteristics of surface tracking on oil-impregnated pressboard under AC voltages," in *Proceedings of IEEE International Conference on Solid Dielectrics, ICSD*, 2013, pp. 1016–1019.

[172] P. M. Mitchinson, P. L. Lewin, B. D. Strawbridge, and P. Jarman, "Tracking and surface discharge at the oilpressboard interface," *IEEE Electrical Insulation Magazine*, vol. 26, no. 2, pp. 35–41, mar 2010. [Online]. Available: https://doi.org/10.1109/MEI.2010.5482553

[173] P. M. Mitchinson, P. L. Lewin, G. Chen, and P. N. Jarman, "A new approach to the study of surface discharge on the oil-pressboard interface," in *2008 IEEE International Conference on Dielectric Liquids, ICDL 2008*, 2008.

[174] B. W. Isah, H. Mohamad, and N. R. Ahmad, "Rock stiffness measurements fibre Bragg grating sensor (FBGs) and the effect of cyanoacrylate and epoxy resin as adhesive materials," *Ain Shams Engineering Journal*, vol. 12, no. 2, pp. 1677–1691, jun 2021.

[175] H. Zainuddin, "Study of Surface Discharge Behaviour at the Oil-Pressboard Interface," Ph.D. dissertation, University of Southampton, 2013. [Online]. Available: https://eprints.soton.ac.uk/361715/1/Zainuddin.pdf

[176] V. Salov, "Notation for Iteration of Functions, Iteral," Tech. Rep., 2012. [Online]. Available: http://arxiv.org/abs/1207.0152

[177] L. Williams, "PYRAMIDAL PARAMETRICS." in *Computer Graphics (ACM)*, vol. 17, no. 3. New York, New York, USA: ACM Press, 1983, pp. 1–11. [Online]. Available: https://doi.org/10.1145/964967.801126

[178] P. Kundu, N. K. Kishore, and A. K. Sinha, "Simulation and analysis of acoustic wave propagation due to partial discharge activity," in *Annual Report - Conference on Electrical Insulation and Dielectric Phenomena, CEIDP*, 2006, pp. 607–610. [Online]. Available: https://doi.org/10.1109/CEIDP.2006.312005

[179] M. R. Hussain, S. S. Refaat, and H. Abu-Rub, "Overview and Partial Discharge Analysis of Power Transformers: A Literature Review," pp. 64 587–64 605, 2021. [Online]. Available: https://doi.org/10.1109/ACCESS.2021.3075288

[180] AnyCubic, "Colored UV Resin 1L - ANYCUBIC," 2020. [Online]. Available: https://www.anycubic.com/collections/uv-resin/products/colored-uv-resin-for-photon-series?variant=30151434895420